



VNIVERSITAT E VALÈNCIA

**Solid-state mechanochemical synthesis of multinary  
metal halide semiconductors for optoelectronics:  
From powder to thin film**



**Yusra El Ajjouri**

Doctoral Thesis in Nanoscience and Nanotechnology

Directors:

Prof. Dr. Hendrik Jan Bolink

Dr. Francisco Palazón

June 2020











VNIVERSITAT DE VALÈNCIA

**Solid-state mechanochemical synthesis of  
multinary metal halide semiconductors for  
optoelectronics: From powder to thin film**

Doctoral thesis submitted by

**Yousra El Ajjouri**

to apply for the degree of Doctor in Nanoscience and Nanotechnology

Directors:

Prof. Dr. Hendrik Jan Bolink

Dr. Francisco Palazón

Molecular Opto-Electronic Devices Group

Institute of Molecular Science

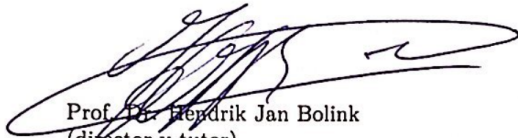
University of Valencia

June 2020




Prof. Dr. Hendrik Jan Bolink y Dr. Francisco Palazón, investigadores de la Universidad de Valencia en el Instituto de Ciencia Molecular (ICMol), certifican que la memoria presentada por la doctoranda Yusra El Ajjouri con el título “Solid-state mechanochemical synthesis of multinary metal halide semiconductors for optoelectronics: From powder to thin film” corresponde a su Tesis Doctoral y ha sido realizada bajo su dirección, autorizando mediante este escrito la presentación de la misma.

En Valencia, a 11 de junio del 2020



Prof. Dr. Hendrik Jan Bolink  
(director y tutor)



Dr. Francisco Palazón  
(director)



*"Anything that works against you can also work for you  
once you understand the Principle of Reverse."*

*Maya Angelou*





# Table of Contents

Acknowledgments	XI
Abstract	XII
<b>1 Introduction</b>	<b>1</b>
1.1 Multinary metal halide semiconductors	1
1.1.1 Perovskites	1
1.1.2 Non-perovskites	4
1.2 Mechanochemical synthesis of multinary metal halides	5
1.2.1 Synthesis of dry powdered, high-purity lead halide perovskites	7
1.2.2 Investigation of mixed-composition halide perovskites	9
1.2.3 Formation of other lead-free multinary metal halides	10
1.3 Thin film formation technologies	11
1.3.1 Solution-processing techniques	11
1.3.2 Thermal vacuum deposition techniques	13
1.4 Aim and overview of the thesis	17
<b>2 Methodology and characterization techniques</b>	<b>18</b>
2.1 Methodology	18
2.2 Characterization techniques	20
2.2.1 X-ray diffraction	20
2.2.2 Optical characterization techniques	23
2.2.3 Photoelectron spectroscopy	24
2.2.4 Electron microscopy	25
2.2.5 Thermal analysis	25
2.2.6 Pulse-radiolysis time-resolved microwave conductivity	26
<b>3 Mechanochemical Synthesis of Inorganic Halide Perovskites: Evolution of Phase-purity, Morphology and Photoluminescence</b>	<b>27</b>
3.1 Introduction	27
3.2 Experimental methods	28
3.2.1 Mechanochemical synthesis via ball-milling	28
3.2.2 Characterization	28
3.3 Results and discussion	29
3.4 Conclusions	33
3.5 Author contribution and acknowledgments	34
<b>4 Incorporation of Potassium Halides in the Mechanochemical Synthesis of Inorganic Perovskites: Feasibility and Limitations of Ion-replacement and Trap Passivation</b>	<b>35</b>
4.1 Introduction	35
4.2 Experimental methods	36
4.2.1 Mechanochemical synthesis via ball-milling	36
4.2.2 Characterization	36
4.3 Results and discussion	37
4.4 Conclusions	40
4.5 Author contribution and acknowledgments	40

<b>5</b>	<b>Mechanochemical Synthesis of Sn(II) and Sn(IV) Iodide Perovskites and Study of Their Structural, Chemical, Thermal, Optical and Electrical Properties</b>	<b>41</b>
5.1	Introduction . . . . .	41
5.2	Experimental methods . . . . .	43
5.2.1	Mechanochemical synthesis via ball-milling . . . . .	43
5.2.2	Characterization . . . . .	43
5.3	Results and discussion . . . . .	44
5.4	Conclusions . . . . .	52
5.5	Author contribution and acknowledgments . . . . .	52
<b>6</b>	<b>Low-Dimensional Non-Toxic <math>A_3Bi_2X_9</math> Compounds Synthesized by a Dry Mechanochemical Route with Tunable Visible Photoluminescence at Room Temperature</b>	<b>53</b>
6.1	Introduction . . . . .	53
6.2	Experimental methods . . . . .	55
6.2.1	Mechanochemical synthesis via ball-milling . . . . .	55
6.2.2	Characterization . . . . .	55
6.3	Results and discussion . . . . .	56
6.4	Conclusions . . . . .	61
6.5	Author contribution and acknowledgments . . . . .	61
<b>7</b>	<b>Single-Source Vacuum Deposition of Mechanochemically- Synthesized Inorganic Halide Perovskites</b>	<b>62</b>
7.1	Introduction . . . . .	62
7.2	Experimental methods . . . . .	62
7.2.1	Mechanochemical synthesis via ball-milling . . . . .	62
7.2.2	Single-source vacuum deposition . . . . .	63
7.2.3	Characterization . . . . .	63
7.3	Results and discussion . . . . .	63
7.4	Conclusions . . . . .	68
7.5	Author contribution and acknowledgments . . . . .	68
<b>8</b>	<b>General conclusions and outlook</b>	<b>69</b>
<b>9</b>	<b>Resumen en castellano</b>	<b>71</b>
	<b>Appendices</b>	<b>81</b>
	<b>Appendix A</b>	<b>83</b>
	<b>Appendix B</b>	<b>93</b>
	<b>Appendix C</b>	<b>102</b>
	<b>Appendix D</b>	<b>119</b>
	<b>Appendix E</b>	<b>129</b>
	<b>List of Publications</b>	<b>139</b>
	<b>List of Figures</b>	<b>141</b>
	<b>List of Tables</b>	<b>145</b>
	<b>List of Abbreviations and Symbols</b>	<b>146</b>
	<b>Bibliography</b>	<b>149</b>





# Acknowledgments

I would like to express my gratitude for having been part of the Molecular Opto-Electronic Devices Group at the Institute of Molecular Science of the University of Valencia, Spain. My experience in this research facility has thought me many lessons, both on a professional, as well as on a personal level. This doctoral thesis is the end product of research of the past three years, that surely would not have been possible without the continuous help, advice, trust and support of my thesis director Prof. Dr. Henk Bolink. I would like to thank Dr. Afshin Hadipour for having introduced me to the person who has been an incredible boss, whom I could rely on much-appreciated, honest and straightforward feedback. I absolutely do not take for granted to have been guided by such an enthusiastic and kind-hearted scientist. I'm also thankful for having had the opportunity to conduct research overseas at Northwestern University, Illinois, which has been an incredible experience. Henk, I think it is safe to say that it has been a rocky road with quite some unforeseen, yet inspiring events and thus having been able to express myself in my mother tongue was a blessing in the midst of it all. *Vanuit de grond van m'n hart, bedankt voor alles!*

Special thanks go to my supervisor Dr. Francisco Palazón for his constructive feedback and guidance throughout this journey. The numerous fruitful discussions have truly helped in extending my knowledge and in becoming a better researcher. Paco, I appreciate the support and effort in bringing this thesis to a good end.

I would like to thank Dr. Michele Sessolo for the interesting discussions and his willingness to help wherever possible. I'm grateful for his patience and understanding he has offered during the years. My appreciation goes to Alejandra Soriano for teaching me about XRD and for her willingness to help in the measurements. I would like to show my gratitude towards my colleagues. The diversity of the group has brought up many interesting events. Special thanks go to Isi for the many laughs and her listening ear, which I take very much to heart. Thanks to Kassio, Nathan, Lidón, Lorenzo, Ana and Abhi for the every-day positive vibes, for their optimism and ability to create a happy atmosphere. I would also like to thank my dear friend Sam Smedts for his incredible creative mind and helping hand in the design of the thesis cover.

Thanks to my roommates and all my friends in Belgium and overseas for the long distance love and support. They have been through thick and thin with me. I thank them for having been part of this amazing experience, for the many laughs and heart-warming, tear-catching hugs.

Finally, I would like to express my appreciation to my family for their support and unconditional love. This thesis and all of my accomplishments in life would not have been possible without them. Thank you for always having been present in times of need.

Thanks to everyone who has been part of this journey.

*Yousra El Ajjouri*

# Abstract

In the past decade, lead halide perovskites, as well as other multinary metal halides – including lead-free alternatives – have shown to be promising materials for their use in optoelectronics. Therefore, new ways of producing high-purity semiconductors in large scale are actively sought after. Hence, the main aim of this doctoral thesis is the development of perovskites and related semiconductors using solvent-free methods. Furthermore, with the prospect of the use of such materials in optoelectronics on an industrial scale, the focus is put on working with benign materials for the development of alternatives to toxic perovskites. Mechanochemical synthesis has recently emerged as a highly convenient and reliable method to obtain high-quality lead halide perovskites, as well as other lead-free multinary metal halides. Hence, this thesis contributes to a material study for the development of perovskites and related materials via a solvent-free mechanochemical route and the investigation of the fundamental characteristics thereof. Furthermore, with the interest in the implementation of these high-purity semiconductors in optoelectronics – besides a material study – this thesis contributes to the investigation of a novel manner for the fabrication of thin film perovskites via single-source vacuum deposition of mechanochemically-synthesized perovskite powders. As such, this work paves the way to a new manner for both understanding the formation of perovskites, as well as an alternative way for thin film development with the prospect of the fabrication of applications in the field of optoelectronics.







# Chapter 1

## Introduction

In the past decades, technology as a whole has grown tremendously, both in interest as well in actual performance, due to the fact that it extends the limits of human beings' capacity and furthermore, offers a series of possibilities towards an improved and sustainable living. More specifically, optoelectronics play a crucial role in both day to day life, as well as in more advanced research areas. This branch of technology concerns the investigation and application of electronics that imply light, either as a source or as a way of detection and control through semiconductors. Hence, optoelectronics can even be seen as a “cultural” technology, since it connects the world by offering the ability to observe, display, store, share and enlighten. Due to the high importance and interest in this field, extensive research is done on semiconducting materials for the development of devices that convert electric energy into light or the reverse, light into electric energy. Among others, this concerns applications in the photovoltaic industry, more specifically solar cells – where solar light is used as the energy source for the production of electricity – as well as photodetectors with the view on applications in for instance the medical field and light-emitting diodes (LEDs), which can be implemented in smart technological devices, such as electronic wearables, smart phones and displays.

### 1.1 Multinary metal halide semiconductors

#### 1.1.1 Perovskites

Over the past decade, a huge interest has been shown towards metal halide perovskites as the active semiconducting material in optoelectronic devices, due to their promising optical and electronic properties. The term “perovskite” stems from calcium titanate ( $\text{CaTiO}_3$ ) that was discovered by Gustav Rose in 1839 in the Ural Mountains of Russia. This mineral, as well as a class of compounds with the same crystal structure as  $\text{CaTiO}_3$  ( $\text{ABX}_3$ ) are named perovskites, after the Russian mineralogist Lev Perovski [1]. In this perovskite structure  $\text{ABX}_3$ ,  $A$  and  $B$  are cations and  $X$  is an anion. The most common perovskites are oxides, although a division is made in perovskite structures composed of ternary metal halides, where in this particular case,  $A$  stands for a monovalent cation,  $B$  a divalent metal (e.g.  $\text{Pb}^{2+}$ ,  $\text{Sn}^{2+}$  and  $\text{Ge}^{2+}$ ) and  $X$  a monovalent halide anion (commonly  $\text{I}^-$ ,  $\text{Br}^-$  or  $\text{Cl}^-$ ). As shown in Figure 1.1, the cubic perovskite crystal structure is composed of corner-sharing  $[\text{BX}_6]^{4-}$  octahedra with an interstitial A-cation.

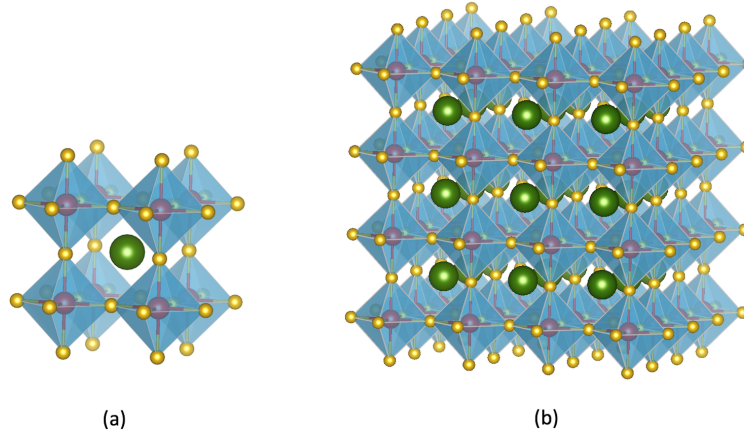


Figure 1.1: Illustration of (a) a unit cell composed of eight corner-sharing  $[BX_6]^{4-}$  octahedra intercalated with an A-cation (b) a repetition of the unit cell in three dimensions. The A and B cations are presented as green and red balls, respectively; whereas the X anion is presented as yellow balls. The ion size depicted is arbitrary.

To obtain a stable cubic  $ABX_3$  perovskite, the A-cation must fit in the cavities created by the inorganic lattice ( $[BX_6]^{4-}$  octahedra). An indicator of the structure's stability is given by the Goldschmidt tolerance factor ( $t$ ). It is generally accepted that the tolerance factor should not be lower than 0.8, nor exceed a value of 1 in order for the compound to be stable. A  $t$ -value outside of this range usually results in non-perovskite structures. The tolerance factor is calculated according to Equation 1.1, where  $r_A$ ,  $r_B$  and  $r_X$ , respectively, stand for the ionic radii of the cation A, metal B and anion X in the  $ABX_3$  perovskite structure [2, 3].

$$t = \frac{r_A + r_X}{\sqrt{2}(r_B + r_X)} \quad (1.1)$$

Cesium ( $\text{Cs}^+$ ), methylammonium ( $\text{MA}/\text{CH}_3\text{NH}_3^+$ ) and formamidinium ( $\text{FA}/\text{CH}(\text{NH}_2)_2^+$ ) are commonly-employed cations to form stable three-dimensional (3D)  $ABX_3$  halide perovskites. Figure 1.2 shows the tolerance factor of lead halide perovskites (LHPs) as a function of the A-cation ionic radius ( $r_A$ ).

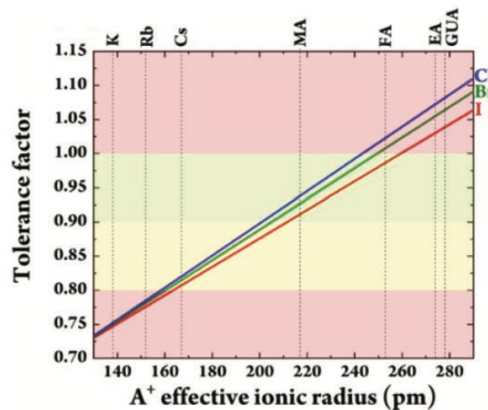


Figure 1.2: Goldschmidt tolerance factor (see Equation 1.1) of lead halide perovskites as a function of the A-cation ionic radius ( $r_A$ ). The ionic radii for different reported atoms and molecules were obtained from R. Shannon et al. [4] and G. Kieslich et al. [5]. EA and GUA stand for ethylammonium and guanidinium, respectively.

As previously mentioned, one of the reasons for the high popularity of metal halide perovskites is based on their attractive photo-physical properties. These characteristics include a high absorption coefficient (the amount of light absorbed by a given thickness of the material), a narrow photoluminescence (PL) spectrum, as well as a high photoluminescence quantum yield (PLQY, the amount of photons emitted per absorbed photons) [6–11]. Furthermore, by varying the perovskite composition, the optical bandgap can be tuned from the near-ultraviolet (near-UV) to the near-infrared (NIR) region of the solar spectrum [12–18]. As such, materials can be obtained with ideal characteristics for the desired application in the field of optoelectronics. Changing the perovskite composition includes substituting and mix-matching the cation component, halide elements, as well as the metal part of the crystal structure. Hence, through this way, novel complex and composed perovskite materials have been investigated [2, 15–17, 19–30]. To illustrate the effect of halide modification on the optical characteristics of the semiconducting material, the perovskite cesium lead halide ( $\text{CsPbX}_3$ ) is taken as an example, where the halide  $X$  is a chloride ( $\text{Cl}^-$ ), bromide ( $\text{Br}^-$ ) or iodide ( $\text{I}^-$ ) anion. Figure 1.3a shows a clear effect of the halide composition on the photoluminescence spectrum of the relevant perovskite; that is a decreased bandgap with increasing anion size. This observation is explained by the molecular orbitals of the perovskite structure. While the conduction band is mostly determined by the p-orbitals of lead, the valence band results from the antibonding orbitals of hybridized Pb s- and X p-orbitals (where  $X$  is the halide) [31–34]. Hence, halide exchange from  $\text{I}^-$  to  $\text{Br}^-$  to  $\text{Cl}^-$  results in a deeper valence band maximum (VBM) as represented in Figure 1.3b and thus an increase in the bandgap.

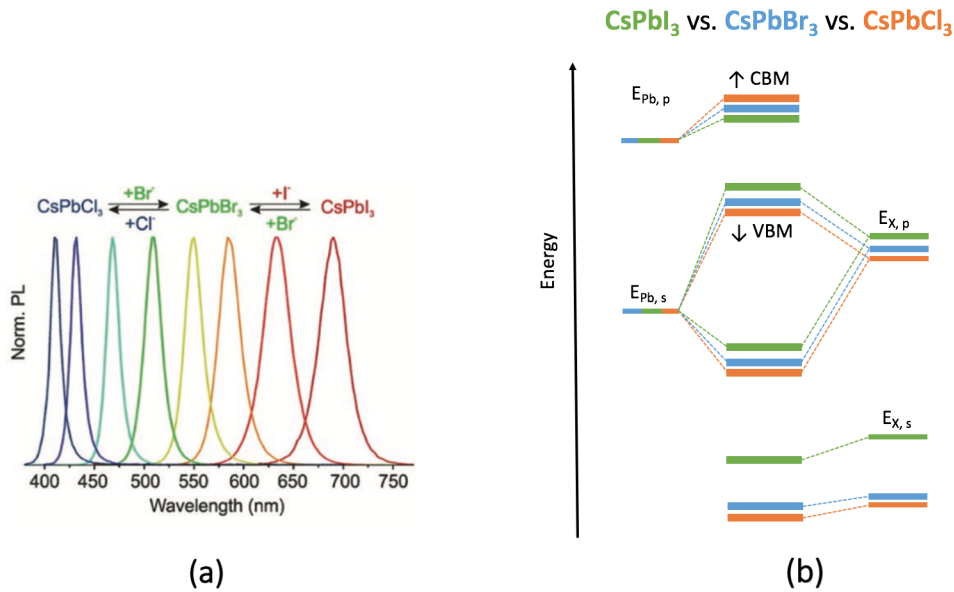


Figure 1.3: (a) Anion-exchange allows to tune the bandgap of halide perovskites across the whole visible range. This illustration is adapted from reference [35]. (b) Orbital diagram of  $\text{CsPbI}_3$  (green),  $\text{CsPbBr}_3$  (blue) and  $\text{CsPbCl}_3$  (orange). The abbreviations CBM and VBM stand for conduction band maximum and valence band maximum, respectively. This illustration is adapted from reference [31].

Whereas modifying the halide anion part of the perovskite structure has a prominent effect on the photo-physical properties of the semiconducting material, also changes on the level of the A-cation of the perovskite indirectly affect the bandgap slightly. When the A-cation is exchanged for a cation of a larger size (e.g. going from  $\text{Cs}^+$  to MA to FA), the volume of the  $\text{ABX}_3$  lattice or the distortion of the framework increase, which increase the ionization energy and the electron affinity [31]. As a result, for a fixed halide perovskite, the bandgap decreases with increasing cation size (e.g. going from  $\text{Cs}^+$  to MA to FA) [31]. More examples of perovskite compositional modifications will be given in Subsection 1.2.2.

### 1.1.2 Non-perovskites

Whereas a perovskite crystal lattice – with the general  $ABX_3$  stoichiometry – is composed of a network of corner-sharing  $[BX_6]^{4-}$  octahedra, many deviations from this stoichiometry can be made. Modifications on the level of the A- and/or B-site cations enable this. Hence, different types of crystal structures can be obtained.

Vacancy-ordered perovskites are crystal structures where the B-cation is partially replaced by a vacancy [36]. Such vacancy-ordered perovskites include  $Cs_2SnI_6$  (see Chapter 5), where half of the B-cations are occupied by Sn(IV) and the other half by vacancies (see Figure 1.4a). Also trivalent metals, such as Bi(III) can form vacancy-ordered perovskites (see Chapter 6). However, in this case the B-sites are not equally divided between the metal and the vacancies. In contrary, these sites are occupied in a 2:1 ratio, which results in a  $A_3B_2X_9$  stoichiometry [36]. These crystal structures form a two-dimensional (2D) layer of  $BX_6$ -octahedra, where the vacancies are ordered along the  $[111]$  planes (see Figure 1.4b). It must be noted that not all  $A_3B_2X_9$  stoichiometries give rise to a vacancy-ordered perovskite phase. For instance,  $Cs_3Bi_2I_9$  (see Chapter 6) is known to crystallize in a non-perovskite phase. This phenomenon is related to the Goldschmidt tolerance factor (see Subsection 1.1.1), indicating the geometrical stability of the perovskite [37–39]. As stated previously, A-site cations that are either too small or too large for the metal halide network, make the halide perovskite framework collapse [40]. In the case of  $Cs_3Bi_2I_9$ , two face-sharing  $BiI_6$ -octahedra give rise to  $[Bi_2I_9]^{3+}$  dimers, separated by  $Cs^+$  ions, which results in a hexagonal zero-dimensional (0D) ternary metal halide (see Figure 1.4c) [41]. Furthermore, other Cs-Bi-X compounds can crystallize in the  $Cs_3BiX_6$  phase, composed of single  $BX_6$ -octahedra [36, 42]. Besides the  $A_3B_2X_9$  stoichiometry, also the  $ABX_3$  stoichiometry can result in non-perovskite structures when the A-cation size does not meet the criteria for the geometrical restrictions upon forming stable perovskites. In the case of A-cations that are too small to stabilize the perovskite structure – which is the case for  $CsPbI_3$  or  $RbPbBr_3$  (see Figure 1.4d) – the material crystallizes in either one-dimensional (1D) or 2D edge-sharing octahedral lattices. On the other hand, when the A-site cation is too large – which is the case for  $FAPbI_3$  – a 1D face-sharing crystal lattice is formed [36].

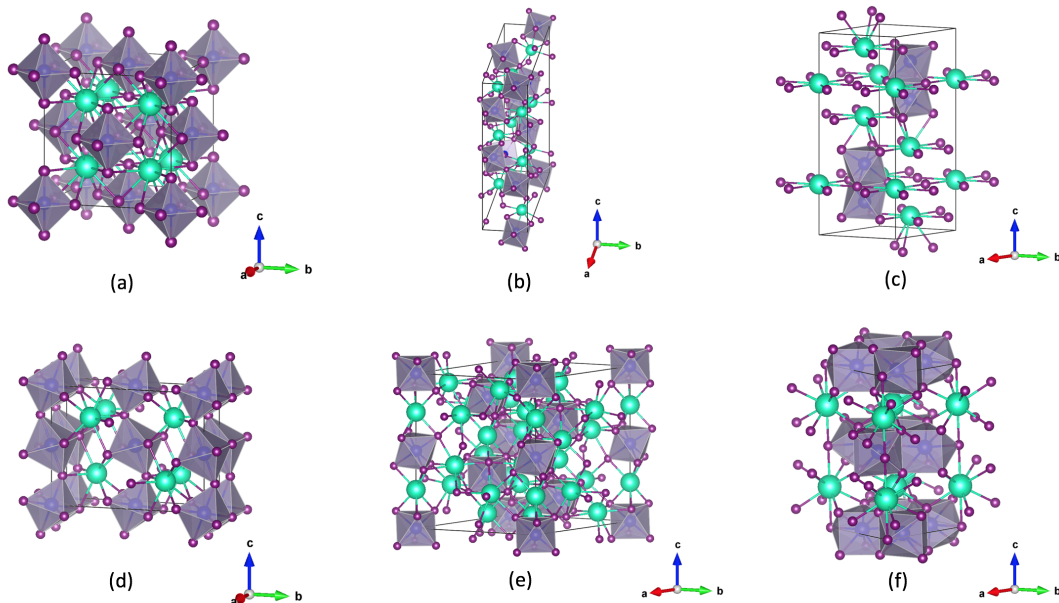


Figure 1.4: Unit cell illustrations of (a)  $Cs_2SnI_6$ , (b)  $Rb_3Bi_2I_9$ , (c)  $Cs_3Bi_2I_9$ , (d)  $RbPbBr_3$ , (e)  $Cs_4PbBr_6$  and (f)  $CsPb_2Br_5$ . In all unit cells, the A-cation is presented as a turquoise ball, the B-cation as a blue ball and the halide anion as a purple ball. The ion size depicted is arbitrary.

Other inorganic ternary B(II) halides (based on  $\text{Pb}^{2+}$  and  $\text{Sn}^{2+}$  ions) can also crystallize in other phases, which are considered non-perovskite structures. For example, the  $\text{A}_4\text{BX}_6$  phase is formed in the case of  $\text{Cs}_4\text{PbBr}_6$  (see Chapter 3), forming a so-called “0D perovskite”, where the  $\text{BX}_6$ -octahedra are not in the same crystallographic positions as the  $\text{A}_2\text{BX}_6$  vacancy-ordered perovskites (see Figure 1.4e) [36, 39, 43]. An additional difference is that the A-cations occupy two different crystallographic sites [36, 44]. As a result, the name “perovskite” is rather arbitrary in the case of the  $\text{A}_4\text{BX}_6$  phase. The  $\text{AB}_2\text{X}_5$  phase (e.g.  $\text{CsPb}_2\text{Br}_5$ ; see Chapter 3) is another ternary phase, which is often referred to as a “2D perovskite” [36]. This material crystallizes as a stack of layers of connected  $[\text{B}_2\text{X}_5]^+$  clusters that are separated by layers of  $\text{Cs}^+$  ions (see Figure 1.4f) [36, 45]. Thus, the framework does not contain  $\text{BX}_6$ -octahedra, which makes it rather inappropriate to call this phase a “perovskite”. However, regardless of this fact, these non-perovskite structures ( $\text{Cs}_4\text{PbBr}_6$  and  $\text{CsPb}_2\text{Br}_5$ ) have drawn attention due to their narrow green photoluminescence spectra [36, 39, 43].

Finally, a division can be made for hybrid organic-inorganic layered metal halides. In the presence of long-chain ammonium (LA) cations, the structure consists of an alternation of layers of corner sharing  $\text{BX}_6$ -octahedra with layers of these large cations. As such, 2D structures with the formula  $(\text{LA})_2\text{PbX}_4$  are formed. Furthermore, low-dimensional perovskites are not restricted to long-chain ammonium cations. Along with the presence of these, short-chain ammonium (SA) cations can accommodate the inorganic framework of the perovskite structure and are commonly known as quasi-2D or Ruddlesden-Popper perovskites with the generic formula  $(\text{LA})_2(\text{SA})_{n-1}\text{Pb}_n\text{X}_{3n+1}$  (see Figure 1.5) [46–53]. In this formula,  $n$  stands for the thickness of the inorganic framework and thus the amount of  $[\text{BX}_6]^{4-}$  octahedra layers that are separated by the long-chain cations and where the short-chain cations intercalate with.

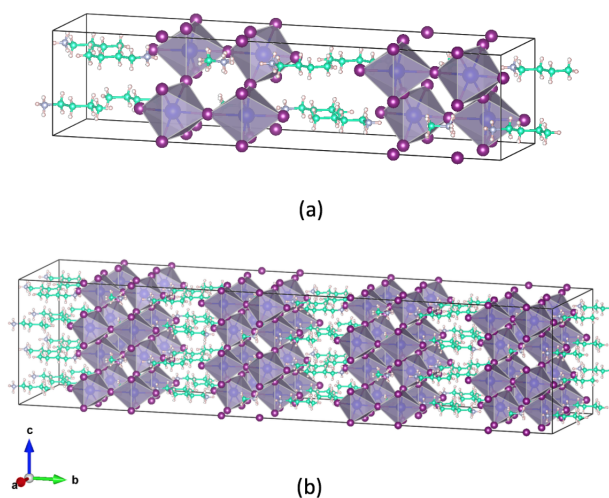


Figure 1.5: Illustration of (a) a unit cell of  $(\text{BA})_2(\text{MA})\text{Pb}_2\text{I}_7$  and (b) a repetition of the unit cell in two dimensions. MA and BA stand for methylammonium and butylammonium, respectively. The A-cation is presented as a turquoise ball, the B-cation as a blue ball and the halide anion as a purple ball. The N, C and H atoms (originating from the organic cations) are presented as light gray, turquoise and light pink balls, respectively. The ion size depicted is arbitrary.

## 1.2 Mechanochemical synthesis of multinary metal halides

Mechanochemistry refers to the branch in chemistry where the activation of the chemical reactions stems from mechanical energy triggers. Impact, compression or shear are several examples of the energy source for such reactions. Mechanochemical synthesis (MCS) can be carried out by hand-grinding with mortar and pestle, by milling in shaking or planetary ball-mills or by mechanical grinding in twin-screw extruders [54]. In this doctoral thesis, solvent-free mechanochemical synthesis was applied for the formation of lead halide perovskites, as well as other (lead-free) multinary

metal halides, enabled by ball-milling of stoichiometric precursors of the desired end product with a shaking ball-mill (see Figure 1.6). A detailed description about the experimental methodology will be described in Chapter 2. The findings made through this synthesis method will be described more in depth in Chapters 3-7.



Figure 1.6: Photograph of a ball-mill jar and two zirconia beads used for the mechanochemical synthesis of multinary metal halide semiconductors. The left vial contains the pristine perovskite precursors ( $\text{CsBr}$  and  $\text{PbBr}_2$ ). The right vial contains the  $\text{CsPbBr}_3$  perovskite that has been formed by ball-milling of the stoichiometric perovskite precursors. See Chapter 2 for a detailed description about the experimental methodology.

A ball-mill is a tool that can grind material into a fine powder by milling the feed material in the presence of a grinding medium (e.g. zirconia beads) at a certain frequency for a certain amount of time. As such, a material with decreased particle size is obtained. Besides the ability of obtaining a finely ground powder, it has also been shown to have the potential of synthesizing new compounds (AB) by grinding precursors (A and B) of the desired end product following reaction 1.2.

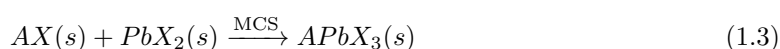


Mechanochemical synthesis offers a series of advantages over conventional solution-based processing techniques (see Subsection 1.3.1). Solvent-free processing comes along with an inherent lower toxicity as organic solvents – that are commonly associated with health and environmental hazards – are avoided. As such, MCS paves the way towards green chemistry, as solvents typically represent relevant amounts of waste. Furthermore, material fabrication in the absence of solvents comes along with a finer control over the stoichiometry of the final products. To date, the exact mechanism behind MCS has not been completely elucidated. However, in 2003, G. Kaupp proposed a three-step mechanism to generally explain molecular solid-state reactions. “The first step comprises the diffusion of the reactants through a mobile phase (gas [55], eutectic [56] or amorphous solid [57]) followed by a chemical reaction. In the second step, the formed product phase undergoes nucleation and growth, after which the product separates in the third step, which provides fresh reactant surfaces” [54, 58–60]. G. Kaupp states that all three steps must succeed in order for the reaction to complete [58].

Due to the operational simplicity of mechanochemistry, as well as its low-toxicity (related to the absence of solvents); this branch in chemistry has recently been explored for the synthesis of functional materials such as organic molecules, exfoliated graphene, metal-organic frameworks (MOFs) and metallic alloys [54, 61–66]. Mechanochemical synthesis has also been employed for the synthesis of different semiconducting materials (e.g. transition metal chalcogenides) [67–69]. Nevertheless – as pointed out by L. Protesescu *et al.* [70] – the numerous structural defects that MCS causes in the rigid crystal lattices of traditional semiconductors, such as cadmium selenide ( $\text{CdSe}$ ) or cadmium telluride ( $\text{CdTe}$ ), has been a major drawback until the advent of lead halide perovskites (LHPs). Crystal defects (e.g. vacancies or interstitials) frequently have energy levels that are within the semiconductor bandgap. As such, they act as electron- or hole-traps, quenching the photoluminescence (increasing non-radiative recombination) and



diminishing the overall semiconducting performances of the material (e.g. lower charge carrier diffusion lengths). As highlighted previously (see Subsection 1.1.1), LHPs have shown excellent photovoltaic (PV), as well as electroluminescent properties, making these semiconductors promising in the field of optoelectronics [71–74]. Besides these characteristics, another reason for their interest and success is the ease of forming high-quality films from a wide range of processing methods (see Subsections 1.3.1–1.3.2) [75–83]. The presence of grain boundaries does not strongly affect the semiconducting properties significantly for low-bandgap LHPs. This means that most structural defects are benign in terms of optoelectronics, as the energy levels introduced by these defects are either located outside of the bandgap (below the valence band or above the conduction band) or close to their edges (shallow traps). Hence, this property of LHPs makes them suitable for the preparation via MCS. By grinding the perovskite precursor binary salts ( $AX$  and  $BX_2$ ), the desired phase ( $APbX_3$ ) can be formed according to reaction 1.3, where  $A$  stands for the monovalent cation (commonly methylammonium, formamidinium or cesium) and  $X$  the monovalent halide anion (commonly  $I^-$ ,  $Br^-$  or  $Cl^-$ ).



In 2013, MCS of LHPs and related compounds was first demonstrated by C. Stoumpos *et al.* by hand-grinding of the precursors with mortar and pestle [84]. In their study, it was noted that a subsequent thermal annealing step in vacuum was necessary in order to get phase-pure products. However, in 2015, D. Prochowicz *et al.* demonstrated the formation of phase-pure methylammonium lead tri-iodide ( $MAPbI_3$ ) using an electric ball-mill without the need of any post-treatments [85]. Since then, several tens of articles have been published, reporting the mechanochemical synthesis of lead halide perovskites and related materials. This indicates a growing interest in this synthesis method for the fabrication of such semiconductors.

In the following, MCS is discussed for (i) the production of high-purity LHPs in the form of dry/bulk powders (see Subsection 1.2.1), (ii) the investigation of fundamental properties of mixed-composition halide perovskites (see Subsection 1.2.2), (iii) the development of lead-free multinary metal halides (see Subsection 1.2.3) and (iv) the implementation of the previously described materials into optoelectronic devices by processing the as-synthesized products into thin films (see Subsection 1.3.2) [86].

### 1.2.1 Synthesis of dry powdered, high-purity lead halide perovskites

MCS is a great alternative to conventional solution-based processing of LHPs, since it is a solvent-free synthesis method that is easily upscalable, that can lead to high-purity materials and that virtually has no limitations in composition or stoichiometry. Furthermore, it has been shown that mechanochemically-synthesized lead halide perovskites have superior stability for long periods of time [87, 88]. Therefore, MCS represents a highly appealing synthetic method from both a scientific point of view (to help to elucidate the fundamental properties of the as-synthesized material) and a technological point of view with the prospect of the incorporation of such LHPs in optoelectronic devices, such as solar cells and light-emitting diodes. Furthermore, MCS shows attraction from a cost-analysis point of view since high yields – with the least amount of solvent used (if any, other than for cleaning purposes) – can be obtained in a highly time efficient manner. Also, energy is saved since MCS does not require high temperatures [70, 89].

After the first demonstration of C. Stoumpos *et al.* [84], this approach was later employed by several other research groups for the preparation of similar LHPs [90, 91]. While from a technical point of view this approach is rather simple, hand-grinding can be tedious and most importantly may lead to unreacted precursor impurities in the sample, as reported by C. Stoumpos *et al.* [84]. Hence, to date, electrically-powered ball-milling is used predominantly as it is a more convenient and widely used technique for MCS [15–17, 21, 23, 26, 47, 59, 70, 92–107]. In this approach, precursors are loaded into sealed milling jars along with several beads that act as a grinding medium (Figure 1.6). The sealing is generally airtight, which allows for the operation in inert atmosphere if the jars are loaded and unloaded in an inert glovebox. The beads and the inside

walls of the jars are typically made out of a high-hardness material, such as zirconia, corundum or agate, although stainless steel is also used. As the jars are set in motion – by either straight shaking or by rotating in planetary ball-mills – mechanical energy (e.g. by compression, shear or friction) is translated from the grinding medium to the reaction mixture. This then leads to the conversion of the precursors into the stable perovskite phase. As described previously, the synthesis occurs as upon ball-milling “fresh” reactant surface is constantly exposed [58, 108, 108–112]. In recent years, pure 3D lead halide perovskites have been prepared by MCS with excellent phase purity, as determined by X-ray diffraction (XRD) [15, 22, 47, 84, 102, 104, 113–117]. MCS is especially promising for industrial upscaling. An interesting example of this was shown by Z. Hong *et al.*, who reported the synthesis of metal halide perovskites by ball-milling on the kilogram-scale [22]. For that matter, MCS is already used in industry for several applications, such as mechanical alloying or pharmaceutical drug synthesis on a larger scale [118].

Several parameters can be tuned during ball-milling that affect the properties of the end product [119, 120]. These include the milling time (which depends on the initial particle size [120, 121]), the rotation or shaking frequency, the properties of the grinding medium (e.g. diameter, material and weight) and the bead-to-reactant weight ratio (BRR) [22, 122–124]. At the time of writing, scarce research is done on the effect of these parameters on the synthesis of perovskites with the view on their use as the active material in solar cells or light-emitting diodes. However, general research on mechanochemical synthesis reveals the following. S. Ohara *et al.* have shown that the time to achieve full conversion of the precursors barium carbonate ( $\text{BaCO}_3$ ) and titanium dioxide ( $\text{TiO}_2$ ) into fine barium titanate ( $\text{BaTiO}_3$ ) nanoparticles using an attrition type milling apparatus, significantly reduces when the powdered reactants are used in the nanoscale [121]. This effect is believed to be related to improved energy transfer between the reactants in the nanoscale compared to larger grains. Furthermore, A. Michalchuk *et al.* have made a correlation between the effect of both the mass, as well as the diameter of the grinding medium on the rate of the mechanochemical co-crystallization of a stoichiometric mixture of powdered theophylline and nicotinamide using a cryomill [125]. The mass of the grinding medium is stated to be correlated to the rate of the mechanochemical transformation. They have shown that shorter milling times are needed for complete conversion of the precursors into the end product when heavier beads are used. Reasoning behind this result is based on the fact that heavier beads possess higher kinetic energy (a relationship that follows directly from the classical mechanical equation of motion) and as such, a deeper penetration into the solid phase is possible. Furthermore, heavier beads are correlated to increased amount of heat generation, which enables the conversion reaction. It needs to be noted that in contrast to dry ball-milling, in this study liquid-assisted grinding (LAG) was performed, since a solvent (ethanol) was added to the reactants mixture. The authors also showed that heavier beads (containing a larger surface area compared to smaller and lighter beads) are correlated to shorter transformation times, since it is believed that the use of heavier and bigger beads increases the contact area with the sample. As such, increased particle-particle contacts (communication between the particles) occur during milling; meaning that more material is involved in the chemical transformation reaction. They conclude that “the reaction rate is correlated to the probability of hitting the sample” [125]. H. Kulla *et al.* investigated the effect of the bead-to-reactant weight ratio (BRR) on mechanochemical transformation reactions [126]. They showed that “the reaction time decreases with increasing BRR, due to the fact that an increased BRR induces a higher bead impact, which enables the energy transfer from grinding medium to reactants” [126]. However, it needs to be noted that higher BRRs are related to a higher probability of a temperature rise in the system, which is believed to be part of the activation energy for the mechanochemical transformation reaction. Finally, also the effect of the milling frequency (number of particle collisions per unit of time) has been investigated. P. Julien *et al.* [127] and G. Schaffer *et al.* [128] state that the milling frequency is related to the mechanochemical activation of the reactants, since this parameter influences the number and rate of impacts of the grinding medium, the overall impact force and heating as an effect of friction. As such, they conclude that “higher frequencies are correlated to a greater number of more energetic mechanical bead impacts and [that] along with the influence of frictional heating, shorter reaction times are needed for full conversion of the reactants”.



While these studies are highly interesting in the field of mechanochemistry, as previously mentioned, little is known about the effect of the ball-milling parameters on the mechanochemical synthesis of perovskites for optoelectronics, such as solar cells and LEDs. For that reason – among other investigations – in this doctoral thesis, research was conducted on the effect of the ball-milling time on the mechanochemical synthesis of the perovskite cesium lead tribromide ( $\text{CsPbBr}_3$ ). A detailed description of this study will be presented in Chapter 3 [129].

### 1.2.2 Investigation of mixed-composition halide perovskites

Halide perovskites can be written as  $\text{ABX}_3$  compounds. However, this simple formula somehow hides one fundamental aspect that has motivated an abundant amount of research on these materials. This aspect refers to the fact that several  $A$ ,  $B$  and  $X$  elements can be combined in a single, homogeneous perovskite structure. The high degree of tolerance towards mixed compositions is not only interesting from a fundamental chemical point of view, but it also provides a wide range of possibilities to fine-tune the optoelectronic properties of the final material for different applications. Up to date, some of the best performances in perovskite photovoltaics have been obtained with rather complex formulations, such as  $(\text{Rb}:\text{Cs}:\text{MA}:\text{FA})\text{Pb}(\text{I}:\text{Br})_3$  [130]. Indeed, mixing different elements in the  $A$ -,  $B$ - and/or  $X$ -sites of halide perovskites may result in several physical and chemical changes. In the following, mechanochemically-based  $A$ -,  $B$ - and  $X$ -site mixing will be discussed with the corresponding literature references.

#### A-site mixing

$A$ -site mixing has been found particularly fruitful to stabilize the perovskite phase by tuning the Goldschmidt tolerance factor (see Subsection 1.1.1, Equation 1.1). As shown by Figure 1.2,  $\text{MA}$ -based lead trihalides have an ideal tolerance factor (between 0.9 and 1), whereas  $\text{Cs}$ -based and  $\text{FA}$ -based ones are at the lower and higher boundaries of 0.8 and 1, respectively. Whereas  $\text{MAPbI}_3$  shows excellent photovoltaic properties [131–133], its significant degradation upon heating and its rather wide bandgap (absorption capacities at relatively low wavelengths; around 1.5 eV  $\sim$  827 nm [19]) for single-junction solar cells make it non-ideal for photovoltaics. On the other hand, formamidinium lead tri-iodide ( $\text{FAPbI}_3$ ) possesses a slightly lower bandgap, improving the absorption in the near-infrared part of the solar spectrum. Furthermore, it shows enhanced thermal stability. Unfortunately,  $\text{FAPbI}_3$  crystallizes in the so-called “yellow” orthorhombic non-perovskite phase ( $\delta$ - $\text{FAPbI}_3$ ) at room temperature, which is linked to its large Goldschmidt tolerance factor (see Figure 1.2). In order to tune this geometric factor and ensure a stable cubic perovskite phase at room temperature, a common strategy is to introduce smaller  $A$ -cations into  $\text{FAPbI}_3$ . The main question that arises is what the minimum amount of smaller  $A$ -cations must be that is introduced into the lattice to maintain the beneficial properties of  $\text{FAPbI}_3$  as much as possible, while ensuring a cubic phase at room temperature. This question can be conveniently investigated by MCS, where it is rather easy to mix different precursors in highly accurate ratios. The first report on mixed-cation halide perovskites prepared by MCS was published by D. Prochowicz *et al.*, where they were able to synthesize mixed-cation  $\text{MA}_x\text{FA}_{1-x}\text{PbI}_3$  with  $x = 0.15, 0.20$  and  $0.25$  [104]. The authors found that a fraction of  $\delta$ - $\text{FAPbI}_3$  was noticeable by X-ray diffraction for  $x = 15\%$  and  $x = 20\%$ , but vanished for compositions with methylammonium above 25%.

Similarly, as will be highlighted in Subsection 1.3.2,  $\text{CsPbI}_3$  and  $\text{FAPbI}_3$  are reported to be thermodynamically unstable in the cubic perovskite phase at room temperature. Nevertheless, as reported by Z. Li *et al.*, mixed  $\text{Cs}_x\text{FA}_{1-x}\text{PbI}_3$  can crystallize in a perovskite structure at room temperature [2]. As such, the introduction of a smaller  $A$ -cation (cesium) into  $\text{FAPbI}_3$  ensures this effect. D. Kubicki *et al.* demonstrated homogeneous mixed-cation  $\text{Cs}_x\text{FA}_{1-x}\text{PbI}_3$  by MCS with a cesium loading up to around 15% [134].

Beyond the three most commonly employed  $A$ -cations in 3D halide perovskites ( $\text{Cs}^+$ ,  $\text{MA}$  and  $\text{FA}$ ), a growing interest is being developed on the possible roles of even smaller inorganic cations such as potassium ( $\text{K}^+$ ). In Chapter 4, the incorporation of different potassium halide salts in the mechanochemical synthesis of  $\text{CsPbBr}_3$  will be discussed [20].

### B-site mixing

While most halide perovskites use lead (Pb(II)) as the only B-cation, the partial or total replacement of Pb(II) by tin (Sn(II)) has also been investigated by MCS [21–23]. In Chapter 5, the synthesis of several mixed lead-tin and pure-tin iodide perovskites, as well as so-called “vacancy-ordered perovskites” (based on Sn(IV)) will be demonstrated. The thermal stability, as well as the optical and electrical characteristics of these compounds – to assess their applicability in photovoltaics and NIR LEDs – will be discussed [23].

### X-site mixing

Most mixed-composition halide perovskites are based on combining different halide anions. Indeed, as previously discussed (see Subsection 1.1.1), out of the three elements present in the  $ABX_3$  structure, a change in X ( $I^-$ ,  $Br^-$ ,  $Cl^-$  or a mixture thereof) is usually the most effective way of tuning the optical bandgap (see Figure 1.3a). Bulk mixed-halide perovskites have been investigated by MCS [15–17, 21, 22, 24–28]. Generally, it is found that Br-I and Br-Cl mixed compositions can be formed with any ratio of both halides. This can be achieved either by mixing the halide precursors or by grinding the preformed single-halide perovskites in the desired ratios. For example, A. Karmakar *et al.* prepared  $MAPb(Br_xCl_{1-x})_3$  perovskites by hand-grinding and ball-milling pre-synthesized methylammonium lead tribromide ( $MAPbBr_3$ ) and methylammonium lead trichloride ( $MAPbCl_3$ ) [17]. Compared to solution-processing, the authors note that “the solvent-free mechanochemical synthesis approach [reveals] identical solid-solution behavior. However, the mechanochemical approach offers superior control over the stoichiometry of the final mixed-halide composition, which is essential for device engineering”. Extensive nuclear magnetic resonance (NMR) characterization showed the perfect mixing of halides in a single crystalline phase without any amorphous or phase segregated domains.

### 1.2.3 Formation of other lead-free multinary metal halides

Whereas the traditional  $ABX_3$  perovskite is composed of corner-sharing  $BX_6$ -octahedra with an interstitial A-cation, grown repeatedly in three dimensions (see Subsection 1.1.1), in some cases, it is shown that decreased structural dimensionality comes along with increased stability, which triggers interest in these materials. Besides Ruddlesden-popper lead halides (see Subsection 1.1.1), a wide variety of multinary metal halides can be obtained by replacing divalent lead by one or several metallic cations of different valences. This is highly sought after as Pb(II) is toxic. Nevertheless, in conventional solution-processing techniques (see Subsection 1.3.1), it is challenging to find common solvents for different metal halides in view of their limited solubilities [48]. Hence, fully dry MCS is a highly promising approach to circumvent this issue and enable a broader screening of a multitude of related materials that are sometimes loosely referred to as “lead-free perovskites”. However, as previously discussed, the reference to the term “perovskite” is rather arbitrary and – based on the crystal structure of many of these – even inappropriate (see Subsection 1.1.2). In the case of the replacement of divalent lead with trivalent metals, such as Bi(III), different zero-dimensional and two-dimensional structures can be obtained with the formula  $A_3B_2X_9$  (see Figure 1.4b and c). In Chapter 6, the mechanochemical synthesis of various hybrid organic-inorganic, as well as fully inorganic bismuth-based  $A_3Bi_2X_9$  crystals – with tunable bandgaps and photoluminescence in the visible range – will be demonstrated and discussed [16].

## 1.3 Thin film formation technologies

Over the past decades, extensive research has been conducted on perovskites and the formation of perovskite-based thin films. The fabrication of the latter is of importance with the prospect of the development of optoelectronic devices, such as solar cells and light-emitting diodes. Herewith, one of the most crucial parameters that affect device performance is the morphology of the perovskite thin film [75]. It has been shown that the morphology of the film and thus the crystallization of the perovskite affects a series of photo-physical properties. These include charge carrier transport, light emission or absorption capacities, as well as the diffusion length, which is the average length a carrier (hole or electron) moves between generation and recombination [8, 75, 76, 135–137]. As such, inhomogeneous morphology, as well as defects in the film form the basis for trap states (states inside the bandgap of the material), which leads to non-radiative recombination and thus affects the overall device performance. The morphology of thin films is closely related to and affected by the film formation process. To date, the different film fabrication procedures for the synthesis of perovskite thin films can be separated in four main technologies [75, 136], including one-step spin-coating deposition [76, 77], sequential solution deposition [138], two-step spin-coating deposition [78] and vapor deposition, including multiple-source vapor co-deposition and sequential vapor deposition [139–144]. An overview of these technologies is illustrated in Figure 1.7 and Figure 1.8. In the following, insight into these technologies are described, as well as their disadvantages and limitations in the field of optoelectronics. Whereas perovskites with different compositions can be formed (multi cation, metal and/or anion perovskites), in the following for the sake of simplicity the methodology will be explained based on the general composition of perovskites with the formula  $ABX_3$ , which is composed of two stoichiometric precursors  $AX$  and  $BX_2$  (1:1 molar ratio). As previously described,  $A$  stands for the monovalent cation,  $B$  the divalent metal and  $X$  the halide anion.

### 1.3.1 Solution-processing techniques

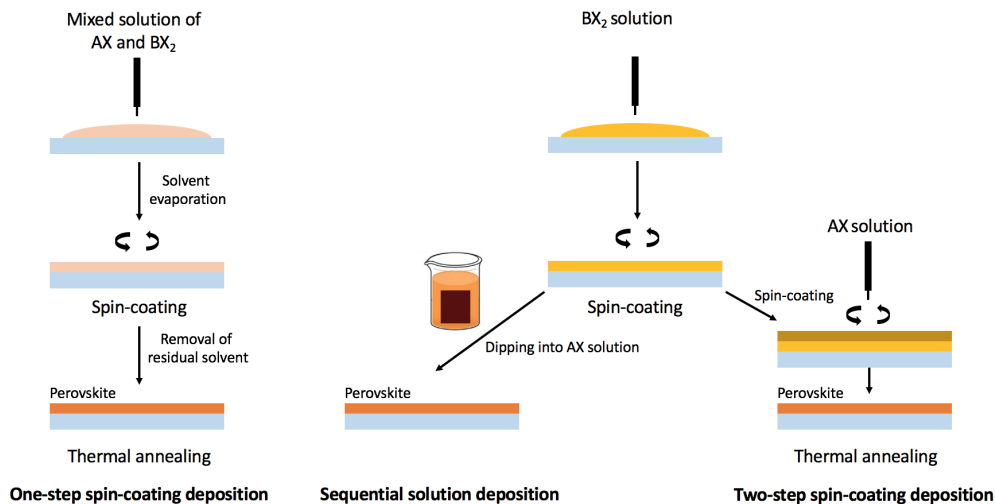


Figure 1.7: Solution-based deposition techniques for the formation of perovskite thin films, including one-step spin-coating deposition, sequential solution deposition and two-step spin-coating deposition. This illustration is inspired by reference [75].

#### One-step spin-coating deposition

One-step solution deposition is a thin film processing technique that involves spin-coating of a precursor solution. The latter contains the perovskite precursors ( $AX$  and  $BX_2$ ), which are dissolved in a certain solvent (e.g. dimethyl sulfoxide (DMSO),  $N,N$ -dimethylformamide (DMF) or  $\gamma$ -butyrolactone (GBL)). As illustrated in Figure 1.7, the perovskite crystallites form and grow

during spin-coating, as a thin wet film is formed, which enables the evaporation of the solvent. Finally, the thin film is subjected to post-thermal annealing to ensure complete crystallization of the perovskite, as well as for the removal of residual solvents [75–77].

In general, the formation of perovskite thin films via solution-processing and more in particular the morphology of such films (and thus the device performance), are highly sensitive to and affected by several processing parameters [75]. These include among others, the solution concentration [25, 78], precursor composition [145, 146], solvent choice [147, 148], annealing temperature [76, 135], type of substrate [149], processing environment (e.g. air or nitrogen) during spin-coating [136] and spin-coating parameters (e.g. spin-coating speed) [150]. For instance, it was found that the perovskite methylammonium lead tri-iodide ( $\text{MAPbI}_3$ ) formed from a GBL solution via one-step spin-coating deposition shows to have a clustered-domain morphology, whereas when the solvent DMF is used in the precursor solution, the structure is composed of interconnected needle-like crystallites [75, 138, 151–153]. As such, the choice of solvent drastically influences the morphology of the perovskite film. Furthermore, G.E. Eperon *et al.* were the first to show an effect of the annealing temperature and initial film thickness on the surface coverage on planar substrates [75, 76, 136]. For the one-step spin-coating solution-based fabrication of  $\text{MAPbI}_{3-x}\text{Cl}_x$  using DMF in the precursor solution containing methylammonium iodide (MAI) and lead chloride ( $\text{PbCl}_2$ ) (3:1 molar ratio), post-thermal annealing at lower temperatures (90 °C compared to 100–170 °C for a film of 450–550 nm for approximately 45 minutes) – under which full crystallization of the perovskite is still enabled – resulted in improved surface coverage [76, 154]. It was shown that the latter property has a direct impact on device performance, as it is demonstrated to be linked to improved photocurrents [76]. A final example of how certain parameters – more specifically the processing environment during spin-coating – in solution-based perovskite thin film processing can influence the morphology of the film, was presented by J. You *et al.* [155] and L. Zeng *et al.* [75]. These researchers have shown that a humid environment (about 30 %) influences the moisture in the grain boundaries, which enables grain merge. As such, reduced pinholes are associated with the amount of humidity in the environment during film fabrication.

Alternatively, rapid crystallization of the perovskite film can be obtained by air-flow assisted deposition [156, 157], vacuum-flash solution processing [158–160] and solvent engineering using anti-solvents, such as among others methylbenzene, dichloromethane, diethyl ether (DEE) and trichloromethane [161–169]. Up to date, the latter technique has proven to obtain optoelectronic devices (solar cells) with the highest confirmed conversion efficiencies [170].

### Sequential solution deposition

The sequential solution deposition technique – proposed by J. Burschka *et al.* – is an alternative route to the one-step spin-coating deposition method for semiconductor thin film fabrication [138]. As illustrated in Figure 1.7, in this technique, spin-coating of a  $\text{BX}_2$ -layer on a substrate is followed by dipping the sample into an  $\text{AX}$ -containing solution after subsequent drying of the former precursor film. This enables the conversion from  $\text{BX}_2$ -layer to  $\text{ABX}_3$  [75, 171]. J. Burschka *et al.* and L. Zheng *et al.* have demonstrated improved morphology control and film homogeneity compared to the one-step spin-coating deposition method [75, 138]. They showed that the incorporation of a prewetting step in isopropanol (IPA), before dipping the former precursor film ( $\text{PbI}_2$  in DMF) in the final precursor solution (MAI in DMF), is related to high photogenerated currents. It is shown that larger crystallites were formed, which is hypothesized to be linked to the diluted MAI solution on the solution-solid interface, which results in reduced nuclei density. As such, prewetting enables improved scattering due to an increased average crystallite size [75, 138].

### Two-step spin-coating deposition

The two-step spin-coating deposition technique – proposed by Z. Xiao *et al.* – is an alternative method to the sequential solution deposition method, where a single precursor-containing solution is deposited at a time [78]. As illustrated in Figure 1.7, a  $\text{BX}_2$ -containing solution is deposited on a substrate via spin-coating, followed by the spin-coating of an  $\text{AX}$ -containing solution. As

previously described, during the latter step,  $BX_2$  reacts with  $AX$  to form the perovskite  $ABX_3$ . Finally, post-thermal annealing ensures the complete conversion from  $BX_2$  to  $ABX_3$ , as well as full crystallization and the removal of residual solvents. In comparison with the one-step spin-coating deposition method, this technique enables the deposition of a higher concentrated  $BX_2$ -layer, which positively affects the absorbance properties of the final  $ABX_3$  film [78, 136, 138, 140, 172, 173]. The morphology of films prepared by two-step spin-coating deposition is shown to be mostly determined by the  $BX_2$ -film, which is applied in the first deposition step. Furthermore, this deposition method has shown to derive more uniform perovskite films, which improves reproducibility [136].

### Disadvantages and limitations of thin film solution-processing techniques

Whereas the three previously described solution-based processing techniques have been implemented in several high-efficiency devices, several drawbacks and limitations are linked to these methods. In general, as previously stated, the formation of perovskite thin films via solution-processing and more in particular the morphology of such films (and thus the device performance), are highly sensitive to and affected by several processing parameters [75]. These include among others, the solution concentration [25, 78], precursor composition [145, 146], solvent choice [147, 148], annealing temperature [76, 135], type of substrate [149], processing environment (e.g. air or nitrogen) during spin-coating [136] and spin-coating parameters (e.g. spin-coating speed) [150]. The large amount of parameters that can influence the morphology of perovskite films hinder the reproducibility of these solution-based processing techniques. Furthermore, it must be mentioned that in order to fabricate perovskite thin films, the perovskite precursors need to be dissolved. As such, the formation of for example cesium-based perovskite films via these methods is rather challenging, due to the poor solubility of cesium halides in common solvents [174, 175]. Furthermore, alternative techniques for rapid perovskite crystallization such as air-flow assisted deposition, vacuum-flash solution processing and solvent engineering using anti-solvents, highly depend on the timing of application during synthesis, which impedes controlling the perovskite crystallization. Finally, upscaling via solution-based processing is also rather challenging. These disadvantages and limitations are bypassed by an alternative thin film processing technique, namely thermal vacuum deposition, which is described in the following subsection.

### 1.3.2 Thermal vacuum deposition techniques

Thermal vacuum deposition (also referred to as vapor deposition) is an alternative method to solution-processing for the fabrication of perovskite thin films. A division between two main approaches is made; dual-source (or more generally multi-source) and sequential vapor deposition (Figure 1.8).

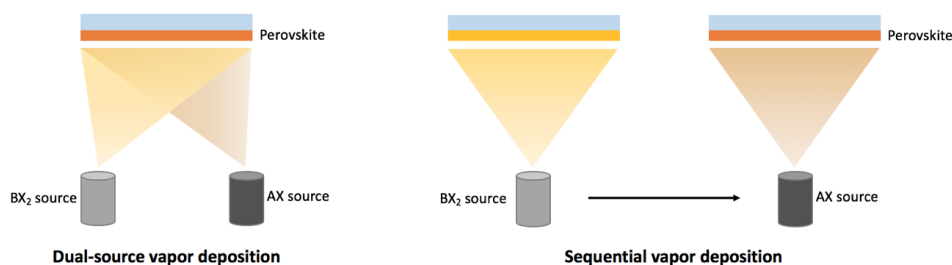


Figure 1.8: Vapor deposition techniques for the formation of perovskite thin films, including dual-source vapor deposition and sequential vapor deposition. This illustration is inspired by reference [75].

#### Dual-source vapor deposition

As illustrated in Figure 1.8, dual-source vapor deposition (also known as co-evaporation) is a thin film processing technique where the perovskite precursors ( $AX$  and  $BX_2$ ) are simultaneously

sublimed<sup>1</sup> in their original powder state from two separate crucibles in a vacuum chamber. During this process, the evaporated precursors condense and react on rotating substrates, which are placed directly above the thermal sources. Rotation of the substrate holder ensures an improved homogeneity of the evaporated material. Careful control of the precursors evaporation rates – by continuously adjusting the source temperatures – the stoichiometry and thus the composition of the final perovskite film, as well as the film thickness can be controlled. In 2013, M. Liu *et al.* were the first to demonstrate the formation of a  $\text{MAPbI}_{3-x}\text{Cl}_x$  thin film via dual-source vapor deposition of the perovskite precursors MAI and  $\text{PbCl}_2$  and subsequent thermal annealing of the formed films [139]. With the increased interest in this thin film fabrication technique, our research group – Molecular Opto-Electronic Devices group supervised by Prof. Dr. Hendrik Jan Bolink at the Institute of Molecular Science of the University of Valencia, Spain – has implemented this method for the deposition of perovskite thin films of different compositions. The first successfully-formed films were  $\text{MAPbI}_3$  perovskite films, where evaporation under stoichiometric conditions enabled the direct formation of the semiconductor [142]. As such, post-thermal annealing is bypassed. Since 2014, our research group has managed to incorporate these and related films (e.g.  $\text{MAPbBr}_3$ ) into optoelectronic devices, such as solar cells and LEDs [82, 141, 176–179]. The discussion of those devices, however, goes beyond the scope of this doctoral thesis. Furthermore, besides adjusting the source temperature and stoichiometry, as demonstrated by L. K. Ono *et al.*, the pressure in the vacuum chamber can be controlled during the evaporation process to obtain similar results [143].

### Sequential vapor deposition

As opposed to dual-source vapor deposition, sequential vapor deposition – as the name implies – is a sequential film formation technique where the evaporation of the precursors ( $\text{AX}$  and  $\text{BX}_2$ ) occurs separately. A schematic of this deposition technique is presented in Figure 1.8. In analogy with the sequential solution deposition method, during the consecutive evaporation sessions,  $\text{BX}_2$  reacts with  $\text{AX}$  to form the perovskite  $\text{ABX}_3$ . The latter step can be enabled by dipping the thin film into the relevant precursor solution to finalize the reaction. However, the use of solvents can be completely avoided by reaction of the relevant precursor with the film via chemical vapor deposition (CVD) [79] or through sequential deposition of the precursor via thermal vacuum deposition [80]. Usually, post-thermal annealing is applied to ensure the complete conversion from the precursors to the perovskite  $\text{ABX}_3$ .

Thermal vacuum deposition offers a series of advantages over solution-based processing of perovskite thin films. First and foremost, in the former technique the use of solvents is generally avoided, which enables the investigation and formation of perovskite thin films composed of halides (such as cesium halides) that are poorly soluble in common solvents (e.g. DMF and DMSO). Solvent-free processing also comes along with an inherent lower toxicity and is related to a higher purity of the used precursors, which diminishes the probability of impurities in the final film. Furthermore, thermal vacuum deposition is related to higher reproducibilities compared to solution-based processing techniques. This characteristic is based on the increased control over both morphology and film thickness. As previously described, by continuously adjusting the evaporation rates by controlling the evaporation temperature(s) of the source(s) – which is monitored via quartz crystal micro-balance (QCM) sensors – homogeneous films can reproducibly be obtained. Also, thermal vacuum deposition is a technique that is compatible with a large assortment of substrates. As mentioned previously, when evaporation of the perovskite precursors is conducted under stoichiometric conditions, post-thermal annealing of the samples is bypassed. As a result, this deposition technique is compatible with temperature-sensitive substrates (e.g. plastic foils and textile). Finally, vapor deposition enables the formation of stacked layers via the evaporation of several precursors or additives. As such, multi-layer architectures (e.g. tandem solar cells) can be investigated.

---

<sup>1</sup>To date, it is unknown whether the material evaporates (and thus first melts) or sublimates (and thus goes straight from the solid to vapor phase). For that reason, the terms “evaporation” and “sublimation” are used arbitrary.

### Disadvantages and limitations of dual-source and sequential vapor deposition

Thermal vacuum deposition via dual-source and sequential vapor deposition offers an assortment of advantages over solution-processing of perovskite thin films. However, these methods come along with several disadvantages and limitations. As previously discussed, in order to obtain the desired, high-purity perovskite thin films via the dual-source and sequential vapor deposition methods, the evaporation rate(s) of the precursor(s) need(s) to be well-adjusted continuously. This on its own can be tedious, but even more so challenging when the investigation of halide perovskites with increased formulation complexity containing up to 6 or 7 different ions is desired. Such more complex perovskites have proven to be beneficial for device performance [180–184]. Multi-cation perovskites enable tuning of the bandgap of the material [183], as well as its Goldschmidt tolerance factor (Equation 1.1) [2, 185]. As previously described (see Subsection 1.1.1), a  $t$ -value outside of the range 0.8-1 usually results in non-perovskite structures. Examples of such crystalline structures are orthorhombic (so-called “yellow phase”) cesium lead iodide ( $\text{CsPbI}_3$ ) and formamidinium lead iodide ( $\text{FAPbI}_3$ ). In the case of  $\text{CsPbI}_3$ , the tolerance factor is too small. Whereas in the case of  $\text{FAPbI}_3$ , the tolerance factor is too large to result in a stable cubic phase at room temperature. However, the multi-cation cesium formamidinium lead iodide perovskite ( $(\text{Cs:FA})\text{PbI}_3$ ) was shown to be stable [183, 186]. This is only an example of the interest of multi-cation perovskites (see Subsection 1.2.2). Whereas the interest for these is a clear fact, it is experimentally challenging via the dual-source and sequential vapor deposition methods, due to the fact that the formation of such complex perovskites requires multiple evaporation sources that need to be well-controlled harmoniously and continuously.

Single-source vacuum deposition (SSVD) represents an interesting alternative to dual-source and sequential vapor deposition, due to its simplicity and speed [187, 188]. Herewith, perovskite precursors are rapidly sublimed via a single evaporation source, as opposed to multiple sources. Alternatively, prior to single-source evaporation, the perovskite of interest can be prepared through mechanochemical synthesis via manually grinding or ball-milling of the perovskite precursors. In the following, the mechanochemical synthesis of semiconductors (see Section 1.2), as well as the subsequent single-source vacuum deposition of the latter (see Subsection 1.3.2) – which both form the scaffold of this doctoral thesis – are described more in depth.

### Processing and applications of mechanochemically-synthesized multinary metal halides: From powder to thin film

Throughout recent years, mechanochemical synthesis has shown to be an ideal method for the synthesis of a broad range of multinary metal halides with interesting optoelectronic properties, due to the fact that in a rather fast and simple manner the desired material can be obtained with high purity. From a pure scientific point of view, MCS is highly attractive, mainly since this synthesis technique helps to elucidate the fundamental properties of the as-synthesized material. Moreover, besides the attractive trait of the ability of conducting materials science by applying MCS; from a technological point of view, MCS is a highly promising synthesis method since it paves the way to an alternative method for the fabrication of semiconducting materials for their use in optoelectronic devices, such as solar cells and LEDs. The main characteristic of MCS is that the material is obtained in a fine powder shape. This feature comes along with both benefits, as well as disadvantages. It allows for the direct characterization of the material independently of interfaces or substrates. However, to employ these materials in diode-based applications, these powders need to be deposited into thin films, where light and/or electrical charges can be injected and extracted.

One strategy for the processing of mechanochemically-synthesized perovskites is the fabrication of pellets by pressing these pre-synthesized powder materials. As an example, Z. Hong *et al.* made pellets (with an average thickness of 2 mm) from ball-milled lead-free  $\text{CsSnBr}_{1.5}\text{Cl}_{1.5}$  powders to derive a visible photodetector [22]. By the evaporation of electrical contacts on the pellet, a rather simple device was obtained. Also, in Chapter 6, the approach of pellet fabrication of pre-synthesized perovskites will be demonstrated for lead-free  $\text{Cs}_3\text{Bi}_2\text{X}_9$  ( $\text{X} = \text{Br}^-$  and  $\text{I}^-$ ) blended with transparent Poly(methyl methacrylate) (PMMA) beads [16]. While these simple applications are interesting proofs of concept, more advanced applications, such as light-emitting

diodes and solar cells cannot be based on the active material being dispersed in an insulating matrix or simply pressed in macroscopic pellets. For a more widespread implementation of MCS, the as-synthesized materials need to be processed into smooth homogeneous thin films, with typical thicknesses ranging from 10 nm to 1  $\mu\text{m}$ . A strategy enabling the formation of such thin films is the dissolution of MCS-perovskites in organic solvents. Such so-called “inks” can be spin-coated on a substrate to fabricate films and devices thereof [22, 25, 87, 88, 189, 190]. Among others, this technique was applied by D. Prochowicz *et al.*, who fabricated  $\text{MAPbI}_3$  thin films from pre-synthesized  $\text{MAPbI}_3$  powders dissolved in DMSO and compared them with films prepared from a solution of the perovskite precursors lead iodide and methylammonium iodide [190]. In both cases, film morphologies were very similar, without pinholes and with average grain sizes around 180-200 nm, as observed by scanning electron microscopy (SEM). Moreover, films prepared from mechanochemically-synthesized  $\text{MAPbI}_3$  could be implemented in a single-junction solar cell with a power conversion efficiency (PCE) similar to that of solution-processed  $\text{MAPbI}_3$  thin films and with lower hysteresis attributed to a lower surface defect density. In a following publication, the authors were able to fabricate cesium/chloride-containing perovskite films by dissolving pre-synthesized perovskites in DMF and DMSO, whereas the precursor cesium chloride ( $\text{CsCl}$ ) was found to be non-soluble in the same solvents [191]. This highlights a clear advantage of using mechanochemically-synthesized perovskites as precursors in solution-processing, rather than their binary salt constituents. Another crucial benefit from a technological point of view was highlighted by B. Dou *et al.* [88]. The authors verified that “inks” made by dissolving previously mechanochemically-synthesized perovskites in the above-mentioned solvents were chemically stable for long periods of time, whereas inks made by dissolving the different precursors salts (without previous MCS) underwent rapid degradation even when stored under nitrogen in dark.

Despite these positive results based on the dissolution of MCS-perovskites, it may be argued that such solution-based processing techniques somehow defeat one of the purposes of dry MCS, which is avoiding organic solvents. Therefore, dry processing methods to convert the as-synthesized powders into thin films are highly sought after. In this doctoral thesis, single-source vacuum deposition (SSVD) of fully inorganic MCS-perovskites was established to fabricate thin films of identical composition and optical properties. SSVD enables the formation of such thin films in a simple and rapid manner by the fast evaporation of mechanochemically-synthesized perovskites at high temperatures, as illustrated in Figure 1.9. As such, the incongruent melting and evaporation of different species at lower sublimation temperatures are avoided. A detailed description of this processing technique will be presented in Chapter 2, followed by the discussion of SSVD of fully inorganic mechanochemically-synthesized perovskite powders in Chapter 7.

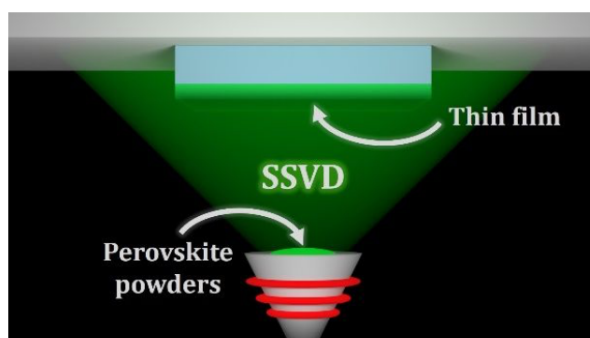


Figure 1.9: Illustration of the single-source vacuum deposition (SSVD) of solvent-free mechanochemically-synthesized perovskite powders for the fabrication of thin films [107].



## 1.4 Aim and overview of the thesis

In the past decade, lead halide perovskites, as well as other multinary metal halides – including lead-free alternatives – have shown to be promising materials for their use in optoelectronics. Therefore, new ways of producing high-purity semiconductors in large scale are actively sought after. Hence, the main aim of this doctoral thesis is the development of perovskites and related semiconductors using solvent-free methods. Furthermore, with the prospect of the use of such materials in optoelectronics on an industrial scale, the focus is put on working with benign materials for the development of alternatives to toxic perovskites. Mechanochemical synthesis has recently emerged as a highly convenient and reliable method to obtain high quality lead halide perovskites, as well as other lead-free multinary metal halides. Hence, this thesis contributes to a material study for the development of perovskites and related materials via a solvent-free mechanochemical route and the investigation of the fundamental characteristics thereof. Furthermore, with the interest in the implementation of these high-purity semiconductors in optoelectronics – besides a material study – this thesis contributes to the investigation of a novel manner for the fabrication of thin film perovskites via single-source vacuum deposition of mechanochemically-synthesized perovskite powders. As such, this work paves the way to a new manner for both understanding the formation of perovskites, as well as an alternative way for thin film development with the prospect of the fabrication of applications in the field of optoelectronics.

First the general experimental methodology will be explained in Chapter 2, along with the characterization techniques used in this doctoral study in order to fully investigate, identify and analyze the obtained materials. Thereafter, five research works will be presented that correspond to five different published articles [16, 23, 95, 107, 192], which can also be found as appendices (Appendices A-E). As such, the thesis is structured as follows:

- Chapter 3: Identification of the optimal solvent-free mechanochemical synthesis conditions for inorganic perovskites [192].
- Chapter 4: Investigation of multi-cation inorganic perovskites via dry mechanochemistry and the subsequent study of ion-replacement and passivation with potassium halide salts [95].
- Chapter 5: Attempt to develop hybrid and inorganic pure-tin and mixed tin-lead iodide perovskites, as well as vacancy-ordered perovskites via a mechanochemical route and the subsequent study of their structural, chemical, thermal, optical and electrical properties [23].
- Chapter 6: Investigation of lead-free perovskite-related semiconductors and the attempt to tune the visible photoluminescence at room temperature by applying compositional engineering of mechanochemically-synthesized low-dimensional, lead-free halide semiconductors [16].
- Chapter 7: Fabrication of thin films via single-source vacuum deposition of mechanochemically-synthesized inorganic perovskite powders [107].

## Chapter 2

# Methodology and characterization techniques

In this chapter the experimental approach in the synthesis and characterization of the relevant materials investigated in this doctoral thesis is described. First, the realization of mechanochemically-synthesized semiconductors, as well as the transformation of these into thin films are explained. Finally, the characterization techniques used in this thesis to investigate the relevant materials are described.

### 2.1 Methodology

As mentioned in Chapter 1, this thesis focuses on the synthesis of multinary metal halide semiconductors via a mechanochemical approach in an all-dry manner. This is enabled by ball-milling stoichiometric precursors of the desired material. Whereas in the upcoming chapters (see Chapters 3-7) different material compositions will be described; for the sake of simplicity in the following, the methodology will be explained based on the general composition of perovskites with the formula  $ABX_3$ , which is composed of two stoichiometric precursors  $AX$  and  $BX_2$  (1:1 molar ratio). As previously described,  $A$  stands for the monovalent cation,  $B$  the divalent metal and  $X$  the halide anion.

In order to conduct the material investigation in a controlled manner and to avoid factors that might influence the synthesis (e.g. oxidation reactions), the complete fabrication of the semiconducting materials was performed in a nitrogen-filled glovebox. In this way, air exposure is prevented, which might initiate degradation or transformation of the desired materials. As such – depending on the technical abilities – the as-synthesized materials could be characterized in their original state (see Section 2.2).

As illustrated in Figure 2.1, the stoichiometric precursors  $AX$  and  $BX_2$  are mixed in a nitrogen-filled glovebox (Figure 2.1; Step 1). It must be noted that all chemicals used in this doctoral thesis were stored under nitrogen-conditions and used as received without further purification. Two separate vials are filled with the desired stoichiometric perovskite precursors. Once the compounds are weighted out, they are transferred to two 10 mL zirconia ball-milling jars, along with the grinding medium, which are two zirconia beads of 10 mm in diameter per jar (Figure 2.1; Step 2). Prior to closing the jars in nitrogen and transferring them to the ball-mill – which is located outside the glovebox and thus is exposed to ambient conditions – an O-ring made of Teflon (PTFE) is placed in the recess of the lid of the jars to prevent air exposure, as well as the possible expulsion of powder during ball-milling (Figure 2.1; Steps 3 and 4). Then, ball-milling is performed with a MM-400 shaking ball-mill from Retsch at a frequency of 30 Hz for a certain amount of time (Figure 2.1; Step 5). The exact ball-milling time used for the preparation of the different compounds investigated in this doctoral thesis is mentioned in Chapters 3-7. For safety reasons, it is important to highlight the fact that during one ball-mill session, two jars are used to

preserve the mass balance. Upon completion of the milling procedure, the jars are transferred to a nitrogen-filled glovebox (Figure 2.1; Steps 6 and 7), where they are separated from the obtained powder materials (Figure 2.1; Step 8). In this way, the synthesized materials are not exposed to air. In order to characterize the powder compounds by X-ray diffraction, UV-Vis absorbance and PL spectroscopy (see Subsections 2.2.1-2.2.2), the powders are placed on double-sided tape-covered glass substrates (Figure 2.1; Step 9).

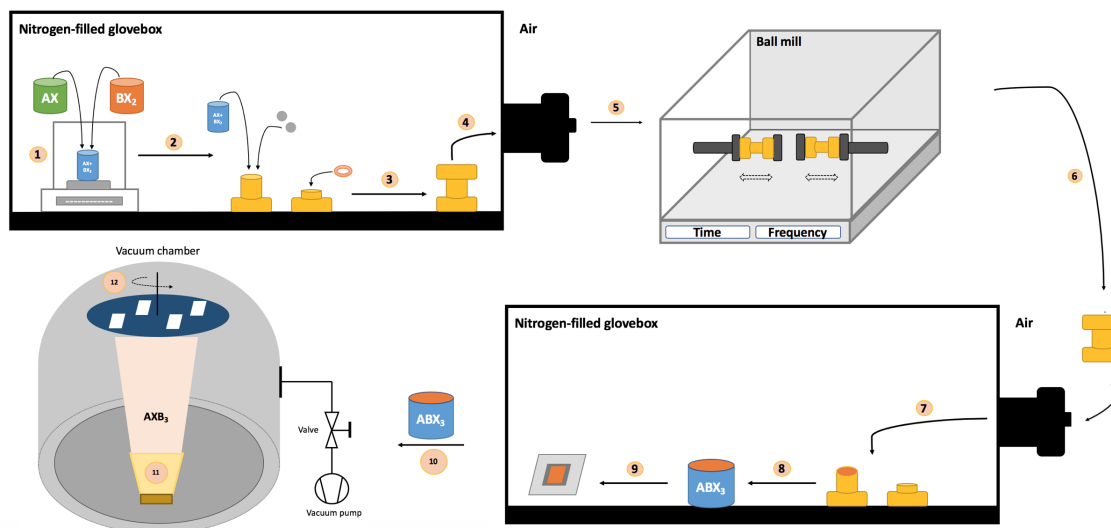


Figure 2.1: Illustration of the methodological approach of the mechanochemical synthesis of multinary metal halide semiconductors and the subsequent conversion of the synthesized powders into thin films via single-source vacuum deposition (SSVD). Stoichiometric precursors AX and BX<sub>2</sub> are mixed in a nitrogen-filled glovebox (Step 1). The weighted powders (made in double or from a different desired composition) are transferred to two 10 mL zirconia ball-milling jars, along with the grinding medium, which are two zirconia beads of 10 mm in diameter per jar (Step 2). Prior to closing the ball-mill jars and transferring to ambient conditions, an O-ring is placed in the recess of the lid of the jars to prevent air exposure, as well as the expulsion of powder during ball-milling (Steps 3 and 4). Ball-milling is performed at a certain frequency for a certain amount of time (Step 5). Upon completion of the milling procedure, the jars are transferred to a nitrogen-filled glovebox (Steps 6 and 7), where they are separated from the obtained powder materials (Step 8). For characterization purposes, the powders are placed on double-sided tape-covered glass substrates (Step 9). The powder materials are converted into thin films by SSVD in a vacuum chamber in a nitrogen-filled glovebox (Step 10). Therefore, the ball-milled powder is transferred to a ceramic crucible (Step 11), followed by the sublimation of its content by applying a high temperature under vacuum conditions. As a result, thin films are formed on the substrates, which are placed in a rotating sample holder, located directly above the evaporation source (Step 12).

Finally, as discussed in Chapter 1 and as will be presented in Chapter 7, the powder materials are converted into thin films by single-source vacuum deposition (SSVD). As shown in Figure 2.1, this procedure is performed in a vacuum chamber (Vaksis R&D and Engineering), which is integrated in a nitrogen-filled glovebox in a class 10,000 clean-room (Figure 2.1; Step 10). For the sublimation of the relevant material, the prepared ball-milled powder is transferred to a ceramic crucible (Figure 2.1; Step 11), which is placed inside a temperature-controlled evaporation source (Creaphys GmbH). The source is placed upwards under an angle of 90° with respect to a rotating (3 rpm) sample holder (Figure 2.1; Step 12), which is placed at approximately 20 cm from it. It must be stated that the vacuum chamber is equipped with two QCM sensors that monitor the evaporation rate. One sensor is placed in the proximity of the sample holder and the other one close to the evaporation source. Whereas in the case of dual/multi co-evaporation, continuous control of the evaporation temperatures and thus evaporation rates of several separate crucibles needs to be performed – as discussed in Chapter 1 – this is not the case for SSVD. Here, the aim is the fast sublimation of the already-prepared material from a single crucible (no evaporation of separate precursors in separate crucibles), which is obtained by applying high temperatures at which the complete material evaporates (the temperature at which no decomposition occurs). As a result, the

evaporation rate is monitored out of interest for the evaporation process (to monitor the highest obtained rate and the time of sublimation completion, which occurs when the rate drops to zero). It must be noted that in this doctoral thesis – where importance is put on the successful formation of plain thin-films – glass substrates were used. Prior to evaporation, the substrates were cleaned with consecutively soap, water and isopropanol in an ultrasonic bath (Elmasonic P), followed by an ultraviolet-ozone plasma surface treatment (OKL 200-4). Once the crucible is loaded with the relevant material and the substrates are placed in the substrate holder, the chamber is evacuated to a pressure of  $10^{-6}$  mbar. Upon reaching this pressure, the desired evaporation temperature is applied at the highest potential possible to ensure the fast heating of the crucible. It must be stressed that the evaporation of the relevant material occurs fast and under high temperatures (higher than the evaporation temperature of the precursor constituents) to avoid the incongruent melting and sublimation of different species at different (lower) temperatures. Furthermore, the film thickness – which is measured by a contact profilometer (Ambios XP-1) – could be controlled by the amount of pre-synthesized material fed into the thermal source, which could then be completely evaporated. However, the relationship between film thickness and the amount of material in the crucible could be impacted by other processing parameters, such as the distance between the source and the substrate.

## 2.2 Characterization techniques

This section describes the characterization techniques used in this doctoral research to analyze the obtained materials. Several analysis methods were used to obtain information on the structural and optical characteristics of the materials, as well as the chemical composition, electrical transport properties and morphological characteristics.

### 2.2.1 X-ray diffraction

In this thesis, structural analysis of the investigated materials was done by X-ray diffraction (XRD) using a Panalytical Empyrean diffractometer equipped with a Cu-K $\alpha$  anode operated at 45 kV and 30 mA and a Pixel 1D detector in scanning line mode. XRD is an analytical technique mainly used for phase identification of a crystalline material. This characterization method can provide information on unit cell dimensions and can perform quantitative analysis of the phase composition. Furthermore, it can be used to determine the crystallite size and micro strain. XRD is extensively used in material characterization, where it is necessary to identify both the element's presence, as well as the structure, in order to fully define the material. It is namely the atomic arrangement that defines the crystal structure. For diffraction applications, short wavelength X-rays are used since they are comparable to the typical interatomic distances in crystalline solids. These are electromagnetic radiation in the range of a few angstroms to 0.1 angstrom (1 keV - 120 keV). In general, the fundamental of X-ray diffraction lays in the constructive interference of monochromatic X-rays scattered from a crystalline sample. X-rays are generally produced by either synchrotron radiation or X-ray tubes, filtered to produce monochromatic radiation. In this doctoral thesis, the latter formed the X-ray source for crystallographic characterization (see Figure 2.2).

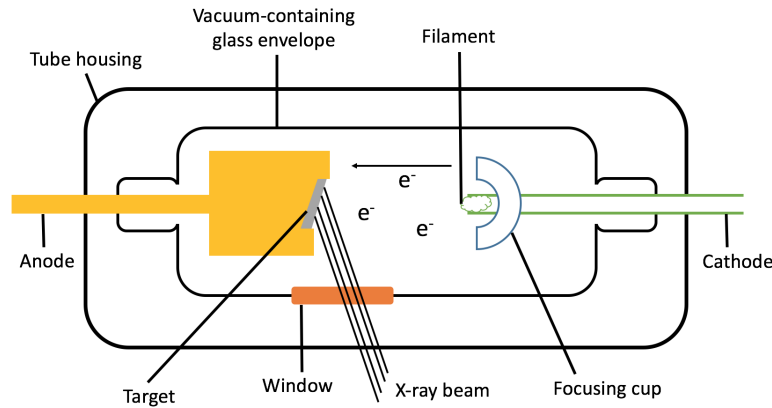


Figure 2.2: X-ray tube as the source of X-rays in an X-ray diffraction tool.

The X-ray tube is either a ceramic or glass envelope that forms an air-free vacuum around the anode and cathode. The totality of the envelope is covered by a tube housing, with the purpose of preventing X-rays from being emitted throughout the characterization room. As such, the tube housing absorbs all the X-ray photons, except from those that are aimed towards the sample. As illustrated in Figure 2.2, the cathode is a tungsten filament, which creates a cloud of free electrons (space charge) through the process of thermionic emission [193,194]. A high voltage is supplied between the cathode and anode, which causes a high voltage field between these two compartments. The electric field accelerates electrons towards the anode and thus the electrons reach the anode with a high kinetic energy. This leads to the generation of secondary electrons that are expelled from the core electron shells of the target anode material, which leave them in an unstable state. As a result, electrons from higher energy levels drop down to fill the core orbitals. As such, energy in the form of X-ray photons is released. Different target materials result in different X-ray spectra. In this thesis, copper was used as the target in the X-ray tube, which emits 8 keV X-rays with a wavelength of 1.54 Å. The energy  $E$  (eV) of an X-ray photon and its wavelength  $\lambda$  (nm) is related by Equation 2.1, where  $h$  is Planck's constant (eV.s) and  $c$  (nm/s) the speed of light.

$$E = \frac{hc}{\lambda} \quad (2.1)$$

The incident X-rays interacting with the sample cause constructive interference when conditions satisfy Bragg's Law (see Equation 2.2);

$$n\lambda = 2d.\sin(\theta) \quad (2.2)$$

where  $n$  is an integer representing the order of the diffraction peak,  $\lambda$  (nm) stands for the wavelength of the incident ray,  $d$  (nm) stands for the inter-planar spacing of the crystal and  $\theta$  (rad) stands for the angle of incidence [194–196]. It needs to be highlighted that besides atoms as scattering points, Bragg's Law applies to scattering centers consisting of any periodic distribution of electron density. In this thesis, the Bragg-Brentano geometry is used, as illustrated in Figure 2.3. This setup includes three main parts: the X-ray source, a sample mount and the detector. In order to encounter the lattice spacing using Bragg's Law, rotation of the X-ray tube and detector must take place so that the X-rays can be detected at various diffraction angles [195,196]. In this work, the sample mount was kept fixed. In Figure 2.3, the angle that forms between the X-ray source and the sample is illustrated as  $\omega$ , whereas the angle between the detector and the incident beam from the X-ray source is presented as  $2\theta$ .

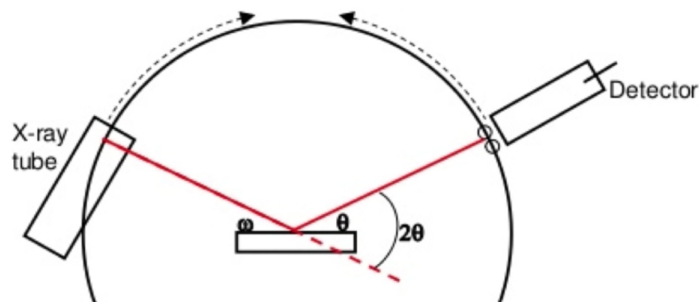


Figure 2.3: Bragg-Brentano setup where both the X-ray source and the detector can rotate relative to a fixed sample holder in order to encounter the lattice spacing using Bragg's law (see Equation 2.2). Here,  $\omega$  is the angle between the X-ray source and the sample holder, whereas the angle between the detector and the incident beam from the X-ray source is illustrated as  $2\theta$ . The illustration is adapted from reference [197].

Finally, the diffracted waves originating from different atoms can interfere with one another. The resultant intensity distribution is strongly influenced by this interaction [194]. In the case of crystals – where the atoms are arranged in a periodic fashion – the diffracted waves consist of peaks (interference maxima) with the same symmetry as in the distribution of atoms. Therefore, diffraction patterns allow the deduction of atom distribution in a crystalline material. This principle is illustrated in Figure 2.4.

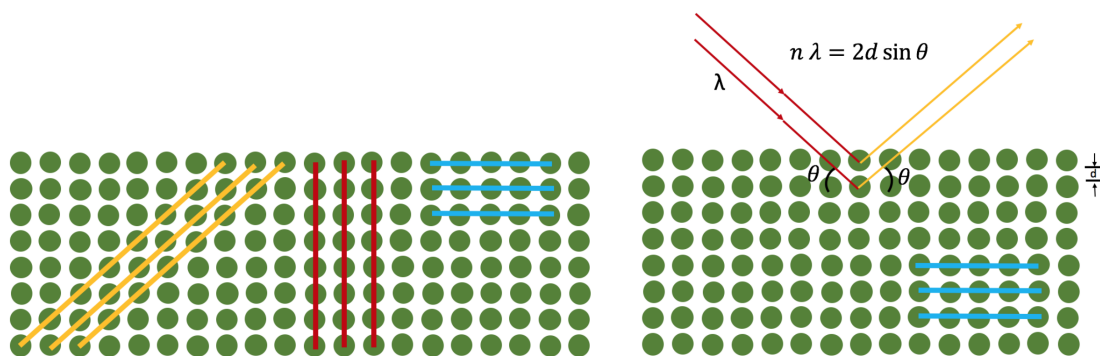


Figure 2.4: Incident X-ray beam interacting with periodically-arranged atoms (green dots) in a crystalline material. The atoms form different planes in the crystal (colored lines in the illustration on the left). The condition for diffraction to occur – for a given set of lattice planes with an inter-plane distance  $d$  – is given by Bragg's law (see Equation 2.2 with  $n = 1$ ; illustration on the right).

Eventually, by converting the diffraction peaks to d-spacings, the relevant material can be identified [194–196]. Typically, this is obtained by comparison of d-spacings with standard reference patterns, which can be retrieved from databases such as the Inorganic Crystal Structure Database (ICSD). Besides comparison with reference patterns, one can extend the identification by structure refinement of the data. This implies using an approximate model of the structure and refining it in such a way that diffraction data calculated from the model structure has a better fit to the observed (measured) data. In this doctoral thesis, Rietveld refinement was conducted to directly obtain relative weight fractions from the structural model; as opposed to conducting individual calculations and comparison with reference patterns (see Chapter 3). The detailed mathematical explanation behind the Rietveld refinement method – which is based on a least squares approach – goes beyond the scope of this thesis.

## 2.2.2 Optical characterization techniques

### Ultraviolet-visible spectroscopy

Ultraviolet-visible (UV-Vis) spectroscopy is an optical characterization technique that measures the amount of light absorbed by a sample. The light of a light source (with a wavelength range of approx. 190-750 nm) passes through a monochromator and as such exits with a single wavelength, with an intensity  $I_0$ . Depending on the material, the light will be partially absorbed by the sample so that the exited light has an intensity  $I$ , which is eventually sent to a detector. Herewith, the transmittance ( $T$ ) is the measure of the fraction of light that passes through the sample and is related according Equation 2.3 [198].

$$T = \frac{I}{I_0} \quad (2.3)$$

Furthermore, the absorbance ( $A$ ) is the amount of light absorbed by the sample and is correlated to the transmittance, following Equation 2.4.

$$A = -\log(T) = -\log\left(\frac{I}{I_0}\right) \quad (2.4)$$

Alternatively, the absorbance can be expressed by Lambert Beer's law, following Equation 2.5,

$$A = \epsilon.l.c \quad (2.5)$$

where  $\epsilon$  (L/(mol.cm)) stands for the molar absorptivity or the molar extinction coefficient,  $l$  (cm) stands for the distance the light travels through the sample and thus corresponds to the thickness of the sample and  $c$  (mol/L) is the concentration of the absorbing species [198]. As a result, the absorbance  $A$  is dimensionless. It needs to be highlighted that the molecular structure of the material determines the wavelength at which maximum light absorption occurs, as well as the intensity at which this phenomenon takes place. This means that the absorption of visible or ultraviolet light causes an electronic transition within the structure [198,199]. In this thesis, UV-Vis absorbance measurements were carried out to identify the bandgap of the prepared semiconductors (energy difference between the top of the valence band and the bottom of the conduction band) by converting the wavelength at which the absorption onset occurs to energy, using Equation 2.1. For these measurements, a High Power UV-Vis fiber light source, integrated sphere and Avantes Starline AVASpec-2048L spectrometer in reflection mode were used to obtain absorption spectra of the relevant materials.

### Photoluminescence spectroscopy

The use of photoluminescence spectroscopy allows to measure the photoluminescence (PL) of a sample. The PL is the emission of light from a sample after photon absorption. As a matter of example, Figure 2.5a shows the energy levels (HOMO and LUMO) of a hypothetical material. The minimum energy needed to excite an electron in the sample can be derived from its absorption spectrum, which is obtained by UV-Vis spectroscopy, as discussed previously. When the energy of the incident light is sufficient enough for the excitation of an electron from the HOMO level to the LUMO level, it reaches a higher energy state where the electron is unstable. Meaning, the electron has the tendency to drop to lower energy levels. In this stage, the electron is relaxed; hence the process is called electron relaxation. During relaxation, energy is lost as heat. Finally, the electron recombines with a hole in the HOMO energy level. This mechanism is also called radiative recombination, since light is produced. The energy of the emitted light is lower (energy of a higher wavelength) compared to the energy of the incident light, which is based on the principle of energy conservation [200,201].

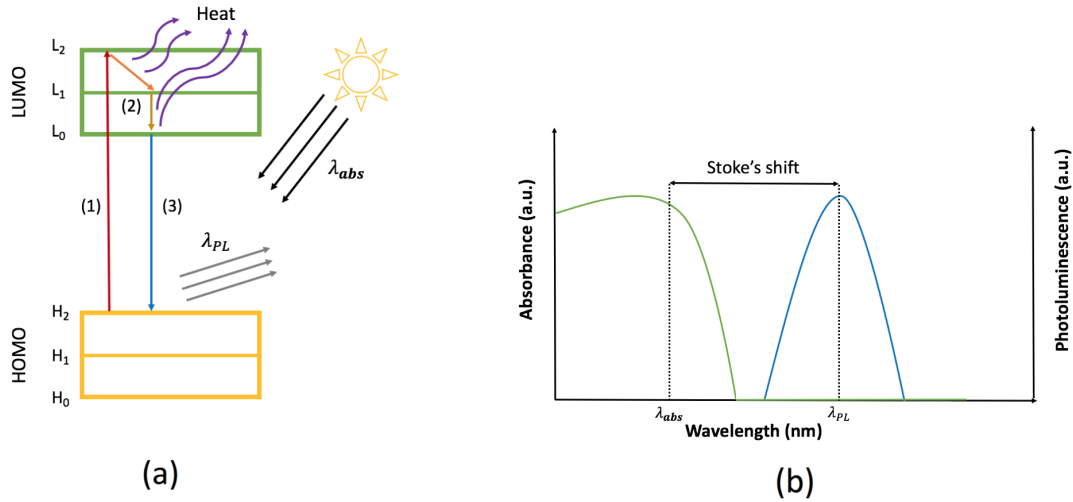


Figure 2.5: (a) Illustration of (1) electron emission, (2) relaxation and (3) recombination. HOMO and LUMO stand for the highest occupied molecular orbital and lowest unoccupied molecular orbital, respectively. Different energy levels are represented by  $H_0$ ,  $H_1$ ,  $H_2$ ,  $L_0$ ,  $L_1$  and  $L_2$  in order of increasing energy. (b) Illustration of energy loss due to electron relaxation, which is presented as the Stokes shift; the difference in wavelength between the maxima of absorption ( $\lambda_{abs}$ ) and emission ( $\lambda_{PL}$ ).

The energy loss due to electron relaxation can be derived. This concept is illustrated in Figure 2.5b, which presents the absorption and photoluminescence spectra of a hypothetical material. As can be noted, there is a difference in wavelength between the maxima of absorption and emission, which is called a Stokes shift [200,201]. The energy loss ( $E_{loss}$ ) (eV) due to electron relaxation can be calculated following Equation 2.6, where  $h$  stands for Planck's constant (eV.s),  $c$  (nm/s) the velocity of light and  $\lambda_{abs}$  (nm) and  $\lambda_{PL}$  (nm) the wavelengths at which, respectively, maximal absorption and emission occur.

$$E_{loss} = E_{excitation} - E_{emission} = \left( \frac{hc}{\lambda_{abs}} \right) - \left( \frac{hc}{\lambda_{PL}} \right) \quad (2.6)$$

It must be noted that besides energy loss in the form of heat due to electron relaxation, an alternative source of energy loss is the presence of trap states, which are states inside the bandgap of the material. The presence of such states is linked to several factors, such as contamination and structural defects [200,201]. In this doctoral thesis, photoluminescence spectroscopy was carried out by excitation of the sample with a continuous wave UV diode laser (with a wavelength suitable for the investigation of the relevant material) with a filter (with a wavelength suitable for the protection of the detector) using a Hamamatsu PMA 11 spectrometer.

### 2.2.3 Photoelectron spectroscopy

In this thesis, X-ray photoelectron spectroscopy (XPS) and Ultraviolet photoelectron spectroscopy (UPS) measurements were performed using a Kratos Axis UltraDLD spectrometer to investigate the elemental composition, oxidation states and valence band of different materials. Both characterization techniques are based on the same principle, but differ in the source of electromagnetic radiation, which is an X-ray photon beam or an ultraviolet photon beam for XPS and UPS, respectively. XPS and UPS are surface sensitive techniques that enable the investigation of the chemical composition (elements and chemical bond nature), as well as the electronic structure of a sample. The working principle is based on the photoelectric effect [202,203]. Inner-shell (or core levels during XPS) or outer shell (during UPS) electrons are ejected when an incident beam of X-ray/ultraviolet photons with sufficient energy are absorbed by atoms in the sample. It is the kinetic energy of the ejected electrons that is collected to analyze the chemical composition, as well as the electronic structure of the sample. The kinetic energy of the ejected electrons ( $E_{kinetic}$ ) can be calculated following Equation 2.7, where  $E_{binding}$  is the binding energy,  $E_{photon}$  the energy of the incident



X-ray/ultraviolet photons and  $\phi$  the work function of the element [202, 203]. The work function is the minimal energy needed to remove an electron from a solid to a point in the vacuum immediately outside the solid surface.

$$E_{binding} = E_{photon} - (E_{kinetic} + \phi) \quad (2.7)$$

Besides electrons ejected by the X-ray/ultraviolet photon beam, also Auger electrons are detected. During the Auger effect a high energy photon (in this case an X-ray/ultraviolet photon) is absorbed by the atom and interacts with an electron in the atom, which causes the electron to be emitted out of the atom. This phenomenon leaves a vacancy in the atom and thus leaves the atom in an unstable state. In order to stabilize it, an electron from the upper shell “falls” into the vacancy, producing an X-ray/ultraviolet ray. This is absorbed by an outer electron of the atom, resulting in the ejection of an electron known as the Auger electron [204]. Finally, a photoelectron spectrum is recorded by counting ejected electrons of a range of electron kinetic energies. Thus, peaks appear in the spectrum from atoms emitting electrons of a particular characteristic energy. The energies and intensities of the photoelectron peaks enable identification and quantification of all surface elements, based on the unique binding energy each element has. The peak areas in such a spectrum can also be used to obtain information on the concentration of the elements on the surface of the sample. As such, the peak area is a measure of the relative amount of the element represented by that peak [202, 203].

## 2.2.4 Electron microscopy

### Scanning electron microscopy

Scanning electron microscopy (SEM) allows to obtain topographical and compositional information of materials (i.a. this can be of powder materials, as well as of thin-films). In principle, scanning coils move an electron beam across an area of the sample. As a result, secondary and back-scattered electrons generate a visual display of the sample surface [205, 206]. In this doctoral thesis, SEM-images were taken to mainly investigate the grain size and homogeneity of the sample, using HRSEM JEOL JSM-7500L equipped with a cold field-emission gun (FEG) operating at 25 kV acceleration voltage.

### Energy-dispersive X-ray spectroscopy

In this work, energy-dispersive X-ray spectroscopy was carried out hand in hand with SEM analysis. EDX is a technique used for microanalysis of a material. This method is based on the detection of characteristic X-rays emitted by atoms that are bombarded with an electron beam. As such, the presence of elements in the material can be revealed [207, 208]. In this study, EDX was performed using an SEM (HRSEM JEOL JSM-7500L) equipped with an EDS Oxford instrument.

## 2.2.5 Thermal analysis

In this doctoral thesis, thermal gravimetric analysis (TGA) and differential thermal analysis (DTA) were carried out to investigate the thermal stability of the relevant compounds, using a LabsysEvo 1600 DTA/TGA (Setaram).

### Thermal gravimetric analysis

Thermal gravimetric analysis is a thermal analysis technique that investigates the chemical and physical characteristics of materials with increasing temperature. The mass change, as a result of the decomposition of the material, is measured as function of the heating temperature [209]. In this thesis, TGA is used as a means to analyze the composition of a material by investigating the temperature at which chemical decomposition of the relevant precursors and/or intermediates occurs (see Chapter 5).

### Differential thermal analysis

In differential thermal analysis, the temperature difference between a sample and a reference material is scanned, while the two compounds are subjected to controlled and identical heating or cooling. A difference between endothermic and exothermic reactions upon the applied temperature can be observed [210,211]. The former are reactions at which chemical or physical change occur due to the absorption of energy from the surrounding, which usually is in the form of heat. In this case, the sample temperature will be lower than the temperature of the reference material. On the other hand, in the case of an exothermic reaction (reaction where energy – in this case in the form of heat – is released), the sample temperature will be higher than that of the reference material. Figure 2.6 shows an illustration of a hypothetical DTA curve, where the difference of sample temperature is plotted as a function of the temperature of the reference material. The upward peak presents an exothermic reaction, whereas the downward peak presents an endothermic reaction [210,211]. Characteristic information – such as sample purity and phase transformations – can be derived from the size and shape of the peaks.

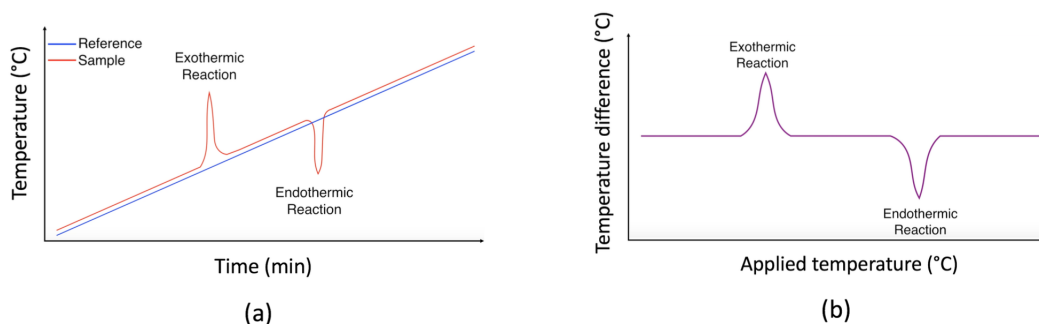


Figure 2.6: Illustration of typical DTA plots of a hypothetical material, where (a) the difference of sample temperature is plotted as a function of the temperature of the reference material and (b) the difference in temperature is plotted as a function of the applied temperature.

#### 2.2.6 Pulse-radiolysis time-resolved microwave conductivity

In pulse-radiolysis time-resolved microwave conductivity (PR-TRMC), the electrical transport properties of a material are measured as a function of time. Herewith, microwaves are used as the probe to evaluate the electrical conductivity [212]. In this thesis, PR-TRMC was carried out on micrometer crystals (approximately 45 mg) placed on a Polyether ether ketone (PEEK) holder. The PEEK holder was placed inside a rectangular waveguide cell (made of chemically inert gold-plated copper). The cell was contained in a cryostat in which the temperature could be varied between 123 K and 473 K. In this study, PR-TRMC was measured using a home built setup from the Optoelectronic Materials Section of the Department of Chemical Engineering at Delft University of Technology, The Netherlands (see Chapter 5).

## Chapter 3

# Mechanochemical Synthesis of Inorganic Halide Perovskites: Evolution of Phase-purity, Morphology and Photoluminescence

### 3.1 Introduction

Over the past decade, organic-inorganic hybrid perovskites (OHPs) have been widely studied. The attractive optical and electronic properties make these materials promising in the field of perovskite optoelectronics [71–74]. However, several drawbacks and limitations hinder the development of OHP optoelectronic devices. One of the main concerns is the environmental instability, which is attributed to the high volatility and moisture sensitivity of the organic compounds [213, 214]. For this reason, investigation is conducted in the all-inorganic, thermally stable, cesium-based lead halide perovskites [12, 215–218]. However, as mentioned previously (see Chapter 1), the poor solubility of cesium halides in common solvents, make the formation of Cs-based perovskites by conventional solution-processing rather challenging [174, 175]. Thus, new ways for producing high-purity lead halide perovskites (LHPs) in large scale are actively sought after. Mechanochemical synthesis (MCS) has recently emerged as an alternative, convenient and reproducible method to obtain high quality (non-)cesium-based LHPs, as well as other lead-free multinary metal halides [15–17, 20, 23, 47, 59, 70, 94, 96, 98, 107, 108, 115, 134, 219]. Whereas the scientific and technological relevance of MCS for the study and fabrication of perovskites and related materials is an undisputed fact, little is known about the reaction kinetics, the formation of intermediate species and the effects of ball-milling on the size and shape of the final particles. Furthermore, questions arise regarding defect formation that can affect the optoelectronic properties of the end product. As a means to clarify these issues, this study presents a systematic investigation of the solvent-free mechanochemical synthesis of inorganic CsPbBr<sub>3</sub>, where the beneficial and detrimental effects of ball-milling on the phase-purity evolution, morphology and optical characteristics of the formed materials are reported as a function of the ball-milling time.

This work was published in Journal of Materials Chemistry C [192]. The complete journal article can be found in Appendix A.

## 3.2 Experimental methods

### 3.2.1 Mechanochemical synthesis via ball-milling

To investigate the different stages of the mechanochemical synthesis of CsPbBr<sub>3</sub>, a ball-milling time dependent study was carried out. The perovskite precursor cesium bromide (CsBr, > 99 %) was purchased from TCI Chemicals and the precursor lead bromide (PbBr<sub>2</sub>, ≥ 98 %) was purchased from Sigma-Aldrich. All chemicals were stored in a nitrogen-filled glovebox and used as received without further purification. The mechanochemical synthesis was carried out by ball-milling of the stoichiometric perovskite precursors at a frequency of 30 Hz for different times (0.5, 1, 2, 3, 4, 5, 30, 60 and 600 min), as previously described in Chapter 2 (see Figure 2.1; Steps 1-9).

### 3.2.2 Characterization

In order to study the evolution of the phase-purity of the formed materials, X-ray diffraction was measured. Furthermore, the effect of the ball-milling time on the mechanochemical synthesis of CsPbBr<sub>3</sub> was investigated by optical spectroscopy and electron microscopy.

#### X-ray diffraction

To identify and quantify the different species and phases formed, X-ray diffraction was measured in the  $2\theta = 10^\circ - 90^\circ$  range with a step size of  $2\theta = 0.026^\circ$ , as described in Chapter 2. Furthermore, microstructural analysis was carried out to extract information on phase quantities. For this, instrumental peak broadening was taken into account by measuring a reference silicon wafer under the same measurement conditions and refining the Thompson-Cox-Hastings (TCH) pseudo-Voigt line shape parameters, used to create the instrument resolution file. All XRD analyses were carried out with Fullprof software. Whole-pattern Le Bail Fits were performed to refine cell parameters and line shape for microstructural analysis. Refined cell parameters were also used to carry out structural Rietveld refinement for quantitative analysis.

#### Electron microscopic characterization

Electron microscopic characterization (SEM and EDX) was performed using HRSEM JEOL JSM-7500L equipped with a cold field-emission gun (FEG) operating at 25 kV acceleration voltage and with an EDS Oxford instrument.

#### Optical characterization

To probe the evaluation of optoelectronic properties of the formed materials, the photoluminescence (PL) was determined by excitation with a continuous wave UV diode laser ( $\lambda = 375$  nm) with a 400 nm filter and Hamamatsu PMA 11 spectrometer. For a typical spectrum, 10 scans of 1 second were averaged. Although the obtained samples are generally not emissive enough to obtain reliable quantum yield measurements; the laser power, acquisition time and sample amount were kept constant in order to get semi-quantitative results. Absorbance spectra were measured with a High Power UV-Vis fiber light source, integrated sphere and Avantes Starline AVASpec-2048L spectrometer in reflection mode.

### 3.3 Results and discussion

In order to investigate the different stages of the synthesis of cesium lead tribromide, the effect of the ball-milling time on the formation of the material was studied. To study the initial stages of the mechanochemical synthesis of  $\text{CsPbBr}_3$ , stoichiometric  $\text{CsBr}:\text{PbBr}_2$  mixtures were ball-milled for 0.5, 1, 2, 3, 4 and 5 minutes. For all samples, high resolution powder X-ray diffractograms (PXRD) were obtained in the range  $2\theta = 10^\circ - 90^\circ$ . This allows the identification, as well as the quantification of the different species formed at each time. Aside from the binary precursors cesium bromide ( $\text{CsBr}$ ) and lead bromide ( $\text{PbBr}_2$ ), three different ternary compounds are known to be stable:  $\text{Cs}_4\text{PbBr}_6$ ,  $\text{CsPb}_2\text{Br}_5$  and  $\text{CsPbBr}_3$ . Based on the structural dimensionality (the interconnectivity of  $[\text{PbBr}_6]^{4-}$  octahedra in crystals), these phases are also referred to as 0D, 2D and 3D crystal structures. Figure 3.1 presents diffractograms of the range  $2\theta = 10^\circ - 20^\circ$  (see Figure A.1 in Appendix A for full patterns). In this range, the three ternary compounds are clearly identified by peaks at approximately  $2\theta = 11.7^\circ$  ( $\text{CsPb}_2\text{Br}_5$ ),  $2\theta = 12.7^\circ$  ( $\text{Cs}_4\text{PbBr}_6$ ) and  $2\theta = 15.0^\circ$  ( $\text{CsPbBr}_3$ ). Whereas the precursor  $\text{PbBr}_2$  is identified by a diffraction peak at around  $2\theta = 18.5^\circ$ . It needs to be stressed that these peaks do not correspond to the main reflections of the phases. However, as they occur in a close, yet not-overlapping region of the diffractogram, these peaks are the most convenient for straightforward identification. As can be seen in Figure 3.1, complete conversion of the binary precursors into the stoichiometric  $\text{CsPbBr}_3$  perovskite is achieved in 5 minutes. This result highlights the fact that mechanochemical synthesis via solvent-free ball-milling is a rather simple, but more in particular, fast technique for the fabrication of phase-pure perovskites. The observations made in the current study indicate that prolonged ball-milling (60 min) – as will be demonstrated in Chapter 7 [107] and as reported by L. Protesescu, *et al.* [70] – might not be needed on the level of phase-purity. However, the effect of prolonged ball-milling times will be discussed.

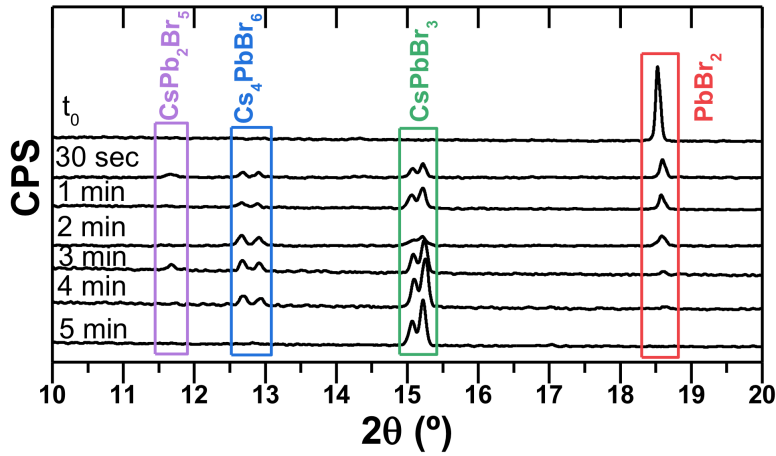


Figure 3.1: X-ray diffraction analysis of stoichiometric  $\text{CsBr}:\text{PbBr}_2$  mixtures ball-milled for different times up to 5 minutes, with a close view of the  $2\theta = 10^\circ - 20^\circ$  range (see full patterns in Figure A.1 in Appendix A) of the diffractograms where characteristic peaks of different phases are highlighted in different colors. The XRD data of a not-ball-milled stoichiometric  $\text{CsBr}:\text{PbBr}_2$  mixture is presented as  $t_0$ .

As mentioned previously, prior to full reaction conversion, the non-stoichiometric compounds  $\text{Cs}_4\text{PbBr}_6$  and  $\text{CsPb}_2\text{Br}_5$  are present at intermediate stages. It is worth noting that the  $\text{PbBr}_2$ -rich phase ( $\text{CsPb}_2\text{Br}_5$ ) is only marginally seen in two of the six samples, while the  $\text{CsBr}$ -rich phase ( $\text{Cs}_4\text{PbBr}_6$ ) is consistently observed in all the intermediate samples. Knowing that the syntheses were carried out under stoichiometric conditions, this observation points towards a lower formation energy for  $\text{CsBr}$ -rich phases. This is in agreement with DFT calculations, which have estimated a formation energy of  $-1.592$  eV/atom for  $\text{Cs}_4\text{PbBr}_6$  and  $-1.321$  eV/atom for  $\text{CsPbBr}_3$  [220, 221]. Furthermore, the fact that the three ternary phases co-exist at short milling times ( $< 5$  min) and eventually convert into phase-pure, stoichiometric  $\text{CsPbBr}_3$ , highlights the chemical and structural versatility of these compounds. Several reports have demonstrated interconversion between these phases. However, most of these were carried

out in solution and/or with different additives such as amines [222],  $\text{ZnX}_2$  [35], Prussian blue [223] or water [224, 225]. Hence, it is worth noting that these interconversion reactions also take place during solid-state synthesis without the presence of additives to mediate the reactions.

In order to obtain a semi-quantitative analysis of the different species, whole-pattern Le Bail fits were conducted on the diffractograms (see Figure A.1 in Appendix A) [226]. Therefore, two quantification methods were used. On one hand, the calculated intensity of the main diffraction peak of each phase was divided by the relative intensity ratio (RIR) of the corresponding phase, as obtained from literature (ICSD database). On the other hand, Rietveld refinements were conducted to directly obtain relative weight fractions from the structural model. Both methods resulted in nearly identical quantification results (see solid and dotted lines in Figure 3.2a – weight fraction as directly obtained from PXRD quantification – and Figure 3.2b – molar fraction as derived from weight fraction and corresponding molecular weight of each phase –), despite slightly different pattern fits (see Figure A.1 in Appendix A). Figure 3.2b shows that CsBr is consumed faster than  $\text{PbBr}_2$ , as mostly CsBr-rich phases ( $\text{CsPbBr}_3$  and  $\text{Cs}_4\text{PbBr}_6$ ) are formed. In fact, between a ball-milling time of 1 minute and 2 minutes, the  $\text{Cs}_4\text{PbBr}_6/\text{CsPbBr}_3$  ratio increases. This observation highlights once again the versatile interconversion between the different ternary phases.

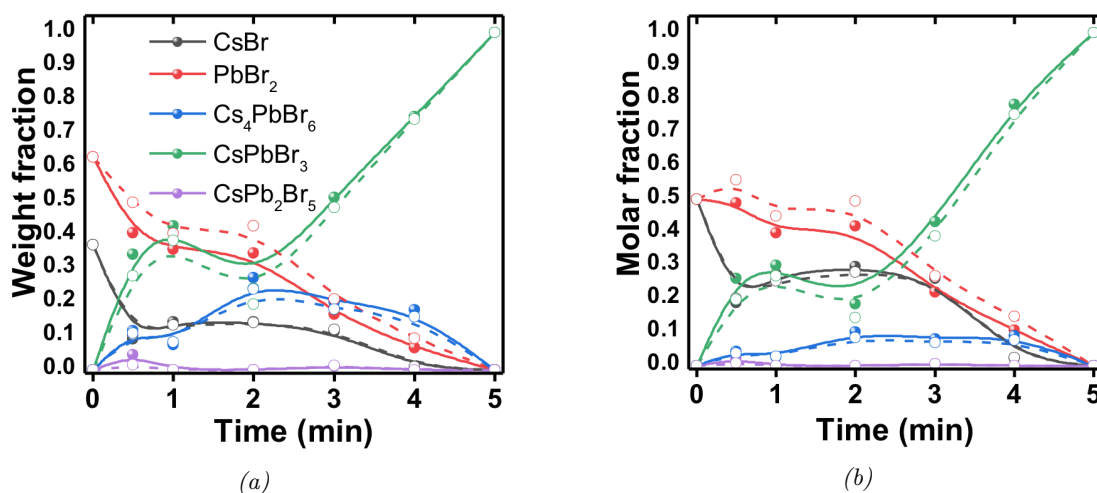


Figure 3.2: (a) Weight fraction of different species as derived from the RIR method (filled spheres and solid lines) and Rietveld refinement (open circles and dashed lines). (b) Molar fraction of different species derived from the RIR method (filled spheres and solid lines) and Rietveld refinement (open circles and dashed lines). B-spline lines are drawn to guide the eye.

Besides PXRD analysis, scanning electron microscopic and energy-dispersive X-ray spectroscopic measurements were carried out on the six different samples. Figure 3.3a-d presents SEM images of the four main different compounds. The images are selected close-ups of different phases identified by EDX. Identification by EDX shows these compounds to be CsBr (49:51 ratio by EDX),  $\text{Cs}_4\text{PbBr}_6$  (37:10:53 ratio by EDX),  $\text{PbBr}_2$  (33:67 ratio by EDX) and  $\text{CsPbBr}_3$  (22:18:60 ratio by EDX). These results are obtained by considering the high-energy lines for each element (Br(K), Cs(L) and Pb(L)). The morphology of the different phases is clearly different. As such, CsBr is formed of large smooth crystals, while  $\text{PbBr}_2$  shows to have a rather small-grain texture. On the other hand,  $\text{Cs}_4\text{PbBr}_6$  and  $\text{CsPbBr}_3$  consist of grains with different typical sizes from sub-100 nm to  $> 1 \mu\text{m}$ . Furthermore,  $\text{CsPbBr}_3$  forms round-shaped aggregates of about 100 microns in size.

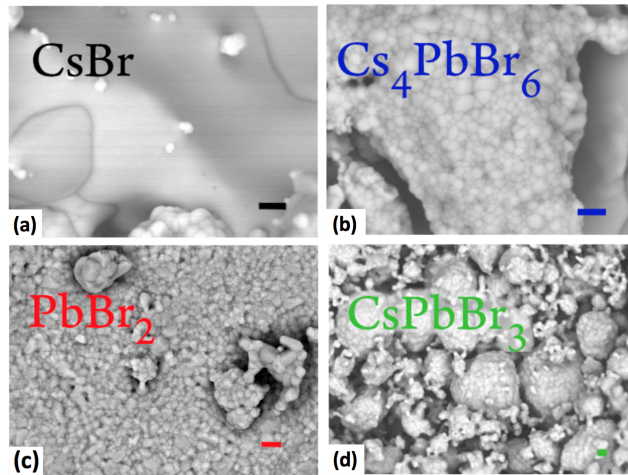


Figure 3.3: Scanning electron microscopic images of the different phases found in the samples and identified by EDX analysis. All scale bars are one micron.

However, it is common to find large particles with different mixed phases. As an example, Figure 3.4 presents an SEM image of a large particle, partly encapsulating fine-grain agglomerates. Corresponding EDX maps and selected small-area spectra show that the large particle is mostly lead-free ( $\text{CsBr}$ ) and that the inside smaller grains are  $\text{CsPbBr}_3$ .

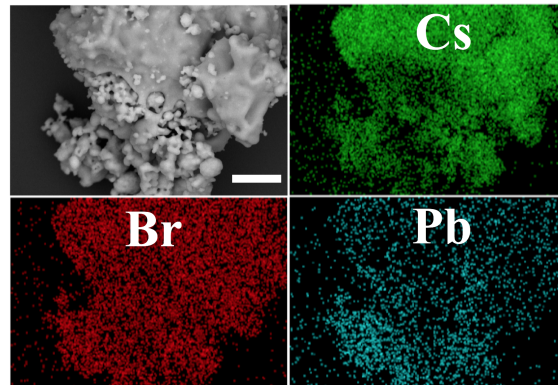


Figure 3.4: SEM images and corresponding EDX maps for Cs (green), Br (red) and Pb (blue). The scale bar is 10 microns. Two distinct materials are observed both from morphology and composition. These correspond to  $\text{CsBr}$  (large smooth particle) and  $\text{CsPbBr}_3$  (fine-grain agglomerates).

As mentioned previously, several reports on mechanochemical synthesis of halide perovskites, including the publication that will be discussed in Chapter 7, use ball-milling times considerably longer than 5 minutes [70, 107]. Hereafter, the effects of prolonged ball-milling for up to 10 hours was investigated. Diffractograms of samples ball-milled for 30 minutes, 1 hour and 10 hours show the presence of a single  $\text{CsPbBr}_3$  phase (see A.2 in Appendix A). This result suggests that once full conversion of the precursors into the stoichiometric  $\text{CsPbBr}_3$  phase is reached (after 5 minutes of ball-milling), the 3D perovskite phase remains stable upon further ball-milling. Since previously it was shown that interconversion between the different ternary phases occurs, this observation is different compared to what one might expect. However, once full conversion into  $\text{CsPbBr}_3$  is achieved without remaining  $\text{CsBr}$  or  $\text{PbBr}_2$ , it appears that no further structural evolutions take place under these conditions. Meaning that  $\text{CsPbBr}_3$  is not reverted into its initial constituents ( $\text{CsBr}$  and  $\text{PbBr}_2$ ) upon prolonged ball-milling. Nonetheless, morphological changes are observed. The XRD peaks are broadened with prolonged ball-milling time (see Figure A.3 in Appendix A). In order to study this effect in more depth, microstructural analysis was performed on the whole-pattern fitted diffractograms (See Figure A.2 in Appendix A). To take instrumental broadening into account, microstructural analysis was carried out after calibration. For this, the Williamson-Hall



(WH) method was used. The WH equation represents an approximate formula for size broadening ( $\beta_L$ ) and strain broadening ( $\beta_\epsilon$ ), following Equation 3.1; where  $k$  is the shape factor,  $\lambda$  (nm) the wavelength of incident radiation,  $L$  (nm) the average crystallite size,  $\theta$  (rad) the diffraction angle and  $\epsilon$  the intrinsic strain (dimensionless or in %) [227].

$$\beta_{hkl} = \beta_L + \beta_\epsilon = \frac{k\lambda}{L \cos(\theta)} + 4\epsilon \cdot \tan(\theta) \Leftrightarrow \beta_{hkl} \cdot \cos(\theta) = \frac{k\lambda}{L} + 4\epsilon \cdot \sin(\theta) \quad (3.1)$$

The Williamson-Hall plots are presented in Figure 3.5a, where as indicated by Equation 3.1, the slope is related to microstructural strain and the extrapolated intercept gives an average isotropic grain size. It needs to be mentioned that for these analyses, the possibility of anisotropy was discarded. This assumption is based on the fact that no 1D (needle-) or 2D (platelet-) shaped crystals were observed from the SEM images (Figure 3.3d and Figure A.4 in Appendix A). For a clearer evaluation, the evolution of the apparent grain size over ball-milling time is presented in Figure 3.5b. An obvious reduction in crystallite size is observed at longer ball-milling times. Nonetheless, it must be noted that this analysis provides an average grain size without information on size dispersity. Indeed, SEM images of the sample ball-milled for 10 hours confirm the presence of small grains (sub-100 nm), as well as the coexistence with larger grains up to 1 micron (see Figure A.4 in Appendix A). To probe the optoelectronic properties of the different ball-milled

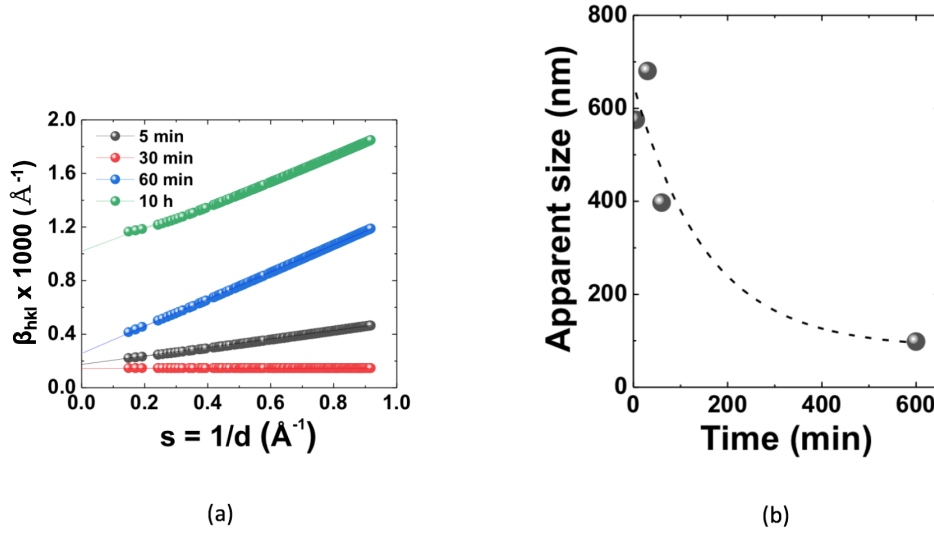


Figure 3.5: Microstructural XRD analysis. (a) Williamson-Hall (WH) plots obtained from Le Bail fits of XRD data acquired on stoichiometric  $\text{CsBr:PbBr}_2$  mixtures ball-milled for 5 minutes up to 10 hours (see Figure A.3 in Appendix A). The fits assume a pseudo-Voigt Thompson-Cox-Hastings (TCH) line shape with Gaussian broadening contribution from strain (slope) and Lorentzian broadening contribution from reduced crystallite size (offset). Here,  $\beta_{hkl}$  stands for the total broadening due to strain and size in a particular peak having the  $(hkl)$  value and “ $s$ ” is the inverse of the inter-planar spacing ( $d$ ) of a crystal in Bragg’s law (b) Apparent isotropic average crystal size deduced from extrapolated value at origin from the WH plots as a function of the ball-milling time.

powders, the photoluminescence was examined. As mentioned previously (see Subsection 3.2.2), due to the fact that these samples are generally not emissive enough to attain reliable quantum yield measurements, the PL measurements were carried out under the same conditions (fixed laser power, acquisition time and sample amount) in order to obtain semi-quantitative results (see Figure 3.6a). The first noticeable result is that the most-emissive samples are those that were ball-milled for a short amount of time ( $t < 5$  min); whereas the samples that were ball-milled for longer times demonstrated significantly lower PL intensities (one to two orders of magnitude lower). This reduction in PL intensity can be explained by the formation of non-radiative trap states resulting from defects induced by ball-milling [70]. Furthermore, besides the drop in PL intensity, a broadening of the spectra is clearly observed when the normalized PL intensity is plotted as a



function of the wavelength (Figure 3.6b). In the first three samples ( $t = 30$  sec, 1 min and 2 min) – which, as previously discussed, correspond to non-phase-pure syntheses – a dominant PL peak at 525 nm is observed, with a second feature centered at 545 nm.

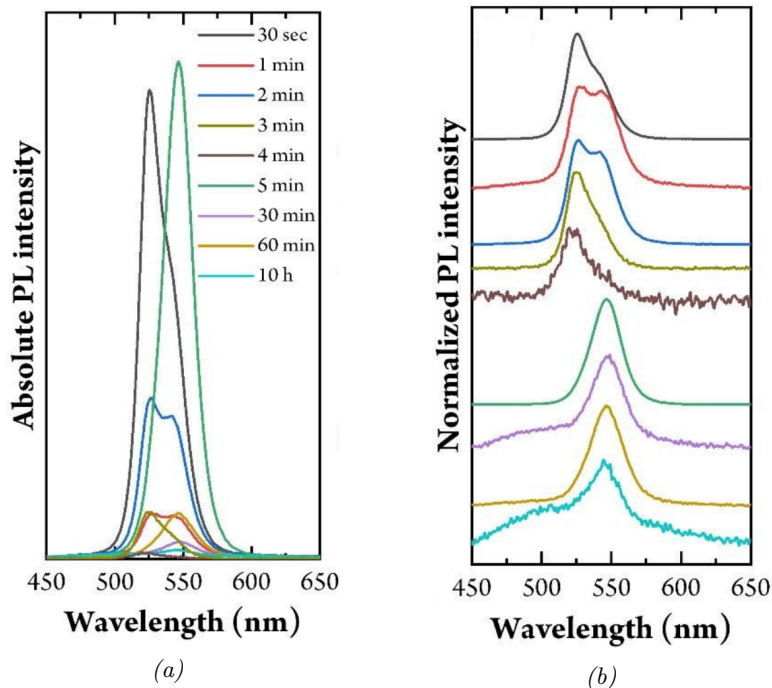


Figure 3.6: (a) Absolute and (b) normalized photoluminescence intensities of samples ball-milled for different times under identical measurement conditions (fixed excitation source, acquisition time and sample amount).

These peaks can be ascribed to weakly-quantum-confined (“nano”) and bulk  $\text{CsPbBr}_3$ , respectively [175, 228]. At  $t = 5$  min, when full conversion of the perovskite precursors into phase-pure  $\text{CsPbBr}_3$  occurs, only one symmetric PL peak – with a narrow full-width at half maximum (FWHM) of 26 nm – corresponding to  $\text{CsPbBr}_3$  is present. When prolonged ball-milling is performed – aside from the previously described drop in PL intensity – the spectra become wider with a broad band at shorter wavelengths (Figure 3.6b). This observation can be ascribed to the exfoliation of small, quantum-confined  $\text{CsPbBr}_3$  nanocrystals [219]. This result is in line with the reduced average crystallite size revealed by microstructural XRD analysis (Figure 3.5). It needs to be stated that exfoliation upon prolonged ball-milling in the presence of solvents and ligand molecules, has been reported [219]. The current results suggest that such small, quantum-confined crystals can be obtained in the absence of solvents and additives, although these are certainly beneficial to passivate the crystal surfaces [229, 230]. This would be of interest to obtain high PL intensities, as in the case of dry ball-milling in the absence of additives, the PL emission is greatly reduced. Finally, it must be noted that in all cases, the optical absorption (see Figure A.5 in Appendix A) is dominated by the lower-bandgap (“bulk”) species.

### 3.4 Conclusions

In this study, the mechanochemical synthesis of  $\text{CsPbBr}_3$  was investigated over time by dry ball-milling of the stoichiometric precursors  $\text{CsBr}$  and  $\text{PbBr}_2$ . Detailed structural, morphological and optical analyses reveal several beneficial and detrimental effects of milling as a function of time for the material and ball-milling system/conditions used. During the process three stages are identified:

(1) At short milling times ( $t < 5$  min), there is a coexistence and interconversion of the three known ternary phases:  $\text{CsPb}_2\text{Br}_5$ ,  $\text{CsPbBr}_3$  and  $\text{Cs}_4\text{PbBr}_6$ . It is noted that the CsBr-rich

phase ( $\text{Cs}_4\text{PbBr}_6$ ) is consistently observed in all intermediate samples. This may be associated to a lower formation energy for this compound. Furthermore, photoluminescence from “nano” and “bulk”  $\text{CsPbBr}_3$  species is observed, centered at 525 nm and 545 nm, respectively.

(2) For the present case, an optimum ball-milling time of 5 minutes exists; this is where the complete transformation of all the reactants and byproducts into phase-pure  $\text{CsPbBr}_3$  has occurred. It is demonstrated that the derived material has a narrow and intense PL corresponding to “bulk”  $\text{CsPbBr}_3$ .

(3) At prolonged ball-milling times (up to 10 hours), smaller quantum-confined  $\text{CsPbBr}_3$  nanocrystals (NCs) are exfoliated from the bulk product, leading to a broad and blue-shifted emission. Furthermore, this phenomenon comes along with a reduction in the photoluminescence intensity, which is ascribed to the formation of surface defects induced by ball-milling under dry and additive-free conditions.

To conclude, the mechanochemical synthesis of fully inorganic lead halide perovskites via ball-milling is a simple, dry and fast (5 min) process that leads to excellent phase-purity. This paves the way to a more generalized use of mechanochemistry for the synthesis of halide perovskites, as will be presented in Chapters 4-7.

### 3.5 Author contribution and acknowledgments

The content of this chapter was reproduced with permission from Journal of Materials Chemistry C [192]. The complete journal article can be found in Appendix A. In this article, Yousra El Ajjouri has been the principal investigator of the experiments carried out at the University of Valencia, in the research group of Prof. Dr. Hendrik Jan Bolink, in which she has devised, has carried out the appropriate measurements (except from the SEM and EDX measurements) and has interpreted the experimental results under direction and supervision of Prof. Dr. Hendrik Jan Bolink and Dr. Francisco Palazón.

The research discussed in this chapter was carried out in collaboration with S. Lauciello under supervision from Dr. L. Manna from the Department of Nanochemistry and the Electron Microscopy Facility at Istituto Italiano di Tecnologia in Genova, Italy, who carried out the SEM and EDX measurements.

The research leading to the results presented in this chapter has received funding from the European Union Program for Research and Innovation Horizon 2020 (2014-2020) under the Marie Skłodowska-Curie Grant Agreement PerovSAMs No. 747599, the Spanish Ministry of Economy and Competitiveness (MINECO) via the Unidad de Excelencia María de Maeztu MDM-2015-0538, MAT2017-88821-R and PCIN-2015-255 and the Generalitat Valenciana (Prometeo/2016/135 and GRISOLIAP/2017/089).

F. Palazón, Y. El Ajjouri, P. Sebastia-Luna, S. Lauciello, L. Manna and H. J. Bolink, Mechanochemical Synthesis of Inorganic Halide Perovskites: Evolution of Phase-purity, Morphology, and Photoluminescence. *J. Mater. Chem. C*, **2019**, 7, 11406-11410. [IF: 6.641 (2019), Q1]

## Chapter 4

# Incorporation of Potassium Halides in the Mechanochemical Synthesis of Inorganic Perovskites: Feasibility and Limitations of Ion-replacement and Trap Passivation

### 4.1 Introduction

Recently, halide perovskites with an increasing complexity in formulation containing up to 6 or 7 different ions have proven to be beneficial for device performance [182–184, 231]. In this context, mechanochemical synthesis by ball-milling represents an ideal platform to test different precursors or additives in a simple manner. As previously mentioned, multi-cation perovskites enable tuning of the bandgap of the material [183], as well as its Goldschmidt tolerance factor ( $t$ ) [2, 3] – an indicator of the stability of the crystal structure of a crystalline material – which is calculated following Equation 1.1 (see Subsection 1.1.1). To obtain a stable cubic  $ABX_3$  perovskite, it is generally accepted that the Goldschmidt tolerance factor should not be lower than 0.8, nor exceed a value of 1 [2, 185]. A  $t$ -value outside of this range usually results in non-perovskite structures. Among other cations, potassium has been recently used as an additive in perovskites, with different conclusions [98, 117, 182, 232–235]. Some reports have shown a benefit from the presence of potassium in mixed (KCs)PbI<sub>3</sub> perovskites, where the guest cation is capable of stabilizing the perovskite structure [233]. Others, based on the small tolerance factor of such a structure, have concluded that incorporating potassium halides (KX) in the synthesis does not lead to the effective incorporation of potassium as replacement of the A-cation within the CsPbI<sub>3</sub> perovskite structure. As a result, potassium stays at the grain boundaries and indirectly contributes to surface passivation by providing additional halides (bound to K<sup>+</sup>), partially compensating the halide vacancies. The halide vacancies are believed to be one of the main quenching traps, which need to be passivated to improve the optoelectronic properties of the perovskite [232, 236]. On the contrary, other reports have concluded that the addition of potassium halides leads to the formation of different separate phases [98, 117]. These discrepancies might originate from the different perovskite crystallization processes used, which can result in different morphology, phase-purity or stoichiometry of the final compound. Therefore, to try and discriminate between these two views, dry mechanochemical synthesis is an ideal preparation method, as it does not involve solvents and it can eliminate the need of thermal treatments to foster the perovskite crystallization. In this work, different halide perovskites were

mechanochemically synthesized by dry ball-milling of equimolar mixtures of  $\text{PbBr}_2$  and  $\text{ABr}$ , where  $\text{A} = \text{K}_{0.2}\text{Cs}_{0.8}$ . The resulting powders were compared with the pure cesium reference ( $\text{A} = \text{Cs}$ ) perovskite. Finally, mixed anion perovskites were studied by replacing potassium bromide ( $\text{KBr}$ ) by  $\text{KX}$  ( $\text{X} = \text{Cl}^-$  or  $\text{I}^-$ ), while keeping  $\text{CsBr}$  and  $\text{PbBr}_2$  as precursors in the mechanochemical synthesis.

This work was published in RSC Advances [95]. The complete journal article can be found in Appendix B.

## 4.2 Experimental methods

### 4.2.1 Mechanochemical synthesis via ball-milling

In order to study the effect of potassium in the  $\text{CsPbBr}_3$  perovskite, stoichiometric  $\text{AX}:\text{PbBr}_2$  mixtures were mechanochemically synthesized by dry ball-milling. Herewith,  $\text{AX}$  stands for  $\text{K}_{0.2}\text{Cs}_{0.8}\text{Y}$  with  $\text{Y} = \text{I}^-$ ,  $\text{Br}^-$  or  $\text{Cl}^-$ . The perovskite precursors cesium bromide ( $\text{CsBr}$ , > 99 %), cesium chloride ( $\text{CsCl}$ , > 99 %) and cesium iodide ( $\text{CsI}$ , > 99 %) were purchased from TCI Chemicals. Potassium bromide ( $\text{KBr}$ , > 99 %) and lead(II) bromide ( $\text{PbBr}_2$ ,  $\geq 98$  %) were purchased from Sigma-Aldrich. All chemicals were stored in a nitrogen-filled glovebox and used as received without further purification. The mechanochemical synthesis of the desired compounds was carried out by ball-milling of the perovskite precursors at a frequency of 30 Hz for 5 hours, as previously described in Chapter 2 (see Figure 2.1; Steps 1-9). Indeed, the ball-milling time applied in this study is higher than what showed to be necessary to obtain phase-pure  $\text{CsPbBr}_3$ , as discussed in Chapter 3. Reasoning thereof is that this study was carried out prior to knowing the minimum ball-milling time necessary for the synthesis of this perovskite. Furthermore, the addition of potassium salts in the precursor mixture might influence the synthesis mechanism. In order to know the minimum ball-milling time for the synthesis of such mixed cation and/or anion perovskites under the same conditions (frequency, BRR, etc.) as used in the synthesis of the reference perovskite (see Chapter 3), an evolution study of the formed phases over time should be carried out. However, this goes beyond the scope of this study. Finally, the perovskite  $\text{CsPbBr}_3$  was synthesized as a reference in an analogous manner by dry ball-milling the stoichiometric precursors  $\text{CsBr}$  and  $\text{PbBr}_2$  under the same ball-milling conditions.

### 4.2.2 Characterization

In this study, the obtained materials were characterized by high resolution X-ray diffraction, absorbance and photoluminescence spectroscopy.

#### X-ray diffraction

High resolution X-ray diffraction (XRD) enabled the identification of the different obtained phases formed. XRD was measured in the  $2\theta = 10^\circ - 50^\circ$  range, as described in Chapter 2.

#### Optical characterization

For the optical characterization of the samples, absorbance was measured with a High Power UV-Vis fiber light source, integrated sphere and Avantes Starline AVASpec-2048L spectrometer in reflection mode. Furthermore, a third harmonic (355 nm) of a Nd:YAG pulsed laser with 1.1 ns pulse duration, 1 kHz pulse repetition frequency and  $20 \mu\text{J}/\text{cm}^2$  excitation density was used as an excitation source for the photoluminescence measurements. To detect the time-resolved PL kinetics, an integrated PL signal was directed through a multimode optical fiber to a time correlated single photon counting electronic board. For the PL spectra measurements, the photoluminescence signal was directed through an optical fiber to an Ocean type spectrometer.

### 4.3 Results and discussion

The crystallinity, as well as the optical characteristics of the formed halide perovskites ( $\text{APbBr}_3$  with  $A = \text{Cs}$  or  $\text{K}_{0.2}\text{Cs}_{0.8}$ ) were analyzed (see Figure 4.1). The main diffraction peaks from the resulting powders are presented in Figure 4.1b, c and e (see Figure B.1 in Appendix B for the complete diffractograms and the reference patterns). These peaks correspond to the orthorhombic  $\text{APbBr}_3$  perovskite. Hence, XRD confirms the formation of the perovskite phase from dry ball-milling of the stoichiometric precursors. Furthermore, the high-resolution signals presented in Figures 4.1b, c and e reveal a shift towards higher angles (smaller interatomic distances) when  $\text{CsBr}$  is partly replaced by  $\text{KBr}$ . This result indicates that  $\text{K}^+$  – which has a smaller ionic radius than  $\text{Cs}^+$  (1.38 Å and 1.67 Å, resp.) – is effectively incorporated in the perovskite crystal structure, leading to the mixed-cation  $(\text{KCs})\text{PbBr}_3$  perovskite. Such a cation-replacement is not trivial, as potassium is thought to be too small to occupy the A-site in  $\text{APbBr}_3$  [98, 134, 232].

Indeed, concomitant to the shift of the main perovskite peaks, it should be noted that new peaks appear in the diffractogram (see Figure 4.1a, d and f and Figure B.1 in Appendix B). These peaks are consistent with the non-perovskite  $\text{APb}_2\text{Br}_5$  phase. For potassium-based lead halide compounds, this phase is the most commonly reported [237, 238]. Besides mixtures of the precursors  $\text{CsBr}$  and  $\text{KBr}$ , also pure  $\text{KBr}$  and  $\text{PbBr}_2$  mixtures (without  $\text{CsBr}$ ) were ball-milled in different ratios ((1:2) and (4:1)). It was found that  $\text{KPb}_2\text{Br}_5$  was the dominant phase (a lead-rich phase) – along with unreacted  $\text{KBr}$  – even in  $\text{KBr}$ -rich conditions (see Figure B.2 in Appendix B). Therefore, It can be concluded that the use of  $\text{KBr}$  as a source of  $\text{K}^+$  to replace  $\text{Cs}^+$  in inorganic perovskites is possible. However, this phenomenon is limited by the higher stability of  $\text{KPb}_2\text{Br}_5$  as compared to  $\text{KPbBr}_3$ . Furthermore, when the amount of  $\text{KBr}$  is reduced to 5 % ( $A = \text{K}_{0.05}\text{Cs}_{0.95}$ ), similar perovskite peak shifts are observed, along with the formation of  $\text{KPb}_2\text{Br}_5$ , although to a lesser extent (see Figure B.4 in Appendix B). This suggests that the amount of  $\text{Cs}^+$  that can be replaced by  $\text{K}^+$  in the perovskite structure (without leading to the formation of  $\text{KPb}_2\text{Br}_5$ ) is below 5 %. This value is lower than previously reported by others [233]. Other characterization methods such as high-resolution transmission electron microscopy and energy dispersive X-ray spectroscopy could possibly further elucidate the amount of potassium that is present under each form (included in the perovskite lattice or as a separated  $\text{KPb}_2\text{Br}_5$  compound).

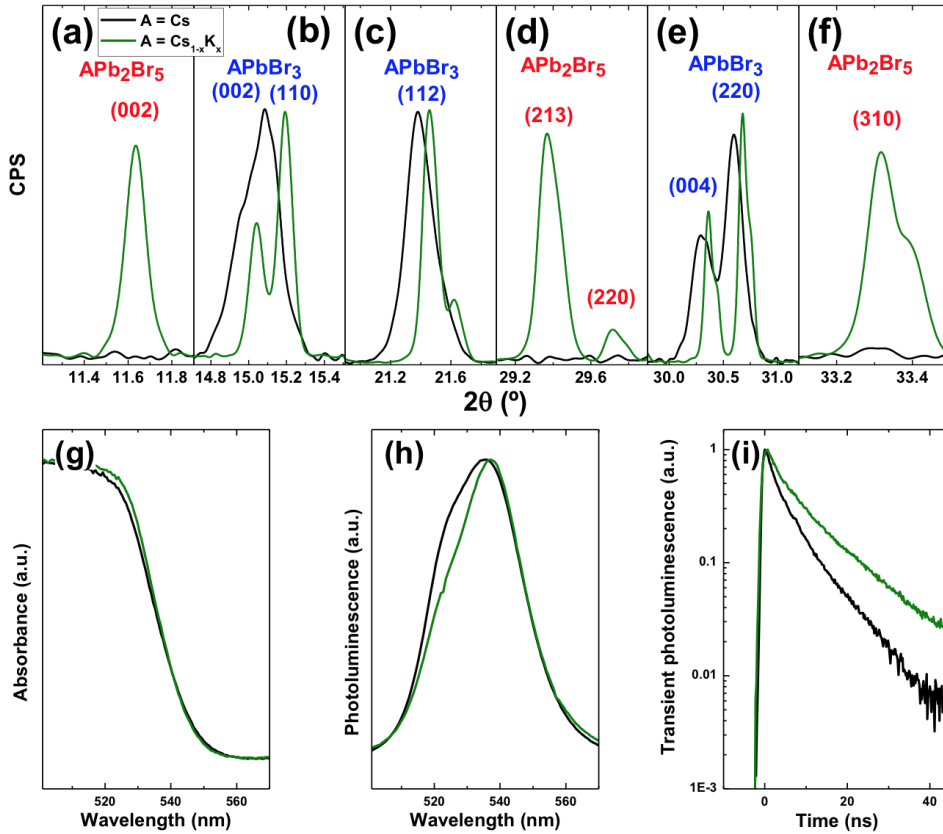


Figure 4.1: XRD (a–f) and optical (g–i) characterization of powders prepared from an equimolar CsBr:PbBr<sub>2</sub> mixture (Reference; black lines) or K<sub>0.2</sub>Cs<sub>0.8</sub>Br:PbBr<sub>2</sub> (green lines). XRD peaks corresponding to the APbBr<sub>3</sub> perovskite (b, c and e) present a shift upon addition of KBr. Panels (a, d and f) present a rise in intensity linked to the formation of the non-perovskite APb<sub>2</sub>Br<sub>5</sub> phase. Complete diffractograms are presented in Figure B.1 in Appendix B. Absorption (g) and photoluminescence (h) spectra remain mostly unchanged, while the photoluminescence lifetime (i) is increased upon the addition of KBr.

The optical characterization of the powders resulting from ball-milling equimolar ABr:PbBr<sub>2</sub> mixtures with A = K<sub>0.2</sub>Cs<sub>0.8</sub> is presented in Figure 4.1g–i. Absorption (Figure 4.1g) and photoluminescence (Figure 4.1h) spectra are mostly unchanged with respect to the reference sample (A = Cs). Photoluminescence spectra (Figure 4.1h) evidently consist of two sub-bands with maxima at approximately 522 nm and 540 nm. To clarify this, Figure B.5 in Appendix B shows the deconvolution of the PL spectra as a sum of two Gaussian contours. Due to the broad and asymmetric nature of the PL spectra, it is not possible to unambiguously evaluate the impact of potassium incorporation on the optical bandgap. Indeed, it could be expected that the observed shrinkage of the lattice would affect the optical bandgap of the material and result in a shift of the PL peak. However, the origin of the two bands observed in both photoluminescence spectra might be due to different reasons. As discussed in Chapter 3, a similar asymmetric spectrum was obtained for mechanochemically-synthesized CsPbBr<sub>3</sub> via ball-milling of equimolar mixtures of CsBr and PbBr<sub>2</sub>, where the two PL bands were attributed to the presence of bulk and nano-sized CsPbBr<sub>3</sub> [70, 129]. Another possible explanation is linked to the emission from free electrons in the conducting band and trap-localized carriers [239]. In this second hypothesis, it is possible that an exchange of a part of Cs-atoms by K-atoms decreases the relative contribution of the PL emission from free electrons at 522 nm and, respectively, increases the contribution of the emission from trap states at 540 nm. Following the delayed luminescence model [240], trap-assisted luminescence should be longer lived than the emission of free electrons from the conducting band, as is indeed observed in Figure 4.1i. However, other possible origins of this longer lifetime cannot be excluded. These might be trap passivation by molecular KBr which fills halide vacancies at the

surface [232] or by the other two mechanisms that the current data prove to happen concomitantly, which are: (i) the replacement of  $\text{Cs}^+$  by  $\text{K}^+$  as a monovalent cation in the perovskite structure and (ii) the formation of  $\text{KPb}_2\text{Br}_5$ , which might act as a passivating layer on top of  $\text{CsPbBr}_3$ . This passivation (independently on the exact mechanism from which it originates) should result in a higher photoluminescence quantum yield (PLQY). However, the absolute PLQY of these powder samples is too low to be able to conduct reliable measurements.

Besides the investigation of the incorporation of  $\text{KBr}$  in  $\text{CsPbBr}_3$ , also research was conducted on the incorporation of  $\text{KX}$  ( $\text{X} = \text{Cl}^-$  or  $\text{I}^-$ ), while keeping  $\text{CsBr}$  and  $\text{PbBr}_2$  as precursors in the mechanochemical synthesis. Figure 4.2 shows XRD and optical characterization of the resulting powders. Figure 4.2a–c demonstrate that the perovskite phase is formed in all cases and that the hetero-anion ( $\text{Cl}^-$  or  $\text{I}^-$ ) introduced via the potassium salt is replacing  $\text{Br}^-$  in the  $\text{APbX}_3$  structure (see Figure B.6 in Appendix B for the complete XRD patterns). Indeed, when  $\text{KI}$  is used, the main perovskite peaks shift towards lower diffraction angles, which is consistent with the introduction of the larger  $\text{I}^-$ -anion compared to  $\text{Br}^-$ . The opposite applies when  $\text{KCl}$  is used. As a result, as shown by absorption and photoluminescence data (Figure 4.2d, e), significant shifts in the bandgap of the perovskite are observed.

Hence, these results show that  $\text{KX}$  can also be used as a source of anions to tune the optical properties of the resulting inorganic perovskite. This means that the halide ( $\text{X}$ ) does not only remain tightly bound to  $\text{K}^+$  at the surface of the perovskite material – as such, affecting only surface-related effects (surface quenching traps) – but also enters the structure and thus affects bulk-related properties (bandgap).

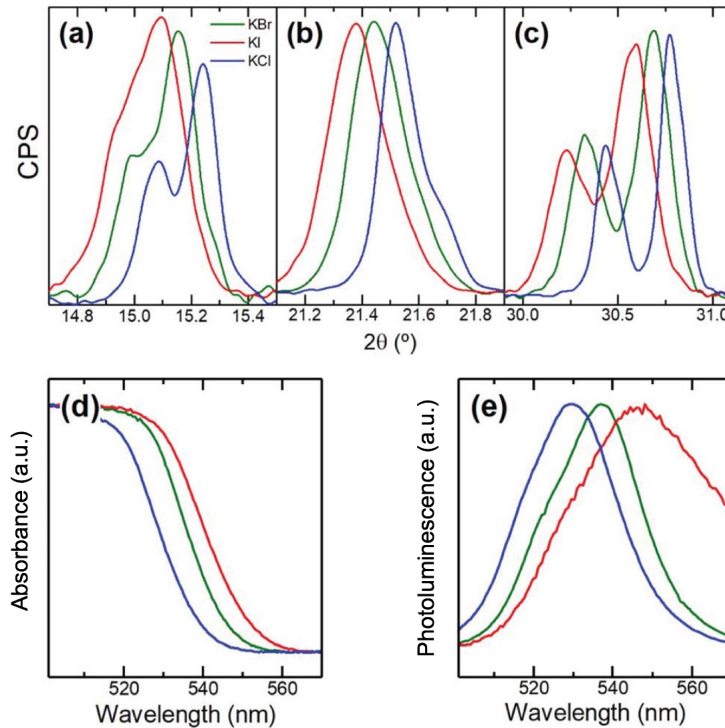


Figure 4.2: XRD (a–c) and optical (d and e) characterization of powders prepared by dry ball-milling of 20 %  $\text{KI}$  (red), 20 %  $\text{KBr}$  (green) and 20 %  $\text{KCl}$  (blue) with  $\text{CsBr}:\text{PbBr}_2$  (1:1) as the perovskite precursors. The XRD patterns present the  $\text{APbX}_3$  perovskite phase. The shifts in the diffractograms are consistent with the incorporation of the hetero-anion ( $\text{I}^-$  or  $\text{Cl}^-$ ) in the perovskite structure. This translates into a smaller ( $\text{KI}$ ) or larger ( $\text{KCl}$ ) bandgap as observed in absorption (d) and photoluminescence (e) spectra. Figure B.6 in Appendix B presents the complete XRD patterns.

## 4.4 Conclusions

In conclusion, it is shown that incorporating potassium halides in the mechanochemical synthesis of inorganic cesium lead halide perovskites leads to several chemical, structural and optical effects. First of all, potassium partly replaces cesium in the  $\text{APbBr}_3$  perovskite structure. Second, the potassium salt can also act as a source of hetero-anions to tune the bandgap of the resulting perovskite. Third, the  $\text{KPb}_2\text{X}_5$  phase forms concomitantly with the perovskite phase. This phase may act as a surface passivation layer as longer lifetimes are observed on samples with added  $\text{KBr}$  with respect to pure  $\text{CsPbBr}_3$ . These findings will aid to further optimize thin film perovskite-based devices such as LEDs and solar cells that recently have shown beneficial effects of incorporating potassium halides [234, 241–244].

## 4.5 Author contribution and acknowledgments

The content of this chapter was reproduced with permission from RSC Advances [95]. The complete journal article can be found in Appendix B.

The research leading to the results presented in this chapter has received funding from the European Union Program for Research and Innovation Horizon 2020 (2014-2020) under the Marie Skłodowska-Curie Grant Agreement PerovSAMs No. 747599. Also financial support from the Spanish Ministry of Economy and Competitiveness (MINECO) via the Unidad de Excelencia María de Maeztu MDM-2015-0538, MAT2017-88821-R and the Generalitat Valenciana (Prometeo/2016/135 and GRISOLIAP/2017/089) is acknowledged.

Y. El Ajjouri, V. S. Chirvony, M. Sessolo, F. Palazón and H. J. Bolink, Incorporation of potassium halides in the mechanochemical synthesis of inorganic perovskites: feasibility and limitations of ion-replacement and trap passivation. *RSC Adv.*, **2018**, 8, 41548-41551. [IF: 3.049 (2018), Q1]



## Chapter 5

# Mechanochemical Synthesis of Sn(II) and Sn(IV) Iodide Perovskites and Study of Their Structural, Chemical, Thermal, Optical and Electrical Properties

### 5.1 Introduction

Previous research conducted on lead iodide perovskites has shown these semiconductors to have excellent photovoltaic (PV), as well as electroluminescent properties [73, 74]. In part due to the toxicity of  $\text{Pb}^{2+}$  ions, other metal halide perovskites are being investigated. As a result, divalent tin is seen as the most straightforward alternative to lead, considering their similar electronic configuration (group 14 in the periodic table) and similar ionic radii [245–273]. Furthermore, mixed Sn-Pb iodide perovskites possess a lower bandgap than pure Pb and Sn ones, with applications in both single junction and tandem solar cells [274]. The latter consist of the combination of a top-cell using a high-bandgap absorber and a bottom-cell using a low-bandgap material. In tandem solar cells, different regions of the solar spectrum can be efficiently absorbed by the different sub-cells, minimizing thermalization losses. This improves the theoretical maximum power conversion efficiency (PCE) of the overall photovoltaic device. One problem that arises with the use of Sn(II) is that it may be easily oxidized to Sn(IV). Two workarounds exist to this problem: (1) limiting the oxidation by using additives, such as  $\text{SnF}_2$  [250, 254, 272, 275] or (2) exploring the properties of Sn(IV)-based materials [276–287]. Regarding the latter,  $\text{A}_2\text{B(IV)X}_6$  compounds – with  $A$  being the cation,  $B$  the metal and  $X$  the halide anion – can be seen as a similar structure to the  $\text{AB(II)X}_3$  perovskite, where every other  $\text{BX}_6$ -octahedra is removed and the metal  $B$  is in the +4 oxidation state to ensure charge neutrality (see Figure 5.1).

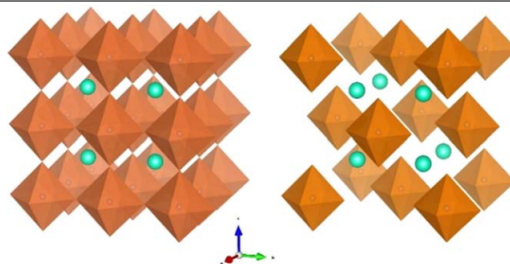


Figure 5.1: Crystal structures of  $\text{CsSnI}_3$  (left) and  $\text{Cs}_2\text{SnI}_6$  (right). The green balls represent  $\text{Cs}^+$  ions and the orange octahedra represent  $\text{SnI}_6$  units. The  $\text{Cs}_2\text{SnI}_6$  crystal structure can be viewed as a derivative from  $\text{CsSnI}_3$  where every other  $\text{SnI}_6$ -octahedra is removed. It needs to be noted that the oxidation state of Sn is consequently +2 in  $\text{CsSnI}_3$  and +4 in  $\text{Cs}_2\text{SnI}_6$ .

These compounds are sometimes referred to as vacancy-ordered double perovskites, where the B-“vacancies” are described as virtual cations (see Subsection 1.1.2).  $\text{Cs}_2\text{SnI}_6$  has been shown to be a degradation product of  $\text{CsSnI}_3$  upon air exposure [285]. Although this compound can be seen as a 0D structure due to the fact that adjacent  $\text{SnI}_6$ -octahedra do not share any corners, their vicinity and consequent orbital overlap result in interesting optoelectronic properties for PV [285].

Mechanochemical synthesis via ball-milling or other techniques (e.g. hand grinding with mortar and pestle) provides an ideal platform to form a wide variety of perovskites in stoichiometric and solvent-free conditions [15–17, 20, 21, 27, 47, 59, 94, 96, 98, 100, 107, 108, 115, 117, 129, 219, 288]. Additionally, these compounds may later be used for thin-film deposition by single-source thermal evaporation [107]. This technique will be discussed in Chapter 7.

Surprisingly, given the interest on tin perovskites, only two publications focusing on the mechanochemical synthesis of such compounds were found at the time of reporting this study. The first one is the seminal work of C. Stoumpos *et al.*, where mechanochemical synthesis – by hand grinding with mortar and pestle – was found to yield non-pure perovskites with considerable amounts of unreacted precursors [84]. The second reference is a work from M. Sasaki *et al.*, where several 3D pure-tin mixed iodide-bromide perovskites were synthesized [21]. At the time of publishing this study, no reports either on mixed Sn-Pb – which are especially relevant for low bandgap applications, as previously discussed – or on 0D iodide perovskites by mechanochemistry exist. Furthermore, at the time of writing, the only report of 3D iodide perovskites made by mechanochemical synthesis [21] does not provide thermal stability or electrical conductivity characterization. Hence, in this study, phase-pure Sn and mixed Sn-Pb iodide perovskites  $\text{CsSnI}_3$ ,  $\text{FASnI}_3$ ,  $\text{Cs}(\text{PbSn})\text{I}_3$  and  $\text{FA}(\text{PbSn})\text{I}_3$  were synthesized by solvent-free ball-milling of the stoichiometric precursors. Additionally, the Sn(IV)-based vacancy-ordered perovskites  $\text{Cs}_2\text{SnI}_6$  and  $\text{FA}_2\text{SnI}_6$  were also formed via mechanochemical synthesis. Furthermore, the influence of  $\text{SnF}_2$ , as an additive in the synthesis, was also investigated. The elemental, chemical and structural characteristics of the as-prepared compounds were investigated by X-ray diffraction and X-ray photoelectron spectroscopy (XPS). The thermal stability was studied by means of differential thermal analysis and thermogravimetry (DTA/TGA). In addition, the energy level diagram was estimated from optical characterization and ultraviolet photoelectron spectroscopy (UPS). Finally, the charge carrier mobility and lifetime of the 3D Sn(II)-based perovskite and the 0D Sn(IV)-based structure were investigated by pulse-radiolysis time-resolved microwave conductivity (PR-TRMC).

This work was published in Energy Technology [23]. The complete journal article can be found in Appendix C.

## 5.2 Experimental methods

### 5.2.1 Mechanochemical synthesis via ball-milling

In this investigation, AI:SnI<sub>2</sub> (1:1), AI:(Sn<sub>0.5</sub>Pb<sub>0.5</sub>)I<sub>2</sub> (1:1) and AI:SnI<sub>4</sub> (2:1) powders (A = Cs<sup>+</sup> or FA) were mixed inside a nitrogen-filled glovebox. Herewith, cesium iodide (CsI, >99 %), tin(II) iodide (SnI<sub>2</sub>, >97 %) and lead iodide (PbI<sub>2</sub>, 99.99 %) were purchased from TCI Chemicals. Tin fluoride (SnF<sub>2</sub>, 99 %) and tin(IV) iodide (SnI<sub>4</sub>, 99.999 %) were purchased from Sigma-Aldrich. Formamidinium iodide (FAI/CH<sub>5</sub>N<sub>2</sub>I) was purchased from GreatCell Solar. All chemicals were stored in a nitrogen-filled glovebox and used as received without further purification. The mechanochemical synthesis of the desired compounds was carried out by ball-milling of the perovskite precursors at a frequency of 30 Hz for 5 hours, as previously described in Chapter 2 (see Figure 2.1; Steps 1-9). Indeed, the ball-milling time applied in this study is higher compared to the study presented in Chapter 3. It needs to be noted that different perovskites were investigated in this study and thus other ball-milling requirements might be needed. Since in this study the main aim was the successful (phase-pure) synthesis of the compounds, a long ball-milling time was chosen. A time dependent study is suggested to be carried out to investigate whether the material can be formed at shorter ball-milling times and whether there are detrimental effects on prolonged milling. Finally, it must be noted that no solvents were used during the ball-milling procedure.

For the sake of simplicity, in the following (see Section 5.3), the mixed tin-lead compounds Cs(Sn<sub>0.5</sub>Pb<sub>0.5</sub>)I<sub>3</sub> and FA(Sn<sub>0.5</sub>Pb<sub>0.5</sub>)I<sub>3</sub> will be noted as Cs(SnPb)I<sub>3</sub> and FA(SnPb)I<sub>3</sub>.

### 5.2.2 Characterization

#### X-ray diffraction

The crystallographic properties of all formed compounds were investigated by X-ray diffraction in the  $2\theta = 10^\circ - 50^\circ$  range, as described in Chapter 2.

#### Optical characterization

Optical characterization was carried out by measuring the absorbance with a High Power UV-Vis fiber light source, integrated sphere and Avantes Starline AVASpec-2048L spectrometer in reflection mode. The photoluminescence was measured with a continuous wave 375 nm diode laser with a 400 nm filter and Hamamatsu PMA 11 spectrometer. For a typical spectrum 10 scans of 1 second were averaged.

#### Differential thermal analysis and thermogravimetric analysis

In order to investigate the thermal stability of the formed compounds, differential thermal analysis (DTA) and thermogravimetric analysis (TGA) were performed using a LabsysEvo 1600 DTA/TGA (Setaram). The samples (approximately 15 mg) were put in an alumina crucible and heated from 30 to 1000 °C at 45 °C/min under a helium-atmosphere (30 mL/min). The DTA and TGA curves were elaborated using the dedicated software Calisto (Setaram). It must be mentioned that prior to DTA/TGA characterization, the samples were shortly exposed to air.

#### X-ray and ultraviolet photoelectron spectroscopy

X-ray and ultraviolet photoelectron spectroscopic (XPS) measurements were carried out with a Kratos Axis UltraDL spectrometer. For this, high-resolution spectra were acquired at a pass energy of 10 eV using a monochromatic Al-K $\alpha$  source (15 kV, 20 mA). Ultraviolet photoelectron spectroscopic (UPS) measurements were performed using a He I (21.22 eV) discharge lamp, on an area of 55  $\mu\text{m}$  in diameter, at a pass energy of 5 eV and with a dwell time of 100 ms. The work function (the position of the Fermi level with respect to the vacuum level) was measured from the threshold energy for the emission of secondary electrons during He I excitation. A - 9.0 V bias was applied to the sample to precisely determine the low-kinetic-energy cutoff. Then, the position

of the valence band maximum (VBM) versus the vacuum level was estimated by measuring its distance from the Fermi level.

### Pulse-radiolysis time-resolved microwave conductivity

Pulse-radiolysis time-resolved microwave conductivity (PR-TRMC) measurements, as described in Chapter 2. The irradiation intensity of the electron pulse was varied between pulse lengths of 0.2 ns to 10 ns (charge carrier concentrations of approximately  $1 \times 10^{15} \text{ cm}^{-3}$  to  $8 \times 10^{16} \text{ cm}^{-3}$ ). The frequency scan (28-38 GHz) fits were measured at a pulse length of 0.5 ns (approximately  $5.8 \times 10^{15} \text{ cm}^{-3}$ ).

## 5.3 Results and discussion

As mentioned in Section 5.2.1, Sn(II)- and Sn(IV)-based compounds were synthesized by dry ball-milling of stoichiometric mixtures of different precursors. Figure 5.2 shows the XRD characterization of all metal iodide perovskites. The X-ray diffractograms of  $\text{CsSnI}_3$ ,  $\text{FASnI}_3$ ,  $\text{Cs}_2\text{SnI}_6$  and  $\text{FA}_2\text{SnI}_6$  match very well with the corresponding reference bulk patterns. No reference pattern is available for mixed tin-lead perovskites  $\text{Cs}(\text{SnPb})\text{I}_3$  and  $\text{FA}(\text{SnPb})\text{I}_3$ . However, these compounds have XRD signals comparable with the pure tin analogues ( $\text{CsSnI}_3$  and  $\text{FASnI}_3$ , respectively) albeit slightly shifted to lower angles; as expected from a partial replacement of tin with a larger cation such as lead. Accordingly, also a shift to lower diffraction angles in FA-based compounds compared to Cs-based ones is observed (Figure 5.2). These differences are more clearly observed in Figure C.1 in Appendix C, which shows the three more relevant regions of each diffractogram. The high phase-purity and match with reference XRD patterns highlight the potential of mechanochemical synthesis to obtain high-quality materials.

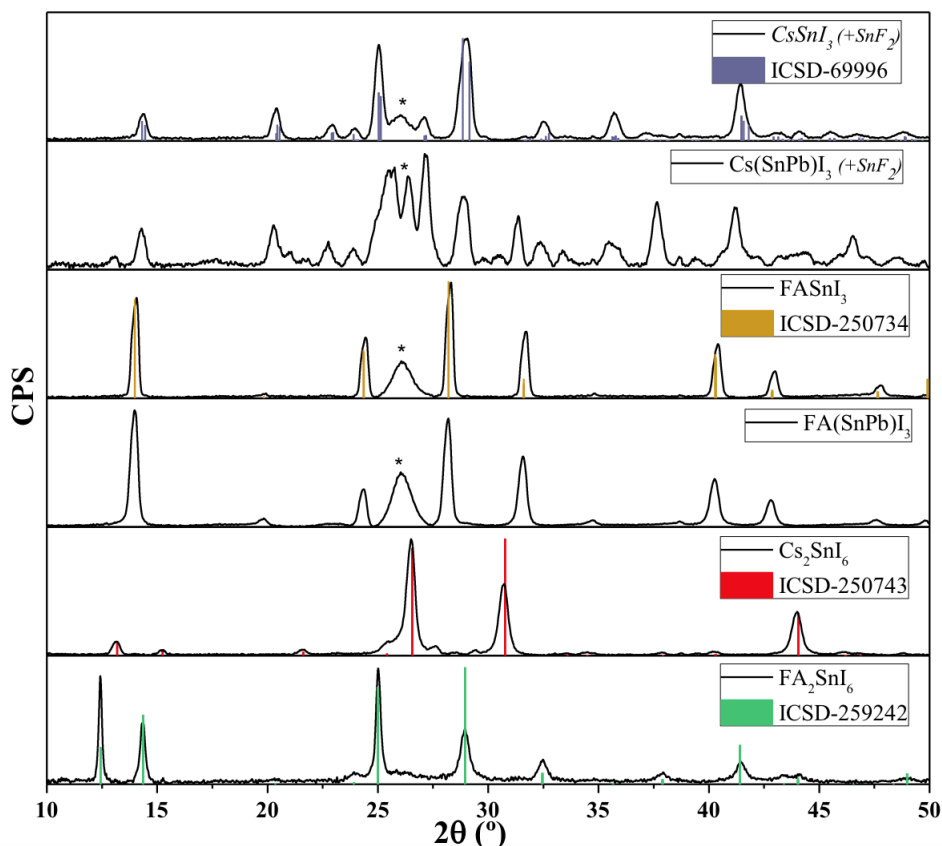


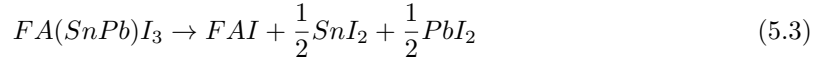
Figure 5.2: X-ray diffractograms of mechanochemically-synthesized tin perovskites (black lines), along with the reference bulk patterns retrieved from the Inorganic Crystal Structure Database (ICSD; colored columns). A broad peak around  $2\theta = 26^\circ$  and marked with an asterisk (\*) is visible in most diffractograms due to parasitic diffraction from the adhesive tape used to fix the powder samples on glass substrates (see Figure B.3 in Appendix B). No reference pattern is available for mixed tin-lead perovskites. However, the main peaks' positions match the reference pure-tin counterpart with a slight shift to lower angles due to the incorporation of the larger lead cation (see Figure C.1 in Appendix C).

As noted in the legend of Figure 5.2,  $\text{CsSnI}_3$  and  $\text{Cs}(\text{SnPb})\text{I}_3$  were formed in the presence of  $\text{SnF}_2$ . This additive was found to be crucial in the synthesis of  $\text{CsSnI}_3$  (but not in the synthesis of  $\text{FASnI}_3$ ) to avoid the formation of  $\text{SnI}_4$ , as revealed by thermal DTA analyses (see Figure 5.3 and Figures C.2-C.4 in Appendix C). In particular, when comparing the DTA signal of  $\text{CsSnI}_3$  synthesized in the presence and absence of  $\text{SnF}_2$  (Figure C.2 in Appendix C), an endothermic peak at approximately  $160^\circ\text{C}$  – ascribed to the melting of  $\text{SnI}_4$  – is visible only in the case where no  $\text{SnF}_2$  is added. This peak is also absent in the case of  $\text{FASnI}_3$  even without the presence of the additive (Figure 5.3). In addition to the effect of  $\text{SnF}_2$ , all the samples were analyzed through DTA/TGA to investigate their thermal stability (Figure 5.3).  $\text{CsSnI}_3$  in the presence of  $\text{SnF}_2$  is stable up to  $450^\circ\text{C}$ , the temperature at which it melts with the subsequent vaporization of  $\text{SnI}_2$  and  $\text{CsI}$  [256]. A very similar behavior was recorded for  $\text{Cs}(\text{SnPb})\text{I}_3$  (Figure C.3 in Appendix C).  $\text{Cs}_2\text{SnI}_6$  seems less stable, since it decomposes at approximately  $320^\circ\text{C}$  due to  $\text{SnI}_4$  (b.p.  $\approx 350^\circ\text{C}$ ), which is more volatile than  $\text{SnI}_2$  (b.p.  $\approx 700^\circ\text{C}$ ). Indeed the TGA variations – equal to 53.6 % and 47.0 % in the first and second step, respectively – are consistent with the loss of  $\text{SnI}_4$  and  $\text{CsI}$  (whose melting point is reported in the DTA curve at  $627^\circ\text{C}$ ).  $\text{FASnI}_3$  and  $\text{FA}(\text{SnPb})\text{I}_3$  have considerable lower stability with respect to the Cs-based counterparts because of the organic cation, which mainly drives the decomposition mechanism [289]. Interestingly,  $\text{FA}_2\text{SnI}_6$  is slightly more stable with respect to  $\text{FASnI}_3$  and  $\text{FA}(\text{SnPb})\text{I}_3$ , with the initial weight loss starting around  $250^\circ\text{C}$  instead of  $200^\circ\text{C}$ . This might be due to a stronger interaction between FA molecules in  $\text{FA}_2\text{SnI}_6$ . However, the weight loss is much faster in this Sn(IV) compound, being completely vaporized at  $400^\circ\text{C}$ ,

which is consistent with reaction 5.1.



Similarly, the decomposition mechanism for  $FASnI_3$  and  $FA(SnPb)I_3$  could be summarized, respectively, following reactions 5.2 and 5.3 [290].



However, their TGA and DTA curves evidence a more complex mechanism involving the formation of several intermediates. The last weight losses in the TGA curves of  $FASnI_3$  and  $FA(SnPb)I_3$  start at approximately 500 °C – the temperature at which  $SnI_2$  is released – as also observed in the inorganic Cs-based counterparts (Figure C.3 in Appendix C). This confirms that Sn remains in the +2 oxidation state in these hybrid perovskites without the addition of  $SnF_2$ .

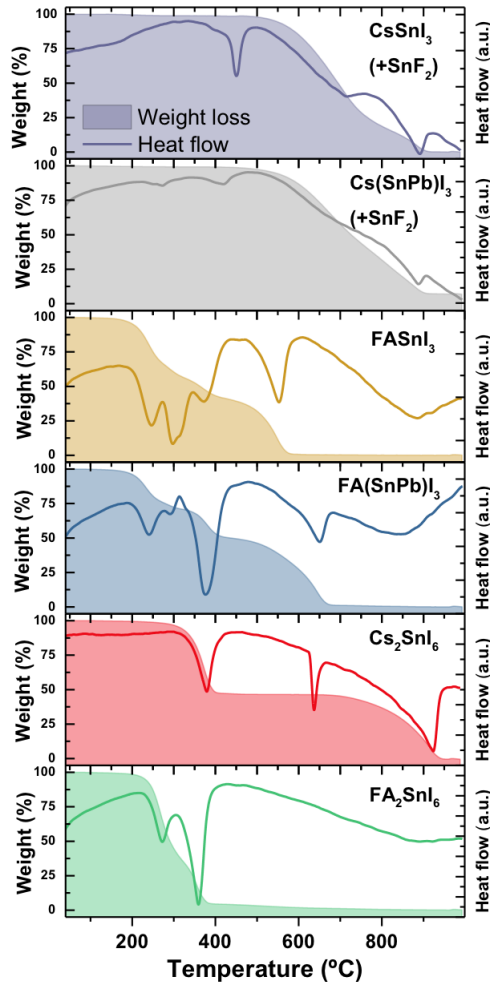


Figure 5.3: Thermogravimetric (TGA, filled area) and differential thermal (DTA, simple line) curves of all Sn(II) and Sn(IV) compounds ( $CsSnI_3$  (+  $SnF_2$ ),  $Cs(SnPb)I_3$  (+  $SnF_2$ ),  $FASnI_3$ ,  $FA(SnPb)I_3$ ,  $Cs_2SnI_6$  and  $FA_2SnI_6$ ) in the 40–1000 °C range.

Besides DTA/TGA measurements, all Sn(II) and Sn(IV) perovskites were also analyzed by high-resolution X-ray photoelectron spectroscopy to gather quantitative information on their chemical composition. Figure 5.4 shows the XPS spectra of all compounds. The atomic percentages of relevant elements are presented in Table 5.1.

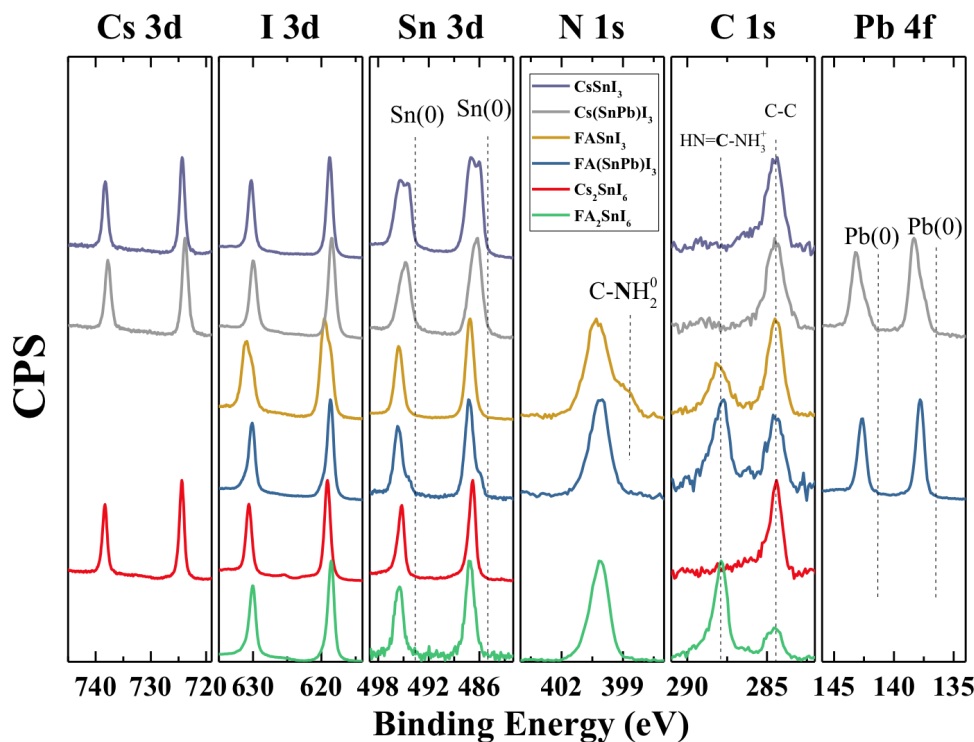


Figure 5.4: High-resolution XPS spectra of all main elements from the different compounds: Cs 3d, I 3d, Sn 3d, N 1s, C 1s and Pb 4f regions. Additional F 1s and O 1s spectra are presented in Figure C.5 and Figure C.6 in Appendix C.

Carbon C 1s spectra of all samples show a peak at low binding energy (BE), which is ascribed to C-C bonds of adventitious carbon originating from exposure to organic volatile compounds in air. The peak is fixed to be BE = 284.5 eV for energy calibration as standard practice. In this region, the FA-based samples show a second peak at BE =  $287.9 \pm 0.2$  eV, which is assigned to the carbon atom in formamidinium cations ( $\text{HC}(\text{NH}_2)_2^+$ ). Although not shown in Figure 5.4, the  $\text{CsSnI}_3$  and  $\text{Cs}(\text{SnPb})\text{I}_3$  samples exhibit an additional peak at BE = 684.0 eV, corresponding to the F 1s orbital from  $\text{SnF}_2$  (see Figure C.5 in Appendix C). Quantitative elemental analysis can be derived from these high-resolution spectra, after correcting for  $\text{SnF}_2$  contribution and considering only the highest energy component of C 1s. The atomic percentages of all relevant elements are given in Table 5.1.

Table 5.1: Atomic percentages of relevant elements based on high-resolution XPS spectra.  $\text{CsSnI}_3$  and  $\text{Cs}(\text{SnPb})\text{I}_3$  were synthesized in the presence of  $\text{SnF}_2$ .

	Cs (at%)	I (at%)	Sn (at%)	N (at%)	C (at%)	Pb (at%)
$\text{CsSnI}_3$	23.8	50.6	25.5	-	-	-
$\text{Cs}(\text{SnPb})\text{I}_3$	26.4	50.7	11.5	-	-	11.4
$\text{FASnI}_3$	-	25.9	21.2	34.6	17.7	-
$\text{FA}(\text{SnPb})\text{I}_3$	-	34.5	9.3	31.0	17.0	8.2
$\text{Cs}_2\text{SnI}_6$	28.0	57.3	14.7	-	-	-
$\text{FA}_2\text{SnI}_6$	-	26.8	1.2	47.4	24.6	-

Several observations can be made from Table 5.1. First of all,  $\text{FA}_2\text{SnI}_6$  seems highly degraded as only a very low amount of tin is detected. This suggests that the compound is severely affected by X-ray radiation and ultrahigh vacuum, leading most likely to the formation and subsequent loss of  $\text{SnI}_4$ . For all the other compounds, the A:B ratios (where A is either Cs or FA and B is either Sn or SnPb) are very close to the expected 1:1 and 2:1 ratios. This further confirms the material purity, which was observed by XRD (Figure 5.2). The same is true for the Sn:Pb ratios,

which are close to 1:1 in both mixed tin-lead perovskites ( $\text{Cs}(\text{SnPb})\text{I}_3$  and  $\text{FA}(\text{SnPb})\text{I}_3$ ). The C:N ratios in FA-based samples are close to the expected 1:2 ratio for formamidinium cations, confirming the assignment of the high-BE component of C 1s spectra to FA. More importantly, it suggests that FA is not degraded during the mechanochemical synthesis. This is not obvious *a priori*, as FAI is known to give different degradation byproducts, such as hydrogen cyanide (HCN) or others, which could be volatile too and hence alter the C:N ratio in the sample [291]. Nonetheless, it has to be noted that in all samples, the measured iodine concentration is lower than expected. In regards to this, it should be noted that also oxygen is observed (see Figure C.6 in Appendix C), which is likely due to oxidation upon air exposure prior to analysis. Indeed, although the synthesis of the compounds was carried out under helium atmosphere (see Subsection 5.2.1), the samples were exposed to air for a short amount of time before characterization. As photoelectron spectroscopies are surface-sensitive characterization techniques – where the depth of analysis is typically a few nanometers – even a small superficial oxidation will have a high impact on the XPS results. In other words, it is unlikely that a significant formation of  $\text{SnO}_x$  affects the bulk of the perovskite in the current case, as these species do not appear in the XRD signal (Figure 5.2). Furthermore, based on the literature, the formation of  $\text{SnO}_x$  in the bulk of the compounds from air exposure is a process that typically takes several days or weeks [285].

A closer look at the XPS spectra (Figure 5.4) allows to further discuss the oxidation states and chemical environments of the different elements in all samples. In the case of the Cs-based samples, the Cs 3d spectra show a doublet with a Cs  $3d_{5/2}$  peak located at  $\text{BE} = 724.0 \pm 0.3$  eV, as well as I 3d spectra with a I  $3d_{5/2}$  peak at  $\text{BE} = 618.7 \pm 0.2$  eV. These values are consistent with the Cs(+1) and I(-1) oxidation states, expected for inorganic iodide perovskites [292]. The Sn 3d spectra of  $\text{CsSnI}_3$  and  $\text{Cs}(\text{SnPb})\text{I}_3$  show two clear components (two doublets) ascribed to the addition of  $\text{SnF}_2$  in these samples, whereas  $\text{Cs}_2\text{SnI}_6$  shows only one component, as expected. Comparing the binding energy values of Sn(II) and Sn(IV) reported in literature, it seems unlikely to easily distinguish them, as these values largely overlap [293]. In the case of  $\text{Cs}(\text{SnPb})\text{I}_3$ , it is noted that the Pb 4f spectra are asymmetric with a low BE component whose origin could not be clearly elucidated. Importantly, no metallic lead ( $\text{Pb}^0$ ) or tin ( $\text{Sn}^0$ ) was observed in any of the samples. In Figure 5.4, the Pb 4f and Sn 3d peak positions for these metallic elements ( $\text{Pb}^0$  and  $\text{Sn}^0$ ) are indicated by dashed lines. The presence of metallic lead or tin could have a detrimental effect on the perovskite optoelectronic properties [294–296].

In the case of FA-based samples, the peak at  $\text{BE} = 287.9 \pm 0.2$  eV is assigned to the carbon atom of the formamidinium cations, as presented by the dashed line ( $\text{HN-C-NH}_2^+$ ) in the C 1s column in Figure 5.4. Accordingly, the N 1s peak is at  $\text{BE} = 400.2 \pm 0.1$  eV, corresponding to the nitrogen atoms of FA. Interestingly, the  $\text{FASnI}_3$  sample shows a second peak at lower BE, which may be ascribed to deprotonated amines in FA. In the graph (Figure 5.4), this is noted as  $\text{C-NH}_2^0$  [297, 298]. Here, the deprotonation of FA is concomitant to the formation of different iodine species, as evidenced by the I 3d spectra, which only in the case of  $\text{FASnI}_3$  shows two different components. It is possible that a partial proton transfer from  $\text{FA}^+$  to  $\text{I}^-$  occurs. Nonetheless, the complexity of iodine chemistry in hybrid perovskites complicates the identification of the exact species formed here [299]. Sn 3d spectra of the three FA-based compounds ( $\text{FASnI}_3$ ,  $\text{FA}(\text{SnPb})\text{I}_3$  and  $\text{FA}_2\text{SnI}_6$ ) show a main Sn  $3d_{5/2}$  peak centered at  $\text{BE} = 487.1 \pm 0.1$  eV, consistent both with Sn(II) and Sn(IV) iodide perovskites [269]. A small component at lower BE appears in the Sn 3d spectrum in the case of  $\text{FA}(\text{SnPb})\text{I}_3$ . This low BE component might be due to oxidation, as previously discussed.

In summary, aside from  $\text{FA}_2\text{SnI}_6$  – which is degraded under characterization – the XPS spectra overall confirm the formation of the entire series of compounds, with signals that match the expected spectra of the different perovskites (and the corresponding signal for  $\text{SnF}_2$  in the  $\text{CsSnI}_3$  and  $\text{Cs}(\text{SnPb})\text{I}_3$  samples).

Additional optical characterization – by diffuse reflectance and photoluminescence spectroscopy – as well as UPS was performed to estimate the energetic positions of the valence band, Fermi level and conduction band of these materials (see Figure 5.5).



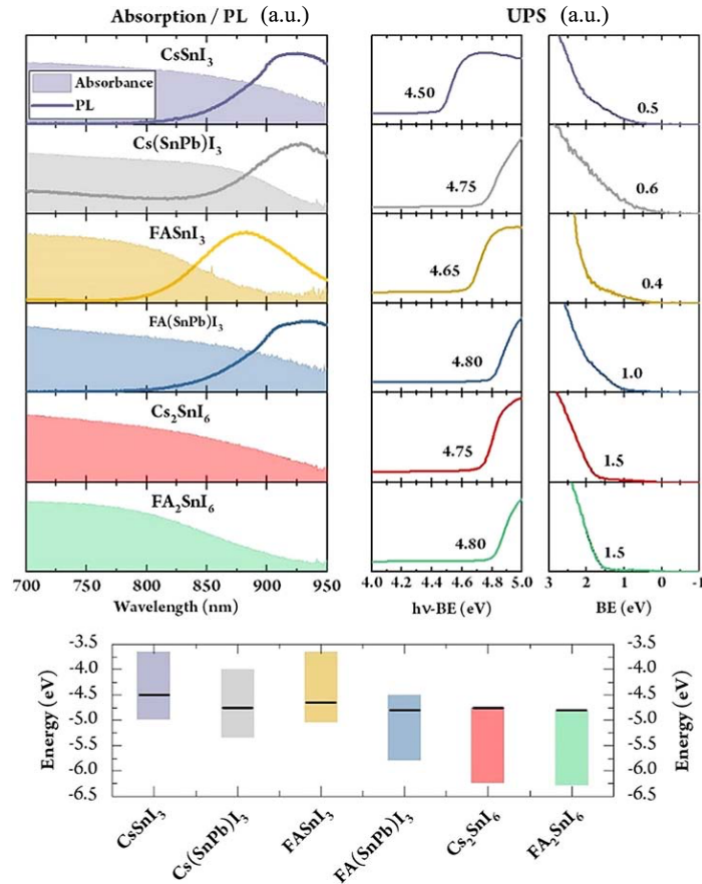


Figure 5.5: Optical characterization (absorbance – presented by the filled areas – and photoluminescence – presented by the simple lines – in the left column), UPS and derived energy diagrams of all Sn(II) and Sn(IV) compounds:  $\text{CsSnI}_3$  (+  $\text{SnF}_2$ ),  $\text{Cs}(\text{SnPb})\text{I}_3$  (+  $\text{SnF}_2$ ),  $\text{FASnI}_3$ ,  $\text{FA}(\text{SnPb})\text{I}_3$ ,  $\text{Cs}_2\text{SnI}_6$  and  $\text{FA}_2\text{SnI}_6$ .

As presented in Figure 5.5, all compounds have an absorption onset (filled areas) in the near-infrared region, suited for single-junction solar cells, as well as rear absorber materials in perovskite-perovskite tandem devices. All Sn(II)-based compounds have a clear Stokes-shifted photoluminescence signal at room temperature (Figure 5.5, left column). This characteristic makes them potentially interesting for also NIR light-emitting diodes.

The UPS secondary electron cutoff (Figure 5.5, middle column) and onset (right column) allow the determination of the work function and the energy difference between the Fermi level and the top of the valence band, respectively. The work function is the energy required to completely withdraw an electron from a solid surface to just outside its surface. Combining the information withdrawn from the middle and right column of Figure 5.5 enables to estimate the characteristic energy levels, as presented at the bottom of Figure 5.5. It is noted that the addition of lead to Sn(II)-based perovskites results in deeper energy levels, as compared with the pure-tin counterparts. This observation is consistent with the literature [300]. Furthermore, a red-shift in PL is clearly observed from pure-tin  $\text{FASnI}_3$  to mixed tin-lead  $\text{FA}(\text{SnPb})\text{I}_3$ . Such behavior has previously been noted by Z. Zhao *et al.*, where mixed tin-lead iodide perovskites were found to have a lower bandgap than both the pure-tin and pure-lead compositions [301]. Interestingly, this phenomenon is not observed in the inorganic Cs-based perovskites ( $\text{CsSnI}_3$  and  $\text{Cs}(\text{SnPb})\text{I}_3$ ). The apparent p-type doping in  $\text{FASnI}_3$  may be ascribed to a partial oxidation of Sn(II) to Sn(IV) [302]. In contrast, mixed tin-lead  $\text{FA}(\text{SnPb})\text{I}_3$  seems to be rather n-type. The origin of this effect is not fully elucidated. However, as noted in the discussion of the XPS data (Figure 5.4, blue spectrum), tin appears to be slightly reduced, which might explain the n-type character observed

here. Again, these effects do not seem to be significant for the inorganic Cs-based compounds ( $\text{CsSnI}_3$  and  $\text{Cs}(\text{SnPb})\text{I}_3$ ), as both appear rather intrinsic semiconductors. However, it must be noted that the latter perovskites were formed with the addition of  $\text{SnF}_2$ . Therefore, it is inferred that  $\text{SnF}_2$  helps maintaining the intrinsic nature of the semiconductor by preventing oxidation of tin.

For the Sn(IV) compounds, a clear difference from the valence band maximum to the Fermi level (Figure 5.5, right column) of 1.5 eV (close to the reported bandgap for the same material) is observed. This value is close to the reported bandgap for the same material [303]. Unfortunately, the optical bandgap cannot be determined, due to the smooth absorption onset and the lack of photoluminescence (Figure 5.5, left column). As it cannot be lower than 1.5 eV, the bandgap is estimated to be 1.5 eV. This seems a reasonable assumption, considering that the sample is clearly black (see Figure C.7 in Appendix C). These observations indicate that the Sn(IV)-based compounds are heavily n-doped. Again, this conclusion is in agreement with literature, where  $\text{Cs}_2\text{SnI}_6$  has been reported by several research groups to be intrinsically n-type [284].

Eventually, the mobility and lifetime of charge carriers were studied by pulse-radiolysis time-resolved microwave conductivity (PR-TRMC). As described in Subsection 5.2.2, in this technique, materials are ionized with a high-energy electron pulse, where the change in conductivity was probed subsequently with GHz microwaves. If radiation leads to mobile charge carriers, these carriers will absorb part of the microwave power, decreasing the microwave power reflected by the cell. This decrease in microwave power is directly related to the change in conductivity and ultimately to the mobility of charge carriers [304]. For most samples, PR-TRMC measurements were not possible due to high or even complete absorption of the microwaves without irradiation. This is indicative of a considerable dark conductivity that hinders the detection of changes in conductivity upon irradiation. This behavior matches with the UPS measurements (Figure 5.5), where it was observed that most samples were doped either with a p-type character – most likely caused by oxidation of  $\text{Sn}^{2+}$  to  $\text{Sn}^{4+}$  – or an n-type character. In the literature, it has been shown that the presence of low concentrations of dark charge carriers has a strong detrimental effect on the electron properties [250, 254, 260, 272, 275]. In fact, a non-quantifiable, short-lived ( $< 5$  ns) change in reflection is observed. This indicates that the generated charge carriers recombine or are trapped within the time resolution of the PR-TRMC experiment (see Figure C.8 in Appendix C). Nevertheless, meaningful results are able to be subtracted from two compounds: the 3D Sn(II)-based compound  $\text{Cs}(\text{SnPb})\text{I}_3$  and the 0D Sn(IV)-based compound  $\text{FA}_2\text{SnI}_6$ . Hereafter, for the sake of simplicity, these materials are referred to as 3D and 0D samples (Figure 5.6a). The fact that these samples can be measured by PR-TRMC matches with the UPS measurements (Figure 5.5), where it was observed that  $\text{Cs}(\text{SnPb})\text{I}_3$  seems to be an intrinsic semiconductor. This intrinsic character is most likely achieved during synthesis. However, decreasing tin-content with lead, along with the addition of  $\text{SnF}_2$  suppress  $\text{Sn}^{2+}$  oxidation to  $\text{Sn}^{4+}$  and as a result decrease the concentration of dark charge carriers. This is also in line with previously reported improved stabilities of tin-based perovskites when lead cations are present [305].

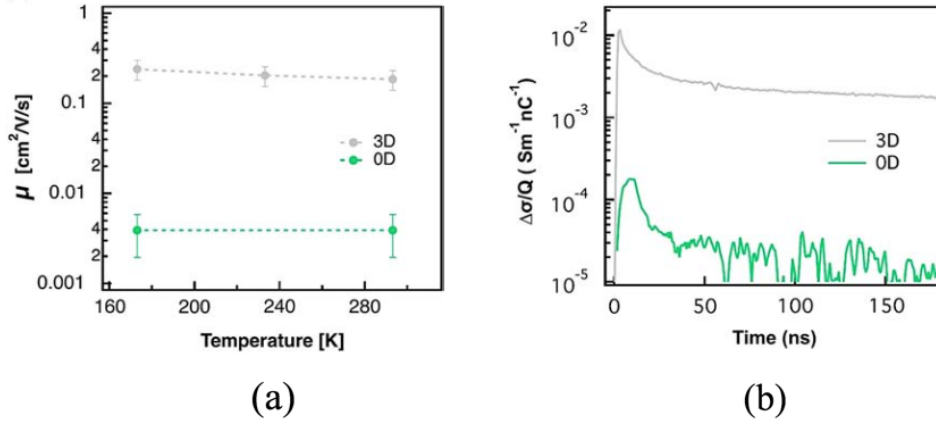


Figure 5.6: (a) Mobility of charge carriers ( $\mu$ ) as a function of temperature and (b) change of conductivity ( $\Delta\sigma/Q$ ) as a function of time of a Sn(II) 3D perovskite (grey) and a Sn(IV) 0D vacancy-ordered perovskite (green). The 3D and 0D samples stand for  $\text{Cs}(\text{SnPb})\text{I}_3$  and  $\text{FA}_2\text{SnI}_6$ , respectively.

As presented in Figure 5.6a, the 3D sample has a charge carrier mobility that is two orders of magnitude higher compared with the 0D sample ( $0.2 \text{ cm}^2 \text{ V}^{-1}$  and  $0.004 \text{ cm}^2 \text{ V}^{-1}$ , respectively). This observation is not surprisingly, considering that the higher dimensionality of the 3D sample leads to a higher overlap of molecular orbitals. In both cases, the mobility was not found to change significantly when cooling from room temperature to 173 K. This indicates that the charge carrier mobility is not dominated by lattice scattering, but rather may be controlled by defects. The mobility of the 3D sample is of the same order of magnitude as for 3D lead-based perovskite samples prepared without the use of solvents [306], where it is one to two orders of magnitude lower than 3D lead-based perovskites prepared by precipitation or single crystals, respectively [306, 307]. This points out that dry mechanochemical synthesis – as performed in this study – might lead to a higher density of defects as opposed to solution-processing. This observation was previously made in the study of the mechanochemical synthesis of  $\text{CsPbBr}_3$  (see Chapter 3) [129]. Nonetheless, the synthesis may be optimized by, for example, reducing the grinding time, which in the current case was 5 hours (see Subsection 5.2.1). As could be concluded from the  $\text{CsPbBr}_3$  study (Chapter 3), such a long ball-milling time is probably unnecessary to yield phase-pure perovskites [129]. Reducing this time will likely limit detrimental effects of prolonged grinding (i.e. tin oxidation).

Figure 5.6b presents the change in time-resolved conductivity as a function of time for the 3D and 0D samples. The 3D sample ( $\text{Cs}(\text{SnPb})\text{I}_3$ ) shows a fast-initial decay in time-resolved conductivity, followed by a long-tail that does not decay to zero, even at very long times. Also, the maximum change in conductivity increases with the initial concentration of charge carriers (increase pulse length; see Figure C.9a in Appendix C). This behavior is similar to that of 3D  $\text{MAPbX}_3$  samples and is attributed to second-order recombination with a limited concentration of trap states [308]. The fast initial decay is caused by trapping of one of the charges, whereas the long tail signal originates from the remaining free charges [307, 308]. Regarding the mobility, the carrier lifetime seems almost unaffected by temperature (see Figure C.9b in Appendix C), indicating that the decay is still dominated by the recombination with a similar concentration of the trap states as at room temperature. In the case of the 0D sample ( $\text{FA}_2\text{SnI}_6$ ), the conductivity signal is very low compared with the 3D sample and decays in less than 50 ns (Figure 5.6b). However, a slight increase in conductivity is observed at low temperatures, which may be related to less thermal vibration of the lattice (see Figure C.10 in Appendix C).

## 5.4 Conclusions

In conclusion, hybrid and inorganic pure-tin and mixed tin-lead iodide perovskites, as well as vacancy-ordered perovskites were successfully synthesized with excellent phase-purity, as revealed by XRD. Detailed thermal stability studies were carried out revealing that all compounds are stable up to 200 °C, which is compatible with common operational conditions in optoelectronic devices. Sn(II)-based inorganic perovskites were found to be stable beyond 400 °C, making them suitable candidates for single-source thermal deposition into thin films. Indeed these compounds show a narrow bandgap suited for photovoltaic devices and NIR light-emitting diodes. The charge carrier mobility was found to be rather low, which could be due to oxidation during the long ball-milling mechanochemical synthesis. However, it was demonstrated that the dark carrier conductivity in organic 3D Sn(II)-based compounds can be improved by the addition of Pb(II) and/or SnF<sub>2</sub> during synthesis. An outlook of this study might be the optimization of the preparation conditions, especially reducing the grinding time to an ideal duration that will ensure a complete synthesis, while avoiding possible detrimental effects.

## 5.5 Author contribution and acknowledgments

The content of this chapter was reproduced with permission from Energy Technology [23]. The complete journal article can be found in Appendix C.

The research discussed in this chapter was carried out in collaboration with Dr. F. Locardi under supervision of Prof. Dr. M. Ferretti from Dipartimento di Chimica e Chimica Industriale at Università degli Studi di Genova in Genova, Italy, who conducted the thermal analyses. Dr. M. Prato from Materials Characterization Facility at Istituto Italiano di Tecnologia in Genova, Italy carried out the XPS and UPS measurements. C. Gélvez-Rueda under supervision from Dr. C. Grozema from the Optoelectronic Materials Section of the Department of Chemical Engineering at Delft University of Technology, The Netherlands carried out the PR-TRMC measurements.

The research leading to the results discussed in this chapter has received funding from the European Union Program for Research and Innovation Horizon 2020 (2014-2020) under the Marie Skłodowska-Curie Grant Agreement PerovSAMs No. 747599 and project INFORM (grant 675867), the Spanish Ministry of Economy and Competitiveness (MINECO) via the Unidad de Excelencia Mariía de Maeztu MDM-2015-0538, MAT2017-88821-R and PCIN-2015-255 and the Generalitat Valenciana (Prometeo/2016/135 and GRISOLIAP/2017/089).

Y. El Ajjouri, F. Locardi, M. C. Gélvez-Rueda, M. Prato, M. Sessolo, M. Ferretti, F. C. Grozema, F. Palazón and H. J. Bolink, Mechanochemical Synthesis of Sn(II) and Sn(IV) Iodide Perovskites and Study of Their Structural, Chemical, Thermal, Optical, and Electrical Properties. *Energy Technol.*, **2019**, 1900788. [IF: 3.020 (2019), Q1]

## Chapter 6

# Low-Dimensional Non-Toxic $A_3Bi_2X_9$ Compounds Synthesized by a Dry Mechanochemical Route with Tunable Visible Photoluminescence at Room Temperature

### 6.1 Introduction

The excellent optoelectronic properties of lead-halide perovskites (LHPs) are a feature of interest in the investigation of these materials. Among others, these characteristics are the result of the intrinsic point defect tolerance of LHPs, which has been suggested to be crucial in achieving long charge carrier diffusion lengths, enabling high efficiencies in perovskite devices [309]. However, the future commercialization of state-of-the-art perovskite optoelectronic devices is hampered by the use of toxic lead and the unclear environmental stability of LHPs. Therefore, lead-free perovskite alternatives are being sought. The defect-tolerant character of LHPs has been linked to the presence of the  $ns^2$  electron lone pair in  $Pb^{2+}$ . This characteristic is shared with  $Bi^{3+}$ , which has a  $6s^2$  electron configuration [310–315]. Hence Bi(III)-halide compounds are envisioned as interesting alternatives with potentially the same defect tolerance as LHPs. Moreover, bismuth is an abundant element on Earth, as well as non-toxic and stable in ambient conditions [311]. It needs to be noted that the replacement of  $Pb^{2+}$  with  $Bi^{3+}$  affects the stoichiometry of the ternary metal halides. As discussed in Chapter 1, the general formula for lead-halide perovskites can be written as  $APbX_3$ , where  $A$  stands for the monovalent cation and  $X$  the monovalent halide anion. However, the bismuth-counterparts have a “3-2-9” stoichiometry corresponding to the general formula  $A_3Bi_2X_9$ . These compounds are sometimes seen as “defect” or “vacancy-ordered” perovskites (see Subsection 1.1.2). K.M. McCall *et al.* define “defect perovskites” as derivative structures that possess the same corner-sharing  $BX_6$ -octahedra as the  $ABX_3$  aristotype (with  $B$  being the divalent metal), but form different structures due to cation deficiencies in order to satisfy charge balance restrictions [316]. Trivalent cations form  $A_3B_2X_9$  structures with 2/3 occupancy of the B-sites of the  $A_3B_3X_9$  perovskite formula [316]. In the case of bismuth as the trivalent cation ( $A_3Bi_2X_9$  compounds), different crystal structures are obtained by varying the chemical composition. As an example, as discussed in Chapter 1, while  $Cs_3Bi_2I_9$  crystallizes in a zero-dimensional structure with fully decoupled dimers of  $BiI_6$ -octahedra (Figure 6.1a),  $Rb_3Bi_2I_9$  crystallizes in a two-dimensional structure with layers of corner-sharing  $BiI_6$ -octahedra (Figure 6.1b) [317]. This reduced dimensionality is the reason why these compounds are also referred to as

low-dimensional perovskites, although the term “perovskite” is questionable here (see Subsection 1.1.2).

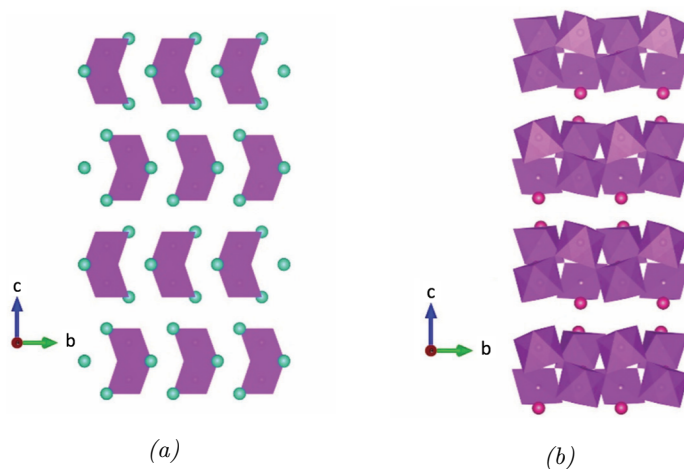


Figure 6.1: Crystal structures of (a)  $Cs_3Bi_2I_9$  and (b)  $Rb_3Bi_2I_9$  viewed from the  $a$ -axis.  $Cs_3Bi_2I_9$  presents a zero-dimensional structure with dimers of fully decoupled  $BiI_6$ -octahedra (purple); while  $Rb_3Bi_2I_9$  presents a two-dimensional structure with layers of corner-sharing  $BiI_6$ -octahedra. The green and red balls represent  $Cs^+$  and  $Rb^+$  cations, respectively.

One of the main bottlenecks in developing bismuth-halide-based compounds resides in the poor solubility of bismuth salts in common solvents [318, 319]. In this study, fifteen different  $A_3Bi_2X_9$  compounds ( $A = K^+, Rb^+, Cs^+, CH_3NH_3^+ - MA -$  or  $HC(NH_2)_2^+ - FA -$ ;  $X = I^-, Br^-$  or  $Cl^-$ ) were synthesized by a dry mechanochemical approach via ball-milling of stoichiometric precursors. In this way, the use of solvents is bypassed. As demonstrated previously (see Chapters 3-5), this technique allows the formation of multinary metal halide compounds in a simple and time-efficient manner [20, 23, 47, 70, 86, 107, 129]. At the time of publishing this study, there was only one previous report on dry mechanochemical synthesis of ternary bismuth-iodide compounds [320]. No reports on the synthesis of several of the chloride and bromide analogues, such as  $FA_3Bi_2Br_9$ ,  $FA_3Bi_2Cl_9$  or  $Rb_3Bi_2Cl_9$  were found. In this chapter, the structural and optical characteristics of the fifteen compounds described above are presented.

This work was published in Journal of Materials Chemistry C [16]. The complete journal article can be found in Appendix D.

## 6.2 Experimental methods

### 6.2.1 Mechanochemical synthesis via ball-milling

In this study,  $AX:BiX_3$  (3:2) powders ( $A = Cs^+, K^+, Rb^+, MA$  or  $FA$  and  $X = Cl^-, Br^-$  or  $I^-$ ) were mixed inside a nitrogen-filled glovebox. Herewith, cesium chloride ( $CsCl$ ,  $> 99\%$ ), cesium bromide ( $CsBr$ ,  $> 99\%$ ) and cesium iodide ( $CsI$ ,  $> 99\%$ ) were purchased from TCI Chemicals. Potassium chloride ( $KCl$ ,  $\geq 99\%$ ), potassium bromide ( $KBr$ ,  $> 99\%$ ) and potassium iodide ( $KI$ ,  $\geq 99.5\%$ ) were purchased from Sigma-Aldrich. Rubidium chloride ( $RbCl$ ,  $99.975\%$ ), rubidium bromide ( $RbBr$ ,  $99.8\%$ ) and rubidium iodide ( $RbI$ ,  $99.8\%$ ) were purchased from Alfa Aesar. Methylammonium bromide ( $CH_3NH_3Br$ ,  $MABr$ ), methylammonium iodide ( $CH_3NH_3I$ ,  $MAI$ ), formamidinium chloride ( $CH_5N_2Cl$ ,  $FACl$ ), formamidinium bromide ( $CH_5N_2Br$ ,  $FABr$ ), and formamidinium iodide ( $CH_5N_2I$ ,  $FAI$ ) were purchased from GreatCell Solar. Methylammonium chloride ( $CH_3NH_3Cl$ ,  $MACl$ ,  $> 99.5\%$ ) was purchased from Lumtec. Furthermore, all chemicals were stored in a nitrogen-filled glovebox and used as received without further purification. The mechanochemical synthesis of the desired compounds was carried out by dry ball-milling of the perovskite precursors at a frequency of 30 Hz for 5 hours, as previously described in Chapter 2 (see Figure 2.1; Steps 1-9). Indeed, the ball-milling time applied in this study is higher compared to the study presented in Chapter 3. It needs to be noted that a different perovskite is investigated in this study and thus other ball-milling requirements might be needed. Since in this study the main aim was the successful (phase-pure) synthesis of the compounds, a long ball-milling time was chosen. A time dependent study is suggested to be carried out to investigate whether the material can be formed at shorter times and whether there are detrimental effects on prolonged milling.

### 6.2.2 Characterization

#### X-ray diffraction

X-ray diffraction enabled the measurement of the crystallographic properties of all compounds. Single XRD scans were acquired in the range  $2\theta = 10^\circ - 50^\circ$  in Bragg-Brentano geometry in air, as described in Chapter 2. The data analysis was performed using HighScore Plus and Fullprof software.

#### Optical characterization

Optical characterization of all compounds was performed by measuring the absorbance with a High Power UV-Vis fiber light source, integrated sphere and Avantes Starline AVASpec2048L spectrometer in reflection mode. Also, the photoluminescence was measured. These measurements were carried out in back-scattering geometry with excitation by  $Nd^{3+}$  YAG laser pulses at 355 nm (pulse duration 1 ns, repetition rate 1 kHz, average power 2.5 mW) and detection by USB 650 Ocean Optics spectrometer. All PL spectra were corrected for spectral sensitivity of the detection system.

### 6.3 Results and discussion

The powders obtained by ball-milling stoichiometric amounts of inorganic AX and  $BiX_3$  were analyzed by XRD (see Figure 6.2).

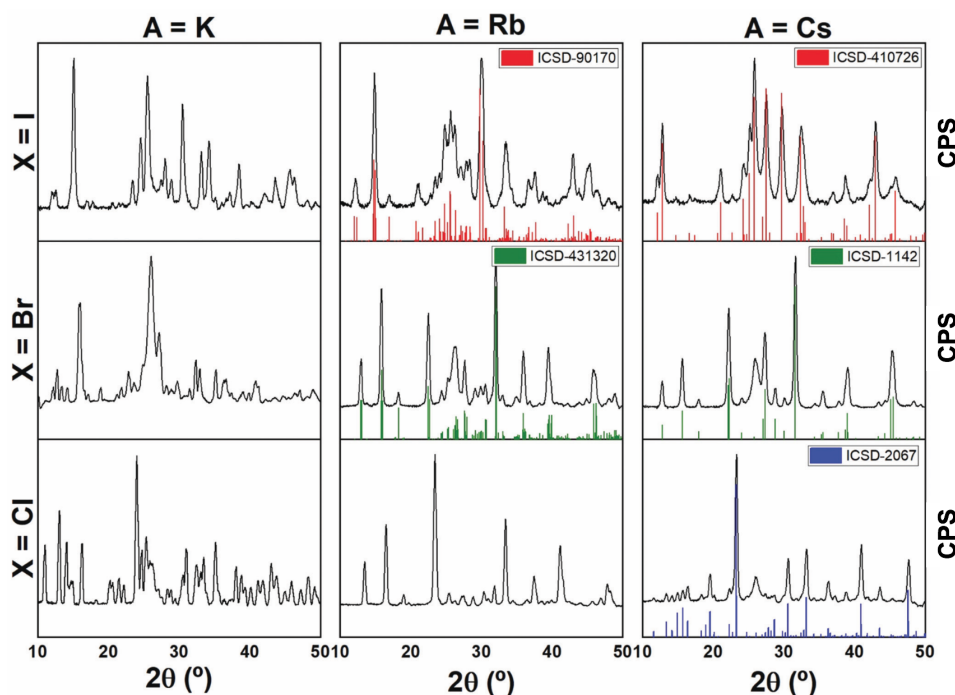


Figure 6.2: XRD characterization of mechanochemically-synthesized inorganic  $A_3Bi_2X_9$  ( $A = K^+, Rb^+, Cs^+$ ;  $X = I^-, Br^-, Cl^-$ ; black lines) and reference bulk patterns when available from the Inorganic Crystal Structure Database (ICSD; colored columns). A broad feature around  $2\theta = 26^\circ$  is sometimes visible due to the parasitic diffraction of the underlying adhesive tape used to fix the powder samples on the holder (see Figure B.3 in Appendix B).

In five out of fifteen cases ( $Cs_3Bi_2I_9$ ,  $Cs_3Bi_2Br_9$ ,  $Cs_3Bi_2Cl_9$ ,  $Rb_3Bi_2I_9$  and  $Rb_3Bi_2Br_9$ ), the obtained diffractograms could be compared with bulk reference patterns published in the International Crystal Structure Database (ICSD). Excellent matches were obtained. This result points towards the high phase-purity obtained with this simple and dry synthesis method. No published reference pattern was found for  $Rb_3Bi_2Cl_9$ . However, when compared to  $Rb_3Bi_2I_9$  and  $Rb_3Bi_2Br_9$ , a clear gradual shift towards higher angles (smaller interatomic distances) is visible when the halide ionic radius is reduced from  $I^-$  to  $Cl^-$ . This suggests a shrinkage of the unit cell. In order to assess this more accurately, whole-pattern Le Bail fits were conducted on all three  $Rb_3Bi_2X_9$  compounds (see Figure D.1 in Appendix D). The refined cell parameters and unit cell volume are summarized in Table 6.1. This is strong evidence for the formation of  $Rb_3Bi_2Cl_9$ , which at the time of publication of this study had not been experimentally synthesized before.



Table 6.1: Refined cell parameters for  $Rb_3Bi_2X_9$  compounds ( $X = I^-$ ,  $Br^-$  or  $Cl^-$ ).

	Reference	This study
<b>Rb<sub>3</sub>Bi<sub>2</sub>I<sub>9</sub></b> (P 1 c 1)	a = 14.690 Å b = 8.195 Å c = 25.645 Å V = 2516.82 Å <sup>3</sup>	a = 14.6874(8) Å b = 8.1982(6) Å c = 25.646(1) Å V = 2517.5(3) Å <sup>3</sup>
<b>Rb<sub>3</sub>Bi<sub>2</sub>Br<sub>9</sub></b> (P 1 2 <sub>1</sub> /a 1)	a = 13.5601(1) Å b = 7.9124(5) Å c = 19.3510(8) Å V = 2076.13 Å <sup>3</sup>	a = 13.570(1) Å b = 7.913(5) Å c = 19.351(1) Å V = 2077.8(3) Å <sup>3</sup>
<b>Rb<sub>3</sub>Bi<sub>2</sub>Cl<sub>9</sub></b> (P 1 2 <sub>1</sub> /a 1)	-	a = 13.3655(9) Å b = 7.9654(8) Å c = 15.423(1) Å V = 1641.8(2) Å <sup>3</sup>

The potassium-based series are more difficult to analyze, as no reference patterns could be found for any  $K_3Bi_2X_9$  compound. Nonetheless, when comparing the diffractograms after ball-milling with the reference patterns of the precursors (see Figure D.2 in Appendix D), it is clear that these have reacted to form a new phase, which seems reasonable to attribute to  $K_3Bi_2X_9$  ( $X = I^-$ ,  $Br^-$  or  $Cl^-$ ). This hypothesis is further supported by the optical absorption spectra (see Figure 6.4).

Besides inorganic Bi-based compounds, also hybrid compounds with organic MA and FA cations were formed by solvent-free ball-milling of inorganic  $BiX_3$  salts and organic AX salts ( $A = MA$  or  $FA$ ). Again, when comparing X-ray diffractograms of the resulting MA-based powders with reference bulk patterns from ICSD (see Figure 6.3), a very good match is observed. This result highlights the high phase-purity of mechanochemically-synthesized hybrid  $MA_3Bi_2X_9$  compounds.

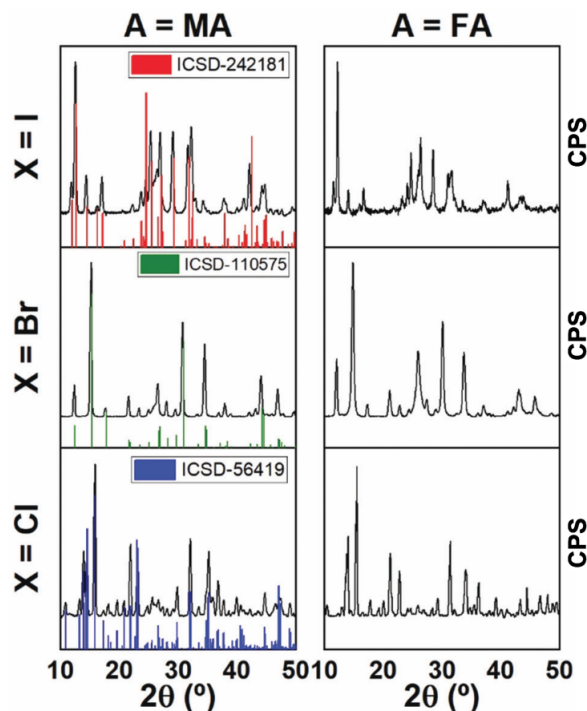


Figure 6.3: XRD characterization of mechanochemically-synthesized hybrid  $A_3Bi_2X_9$  ( $A = MA$  or  $FA$ ;  $X = I^-$ ,  $Br^-$  or  $Cl^-$ ; black lines) and reference bulk patterns from the Inorganic Crystal Structure Database (ICSD) for the MA-based compounds (colored columns). A more detailed comparison on diffractograms of the same halide composition, but different A-cation is presented in Figures D.3-D.5 in Appendix D. A broad feature around  $2\theta = 26^\circ$  is sometimes visible due to the parasitic diffraction of the underlying adhesive tape used to fix the powder samples on the holder (see Figure B.3 in Appendix B).

At the time of publishing this study, only scarce reports on  $FA_3Bi_2I_9$  existed [74,318], while no reports on  $FA_3Bi_2Br_9$  or  $FA_3Bi_2Cl_9$  were found. For the complete halide series, the diffractograms of the compounds obtained with formamidinium as the cation, closely match those of the corresponding methylammonium-analogues with a slight shift to lower angles, due to the higher ionic radius of FA (2.53 Å) compared to MA (2.17 Å) [5]. Whole-pattern fits were conducted for all six hybrid compounds (see Figures D.3-D.5 in Appendix D). The refined cell parameters confirm the cell expansion upon increase in size of the organic cation from MA to FA (see Table 6.2). Hence, again, the formation of highly phase-pure materials for all  $FA_3Bi_2X_9$  compounds is deduced.

Table 6.2: Refined cell parameters for the hybrid organic-inorganic compounds  $MA_3Bi_2X_9$  and  $FA_3Bi_2X_9$  ( $X = I^-$ ,  $Br^-$  or  $Cl^-$ ).

	Reference	This study
<b>MA<sub>3</sub>Bi<sub>2</sub>I<sub>9</sub></b> (C 1 2/c 1)	a = 8.4952(6) Å b = 14.7126(10) Å c = 21.6855(14) Å V = 2710.39 Å <sup>3</sup>	a = 8.5340(5) Å b = 14.654(1) Å c = 21.653(1) Å V = 2707.9(3) Å <sup>3</sup>
<b>FA<sub>3</sub>Bi<sub>2</sub>I<sub>9</sub></b> (C 1 2/c 1)	-	a = 8.8389(8) Å b = 14.909(2) Å c = 21.851(3) Å V = 2879.5(6) Å <sup>3</sup>
<b>MA<sub>3</sub>Bi<sub>2</sub>Br<sub>9</sub></b> (P -3 m 1)	a = 8.188(2) Å b = 8.188(2) Å c = 9.927(3) Å V = 576.374 Å <sup>3</sup>	a = 8.2086(2) Å b = 8.2086(2) Å c = 10.025(1) Å V = 585.03(6) Å <sup>3</sup>
<b>FA<sub>3</sub>Bi<sub>2</sub>Br<sub>9</sub></b> (P -3 m 1)	-	a = 8.4071(8) Å b = 8.4071(8) Å c = 10.183(2) Å V = 623.3(1) Å <sup>3</sup>
<b>MA<sub>3</sub>Bi<sub>2</sub>Cl<sub>9</sub></b> (P m c n)	a = 7.713(8) Å b = 13.26(2) Å c = 20.43(3) Å V = 2089.47 Å <sup>3</sup>	a = 7.7109(3) Å b = 13.2628(6) Å c = 20.4313(6) Å V = 2089.5(1) Å <sup>3</sup>
<b>FA<sub>3</sub>Bi<sub>2</sub>Cl<sub>9</sub></b> (P m c n)	-	a = 8.045(1) Å b = 13.387(2) Å c = 21.062(3) Å V = 2268.3(6) Å <sup>3</sup>

The optical properties of the inorganic and hybrid compounds (see Figure 6.4) were analyzed by sandwiching the powders in between two quartz plates. The optical bandgaps of all materials – as derived from their absorption onsets (see Figure 6.4) – span from the near-UV (3.3 eV/380 nm for  $K_3Bi_2Cl_9$ ) to the red part of the visible spectrum (1.9 eV/650 nm for  $Cs_3Bi_2I_9$ ). Similar to what is observed in lead halide perovskites, also for these “3-2-9”-bismuth compounds, the bandgap is strongly dependent on the X-anion. The compounds with the smaller anion ( $Cl^-$ ) give the larger bandgaps and vice versa [321]. To a lesser extent, the same trend is visible with varying the ionic radius of the A-cation with  $X = Cl^-$  and  $X = Br^-$ . Indeed, for these halides it is observed that the bandgap is systematically wider for  $A = K^+$ , followed by  $A = Rb^+$ , followed by the other cations. However, this trend does not seem to apply for  $X = I^-$ . While the difference between the bandgaps of the iodide compounds is smaller (about 0.1 eV; from 610 nm to 650 nm) as compared to the chloride-series (0.3 eV difference corresponding to absorption onsets of 380 nm to 420 nm), it must be noted that – as opposed to 3D halide perovskites – these low-dimensional  $A_3Bi_2X_9$  compounds crystallize in very different structures depending on their composition, as explained in the introduction (see Section 6.1 and Figure 6.1). Hence, it is not surprising that the variations of optical properties with composition do not follow a homogeneous trend for all cases. Moreover, the presence of a secondary absorption peak – blue-shifted by ca. 50 nm in almost all compounds – is noted. Although the origin of this feature is unclear, it is consistent with previous reports on the same and related materials [320, 322]. Despite the not yet encouraging results in photovoltaics [311, 323–325], these compounds are promising candidates in electroluminescence applications [316, 326–331]. At the time of writing, a few reports have demonstrated high photoluminescence quantum yields (PLQYs) from ligand-passivated colloidal nanoparticles of  $Cs_3Bi_2Br_9$ ,  $MA_3Bi_2Br_9$  and  $MA_3Bi_2Cl_9$  in solution [326, 330–333]. In contrast, others have not detected visible photoluminescence in similar colloidal quantum dots [74] or achieved PLQYs lower than 1 % [334].

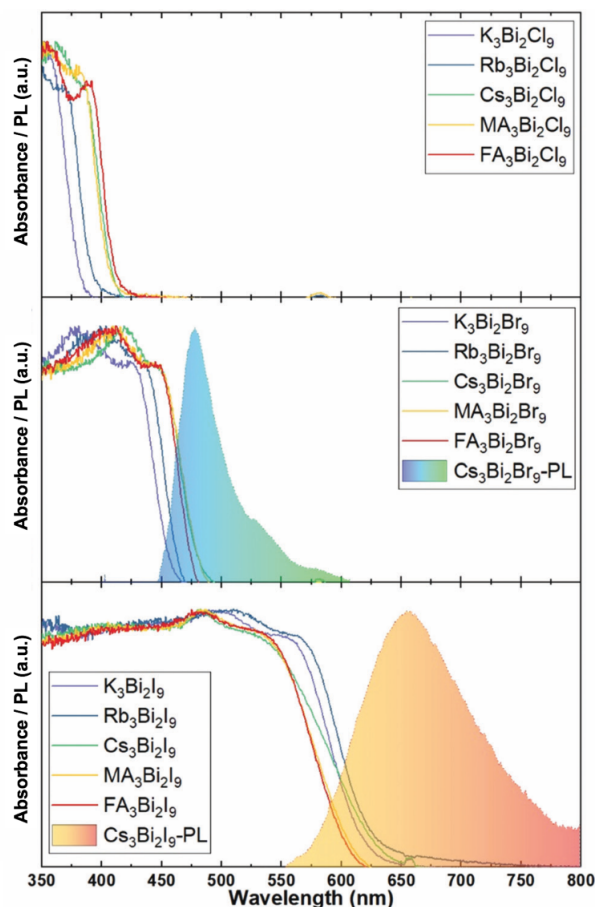


Figure 6.4: Normalized absorbance spectra of all  $A_3Bi_2X_9$  compounds (solid lines) and photoluminescence spectra of  $Cs_3Bi_2Br_9$  and  $Cs_3Bi_2I_9$  (dashed lines with filled area under curve). In the formula  $A_3Bi_2X_9$ ,  $A$  stands for  $K^+$ ,  $Rb^+$ ,  $Cs^+$ ,  $MA$  or  $FA$  and  $X$  for  $I^-$ ,  $Br^-$  or  $Cl^-$ .

In the current study, dry mechanochemically-synthesized powders of  $Cs_3Bi_2Br_9$  and  $Cs_3Bi_2I_9$  clearly show visible photoluminescence at room temperature (see Figure 6.4). This PL signal is slightly Stokes-shifted from the absorption edge, with maxima at 478 nm and 657 nm, respectively for  $X = Br^-$  and  $X = I^-$ . In both cases, the PL spectra are broad and asymmetric, which is consistent with previous reports [326, 330, 331, 334]. As a result, the visible spectrum is almost fully covered from 450 nm to 800 nm with these two compounds, which is of interest for the generation of white light. In order to demonstrate this as a proof of concept, a pellet was fabricated by pressing a finely ground mixture of both powders ( $Cs_3Bi_2Br_9$  and  $Cs_3Bi_2I_9$ ) with transparent poly(methyl methacrylate) (PMMA) beads. The corresponding PL spectrum (see Figure 6.5) presents a broad emission with CIE-coordinates (0.42, 0.45) corresponding to a warm white light with a correlated color temperature of 3615 K.

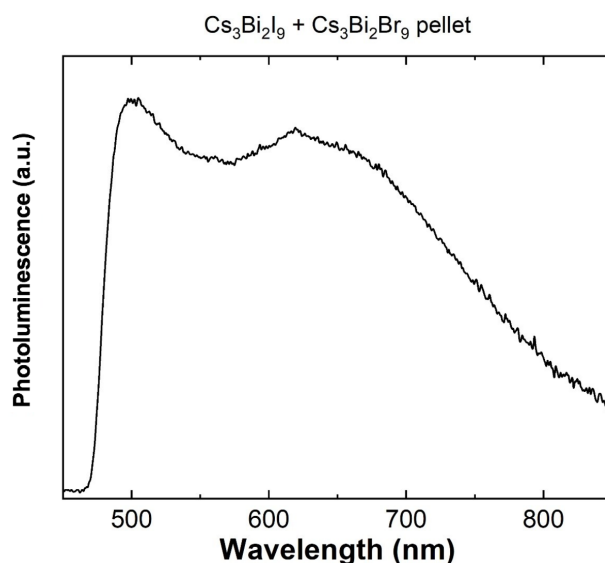


Figure 6.5: Photoluminescence spectrum of a solid pellet made from a finely ground mixture of mechanochemically-synthesized  $\text{Cs}_3\text{Bi}_2\text{Br}_9$  and  $\text{Cs}_3\text{Bi}_2\text{I}_9$  together with transparent PMMA beads.

## 6.4 Conclusions

In summary, fifteen different non-toxic, bismuth halide ternary compounds ( $\text{A}_3\text{Bi}_2\text{X}_9$ ) were successfully synthesized by dry ball-milling of stoichiometric precursors ( $\text{AX}:\text{BiX}_3$  (3:2) with  $\text{A} = \text{Cs}^+$ ,  $\text{K}^+$ ,  $\text{Rb}^+$ ,  $\text{MA}$  or  $\text{FA}$  and  $\text{X} = \text{Cl}^-$ ,  $\text{Br}^-$  or  $\text{I}^-$ ). Structural characterization by X-ray diffraction revealed the excellent quality of the thus-formed materials, without noticeable, unreacted precursors or byproducts. Furthermore, these compounds have useful bandgaps for lighting applications, as they cover most of the visible spectrum. Moreover, dry bulk  $\text{Cs}_3\text{Bi}_2\text{Br}_9$  and  $\text{Cs}_3\text{Bi}_2\text{I}_9$  exhibit photoluminescence at room temperature, even without passivating agents. This holds promise to obtain high photoluminescence efficiency when passivating agents are added. The current results pave the way to the widespread use of these non-toxic, perovskite-related materials for lighting applications.

## 6.5 Author contribution and acknowledgments

The content of this chapter was reproduced with permission from Journal of Materials Chemistry C [16]. This publication was added to an online collection that highlights the most popular articles published in Journal of Materials Chemistry C in 2019. The complete journal article can be found in Appendix D.

The research leading to the results presented in this chapter has received funding from the European Union Program for Research and Innovation Horizon 2020 (2014-2020) under the Marie Skłodowska-Curie Grant Agreement PerovSAMs No. 747599 and project INFORM (grant 675867), the Spanish Ministry of Economy and Competitiveness (MINECO) via the Unidad de Excelencia María de Maeztu MDM- 2015-0538, MAT2017-88821-R and PCIN-2015-255 and the Generalitat Valenciana (Prometeo/2016/135 and GRISOLIAP/2017/089).

Y. El Ajjouri, V. S. Chirvony, N. Vassilyeva, M. Sessolo, F. Palazón and H. J. Bolink, Low-Dimensional Non-Toxic  $\text{A}_3\text{Bi}_2\text{X}_9$  Compounds Synthesized by a Dry Mechanochemical Route with Tunable Visible Photoluminescence at Room Temperature. *J. Mater. Chem. C*, **2019**, 7, 6236-6240. [IF: 6.641 (2019), Q1]

## Chapter 7

# Single-Source Vacuum Deposition of Mechanochemically-Synthesized Inorganic Halide Perovskites

### 7.1 Introduction

As previously discussed, MCS is a promising technique to investigate fundamental properties of i.a. perovskites and related materials, as well as the study of new compounds. In this chapter, MCS will also be demonstrated as a means to fabricate perovskite precursors for single-source vacuum deposition (SSVD). Hereafter, thin films of different cesium lead halide compounds were fabricated by means of SSVD of CsX and PbX<sub>2</sub> (X = Cl<sup>-</sup>, Br<sup>-</sup> or I<sup>-</sup>) precursors that were simply mixed in a crucible. Furthermore, solvent-free mechanochemical synthesis of CsPbX<sub>3</sub> perovskites was carried out by ball-milling. Also, the latter pre-synthesized powder perovskite compounds were converted into thin films by SSVD. Performing a detailed and systematic structural and optical analysis enabled the characterization of the different thin films – formed by SSVD of pristine, as well as ball-milled chloride, bromide and iodide precursors – at room temperature, as well as upon thermal annealing.

This work was published in Chemistry of Materials [107]. The complete journal article can be found in Appendix E.

### 7.2 Experimental methods

#### 7.2.1 Mechanochemical synthesis via ball-milling

The mechanochemical synthesis of CsPbX<sub>3</sub> (X = Cl<sup>-</sup>, Br<sup>-</sup> or I<sup>-</sup>) was carried out by mixing equimolar CsX:PbX<sub>2</sub> powders inside a nitrogen-filled glovebox. Herewith, cesium chloride (CsCl, > 99 %), cesium bromide (CsBr, > 99 %), cesium iodide (CsI, > 99 %) and lead(II) iodide (PbI<sub>2</sub>, ≥ 98 %) were purchased from TCI Chemicals. Lead(II) bromide (PbBr<sub>2</sub>, ≥ 98 %) and lead(II) chloride (PbCl<sub>2</sub>, 98 %) were purchased from Sigma-Aldrich. All chemicals were stored in a nitrogen-filled glovebox and used as received without further purification. The mechanochemical synthesis of the desired compounds was carried out by dry ball-milling of the perovskite precursors at a frequency of 30 Hz for 5 hours, as previously described in Chapter 2 (see Figure 2.1; Steps 1-9). Indeed, the ball-milling time applied in this study is higher compared to the study presented in Chapter 3. Reasoning thereof is that this study was carried out prior to knowing the minimum ball-milling time necessary for the synthesis of this perovskite.

### 7.2.2 Single-source vacuum deposition

In order to convert the powder pristine, as well as ball-milled perovskite precursors into thin films, a single-source vacuum deposition technique (SSVD) was performed (see Figure 2.1; Steps 10-12). The perovskite thin films were deposited in a high vacuum chamber (Vaksis R&D and Engineering) equipped with temperature controlled alumina thermal sources (Creaphys GmbH) and quartz crystal microbalance thickness sensors, as previously described in Chapter 2. Mechanical shutters both at the thermal source and at the substrate holder were used to control the deposition process. The obtained thin films were kept in a nitrogen-filled glovebox.

### 7.2.3 Characterization

#### X-ray diffraction

X-ray diffraction was measured in the  $2\theta = 10^\circ - 50^\circ$  range, as described in Chapter 2.

#### Optical characterization

For the optical characterization of the obtained samples, absorbance was measured with a High Power UV-Vis fiber light source, integrated sphere and Avantes Starline AVASpec-2048L spectrometer in reflection mode. Furthermore, photoluminescence was measured with a continuous wave 375 nm diode laser with a 400 nm filter and Hamamatsu PMA 11 spectrometer. For a typical spectrum 10 scans of 1 second were averaged.

## 7.3 Results and discussion

First, thin films of simply mixed CsX and PbX<sub>2</sub> ( $X = \text{Cl}^-$ ,  $\text{Br}^-$  or  $\text{I}^-$ ) were prepared by SSVD. Figure 7.1 and Figure 7.2 show the structural and optical characterization of the films as-prepared at room temperature (RT), as well as after thermal annealing at 225 °C for 15 minutes on a hotplate (Stuart US152) in a nitrogen-filled glovebox for  $X = \text{Cl}^-$  and  $\text{Br}^-$  (for the data of  $X = \text{I}^-$ , see Figure E.2 in Appendix E). All films fabricated in this study have an average thickness of 250 nm, measured by a contact profilometer (Ambios XP-1). As can be seen by X-ray diffraction (Figure 7.1), the as-prepared films consist of a mixture of CsPb<sub>2</sub>X<sub>5</sub> and CsPbX<sub>3</sub> [215]. However, the relative amount of both compounds is different for the different anions ( $X = \text{Cl}^-$  and  $\text{Br}^-$ ). In the case of the smaller anion ( $X = \text{Cl}^-$ ), the film is mostly consistent of CsPbCl<sub>3</sub> (Figure 7.1a) and exhibits the corresponding absorption onset around 400 nm and Stokes-shifted photoluminescence centered at 412 nm (Figure 7.2a).

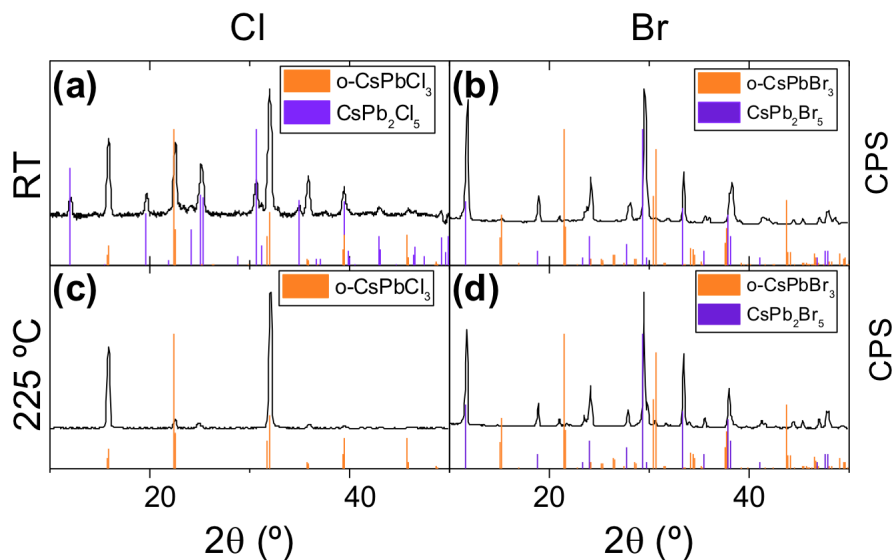


Figure 7.1: XRD characterization of thin films prepared by SSVD of simply mixed  $\text{CsCl} + \text{PbCl}_2$  (a, c) and  $\text{CsBr} + \text{PbBr}_2$  (b, d) at room temperature (a, b), as well as after thermal annealing at 225 °C for 15 minutes on a hotplate in a nitrogen-filled glovebox (c, d). The reference patterns for orthorhombic  $\text{CsPbCl}_3$  (ICSD-243734), orthorhombic  $\text{CsPbBr}_3$  (ICSD-97851), as well as  $\text{CsPb}_2\text{Cl}_5$  (ICSD-249888) and  $\text{CsPb}_2\text{Br}_5$  (PDF-25-0211) are shown along the experimental data (black lines) as colored columns.

On the other hand, for the larger anion ( $X = \text{Br}^-$ ), the  $\text{CsPb}_2\text{Br}_5$  compound is dominant (Figure 7.1b). A closer look reveals that reflections characteristic of  $\text{CsPbBr}_3$  are also present, although they are broad and not intense. This observation suggests that small domains of  $\text{CsPbBr}_3$  are embedded in a  $\text{CsPb}_2\text{Br}_5$  matrix. The optical characterization of this film (Figure 7.2b) shows no marked absorption onset in this range, but only a signal due to optical interferences (see Figure E.1 in Appendix E for the complete absorption spectrum). However, a rather intense photoluminescence peak centered at 517 nm is visible. This value is slightly blue-shifted from the bulk PL of  $\text{CsPbBr}_3$  [335]. This blue-shift is consistent with the hypothesis of small (tens of nanometers)  $\text{CsPbBr}_3$  domains in the weak quantum confinement regime [10], possibly passivated by a  $\text{CsPb}_2\text{Br}_5$  matrix.



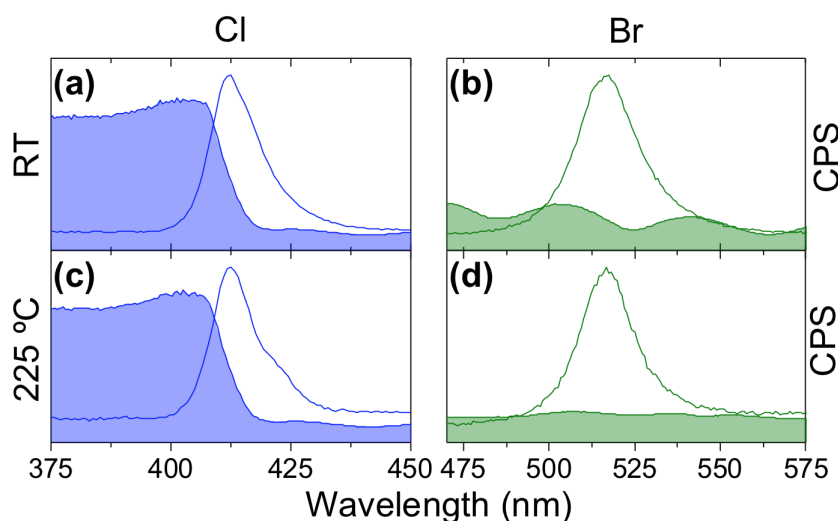


Figure 7.2: Normalized absorption and photoluminescence spectra of thin films prepared by SSVD of simply mixed  $\text{CsCl} + \text{PbCl}_2$  (a, c) and  $\text{CsBr} + \text{PbBr}_2$  (b, d) at room temperature (a, b), as well as after thermal annealing at  $225\text{ }^\circ\text{C}$  (c, d) for 15 minutes. The absorption signal present in panel (b) is linked to optical interferences. The absorption spectrum of this film throughout a broader wavelength range is presented in Figure E.1 in Appendix E.

When the chloride films are annealed at  $225\text{ }^\circ\text{C}$  for 15 minutes, the fraction of  $\text{CsPb}_2\text{Cl}_5$  is substantially reduced so that almost phase-pure  $\text{CsPbCl}_3$  is obtained (Figure 7.1c). This is not the case for the bromide films where  $\text{CsPb}_2\text{Br}_5$  remains the dominant crystalline compound (Figure 7.1d). The optical characteristics of both films remain similar after thermal annealing (Figure 7.1c-d). In conclusion, single-source vacuum deposition of raw precursors (not-mechanochemically-synthesized mixtures of precursors) can yield good-quality  $\text{CsPbX}_3$  perovskites only for the smaller halide ( $\text{X} = \text{Cl}^-$ ), while  $\text{PbX}_2$ -rich compounds are mainly formed for the larger halide ( $\text{X} = \text{Br}^-$ ). This trend is confirmed by looking at the results of the iodide compounds (thin film of simply mixed  $\text{CsI} + \text{PbI}_2$ ), where no significant  $\text{CsPbI}_3$  could be formed with this method (see Figure E.2 in Appendix E).

In order to obtain higher purity perovskite films by SSVD, mechanochemical synthesis of  $\text{CsPbX}_3$  was carried out by dry ball-milling of stoichiometric precursors (see Subsection 7.2.1). At the time of publishing these results, few reports had demonstrated similar mechanochemical synthesis with highly energetic planetary ball-mills [59, 174].

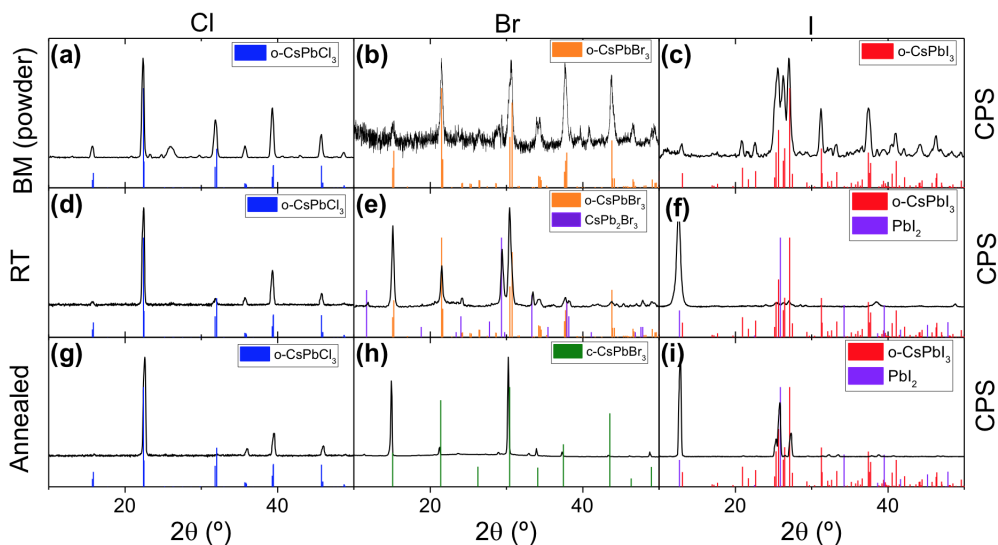


Figure 7.3: XRD characterization of ball-milled (BM)  $\text{CsX} + \text{PbX}_2$  powders (a-c), as well as thin films prepared by SSVD of the resulting powders at room temperature (d-f) and after thermal annealing for 15 minutes on a hotplate in a nitrogen-filled glovebox (g-i). Note that the annealing temperature is  $225^\circ\text{C}$  for  $X = \text{Cl}^-$  and  $\text{Br}^-$  (g, h), while it is  $325^\circ\text{C}$  for  $X = \text{I}^-$  (i). The reference patterns for orthorhombic  $\text{CsPbCl}_3$  (ICSD-243734), orthorhombic  $\text{CsPbBr}_3$  (ICSD-97851), orthorhombic  $\text{CsPbI}_3$  (ICSD-161480), cubic  $\text{CsPbBr}_3$  (ICSD-29073),  $\text{CsPb}_2\text{Br}_5$  (PDF-25-0211) and  $\text{PbI}_2$  (ICSD-68819) are shown along the experimental data (black lines) as colored columns.

XRD and optical analyses (Figure 7.3a-c and Figure 7.4a-c, respectively) reveal that ball-milling  $\text{CsX}$  and  $\text{PbX}_2$  compounds ( $X = \text{Cl}^-$ ,  $\text{Br}^-$  or  $\text{I}^-$ ) at room temperature with a shaking (non-planetary) setup, results in the formation of high purity  $\text{CsPbX}_3$  perovskite powders for all halides. When these powders are used for SSVD, the resulting films exhibit a higher purity (higher relative concentration of  $\text{CsPbX}_3$ ) than when non-ball-milled powders are used. This suggests that the pre-formed perovskites sublime – at least partially – as a single compound ( $\text{CsPbX}_3$ ), instead of undergoing a transformation back into  $\text{CsX} + \text{PbX}_2$  followed by subsequent separate evaporation of both components. Indeed, in the case of the chloride-based compounds, the diffractogram of the film at room temperature (Figure 7.3d) – which is essentially temperature-independent (Figure 7.3g) – shows no signal for  $\text{CsPb}_2\text{Cl}_5$ . This means that the purity of the thin film deposited at room temperature is already higher than what can be achieved with non-ball-milled precursors, even after they were annealed at  $225^\circ\text{C}$  (Figure 7.1c). The difference is also evident for  $X = \text{Br}^-$ . Although  $\text{CsPb}_2\text{Br}_5$  is present in the as-deposited film (Figure 7.3e), its relative content is much reduced as compared to the non-ball-milled samples (Figure 7.1 b). Furthermore, this compound disappears after annealing at  $225^\circ\text{C}$  (Figure 7.3h; see Figure E.3 in Appendix E for XRD characterization at different temperatures) and  $\text{CsPbBr}_3$  remains the only detectable crystalline compound. This transformation suggests that the original film (prior to thermal annealing) has an excess of  $\text{CsBr}$  that can lead to the formation of  $\text{CsPbBr}_3$  by reacting with  $\text{CsPb}_2\text{Br}_5$ . Another possible hypothesis would be the loss or amorphization of  $\text{PbBr}_2$ , which is unlikely due to its high melting point ( $373^\circ\text{C}$ ). The presence of  $\text{CsBr}$  together with  $\text{CsPb}_2\text{Br}_5$  is hard to detect since its main diffraction peak located at  $2\theta = 29.38^\circ$  (ICSD: 98-005-3848) overlaps with the signal of  $\text{CsPb}_2\text{Br}_5$ , as has been previously noted by F. Palazón *et al.* [336]. It is also worth noting that no residual powder is left in the crucible after SSVD, which again suggests the presence of excess  $\text{CsBr}$  in the film before thermal annealing. Previous mechanochemical synthesis of  $\text{CsBr}:\text{PbBr}_2$  stoichiometric precursors also seems to result in better morphology of the final film (see Figure E.4 in Appendix E). Indeed, the film prepared from the pristine  $\text{CsBr} + \text{PbBr}_2$  mixture presents a patchy morphology at high magnification and cracks are visible at lower magnification. In contrast to this, the film prepared from mechanochemically-synthesized  $\text{CsPbBr}_3$  shows much higher homogeneity with typical grain sizes of several hundred nanometers. No obvious pinholes are observed.

As previously mentioned, iodide perovskites remain the most difficult to form. Although mechanochemical synthesis of powder  $\text{CsPbI}_3$  is achieved (see Figure 7.3c), the resulting films are mainly composed of  $\text{PbI}_2$  (Figure 7.3f). Only after thermal annealing at  $325^\circ\text{C}$  for 15 minutes on a hotplate (Stuart US152) in a nitrogen-filled glovebox – which is a higher temperature than used for the chloride- and bromide-based films – the fraction of  $\text{CsPbI}_3$  rises significantly, although  $\text{PbI}_2$  remains dominant. It must be noted that XRD characterization had to be carried out in air, due to the restrictions in the experimental setup at the time of execution. It is known that  $\text{CsPbI}_3$  degrade under ambient conditions [337,338]. This was also observed for the mechanochemically-synthesized  $\text{CsPbI}_3$  powder. The as-prepared compound is black in nitrogen – indicating a cubic crystal structure – and remains black (cubic) when stored under nitrogen for over one month (see Figure E.5 in Appendix E). However, it quickly returns to the “yellow” orthorhombic phase when it is exposed to air before XRD characterization can be completed (Figure 7.3c). A similar observation is made on the thin film after annealing; the partial conversion to the black phase is clearly visible by eye (see Figure E.6 in Appendix E). It must be noted that the applied annealing temperature is close to the phase transition [339]. Hence, it is possible that annealing at a higher temperature – which was impossible in the current case for technical reasons – might result in a full conversion. When the samples are kept under inert atmosphere (Figure E.6 in Appendix E), the black phase remains stable for several days.

The optical characterization of the ball-milled powders, as well as the resulting films by SSVD, is presented in Figure 7.4.

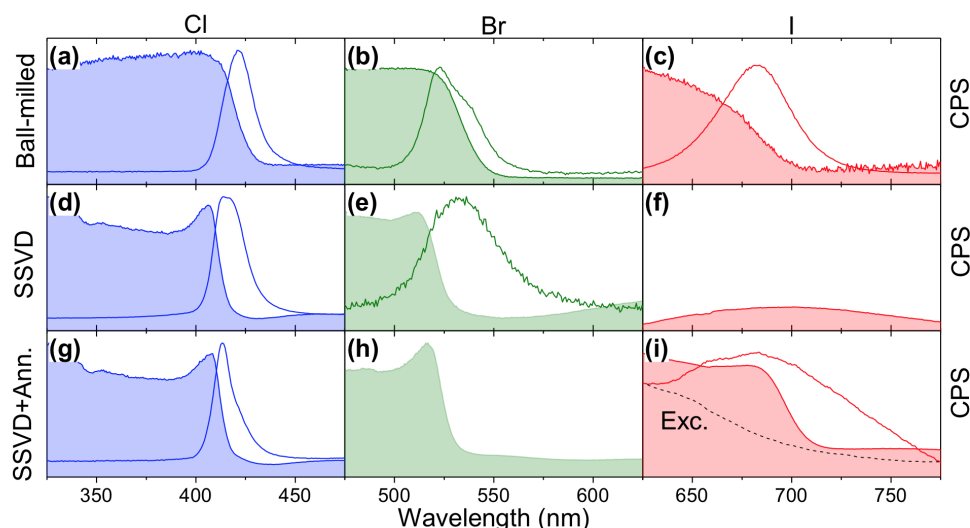


Figure 7.4: Normalized absorption and photoluminescence spectra of ball-milled  $\text{CsX} + \text{PbX}_2$  powders (a-c), as well as thin films prepared by SSVD of the resulting powders at room temperature (d-f) and after thermal annealing (Ann.) for 15 minutes on a hotplate in a nitrogen-filled glovebox (g-i). Note that the annealing temperature is  $225^\circ\text{C}$  for  $X = \text{Cl}^-$  and  $\text{Br}^-$  (g, h) while it is  $325^\circ\text{C}$  for  $X = \text{I}^-$  (i). The absorption signal observed in panel (f) originates from optical interferences. The absorption spectrum of this film throughout a broader wavelength range is presented in Figure E.7 in Appendix E.

All powders (Figure 7.4a-c) exhibit the expected absorbance and PL spectra for the  $\text{CsPbX}_3$  compounds, confirming the high quality of mechanochemically-synthesized inorganic halide perovskites. Thin films prepared thereof by SSVD present different characteristics as a function of the halide and temperature. For the smaller chloride anion, the expected absorbance and PL are present both at room temperature and after annealing at  $225^\circ\text{C}$ , as in the case of non-ball-milled precursors (Figure 7.2c, d). For  $X = \text{Br}^-$ , a strong absorption onset is visible already at room temperature (Figure 7.4e) and gets steeper after annealing (Figure 7.4h), indicating a higher degree of crystallinity and order in the material. This absorption was not seen in the case of non-ball-milled precursors (Figure 7.2b-d) and reinforces the conclusion that  $\text{CsPbBr}_3$  is favored when using previously mechanochemically-synthesized powders, while  $\text{CsPb}_2\text{Br}_5$  was mainly formed when using

pristine precursors, as previously discussed. It must be noted that the bromide-based sample shows a weak PL in the as-deposited film (Figure 7.4e), which is ultimately lost after annealing (Figure 7.4h). The PL quenching of CsPbBr<sub>3</sub> upon thermal annealing is already reported and may be due to the creation of more trap states in the film [336, 340–342]. Indeed, XRD shows that peaks associated with CsPbBr<sub>3</sub> get thinner upon annealing (Figure 7.3e, h), which denotes a grain growth. Another possible explanation of the PL loss is linked to higher diffusivity of carriers. As grains become larger upon annealing, it may be expected that diffusion lengths increase and thus electrons and holes can reach surface trap states more easily. Eventually, for the iodide film, no significant absorption or photoluminescence is detected at room temperature at the wavelengths of interest (Figure 7.4f; see Figure E.7 in Appendix E for the complete absorption spectrum). This result is consistent with the almost inexistent XRD signal for CsPbI<sub>3</sub> in the as-prepared film (Figure 7.3f). However, after annealing at 325 °C and rapid quenching, a clear absorption onset is visible around 680 nm. Photoluminescence is also visible, though not intense and broad. The broad PL signal is partially attributed to the overlap of the sample's PL with the excitation source, which has a weak visible component in addition to the main UV peak at 375 nm, as represented as a reference in Figure 7.4i.

## 7.4 Conclusions

In this study, fully inorganic cesium lead halide thin films were fabricated by means of fast single-source vacuum deposition. It is noted that in the case of SSVD of pristine mixed precursors, high-purity perovskite CsPbX<sub>3</sub> could only be obtained for X = Cl<sup>-</sup> after thermal annealing. However, when CsX and PbX<sub>2</sub> are previously ball-milled at room temperature, high-purity CsPbX<sub>3</sub> are formed. Single-source vacuum deposition of the so-formed perovskites results in much-improved films both as-prepared, as well as after thermal annealing. In this way, perovskite films with optical transitions throughout the visible spectrum from around 400 nm (X = Cl<sup>-</sup>) to around 700 nm (X = I<sup>-</sup>) could be obtained. As such, it is demonstrated that single-source vacuum deposition of ball-milled perovskites represents an easy, fast and dry process to form high-quality thin films of fully inorganic perovskites. Future work of interest might focus on the implementation of these films into different optoelectronic devices – such as light-emitting diodes or solar cells – where it will be crucial to avoid chemical impurities and to finely control the film morphology. As a final note, it must be stressed that the film thickness could be controlled by the amount of precursors fed into the thermal source, which could then be totally evaporated. However, the relationship between film thickness and precursor amount could be impacted by other processing parameters, such as the distance between the source and the substrate.

## 7.5 Author contribution and acknowledgments

The content of this chapter was reproduced with permission from Chemistry of Materials [107]. The complete journal article can be found in Appendix E.

The research leading to the results reported in this chapter has received funding from the European Union Program for Research and Innovation Horizon 2020 (2014-2020) under the Marie Skłodowska-Curie Grant Agreement PerovSAMs No. 747599 and project INFORM (grant 675867), the Spanish Ministry of Economy and Competitiveness (MINECO) via the Unidad de Excelencia María de Maeztu MDM-2015-0538, MAT2017-88821-R and PCIN-2015-255 and the Generalitat Valenciana (Prometeo/2016/135 and GRISOLIAP/2017/089).

Y. El Ajjouri, F. Palazón, M. Sessolo and H. J. Bolink, Single-Source Vacuum Deposition of Mechano-synthesized Inorganic Halide Perovskites. *Chem. Mater.*, **2018**, 30 (21), 7423-7427. [IF: 10.159 (2018), Q1]

## Chapter 8

# General conclusions and outlook

The general aim of this doctoral thesis was the development and the investigation of the fundamental characteristics of perovskites and related materials via a solvent-free mechanochemical route. Furthermore, with the interest in the implementation of these high-purity semiconductors in optoelectronics, the thesis also covered the investigation of a novel manner for the fabrication of thin film perovskites via single-source vacuum deposition of mechanochemically-synthesized perovskite powders.

According to the aims described in Chapter 1, the goal of the first presented publication (Chapter 3) was the identification of the optimal solvent-free mechanochemical synthesis conditions for inorganic CsPbBr<sub>3</sub> [192]. In this study, the beneficial and detrimental effects of ball-milling on the phase-purity evolution, morphology and optical characteristics of the formed material were reported as a function of the ball-milling time. This is a topic of interest since little was known about the reaction kinetics, the formation of intermediate species and the effects of ball-milling on the size and shape of the final particles. During the ball-mill process three stages were identified: (1) At short milling times ( $t < 5$  min), there is a coexistence and interconversion of the three Cs-Pb-Br ternary phases known to be stable: CsPb<sub>2</sub>Br<sub>5</sub>, CsPbBr<sub>3</sub> and Cs<sub>4</sub>PbBr<sub>6</sub>. Herewith, it is noted that the CsBr-rich phase (Cs<sub>4</sub>PbBr<sub>6</sub>) is consistently observed in all intermediate samples. This may be associated to a lower formation energy for this compound. Furthermore, photoluminescence from “nano” and “bulk” CsPbBr<sub>3</sub> species is observed, centered at 525 nm and 545 nm, respectively. (2) For the present case, an optimum ball-milling time of 5 minutes exists; this is where the complete transformation of all the reactants and byproducts into phase-pure CsPbBr<sub>3</sub> has occurred. It is demonstrated that the derived material has a narrow and intense PL corresponding to “bulk” CsPbBr<sub>3</sub>. (3) At prolonged ball-milling times (up to 10 hours), smaller quantum-confined CsPbBr<sub>3</sub> nanocrystals are exfoliated from the bulk product, leading to a broad and blue-shifted emission. Furthermore, this phenomenon comes along with a reduction in the photoluminescence intensity, which is ascribed to the formation of surface defects induced by ball-milling under dry and additive-free conditions. As such, the mechanochemical synthesis of fully inorganic lead halide perovskites via ball-milling is a simple, dry and fast (5 min) process that leads to excellent phase-purity.

The aim of the publication presented in Chapter 4 was the investigation of multi-cation inorganic perovskites via solvent-free mechanochemistry [95]. The ion-replacement and passivation with potassium halide salts in the mechanochemical synthesis of inorganic perovskites was presented. The dry mechanochemical synthesis reported showed to be an ideal preparation method, as it does not involve solvents and can eliminate the need of thermal treatments to foster the perovskite crystallization. It was shown that incorporating potassium halides in the mechanochemical synthesis of inorganic cesium lead halide perovskites leads to several chemical, structural and optical effects. First of all, potassium partly replaces cesium in the APbBr<sub>3</sub> perovskite structure. Second, the potassium salt can also act as a source of hetero-anions to tune the bandgap of the resulting perovskite. Third, the KPb<sub>2</sub>X<sub>5</sub> phase forms concomitantly with the perovskite phase. This phase may act as a surface passivation layer as

longer photoluminescence lifetimes are observed on samples with added KBr with respect to pure CsPbBr<sub>3</sub>. These findings will aid to further optimize thin film perovskite-based devices such as LEDs and solar cells that recently have shown beneficial effects of incorporating potassium halides.

The goal of the publication presented in Chapter 5 was the attempt to develop Sn(II) and Sn(IV) iodide perovskites via a mechanochemical route. Subsequently, their structural, chemical, thermal, optical and electrical properties were studied [23]. Hybrid and inorganic pure-tin and mixed tin-lead iodide perovskites, as well as vacancy-ordered perovskites were successfully synthesized with excellent phase-purity, as revealed by XRD. Detailed thermal stability studies were carried out revealing that all compounds are stable up to 200 °C, which is compatible with common operational conditions in optoelectronic devices. Sn(II)-based inorganic perovskites were found to be stable beyond 400 °C, making them suitable candidates for single-source thermal deposition into thin films. Indeed, these compounds show a narrow bandgap suited for photovoltaic devices and NIR light-emitting diodes. The charge carrier mobility was found to be rather low, which could be due to oxidation during the long ball-milling mechanochemical synthesis. However, it was demonstrated that the dark carrier conductivity in organic 3D Sn(II)-based compounds can be improved by the addition of Pb(II) and/or SnF<sub>2</sub> during synthesis. An outlook of this study might be the optimization of the preparation conditions; especially reducing the grinding time to an ideal duration that will ensure a complete synthesis while avoiding possible detrimental effects.

The aim of the publication presented in Chapter 6 was the investigation of lead-free perovskite-related semiconductors and the attempt to tune the visible photoluminescence at room temperature by applying compositional engineering of mechanochemically-synthesized low-dimensional, lead-free halide semiconductors [16]. The publication reports on the successful mechanochemical synthesis of fifteen different low-dimensional, non-toxic bismuth halide ternary compounds (A<sub>3</sub>Bi<sub>2</sub>X<sub>9</sub>; AX:BiX<sub>3</sub> (3:2) with A = Cs<sup>+</sup>, K<sup>+</sup>, Rb<sup>+</sup>, MA or FA and X = Cl<sup>-</sup>, Br<sup>-</sup> or I<sup>-</sup>), following a solvent-free route. Structural characterization by X-ray diffraction revealed the excellent quality of the thus-formed materials, without noticeable unreacted precursors or byproducts. Furthermore, this study has successfully shown the ability of tuning the visible photoluminescence at room temperature by applying compositional engineering of lead-free, low-dimensional halide semiconductors. Hence, semiconducting materials with useful bandgaps for lighting applications – as they cover most of the visible spectrum – were obtained. Moreover, dry bulk Cs<sub>3</sub>Bi<sub>2</sub>Br<sub>9</sub> and Cs<sub>3</sub>Bi<sub>2</sub>I<sub>9</sub> exhibit photoluminescence at room temperature, even without passivating agents. This holds promise to obtain high photoluminescence efficiency when passivating agents are added. The current results pave the way to the widespread use of these non-toxic, perovskite-related materials for lighting applications.

Finally, with the prospect of the implementation of high-purity perovskites obtained via dry mechanochemistry in optoelectronic devices, the aim of the publication presented in Chapter 7 was the fabrication of thin films via single-source vacuum deposition (SSVD) of mechanochemically-synthesized inorganic perovskite powders [107]. It was noted that in the case of SSVD of pristine mixed precursors, high-purity perovskite CsPbX<sub>3</sub> could only be obtained for X = Cl<sup>-</sup> after thermal annealing. However, when CsX and PbX<sub>2</sub> are previously ball-milled at room temperature, high-purity CsPbX<sub>3</sub> are formed. Single-source vacuum deposition of the so-formed perovskites results in much-improved films both as-prepared, as well as after thermal annealing. In this way, perovskite films with optical transitions throughout the visible spectrum from around 400 nm (X = Cl<sup>-</sup>) to around 700 nm (X = I<sup>-</sup>) could be obtained. As such, it was demonstrated that single-source vacuum deposition of ball-milled perovskites represents an easy, fast and dry process to form high-quality thin films of fully inorganic perovskites. Future work of interest might focus on the implementation of these films into different optoelectronic devices – such as light-emitting diodes or solar cells – where it will be crucial to avoid chemical impurities and to finely control the film morphology.

Hence, the solvent-free mechanochemical route for perovskite (and related materials) synthesis and the subsequent single-source vacuum deposition thereof for the development of thin films are believed to contribute to advancements in the field of perovskite optoelectronics.

# Chapter 9

## Resumen en castellano

### 9.1 Introducción

Hoy en día, existe una investigación muy activa sobre materiales semiconductores para el desarrollo de dispositivos optoelectrónicos. Estos son dispositivos que convierten la energía eléctrica en luz o viceversa. Entre otros, esto se refiere a las aplicaciones en fotovoltaica (células solares), donde la luz solar se utiliza para la producción de electricidad, así como a la emisión de luz a través de diodos electroluminiscentes (LEDs, por sus siglas en inglés), que se pueden implementar en dispositivos tecnológicos inteligentes, como dispositivos electrónicos portátiles, teléfonos inteligentes y pantallas.

#### 9.1.1 Semiconductores

##### Perovskitas de halogenuros metálicos

Durante la última década, se ha desarrollado un gran interés por las perovskitas de haluro metálico como material semiconductor activo en dispositivos optoelectrónicos, debido a sus prometedoras propiedades ópticas y electrónicas. El término “perovskita” proviene del nombre dado históricamente al titanato de calcio ( $\text{CaTiO}_3$ ) [1] y se aplica por extensión a una familia de compuestos que comparten su misma estructura cristalina (véase la Figura 1.1). La fórmula química general de las perovskitas es  $\text{ABX}_3$ , donde  $A$  y  $B$  son cationes monovalentes y divalentes respectivamente y  $X$  es un anión monovalente. Aquí nos interesamos particularmente a las perovskitas de haluro, y más precisamente a aquellas donde  $X$  es  $\text{I}^-$ ,  $\text{Br}^-$  o  $\text{Cl}^-$ .

Para obtener una estructura perovskita (cúbica) estable, el catión  $A$  debe insertarse en las cavidades creadas por la red inorgánica de octaedros de  $[\text{BX}_6]^{4-}$  (véase la Figura 1.1), lo cual impone ciertas restricciones en los radios iónicos de los tres elementos. El factor de tolerancia de Goldschmidt ( $t$ ), definido en la ecuación 9.1 (donde  $r_A$ ,  $r_B$  y  $r_X$ , respectivamente, representan los radios iónicos del catión  $A$ , metal  $B$  y anión  $X$ ) proporciona un indicador de la estabilidad de la estructura. En general,  $t$  debe estar comprendido entre 0.8 y 1 para obtener una perovskita estable [2, 3]

$$t = \frac{r_A + r_X}{\sqrt{2}(r_B + r_X)} \quad (9.1)$$

Cesio ( $\text{Cs}^+$ ), metilamonio ( $\text{MA}/\text{CH}_3\text{NH}_3^+$ ) y formamidinio ( $\text{FA}/\text{CH}(\text{NH}_2)_2^+$ ) son cationes comúnmente empleados para formar perovskitas de haluro tridimensionales (3D)  $\text{ABX}_3$  estables. La figura 1.2 muestra el factor de tolerancia de las perovskitas de haluro de plomo (LHP, por sus siglas en inglés) en función del radio iónico del catión ( $r_A$ ).

Como se mencionó anteriormente, una de las razones de la gran popularidad de las perovskitas de haluro metálico se basa en sus atractivas propiedades fotofísicas. Estas características incluyen un alto coeficiente de absorción óptica, un espectro estrecho de fotoluminiscencia (PL), así como un alto rendimiento cuántico de fotoluminiscencia (PLQY). Además, al variar la composición de la perovskita, se puede cambiar la energía de banda prohibida desde la región ultravioleta

cercana a la infrarroja cercana (NIR). Estos cambios en la energía de banda prohibida se pueden obtener sustituyendo o mezclando cualquiera de los tres iones de las perovskitas. Esto explica el gran interés que hay en el desarrollo de formulaciones complejas de perovskitas [2, 15–17, 19–30]. Para ilustrar el efecto de la modificación del haluro sobre las características ópticas del material semiconductor, tomemos como ejemplo el trihaluro de plomo de cesio ( $\text{CsPbX}_3$ ). La Figura 1.3 muestra claramente la disminución de la banda prohibida con el aumento del tamaño del anión. Esta observación se explica por los orbitales moleculares de la estructura de perovskita. Mientras que la banda de conducción está determinada principalmente por los orbitales p del plomo, la banda de valencia resulta de los orbitales de antienlace provenientes de la hibridización de los orbitales s del plomo y p del haluro [31–34]. Por lo tanto, el intercambio de haluros de  $\text{I}^-$  a  $\text{Br}^-$  a  $\text{Cl}^-$  da como resultado un máximo de la banda de valencia (VBM) más profundo como se representa en la Figura 1.3 by así aumenta la anchura de banda prohibida.

### Otros haluros metálicos multinarios

Partiendo de la perovskita cúbica  $\text{ABX}_3$  tal y como está representada en la figura 1.4, distintas modificaciones de los cationes  $A$  y  $B$  pueden llevar a diferentes estequiometrías y estructuras cristalinas.

Las perovskitas ordenadas por vacantes son estructuras cristalinas donde el catión  $B$  se reemplaza parcialmente por una vacante [36]. Tales perovskitas ordenadas por vacantes incluyen  $\text{Cs}_2\text{SnI}_6$  (véase la tercera publicación), donde la mitad de los cationes  $B$  están ocupados por  $\text{Sn(IV)}$  y la otra mitad por vacantes (Figura 1.4a). También los metales trivalentes, como  $\text{Bi(III)}$  pueden formar perovskitas ordenadas por vacantes (véase la cuarta publicación). Sin embargo, en este caso, los sitios  $B$  no se dividen por igual entre el metal y las vacantes. Por el contrario, estos sitios están ocupados en una proporción de 2:1, lo que resulta en una estequiometría [36]  $\text{A}_3\text{B}_2\text{X}_9$ . Estas estructuras cristalinas forman una capa bidimensional (2D) de  $\text{BX}_6$  octaedros, donde las vacantes se ordenan a lo largo de los planos [111] (Figura 1.4b). Cabe señalar que no todas las estequiometrías  $\text{A}_3\text{B}_2\text{X}_9$  dan lugar a una fase de perovskita ordenada por vacante. Por ejemplo, se sabe que  $\text{Cs}_3\text{Bi}_2\text{I}_9$  (véase la cuarta publicación) se cristaliza en una fase que no es de perovskita. Este fenómeno está relacionado con el factor de tolerancia Goldschmidt, que indica la estabilidad geométrica de la perovskita [37–39]. Como se indicó anteriormente, los cationes del sitio  $A$  que son demasiado pequeños o demasiado grandes para la red de halogenuros metálicos hacen que el marco de perovskita de haluro colapse [343]. En el caso de  $\text{Cs}_3\text{Bi}_2\text{I}_9$ , la estructura está compuesta de dímeros de  $\text{BiI}_6$  separados por cationes  $\text{Cs}^+$  (Figura 1.4c) [41]. Además de la estequiometría  $\text{A}_3\text{B}_2\text{X}_9$ , también la estequiometría  $\text{ABX}_3$  puede dar lugar a estructuras que no son de perovskita, como es el caso por ejemplo de  $\text{CsPbI}_3$  o  $\text{RbPbBr}_3$  (Figura 1.4d).

También existen otras fases de haluros metálicos ternarios como  $\text{Cs}_4\text{PbX}_6$  o  $\text{CsPb}_2\text{X}_5$  (véase la primera publicación) que ocasionalmente han sido llamadas “perovskitas de baja dimensionalidad”, aunque ese nombre es impropio ya que no pueden considerarse perovskitas, dadas las grandes diferencias en sus estructuras cristalinas (Figura 1.4e y Figura 1.4f) [36, 44].

## 9.2 Síntesis mecanoquímica de semiconductores

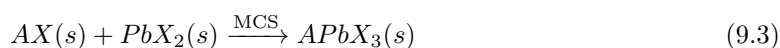
Se entiendo por mecanoquímica el uso de energía mecánica para provocar reacciones químicas. La síntesis mecanoquímica (MCS) puede llevarse a cabo de distintas formas como por molienda manual con mortero o por molino de bolas eléctrico [54]. En esta tesis doctoral, he realizado la síntesis mecanoquímica en seco de perovskitas de haluro de plomo, así como otros haluros metálicos multinarios (sin plomo), por molienda en molino de bolas. En esta técnica se utilizan bolas de un material de alta dureza (en este caso óxido de circonio) introducidas en un tarro cerrado herméticamente con los reactivos en polvo. La agitación de esas bolas dentro del tarro a cierta frecuencia puede provocar la reducción de tamaño de los reactivos (acción puramente mecánica), pero también la síntesis de nuevos compuestos (AB) a partir de los precursores (A y B) según la



reacción 9.2.



Hasta la fecha, el mecanismo exacto detrás de la MCS no se ha aclarado por completo. Sin embargo, se acepta comúnmente que la reducción en el tamaño de partícula inducida por la molienda conduce a la exposición continua de nuevas superficies reactivas que favorecen la finalización de la reacción química deseada [54]. La síntesis mecanoquímica ofrece una serie de ventajas sobre las técnicas clásicas de síntesis por disolución. Efectivamente, al evitar el uso de disolventes orgánicos se limita en gran parte la cantidad de residuos tóxicos, por lo que la MCS se puede considerar como un proceso de química verde. Además, la MCS en seco permite un mayor rango y control sobre la estequiometría ya que no intervienen las diferentes solubilidades de los reactivos. Esta técnica también es fácilmente escalable para la producción de grandes cantidades de material de una manera económica. En el caso de la MCS de perovskitas de haluro de plomo, la reacción 9.2 puede reescribirse de acuerdo a la reacción 9.3, donde  $A$  representa el catión monovalente (comúnmente metilamonio, formamidinio o cesio) y  $X$  el anión haluro monovalente (comúnmente  $I^-$ ,  $Br^-$  o  $Cl^-$ ).



Si bien es cierto que la molienda en seco puede provocar un aumento de los defectos estructurales, las perovskitas de haluro de plomo son generalmente consideradas materiales “tolerante a defectos”, en el sentido de que muchos de estos defectos cristalinos no introducen trampas profundas en la banda prohibida de energía y por lo tanto se consideran benignos desde el punto de vista optoelectrónico. Además, se ha demostrado que las perovskitas de haluro de plomo derivadas mecanoquímicamente tienen una estabilidad superior durante largos períodos de tiempo [87, 88]. Por lo tanto, la MCS representa un método muy atractivo para el estudio y la producción de estos materiales.

Para investigar el proceso de MCS, la primera publicación [192] de esta tesis estudia en detalle en función del tiempo el resultado de la molienda de CsBr y PbBr<sub>2</sub> para la obtención de CsPbBr<sub>3</sub>, tomado como modelo de perovskita de haluro inorgánica.

### 9.3 De material en polvo a capa delgada: procesamiento y aplicaciones de haluros metálicos multinarios sintetizados por vía mecanoquímica

La fabricación de películas delgadas es importante para el desarrollo de dispositivos optoelectrónicos. En esta tesis presento la deposición en vacío con fuente única (SSVD, por sus siglas en inglés) como una forma novedosa de fabricar películas delgadas a partir de perovskitas derivadas de la mecanoquímica. La SSVD representa una alternativa interesante a la co-deposición de distintos precursores, debido a su simplicidad y velocidad [187, 188]. A continuación describo en mayor profundidad la síntesis mecanoquímica y posterior SSVD de distintos haluros metálicos.

### 9.4 Objetivo y visión general de la tesis

En la última década, las perovskitas de haluro de plomo, así como otros haluros metálicos multinarios, incluidas las alternativas sin plomo, han demostrado ser materiales prometedores para su uso en optoelectrónica. Por lo tanto, se buscan activamente nuevas formas de producir dichos semiconductores de alta pureza a gran escala. La síntesis mecanoquímica ha surgido recientemente como un método altamente conveniente y reproducible para obtener perovskitas de haluro de plomo de alta calidad, así como otros haluros metálicos multinarios sin plomo. En esta tesis se estudian distintas propiedades de las perovskitas y materiales relacionados obtenidos a través de una ruta mecanoquímica en seco. Además, se desarrolla también la deposición de dichos materiales en capa fina a través de un proceso novedoso de deposición en vacío con fuente única.

Primero, la metodología experimental general se explicará en la sección de métodos. Posteriormente, se detallarán cuatro trabajos de investigación que corresponden a cinco artículos publicados en revistas internacionales [16, 95, 107, 192, 192], que también se pueden encontrar como apéndices (Apéndices A-E).

La primera publicación se centra en la investigación sistemática de la síntesis mecanoquímica en seco de  $\text{CsPbBr}_3$ . La evolución de la pureza, morfología y las características ópticas del material se detallan en función del tiempo de síntesis [192].

En la segunda publicación se investigan las perovskitas inorgánicas de múltiples cationes a través de la mecanoquímica [95]. Se presentará el reemplazo de iones y la pasivación con haluros de potasio en la síntesis mecanoquímica de perovskitas inorgánicas.

La tercera publicación presenta la síntesis mecanoquímica de las perovskitas de yoduro de Sn(II) y Sn(IV) y el estudio de sus propiedades estructurales, químicas, térmicas, ópticas y eléctricas. El estaño divalente se considera la alternativa más directa al plomo (tóxico), teniendo en cuenta las similitudes en la configuración electrónica y radio iónico. Un problema que surge con el uso de Sn(II) es que puede oxidarse fácilmente a Sn(IV). Se discutirán dos soluciones a este problema: (1) limitar la oxidación mediante el uso de aditivos, como  $\text{SnF}_2$  y (2) explorar las propiedades de los materiales basados en Sn(IV).

La cuarta publicación presenta la síntesis mecanoquímica de compuestos ternarios de haluro de bismuto de baja dimensión y no tóxicos ( $\text{A}_3\text{Bi}_2\text{X}_9$ ) [16].

Finalmente, para la posible implementación de perovskitas de alta pureza obtenidas mediante mecanoquímica seca en dispositivos optoelectrónicos, en el capítulo 9, la quinta publicación presenta la deposición en vacío con fuente única de perovskitas de haluro inorgánico derivadas mecanoquímicamente para la fabricación de películas delgadas [107].

## 9.5 Metodología

En esta tesis he sintetizado distintos materiales por molienda de bolas de los precursores en nitrógeno seco. Para mayor simplicidad, tomaremos a continuación un ejemplo genérico de síntesis de perovskita  $\text{ABX}_3$ , donde  $A$  es un catión monovalente,  $B$  un catión divalente y  $X$  un haluro. Los precursores  $\text{AX}$  y  $\text{BX}_2$  en polvo se mezclan en cantidades estequiométricas (típicamente 3 gramos de masa total) en una caja seca en nitrógeno (Figura 2.1; Paso 1). La mezcla se introduce en dos tarros de molienda de óxido de circonio de 10 ml, junto con el medio de molienda, que son dos bolas de óxido de circonio de 10 mm de diámetro en cada tarro (Figura 2.1; Paso 2). Los tarros se cierran herméticamente para trasladarlos al molino de bolas, que está fuera de la caja seca (Figura 2.1; Pasos 3 y 4). Finalmente, la molienda se realiza con un molino de bolas de agitación MM-400 de Retsch a una frecuencia de 30 Hz durante un cierto tiempo que varía de un trabajo a otro y será especificado en cada uno de los capítulos (2.1; Paso 5). Al finalizar el procedimiento de molienda, los frascos se transfieren a una caja de guantes con nitrógeno (Figura 2.1; Pasos 6 y 7), donde se separan de los materiales en polvo obtenidos (Figura 2.1; Paso 8). Así, los materiales nunca están expuestos al aire. Para caracterizar los compuestos en polvo por difracción de rayos X, absorbancia UV/VIS y PL, se preparan las muestras colocando el polvo en sustratos de vidrio recubiertos con cinta adhesiva de doble cara (Figura 2.1; Paso 9).

## 9.6 Síntesis mecanoquímica de perovskitas de haluro inorgánico: evolución de la pureza de fase, morfología y fotoluminiscencia

### 9.6.1 Introducción

La síntesis mecanoquímica (MCS) ha surgido recientemente como un método alternativo, conveniente y reproducible para obtener perovskitas y otros haluros metálicos multinarios [15–17, 20, 23, 47, 59, 70, 94, 96, 98, 107, 108, 115, 134, 219]. Sin embargo, se sabe poco sobre la cinética de reacción, la formación de especies intermedias y los efectos de la molienda de bolas en el tamaño y la forma de las partículas finales. Además, surgen preguntas sobre la formación de defectos que pueden afectar las propiedades optoelectrónicas del producto final. Este estudio presenta una investigación sistemática de la MCS de  $\text{CsPbBr}_3$ , donde los efectos beneficiosos y perjudiciales de la molienda de bolas en la evolución de la pureza de fase, la morfología y las características ópticas de los materiales formados se informan en función del tiempo de molienda de bolas.

Este trabajo fue publicado en *Journal of Materials Chemistry C* [192]. El artículo completo de la revista se puede encontrar en el Apéndice A.

### 9.6.2 Método experimental

La perovskita  $\text{CsPbBr}_3$  fue sintetizada por molienda en seco de  $\text{CsBr}$  y  $\text{PbBr}_2$  por distintos tiempos (0.5, 1, 2, 3, 4, 5, 30, 60 y 600 min) tal y como está detallado en el apartado de metodología general de este resumen.

### 9.6.3 Resultados y conclusiones

En este estudio (presentado íntegramente en el apéndice A), la síntesis mecanoquímica de  $\text{CsPbBr}_3$  se investigó en función del tiempo de molienda. Los análisis estructurales (XRD), morfológicos (SEM) y ópticos (PL) revelan varios efectos beneficiosos y perjudiciales de la molienda. En particular, durante el proceso se identifican tres etapas:

1. En tiempos de molienda cortos ( $t < 5$  min), existe una coexistencia e interconversión de las tres fases ternarias conocidas:  $\text{CsPb}_2\text{Br}_5$ ,  $\text{CsPbBr}_3$  y  $\text{Cs}_4\text{PbBr}_6$ . Además, se observa fotoluminiscencia característica de especies  $\text{CsPbBr}_3$  “nano” y “bulk”, centradas a 525 nm y 545 nm, respectivamente. Esto demuestra una gran polidispersidad en tamaño de las partículas formadas.
2. Para el presente caso, existe un tiempo óptimo de molienda de bolas de 5 minutos; Aquí es donde se ha producido la transformación completa de todos los reactivos y sub-productos en la fase deseada  $\text{CsPbBr}_3$ . Además, la fotoluminiscencia presenta un único pico estrecho e intenso correspondiente a  $\text{CsPbBr}_3$  “bulk”.
3. Si se continua la molienda, se exfolian nanocristales (NC) de  $\text{CsPbBr}_3$  lo que conduce a una emisión amplia y desplazada hacia el azul por el confinamiento cuántico. Además, este fenómeno viene junto con una reducción en la intensidad de fotoluminiscencia, que se atribuye a la formación de defectos superficiales inducidos por el molino de bolas en condiciones secas y sin aditivos.

Para concluir, la síntesis mecanoquímica de las perovskitas de haluro de plomo completamente inorgánicas mediante molienda de bolas es un proceso simple, completamente seco y rápido (5 min) que conduce a una excelente pureza de fase. Esto allana el camino para un uso más generalizado de la mecanoquímica para la síntesis de perovskitas de haluro, como se presentará en las siguientes publicaciones.

## 9.7 Incorporación de haluros de potasio en la mecano-síntesis de perovskitas inorgánicas: factibilidad y limitaciones del reemplazo de iones y pasivación de trampas

### 9.7.1 Introducción

El potasio se ha utilizado recientemente como aditivo en perovskitas, con diferentes conclusiones [98, 117, 182, 232–235]. Las discrepancias que existen en la literatura sobre cómo el potasio interactúa con la perovskita pueden originarse en los diferentes procesos de cristalización de perovskita utilizados, lo que puede dar como resultado una morfología, pureza o estequiometría diferentes del compuesto final [98, 117, 182, 232–235]. Por lo tanto, la síntesis mecanoquímica seca es un método de preparación ideal, ya que no involucra solventes y puede eliminar la necesidad de tratamientos térmicos para fomentar la cristalización de la perovskita. En este trabajo se sintetizaron mecanoquímicamente diferentes perovskitas de haluro inorgánicas por molienda en seco de mezclas equimolares de  $\text{PbBr}_2$  y  $\text{ABr}$ , donde  $\text{A} = \text{Cs}$  o  $\text{A} = \text{K}_{0.2}\text{Cs}_{0.8}$ . Finalmente, se estudiaron las perovskitas de aniones mixtos reemplazando el bromuro de potasio ( $\text{KBr}$ ) por  $\text{KX}$  ( $\text{X} = \text{Cl}^-$  o  $\text{I}^-$ ), mientras se mantenían  $\text{CsBr}$  y  $\text{PbBr}_2$  como precursores en la síntesis mecanoquímica.

Este trabajo fue publicado en RSC Advances [95]. El artículo completo de la revista se puede encontrar en el Apéndice B.

### 9.7.2 Método experimental

Los materiales fueron sintetizados por molienda en seco durante 5 horas, según el proceso descrito previamente en la metodología general.

### 9.7.3 Resultados y conclusiones

En este trabajo mostramos que la incorporación de haluros de potasio en la síntesis mecanoquímica de las perovskitas de haluro de plomo y cesio produce varios efectos químicos, estructurales y ópticos. En primer lugar, el potasio reemplaza en parte al cesio en la estructura de perovskita  $\text{APbBr}_3$  tal y como lo indica el desplazamiento de los picos de difracción hacia ángulos más altos. Efectivamente, el menor radio iónico de  $\text{K}^+$  respecto a  $\text{Cs}^+$  explica la reducción de las distancias interatómicas, lo que se traduce según la ley de Bragg en unos picos de difracción a ángulos mayores. En segundo lugar, las sales de potasio también pueden actuar como una fuente de hetero-aniones para modular la energía de banda prohibida de la perovskita resultante, lo cual se observa por un desplazamiento hacia el rojo (con introducción de yoduro de potasio) o hacia el azul (con introducción de cloruro de potasio) de los espectros de absorbancia y fotoluminiscencia. En tercer lugar, observamos la formación de la fase  $\text{KPb}_2\text{X}_5$  como impureza identificada por sus picos de difracción característicos (en particular alrededor de  $11,7^\circ$ ). Esta fase puede actuar como una capa de pasivación superficial a la perovskita, ya que esta demuestra tiempos de vida de fotoluminiscencia más largos. Estos resultados ayudarán a optimizar los dispositivos basados en perovskita de película delgada como los LED y las células solares que recientemente han mostrado efectos beneficiosos al incorporar haluros de potasio.

## 9.8 Síntesis mecanoquímica de las perovskitas de yoduro de Sn(II) y Sn(IV) y estudio de sus propiedades estructurales, químicas, térmicas, ópticas y eléctricas

### 9.8.1 Introducción

Investigaciones previas realizadas sobre perovskitas de yoduro de plomo han demostrado que estos semiconductores tienen excelentes propiedades fotovoltaicas y electroluminiscentes [73, 74]. Sin embargo, en parte debido a la toxicidad de los iones  $Pb_2^+$ , se están investigando otras perovskitas de haluro metálico. Así pues, el estaño divalente se considera la alternativa más directa al plomo, considerando sus similitudes en cuanto a configuración electrónica (grupo 14 en la tabla periódica) y radio iónico [245–247, 247–273]. Además, las perovskitas mixtas de yoduro de estaño y plomo (Sn-Pb) poseen una energía de banda prohibida menor que las Pb y Sn puras, con aplicaciones en células solares en unión simple y en tándem [274]. Un problema que surge con el uso de Sn(II) es que puede oxidarse fácilmente a Sn(IV). Existen dos soluciones para este problema: (1) limitar la oxidación mediante el uso de aditivos, como  $SnF_2$  [250, 254, 272, 275] o (2) explorar las propiedades de materiales a base de Sn(IV) [276–287]. Efectivamente, los compuestos de tipo  $A_2B(IV)X_6$  –  $A$  siendo el catión monovalente,  $B$  el metal divalente y  $X$  el anión haluro – pueden verse como una estructura similar a la perovskita  $AB(II)X_3$ , donde se eliminan uno de cada dos octaedros  $BX_6$  y el metal  $B$  está en el estado de oxidación +4 para garantizar la neutralidad de carga (Figura 5.1).

En este estudio, he sintetizado las perovskitas  $CsSnI_3$ ,  $FASnI_3$ ,  $Cs(PbSn)I_3$  y  $FA(PbSn)I_3$  además, de las perovskitas ordenadas por vacante basadas en Sn(IV)  $Cs_2SnI_6$  y  $FA_2SnI_6$ . También he investigado la influencia de  $SnF_2$ , como aditivo en la síntesis. Las características elementales, químicas y estructurales de los compuestos preparados se investigaron mediante difracción de rayos X. La estabilidad térmica se estudió mediante análisis térmico diferencial y termogravimetría (DTA/TGA). Finalmente, la movilidad y tiempo de vida de los portadores de carga de perovskitas basadas en Sn(II) y Sn(IV) se evaluó mediante conductividad de microondas resuelta en el tiempo (PR-TRMC).

Este trabajo fue publicado en Energy Technology [23]. El artículo completo de la revista se puede encontrar en el Apéndice C.

### 9.8.2 Método experimental

Los materiales fueron sintetizados por molienda en seco durante 5 horas, según el proceso descrito previamente en la metodología general.

### 9.8.3 Resultados y conclusiones

Las perovskitas híbridas orgánicas-inorgánicas así como las puramente inorgánicas, tanto basadas en Sn(II) como en Sn(IV) fueron sintetizadas con éxito con una excelente pureza de fase, como revela el análisis de XRD. Se llevaron a cabo estudios detallados de estabilidad térmica que revelaron que todos los compuestos son estables hasta 200 °C, lo cual asegura que estos materiales sean compatibles con el funcionamiento de la mayoría de los dispositivos optoelectrónicos. Se descubrió que las perovskitas inorgánicas basadas en Sn(II) eran estables más allá de 400 °C, lo que las hace adecuadas para la deposición térmica de una sola fuente en películas delgadas. De hecho, estos compuestos muestran una baja energía de banda prohibida (alrededor de 1.3 eV - 1.4 eV) adecuada para dispositivos fotovoltaicos y diodos emisores de luz NIR. La movilidad de los portadores de carga es generalmente bastante baja pero se demostró que la conductividad se puede mejorar mediante la adición de Pb(II) y/o  $SnF_2$  durante la síntesis.

## 9.9 Compuestos No tóxicos de baja dimensión $A_3Bi_2X_9$ sintetizados por una ruta mecanoquímica seca con fotoluminiscencia visible modulable a temperatura ambiente

### 9.9.1 Introducción

La comercialización futura de dispositivos optoelectrónicos de perovskita de última generación se ve obstaculizada por el uso de plomo tóxico y la estabilidad ambiental poco clara de los LHP. Por lo tanto, se buscan alternativas a las perovskitas de plomo. Los compuestos de haluro de Bi(III) se consideran alternativas interesantes posiblemente con la misma tolerancia a defectos que los LHP. Además, el bismuto es un elemento abundante en la Tierra, además de no ser tóxico y ser estable en condiciones ambientales [311]. El reemplazo de  $Pb_2^+$  con  $Bi_3^+$  afecta la estequiometría de los haluros metálicos ternarios. Así pues, existen compuestos de bismuto con una estequiometría “3-2-9” correspondiente a la fórmula general  $A_3Bi_2X_9$ . Uno de los principales cuellos de botella en el desarrollo de compuestos a base de haluro de bismuto reside en la escasa solubilidad de las sales de bismuto en disolventes comunes [318, 319]. En este estudio, quince compuestos diferentes con la fórmula general  $A_3Bi_2X_9$  ( $A = K^+, Rb^+, Cs^+, CH_3NH_3^+ - MA - o HC(NH_2)_2^+ - FA -$ ;  $X = I^-, Br^- o Cl^-$ ) se sintetizaron mediante síntesis mecanoquímica en seco.

Este trabajo fue publicado en Journal of Materials Chemistry C [16]. El artículo completo de la revista se puede encontrar en el Apéndice D.

### 9.9.2 Método experimental

Los materiales fueron sintetizados por molienda en seco durante 5 horas, según el proceso descrito previamente en la metodología general. En este caso, los precursores AX y  $BiX_3$  se mezclaron en proporción 3:2 para obtener compuestos con la estequiometría deseada  $A_3Bi_2X_9$ .

### 9.9.3 Resultados y conclusiones

La caracterización estructural por difracción de rayos X reveló la excelente calidad de los quince compuestos formados por síntesis mecanoquímica, sin que se hallase entre los productos restos de precursores sin reaccionar ni otros subproductos notables. La caracterización óptica reveló que las energías de banda prohibida de dichos compuestos cubren la mayor parte del espectro visible, lo que los hace especialmente prometedores para aplicaciones en iluminación. Los compuestos de cesio y bromo ( $Cs_3Bi_2Br_9$ ) y cesio y yodo ( $Cs_3Bi_2I_9$ ) resultaron tener la fotoluminiscencia más intensa, con emisiones respectivas correspondientes al verde y al rojo. Finalmente, como prueba de concepto, se fabricó una fuente de luz blanca a partir de un LED comercial azul, sobre el que una pastilla de dichos materiales mezclados con PMMA fue depositada a modo de fósforos (funcionamiento típico de las fuentes de LED blancas).

## 9.10 Deposición en vacío con fuente única de perovskitas de haluro inorgánicas mecanosintetizadas

### 9.10.1 Introducción

En este estudio se demuestra que la MCS también sirve para fabricar perovskitas que sirvan de precursores para la deposición en vacío con fuente única (SSVD) de capas delgadas. La realización de un análisis estructural y óptico detallado y sistemático permitió la caracterización de las diferentes películas delgadas, formadas por SSVD de precursores de cloruro, bromuro y yoduro a temperatura ambiente, así como durante el recocido térmico

Este trabajo fue publicado en Chemistry of Materials [107]. El artículo completo de la revista se puede encontrar en el Apéndice E.

### 9.10.2 Metodos experimentales

#### Síntesis mecanoquímica mediante molienda de bolas

Los materiales fueron sintetizados por molienda en seco durante 5 horas, según el proceso descrito previamente en la metodología general.

#### Deposición en vacío con fuente única

Para el estudio de la deposición en capa delgada de los materiales se usaron sustratos de vidrio previamente lavados con jabón, agua e isopropanol en un baño ultrasónico, seguido de un tratamiento con plasma de ozono ultravioleta. El material en polvo se introduce en un crisol cerámico (fuente) dentro de una cámara de vacío evacuada a  $10^{-6}$  mbar, con los sustratos colocados a unos 20 cm de altura por encima de la fuente. Una vez en vacío, el crisol se calienta rápidamente a alta temperatura (más alta que la temperatura de evaporación de los precursores constituyentes del material) para evitar la fusión incongruente y la sublimación de diferentes especies a diferentes temperaturas (más bajas). La evaporación se lleva a cabo hasta que no queda material en el crisol y la velocidad de deposición indicada es nula. Así, el espesor de la película puede controlarse mediante la cantidad de material introducida en la fuente térmica. Sin embargo, la relación entre el grosor de la película y la cantidad de precursor podría verse afectada por otros parámetros de procesamiento, como la distancia entre la fuente y el sustrato.

### 9.10.3 Resultados y conclusiones

En este estudio, se fabricaron películas delgadas de perovskitas de haluro de plomo y cesio completamente inorgánicas mediante deposición rápida en vacío con fuente única (SSVD). Se observa que en el caso de SSVD de precursores mixtos prístinos (sin síntesis mecanoquímica previa), la perovskita de alta pureza  $\text{CsPbX}_3$  solo se puede obtener para  $X = \text{Cl}^-$  después del recocido térmico. Sin embargo, cuando  $\text{CsX}$  y  $\text{PbX}_2$  se muelen previamente a temperatura ambiente, se forma  $\text{CsPbX}_3$  de alta pureza. La deposición en vacío con una sola fuente de las perovskitas así formadas da resultados significativamente mejores en términos de pureza y propiedades ópticas de las capas. De esta manera, se han podido obtener capas de perovskita con absorción y emisión óptica en todo el espectro visible desde alrededor de 400 nm ( $X = \text{Cl}^-$ ) hasta alrededor de 700 nm ( $X = \text{I}^-$ ). Así pues, queda demostrado que la deposición en vacío con una sola fuente de perovskitas sintetizadas por vía mecanoquímica representa un proceso fácil, rápido y seco para formar películas delgadas de alta calidad de perovskitas completamente inorgánicas. En el futuro el trabajo debería centrarse en la implementación de estas películas en diferentes dispositivos optoelectrónicos, como diodos emisores de luz o células solares, donde será crucial evitar las impurezas químicas y controlar con precisión la morfología de la capa.

## 9.11 Conclusiones generales y perspectivas

El objetivo de esta tesis doctoral ha sido la investigación de las características fundamentales de las perovskitas de haluro y materiales relacionados a través de la síntesis mecanoquímica sin disolventes. Además, dado el interés en la implementación de estos semiconductores de alta pureza en dispositivos optoelectrónicos, en esta tesis también se desarrolló un método novedoso de formación de capa fina a través de la deposición térmica en vacío con fuente única de perovskitas previamente sintetizadas por molienda en seco.

La primera publicación presentada se centró en una investigación sistemática de la síntesis mecanoquímica en seco de  $\text{CsPbBr}_3$ , donde los efectos beneficiosos y perjudiciales de la molienda con bolas sobre la pureza de fase, la morfología y las características ópticas del material formado se evaluaron en función del tiempo de síntesis [192]. Así, se identificaron tres etapas: (1) Una etapa inicial donde coexisten precursores sin reaccionar y distintas fases ternarias a parte del compuesto estequiométrico  $\text{CsPbBr}_3$ . (2) Un tiempo óptimo (alrededor de cinco minutos en este caso) donde la reacción es completa y la fotoluminiscencia es intensa y estrecha. (3) Una última etapa donde la molienda prolongada (hasta 10 horas) conlleva la exfoliación de nanocristales de perovskita que ensanchan y disminuyen la fotoluminiscencia debido a una alta densidad de defectos cristalinos.

La investigación de las perovskitas inorgánicas de múltiples cationes a través de la mecanoquímica se destacó en la segunda publicación [95], donde se presentó el reemplazo de iones y la pasivación con haluros de potasio en la síntesis mecanoquímica de perovskitas inorgánicas. La síntesis mecanoquímica seca presentada demostró ser un método de preparación ideal, ya que no implica el uso de disolventes y puede eliminar la necesidad de tratamientos térmicos para fomentar la cristalización de la perovskita. Se demostró que la incorporación de haluros de potasio en la síntesis mecanoquímica de las perovskitas inorgánicas de haluro de plomo y cesio conduce a varios efectos químicos, estructurales y ópticos. En primer lugar, el potasio reemplaza en parte al cesio en la estructura de perovskita  $\text{APbBr}_3$ . En segundo lugar, la sal de potasio también puede actuar como una fuente de hetero-aniones para modular la energía de la banda prohibida de la perovskita resultante. En tercer lugar, la fase  $\text{KPb}_2\text{X}_5$  se forma concomitantemente con la fase de perovskita. Esta fase puede actuar como una capa de pasivación superficial ya que se observan tiempos de vida de fotoluminiscencia más largos en muestras con  $\text{KBr}$  añadido con respecto a las muestras de  $\text{CsPbBr}_3$  puro. Estos resultados ayudarán a optimizar aún más los dispositivos basados en perovskita de película delgada como los LED y las células solares que recientemente han mostrado efectos beneficiosos al incorporar haluros de potasio.

La tercera publicación presentada se centró en la síntesis mecanoquímica de las perovskitas de yoduro de  $\text{Sn(II)}$  y  $\text{Sn(IV)}$  y el estudio de sus propiedades estructurales, químicas, térmicas, ópticas y eléctricas [23]. El estaño divalente se considera la alternativa más directa al plomo tóxico, teniendo en cuenta sus similitudes en cuanto a configuración electrónica radios iónico. Así pues, se sintetizaron perovskitas híbridas orgánicas-inorgánicas y puramente inorgánicas de estaño, así como perovskitas ordenadas por vacantes. Se llevaron a cabo estudios detallados de estabilidad térmica que revelaron que todos los compuestos son estables hasta  $200\text{ }^\circ\text{C}$ , y en el caso de las perovskitas inorgánicas basadas en  $\text{Sn(II)}$  hasta más allá de  $400\text{ }^\circ\text{C}$ , lo que las hace adecuadas para la deposición térmica de una sola fuente en películas delgadas. De hecho, la baja energía de banda prohibida de estos semiconductores resulta ideal para dispositivos fotovoltaicos y diodos emisores de luz NIR. A pesar de que se determinó una baja movilidad de portadores de carga, ésta mejora mediante la adición de  $\text{Pb(II)}$  y/o  $\text{SnF}_2$  durante la síntesis.

La cuarta publicación versa sobre la síntesis mecanoquímica de quince compuestos ternarios de haluro de bismuto no tóxicos de baja dimensión con la fórmula general  $\text{A}_3\text{Bi}_2\text{X}_9$  con  $\text{A} = \text{Cs}^+, \text{K}^+, \text{Rb}^+, \text{MA} \text{ o } \text{FA}$  y  $\text{X} = \text{Cl}^-, \text{Br}^- \text{ o } \text{I}^-$  [16]. La caracterización estructural por difracción de rayos X reveló la excelente calidad de los materiales formados por vía mecanoquímica. La caracterización óptica reveló que las energías de banda prohibida de dichos compuestos cubren la mayor parte del espectro visible, lo que los hace especialmente prometedores para aplicaciones



---

en iluminación. Los compuestos de cesio y bromo ( $\text{Cs}_3\text{Bi}_2\text{Br}_9$ ) y cesio y yodo ( $\text{Cs}_3\text{Bi}_2\text{I}_9$ ) resultaron tener la fotoluminiscencia más intensa, con emisiones respectivas correspondientes al verde y al rojo. Finalmente, como prueba de concepto, se fabricó una fuente de luz blanca a partir de un LED comercial azul, sobre el que una pastilla de dichos materiales mezclados con PMMA fue depositada a modo de fósforos (funcionamiento típico de las fuentes de LED blancas).

Finalmente, con la perspectiva de la implementación de perovskitas de alta pureza obtenidas a través de la mecanoquímica seca en dispositivos optoelectrónicos, en la quinta publicación se presentó la deposición en vacío con fuente única (SSVD) de perovskitas de haluro de plomo de cesio derivadas mecanoquímicamente para la fabricación de capas finas [107]. Se observó que en el caso de SSVD de precursores mixtos sin molienda previa, la perovskita de alta pureza  $\text{CsPbX}_3$  solo se podía obtener para  $\text{X} = \text{Cl}^-$  después del recocido térmico. Sin embargo, cuando  $\text{CsX}$  y  $\text{PbX}_2$  se muelen previamente a temperatura ambiente, se forma  $\text{CsPbX}_3$  de alta pureza. La deposición por SSVD de las perovskitas así formadas da como resultado capas finas mejoradas con o sin recocido térmico. De esta manera, se han podido obtener capas de perovskita con transiciones ópticas en todo el espectro visible desde alrededor de 400 nm ( $\text{X} = \text{Cl}^-$ ) hasta alrededor de 700 nm ( $\text{X} = \text{I}^-$ ). Así pues, se demostró que la SSVD de perovskitas sintetizadas por vía mecanoquímica representa un proceso fácil, rápido y seco para formar películas delgadas de alta calidad de perovskitas completamente inorgánicas. En el futuro el desarrollo de este trabajo debería centrarse en la implementación de estas películas en diferentes dispositivos optoelectrónicos, como diodos emisores de luz o células solares, donde será crucial evitar las impurezas químicas y controlar con precisión la morfología de la película.

En conclusión, los procesos en seco de síntesis mecanoquímica y deposición en vacío con fuente única de perovskitas de haluro y materiales relacionados desarrollados en esta tesis representan un avance fundamental para la fabricación y procesamiento de nuevos materiales para la optoelectrónica.



# Appendices

# Appendix A

## COMMUNICATION

## Mechanochemical Synthesis of Inorganic Halide Perovskites: Evolution of Phase-purity, Morphology, and Photoluminescence

Received 00th January 20xx,  
Accepted 00th January 20xx

Francisco Palazon,<sup>a,b\*</sup> Youstra El Ajjouri,<sup>a</sup> Paz Sebastia-Luna,<sup>a</sup> Simone Lauciello,<sup>c</sup> Liberato Manna,<sup>b</sup> and Henk J. Bolink<sup>a</sup>

DOI: 10.1039/x0xx00000x

Dry mechanochemical ball-milling of halide precursor salts is a promising route for the synthesis of high-purity halide perovskites in a fast and solvent-free manner. However, there is a lack of information on the process mechanisms, kinetics, and possible side-effects. Here, we investigated in detail the mechanochemical synthesis of fully-inorganic CsPbBr<sub>3</sub> by ball-milling of stoichiometric CsBr and PbBr<sub>2</sub>. Detailed structural, morphological and optical analyses reveal several beneficial and detrimental effects of milling as a function of time. Three stages are identified during the process: (i) At short milling times (t<5min) different ternary compounds are formed, including stoichiometric CsPbBr<sub>3</sub> as well as Cs<sub>4</sub>PbBr<sub>6</sub>, and to a lesser extent, CsPb<sub>2</sub>Br<sub>5</sub>. Photoluminescence from “nano” and “bulk” CsPbBr<sub>3</sub> species is observed, centered at 525 nm and 545 nm, respectively. (ii) At the optimum time (around 5 min for the present case) the complete transformation of all reactants and byproducts into phase-pure CsPbBr<sub>3</sub> has occurred. Photoluminescence corresponds to bulk CsPbBr<sub>3</sub>; (iii) At much longer milling times (up to 10 hours) eventually smaller quantum-confined CsPbBr<sub>3</sub> NCs are exfoliated from the bulk product leading to a broad and blue-shifted emission. At this stage the photoluminescence intensity is strongly reduced which is ascribed to the formation of surface defects induced by ball-milling in dry conditions.

One decade after their first use in photovoltaics,<sup>1</sup> lead halide perovskites (LHPs) have become very promising materials for a wide range of optoelectronic applications such as solar cells<sup>2</sup> and light-emitting diodes (LEDs).<sup>3</sup> Thus, new ways of producing high-purity LHPs in large scale are actively sought after. Mechanochemical synthesis (MCS) has recently emerged as a very convenient and reliable method to obtain high quality LHPs as well as other lead-free multinary metal halides.<sup>4,5,14–23,6–13</sup> Bulk materials have been obtained with a variety of compositions including fully-inorganic as well as hybrid organic-inorganic perovskites. MCS has been used to investigate the role of additives and dopants introduced in well-controlled small amounts.<sup>4,21,24,25</sup> Colloidal quantum dots with photoluminescence quantum yields over 80% have also been

produced by MCS.<sup>9,17,20,24,26</sup> Eventually, ternary nonperovskite metal halides such as guanidinium-based 2D and 1D structures<sup>19</sup> or bismuth-based 2D and 0D crystals<sup>22</sup> have also been produced and shown to possess promising optoelectronic properties by MCS. It is also worth noting that materials prepared by MCS can be turned into thin films by solution- or vacuum-deposition techniques, thus enabling their use in common thin-film-based devices (e.g., solar cells or LEDs).<sup>5,6,8,11,15,18,24,26–28</sup> All of these recent publications highlight the scientific and technological relevance of MCS for the study and production of LHPs and related materials. Nonetheless, there is scarce data in literature describing the process in detail. Little is known about the reaction kinetics, the formation of intermediate species (including impurities) and the effects of ball-milling on the size and shape of the final particles. The same is true about the formation of defects that can affect the optoelectronic properties of the material formed. To shed a new light on these issues, we carry out a systematic investigation of the mechanochemical synthesis of inorganic CsPbBr<sub>3</sub> by dry ball-milling of stoichiometric CsBr:PbBr<sub>2</sub> mixtures. We evaluate the crystallinity, morphology and optical properties of the formed materials as a function of ball-milling time. Because we carried out this study without any solvents or additives, in stoichiometric conditions and with well-fixed parameters in a ball-mill (i.e., not by hand grinding, where applied forces can be more variable) we expect that our results are symptomatic for the mechanochemical synthesis of halide perovskites in general.

To study the initial stages of the synthesis, stoichiometric CsBr:PbBr<sub>2</sub> mixtures were ball-milled for 0.5, 1, 2, 3, 4, and 5 minutes. High-resolution PXRD data were acquired for all samples in the range 2θ = 10° to 2θ = 90° to identify and quantify the different species formed at each time. Aside from the binary precursors CsBr and PbBr<sub>2</sub>, three different ternary compounds are known to be stable: CsPb<sub>2</sub>Br<sub>5</sub>, CsPbBr<sub>3</sub>, and Cs<sub>4</sub>PbBr<sub>6</sub>. These phases are sometimes referred to as 2D, 3D, and 0D, based on their structural dimensionality, that is, the interconnectivity of PbBr<sub>6</sub> octahedra in the crystals. Figure 1a presents a close view of the 2θ = 10° to 2θ = 20° range (see full patterns in Figure S1) where the three ternary compounds are clearly identified by peaks around 2θ = 11.7° (CsPb<sub>2</sub>Br<sub>5</sub>), 2θ = 12.7° (Cs<sub>4</sub>PbBr<sub>6</sub>) and 2θ = 15.0° (CsPbBr<sub>3</sub>), while PbBr<sub>2</sub> is identified by a peak around 2θ = 18.5°. Note that these are not the main reflections of any of the phases. However, as they occur in a close yet not-overlapping region of the diffractogram, they are the most convenient for straightforward identification. As can be seen in Figure 1a, complete reaction into stoichiometric CsPbBr<sub>3</sub> perovskite is achieved in less than 5 minutes. This highlights that

<sup>a</sup> Instituto de Ciencia Molecular, Universidad de Valencia, C/ Catedrático J. Beltrán 2, 46100 Burjassot, Spain.

<sup>b</sup> Nanochemistry Department and <sup>c</sup>Electron Microscopy Facility, Istituto Italiano di Tecnologia (IIT), Genova, Italy.

Electronic Supplementary Information (ESI) available: Experimental details and XRD. See DOI: 10.1039/x0xx00000x

simple dry ball-milling is an excellent technique to produce phase-pure perovskites in a very fast and easy manner. Indeed, in view of these results it may seem that much longer times of several hours of ball-milling as reported by us and others previously might not be needed.<sup>15,20</sup> However, we will discuss the effects of prolonged ball-milling later. Although high phase-purity is achieved in less than 5 minutes, non-stoichiometric  $\text{CsPb}_2\text{Br}_5$  and  $\text{Cs}_4\text{PbBr}_6$  is also present at intermediate stages, as previously discussed. It is worth noting that the  $\text{PbBr}_2$ -rich phase  $\text{CsPb}_2\text{Br}_5$  is only marginally seen in two of the six samples (<5% in all cases), while the CsBr-rich phase  $\text{Cs}_4\text{PbBr}_6$  is consistently observed in the all intermediate samples, reaching >20% in weight. As the synthesis is carried out under stoichiometric conditions, this fact points towards a lower formation energy for CsBr-rich phases. This is in agreement with DFT calculations which have estimated a formation energy of -1.592 eV/atom for  $\text{Cs}_4\text{PbBr}_6$  and -1.321 eV/atom for  $\text{CsPbBr}_3$ .<sup>29,30</sup>

Furthermore, the fact that the three ternary phases co-exist at short milling times and eventually convert into phase-pure stoichiometric  $\text{CsPbBr}_3$  highlights the chemical and structural versatility of these compounds. Several reports have demonstrated interconversion between these phases. However, most of these were carried out in solution and/or with different additives such as amines,<sup>31</sup>  $\text{ZnX}_2$ ,<sup>32</sup> Prussian blue,<sup>33</sup> or water.<sup>34,35</sup> Hence, it is worth noting that these interconversion reactions also take place during solid-state synthesis without any additive to mediate the reactions.

In order to obtain a semi-quantitative analysis of the different species, whole-pattern Le Bail fits were conducted (see Figure S1).<sup>36</sup> Based on these, two quantification methods were used: On one hand, the calculated intensity of the main diffraction peak of each phase was divided by the relative intensity ratio (RIR) of the corresponding phase as obtained from literature (ICSD database). On the other hand, Rietveld refinements were conducted to directly obtain relative weight fractions from the structural model. Both methods resulted in nearly identical quantification results (see solid and dotted lines in Figure 1b –weight fraction as directly obtained from PXRD quantification- and Figure 1c –molar fraction as derived from weight fraction and corresponding molecular weight of each phase-), despite slightly different pattern fits (Figure S1). Figure 1c shows that CsBr is consumed faster than  $\text{PbBr}_2$  as mostly CsBr-rich phases are formed. In fact, between  $t = 1$  min and  $t = 2$  min we observe a growth of the  $\text{Cs}_4\text{PbBr}_6 / \text{CsPbBr}_3$  ratio. This highlights once again the versatile interconversion between the different ternary phases. The different reaction mixtures were also examined by scanning electron microscopy (SEM) and energy-dispersive X-ray spectroscopy (EDX).

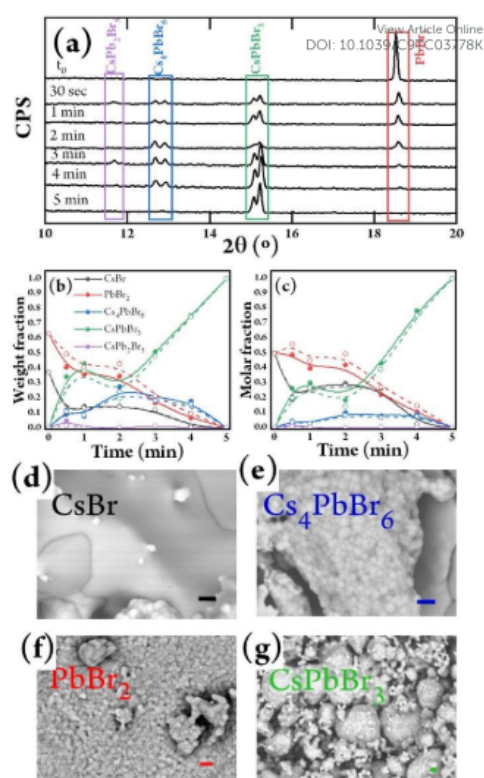


**Figure 1.** X-ray diffraction and scanning electron microscopy analysis of samples ball-milled for different times up to 5 min. (a) Close view of the  $2\theta = 10^\circ$  to  $2\theta = 20^\circ$  range (see full patterns in Figure S1) of the diffractograms where characteristic peaks of different phases are highlighted in different colors. (b) Weight fraction of different species as derived from RIR method (filled spheres and solid lines) and Rietveld refinement (open circles and dashed lines). (c) Molar fraction of different species from RIR method (filled spheres and solid lines) and Rietveld refinement (open circles and dashed lines). B-spline lines are drawn to guide the eye. (d)–(g) Scanning electron microscopy of different phases found in the samples and identified by EDX analysis. All scale bars are one micron.

Figure 1d-g presents SEM images of the four main different compounds which are identified by EDX to be CsBr (49:51 ratio by EDX),  $\text{Cs}_4\text{PbBr}_6$  (37:10:53 ratio by EDX),  $\text{PbBr}_2$  (33:67 ratio by EDX), and  $\text{CsPbBr}_3$  (22:18:60 ratio by EDX). These results are obtained by considering the high-energy lines for each element (Br(K), Cs(L), and Pb(L)). The morphology of the different phases is clearly different: CsBr is formed of large smooth crystals while  $\text{PbBr}_2$  presents a rather small-grain texture.  $\text{Cs}_4\text{PbBr}_6$  and  $\text{CsPbBr}_3$  consist of grains with different typical sizes from sub-100nm to  $>1\mu\text{m}$ .  $\text{CsPbBr}_3$  forms round-shaped aggregates of about 100 microns in size. Images presented in Figure 1d-g are selected close views of different phases identified by EDX. However, it is common to find large particles with different mixed phases. As an example, Figure 2 presents an SEM image of a large particle partly encapsulating fine-grain agglomerates. Corresponding EDX maps and selected small-area

Journal Name

spectra show that the large particle is mostly Pb-free (CsBr) and the inside smaller grains are CsPbBr<sub>3</sub>.

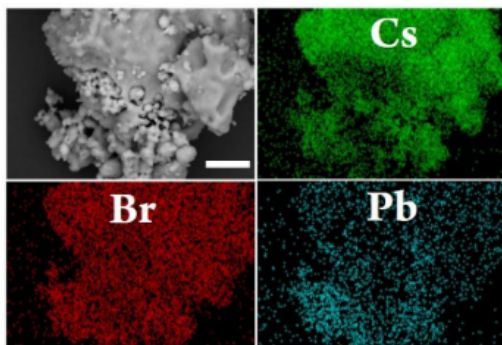


**Figure 2.** SEM image and corresponding EDX maps for Cs (green), Br (red), and Pb (blue). Scale bar is 10 microns. Two distinct materials are observed both from morphology and composition. These corresponds to CsBr (large smooth particle) and CsPbBr<sub>3</sub> (fine-grain agglomerates).

As mentioned before, several reports on mechanochemical synthesis of halide perovskites, including our own,<sup>15</sup> use ball-milling times considerably longer than 5 minutes. Hereafter we investigated the effects of prolonged ball-milling for up to 10 hours. Diffractograms of samples ball-milled for 30 min, 1h and 10 h can be fitted with a single CsPbBr<sub>3</sub> phase (see Figure S2). This suggests that after full conversion into the stoichiometric CsPbBr<sub>3</sub> phase, this perovskite 3D phase remains stable upon further ball-milling. This fact is not obvious *a priori*, as we have previously seen that interconversion between the different ternary phases can happen. However, once full conversion into CsPbBr<sub>3</sub> is achieved without remaining PbBr<sub>2</sub> or CsBr, it appears that no further structural evolutions take place under these conditions. In other words, CsPbBr<sub>3</sub> is not reverted into its initial constituents CsBr + PbBr<sub>2</sub> upon ball-milling. Nonetheless, morphological changes are observed. The XRD peaks are broadened with prolonged MCS time (see Figure S3 for a qualitative assessment of line broadening). In order to study this in detail, microstructural analysis was performed on the whole-pattern fitted diffractograms (Figure S2). This was done after calibration to take into account instrumental broadening. Williamson-Hall plots (peak integral breadth vs inverse interatomic spacing) are presented in Figure 3a, where the slope is related to microstructural strain and the extrapolated value at origin gives an average isotropic grain size. For these analyses we discarded the possibility of anisotropy as no 1D (needle-) or 2D (platelet-) shaped crystals were observed from the SEM images (Figures 1g and S4). For an easier evaluation the evolution of the apparent grain size is plotted in Figure 3b. A clear reduction in crystalline size is visible at longer milling times (t=10h). Nonetheless, it must be noted that this analysis provides an average size without information on size dispersity. Indeed, SEM images of the sample ball-milled for 10h confirm the presence of small grains (sub-100nm) but also the coexistence with larger grains up to 1 micron (see Figure S4).

COMMUNICATION

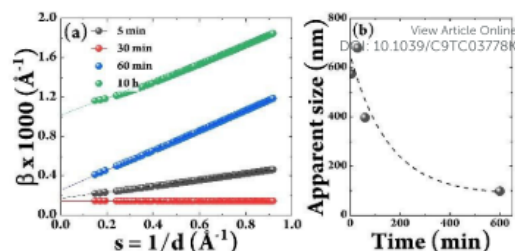


**Figure 3.** Microstructural XRD analysis. (a) Williamson-Hall (WH) plots obtained from Le Bail fits of XRD data acquired on samples ball-milled for t=5 min to t=10h (see Figure S3). Fits assume a pseudo-Voigt Thompson-Cox-Hastings (TCH) lineshape with gaussian broadening contribution from strain (slope) and lorentzian broadening contribution from reduced crystallite size (offset). (b) Apparent isotropic average crystal size deduced from extrapolated value at origin from WH plots.

To probe the evaluation of optoelectronic properties of the different powders the photoluminescence was determined by excitation with a UV laser ( $\lambda = 375$  nm) excitation (see Figure 4). Although these samples are generally not emissive enough to obtain reliable quantum yield measurements, we measured them in the same conditions (fixing the laser power, acquisition time, and sample amount) in order to get semi-quantitative results (Figure 3a). The first noticeable result is that the most-emissive samples are those that were ball-milled for short times (t<5min), whereas the samples ball-milled for longer times demonstrated significantly lower PL intensities (one to two orders of magnitude lower). This reduction in PL intensity can be explained by the formation of non-radiative trap states resulting from defects induced by ball-milling. Besides the drop in PL intensity, a broadening of the spectra is observed (Figure 4b). In the first three samples (t=30 sec, 1 min, and 2 min) which correspond to non-phase-pure synthesis as previously discussed, a dominant PL peak is observed centered at 525 nm, with a second feature centered 545 nm. These can be ascribed to weakly-quantum-confined (i.e., "nano") and bulk CsPbBr<sub>3</sub>. At t=5 min, when the synthesis is complete, only a symmetric peak corresponding to bulk CsPbBr<sub>3</sub> is present, with a narrow full-width at half maximum of 26 nm. If further ball-milling is performed, aside from the already-mentioned drop in PL intensity, the spectra become wider with a broad band at shorter wavelengths (Figure 4b). This can be ascribed to the exfoliation of small, quantum-confined CsPbBr<sub>3</sub> nanocrystals.<sup>9</sup> This observation is in agreement with the reduced average crystallite size revealed by microstructural XRD analysis (Figure 3). We note that exfoliation has been observed before upon prolonged ball-milling in the presence of solvents and ligand molecules.<sup>9</sup> Our results suggest that these are not needed to obtain these smaller, quantum-confined crystals, although they are certainly beneficial to passivate their surfaces. This would appear critical to obtain high PL intensities as in our case, (by dry ball-milling without additives) the PL emission is greatly reduced. Eventually, it must be noted that optical absorption (Figure S5) is dominated by the lower-bandgap "bulk" species in all cases.



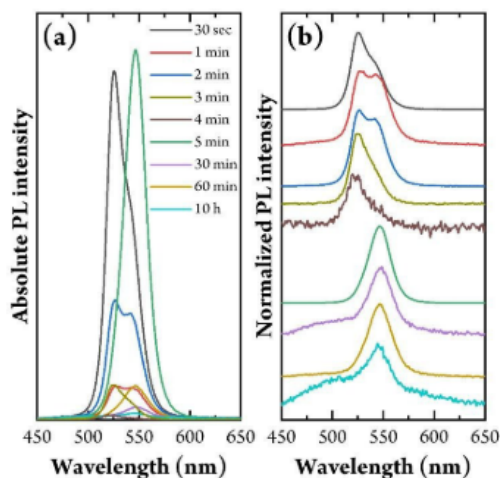


**Figure 4.** Absolute (a) and normalized (b) PL intensities of samples ball-milled for different times under identical measurement conditions (excitation source, acquisition time, and sample amount).

## Conclusions

In summary, we followed over time the mechanochemical synthesis of an archetype halide perovskite,  $\text{CsPbBr}_3$ , by dry ball-milling of stoichiometric precursors. An optimum ball-milling time exists (around 5 min for the material and ball milling system used; see experimental section for details) to obtain phase-pure 3D perovskites with narrow and intense PL emission. We believe it is important to underline that prolonged ball-milling, as has been used by us and others in the past leads to a broadening of the spectra and most importantly to an important loss of PL. From a more fundamental point of view, we have demonstrated the coexistence and interconversion of the three known ternary phases:  $\text{Cs}_4\text{PbBr}_6$ ,  $\text{CsPbBr}_3$ , and  $\text{CsPb}_2\text{Br}_5$  at short milling times. In particular, we note that the CsBr-rich phase is particularly important in the three samples obtained after ball-milling at short times. This may be associated to a lower formation energy for this compound. It is important to conclude that such a simple, fully dry, and fast (5 min) process leads to excellent phase-purity of fully-inorganic lead halide perovskites. This paves the way to a more generalized use of mechanochemistry for the synthesis of halide perovskites.

## Conflicts of interest

There are no conflicts to declare.

## Acknowledgements

The research leading to these results has received funding from the European Union Programme for Research and Innovation Horizon 2020 (2014-2020) under the Marie Skłodowska-Curie Grant Agreement PerovSAMS No. 747599, the Spanish Ministry of Economy and Competitiveness (MINECO) via the Unidad de Excelencia María de Maeztu MDM-2015-0538, MAT2017-88821-R and PCIN-2015-255, and the Generalitat Valenciana (Prometeo/2016/135 and

GRISOLIAP/2017/089). F.P. thanks Javier Castells from Universidad de Valencia and Marine Reynaud from CIC energiGUNE for guidance in the use of Fullprof suite.

## References

- 1 A. Kojima, K. Teshima, Y. Shirai and T. Miyasaka, *J. Am. Chem. Soc.*, 2009, **131**, 6050–6051.
- 2 A. K. Jena, A. Kulkarni and T. Miyasaka, *Chem. Rev.*, 2019, **119**, 3036–3103.
- 3 X. Zhao, J. D. A. Ng, R. H. Friend and Z. K. Tan, *ACS Photonics*, 2018, **5**, 3866–3875.
- 4 Y. El Ajjouri, V. S. Chirvony, M. Sessolo, F. Palazon and H. J. Bolink, *RSC Adv.*, 2018, **8**, 41548–41551.
- 5 D. Prochowicz, P. Yadav, M. Saliba, D. J. Kubicki, M. M. Tavakoli, S. M. Zakeeruddin, J. Lewiński, L. Emsley and M. Grätzel, *Nano Energy*, 2018, **49**, 523–528.
- 6 O. Y. Posudievsky, N. V. Konoshchuk, V. L. Karbivskyy, O. P. Boiko, V. G. Koshechko and V. D. Pokhodenko, *Theor. Exp. Chem.*, 2017, **53**, 235–243.
- 7 J. Breternitz, S. Levchenko, H. Hempel, G. Gurieva, A. Franz, A. Hoser and S. Schorr, *J. Phys. Energy*, 2018, **1**, 25003.
- 8 O. Y. Posudievsky, N. V. Konoshchuk, A. G. Shkavro, V. L. Karbivskiy, V. G. Koshechko and V. D. Pokhodenko, *ACS Appl. Nano Mater.*, 2018, **1**, 4145–4155.
- 9 S. Yun, A. Kirakosyan, S. G. Yoon and J. Choi, *ACS Sustain. Chem. Eng.*, 2018, **6**, 3733–3738.
- 10 M. Wilke and N. Casati, *Chem. - A Eur. J.*, DOI:10.1002/chem.201804066.
- 11 D. Prochowicz, P. Yadav, M. Saliba, M. Sasaki, S. M. Zakeeruddin, J. Lewiński, M. Grätzel, M. Saliba, M. Sasaki, S. M. Zakeeruddin, J. Lewiński, M. Grätzel, M. Saliba, M. Sasaki, S. M. Zakeeruddin, J. Lewiński and M. Grätzel, *Sustain. Energy Fuels*, 2017, **1**, 1–5.
- 12 P. Pal, S. Saha, A. Banik, A. Sarkar and K. Biswas, *Chem. - A Eur. J.*, 2018, **24**, 1811–1815.
- 13 A. M. Askar, A. Karmakar, G. M. Bernard, M. Ha, V. V. Terskikh, B. D. Wiltshire, S. Patel, J. Fleet, K. Shankar and V. K. Michaelis, *J. Phys. Chem. Lett.*, 2018, **9**, 2671–2677.
- 14 A. Karmakar, A. M. Askar, G. M. Bernard, V. V. Terskikh, M. Ha, S. Patel, K. Shankar and V. K. Michaelis, *Chem. Mater.*, 2018, **30**, 2309–2321.
- 15 Y. El Ajjouri, F. Palazon, M. Sessolo and H. J. Bolink, *Chem. Mater.*, 2018, **30**, 7423–7427.
- 16 D. J. Kubicki, D. Prochowicz, A. Hofstetter, S. M. Zakeeruddin, M. Grätzel and L. Emsley, *J. Am. Chem. Soc.*, 2018, **140**, 7232–7238.
- 17 Z.-Y. Y. Zhu, Q.-Q. Yang, L.-F. F. Gao, L. Zhang, A.-Y. Y. Shi, C.-L. L. Sun, Q. Wang and H.-L. L. Zhang, *J. Phys. Chem. Lett.*, 2017, **8**, 1610–1614.
- 18 D. Prochowicz, M. Franckevičius, A. M. Cieślak, S. M. Zakeeruddin, M. Grätzel and J. Lewiński, *J. Mater. Chem. A*, 2015, **3**, 20772–20777.
- 19 A. D. Jodlowski, A. Yépez, R. Luque, L. Camacho and G. de Miguel, *Angew. Chemie - Int. Ed.*, 2016, **55**, 14972–14977.
- 20 L. Protesescu, S. Yakunin, O. Nazarenko, D. N. Dirin and M. V. Kovalenko, *ACS Appl. Nano Mater.*, 2018, **1**, 1300–1308.
- 21 D. J. Kubicki, D. Prochowicz, A. Hofstetter, S. M. Zakeeruddin, M. Grätzel and L. Emsley, *J. Am. Chem. Soc.*,



## Journal Name

## COMMUNICATION

- 2017, **139**, 14173–14180.
- 22 Y. El Ajjouri, V. S. Chirvony, N. Vassilyeva, M. Sessolo, F. Palazon and H. J. Bolink, *J. Mater. Chem. C*, , DOI:10.1039/C9TC01765H.
- 23 Y. El Ajjouri, F. Locardi, M. C. Gélvez-Rueda, M. Prato, M. Sessolo, M. Ferretti, F. C. Grozema, F. Palazon and H. J. Bolink, *Energy Technol.*, 2019, ente.201900788.
- 24 W. Xiang, Z. Wang, D. J. Kubicki, W. Tress, J. Luo, D. Prochowicz, S. Akin, L. Emsley, J. Zhou, G. Dietler, M. Grätzel and A. Hagfeldt, *Joule*, 2019, **3**, 205–214.
- 25 M. M. Tavakoli, W. Tress, J. V. Milić, D. Kubicki, L. Emsley and M. Grätzel, *Energy Environ. Sci.*, 2018, **11**, 3310–3320.
- 26 D. Chen, J. Li, X. Chen, J. Chen and J. Zhong, *ACS Appl. Mater. Interfaces*, 2019, **11**, 10059–10067.
- 27 D. J. Kubicki, D. Prochowicz, A. Hofstetter, M. Sasaki, P. Yadav, D. Bi, N. Pellet, J. Lewiński, S. M. Zakeeruddin, M. Grätzel and L. Emsley, *J. Am. Chem. Soc.*, 2018, **140**, 3345–3351.
- 28 B. Dou, L. M. Wheeler, J. A. Christians, D. T. Moore, S. P. Harvey, J. J. Berry, F. S. Barnes, S. E. Shaheen and M. F. A. M. Van Hest, *ACS Energy Lett.*, 2018, **3**, 979–985.
- 29 K. Persson, , DOI:10.17188/1199510.
- 30 K. Persson, .
- 31 F. Palazon, G. Almeida, Q. A. Akkerman, L. De Trizio, Z. Dang, M. Prato and L. Manna, *Chem. Mater.*, 2017, **29**, 4167–4171.
- 32 S. K. Sharma, S. Mangain, B. Attarwala and A. Yella, *Nanoscale Adv.*, 2019, **00**, 1–8.
- 33 F. Palazon, C. Urso, L. De Trizio, Q. Akkerman, S. Marras, F. Locardi, I. Nelli, M. Ferretti, M. Prato and L. Manna, *ACS Energy Lett.*, 2017, 2445–2448.
- 34 X. Yu, L. Wu, H. Hu, M. Chen, Y. Tan, D. Yang, Q. Pan, Q. Zhong, T. Supasai and Q. Zhang, *Langmuir*, 2018, **6**, acs.langmuir.8b01683.
- 35 L. Wu, H. Hu, Y. Xu, S. Jiang, M. Chen, Q. Zhong, D. Yang, Q. Liu, Y. Zhao, B. Sun, Q. Zhang and Y. Yin, *Nano Lett.*, 2017, **6**, acs.nanolett.7b02896.
- 36 A. Le Bail, *Powder Diffr.*, 2005, **20**, 316–326.

View Article Online  
DOI: 10.1039/C9TC03778K

## Supporting Information

### Mechanochemical Synthesis of Inorganic Halide Perovskites: Evolution of Phase-purity, Morphology and Photoluminescence

Francisco Palazon,<sup>a,b\*</sup> Yousra El Ajjouri,<sup>a</sup> Paz Sebastia-Luna,<sup>a</sup> Simone Lauciello,<sup>c</sup> Liberato Manna,<sup>b</sup> and Henk J. Bolink<sup>a</sup>

<sup>a</sup> Instituto de Ciencia Molecular, ICMol, Universidad de Valencia, C/ Catedrático J. Beltrán 2, 46980 Paterna, Spain

<sup>b</sup> Nanochemistry Department

<sup>c</sup> Electron Microscopy Facility, Istituto Italiano di Tecnologia (IIT), Genova, Italy

#### Experimental details

##### Materials

Cesium bromide (CsBr, > 99 %) was purchased from TCI and lead(II) bromide (PbBr<sub>2</sub>, ≥ 98 %) was purchased from Sigma-Aldrich. All chemicals were stored in a nitrogen-filled glovebox and used as received without further purification.

##### Mechanochemical synthesis

Equimolar CsBr:PbBr<sub>2</sub> powders were mixed inside a nitrogen-filled glovebox. Then, approximately 3 grams of the mixed precursors powders was introduced inside 10 mL zirconia ball-mill jars with 2 zirconia beads of 10 mm in diameter per jar. The jars were closed under nitrogen so that the powders were not exposed to air. Then, ball-milling was performed with a MM-400 straight ball-mill from Retsch, at a frequency of 30 Hz for different times.

##### XRD characterization

X-ray diffraction was measured with a Panalytical Empyrean diffractometer equipped with a Cu-K $\alpha$  anode operated at 45 kV and 30 mA and a Pixel 1D detector in scanning line mode. Single scans were acquired in the  $2\theta = 10^\circ$  to  $90^\circ$  range with a step size of  $2\theta = 0.026^\circ$  in BraggBrentano geometry in air. For microstructural analysis, instrumental peak broadening was taken into account by measuring a reference silicon wafer under the same measurement conditions and refining the Thompson-Cox-Hastings pseudo-Voigt line shape parameters, used to create the instrument resolution file. All XRD analyses were carried out with Fullprof software. Whole-pattern Le Bail Fits are performed to refine cell parameters and line shape for microstructural analysis. Refined cell parameters are also used to carry out structural Rietveld refinement for quantitative analysis.

##### SEM / EDX characterization

Electron microscopy characterization (SEM and EDX) was performed using HRSEM JEOL JSM-7500L equipped with a cold field-emission gun (FEG) operating at 25 kV acceleration voltage and with an EDS Oxford instrument.

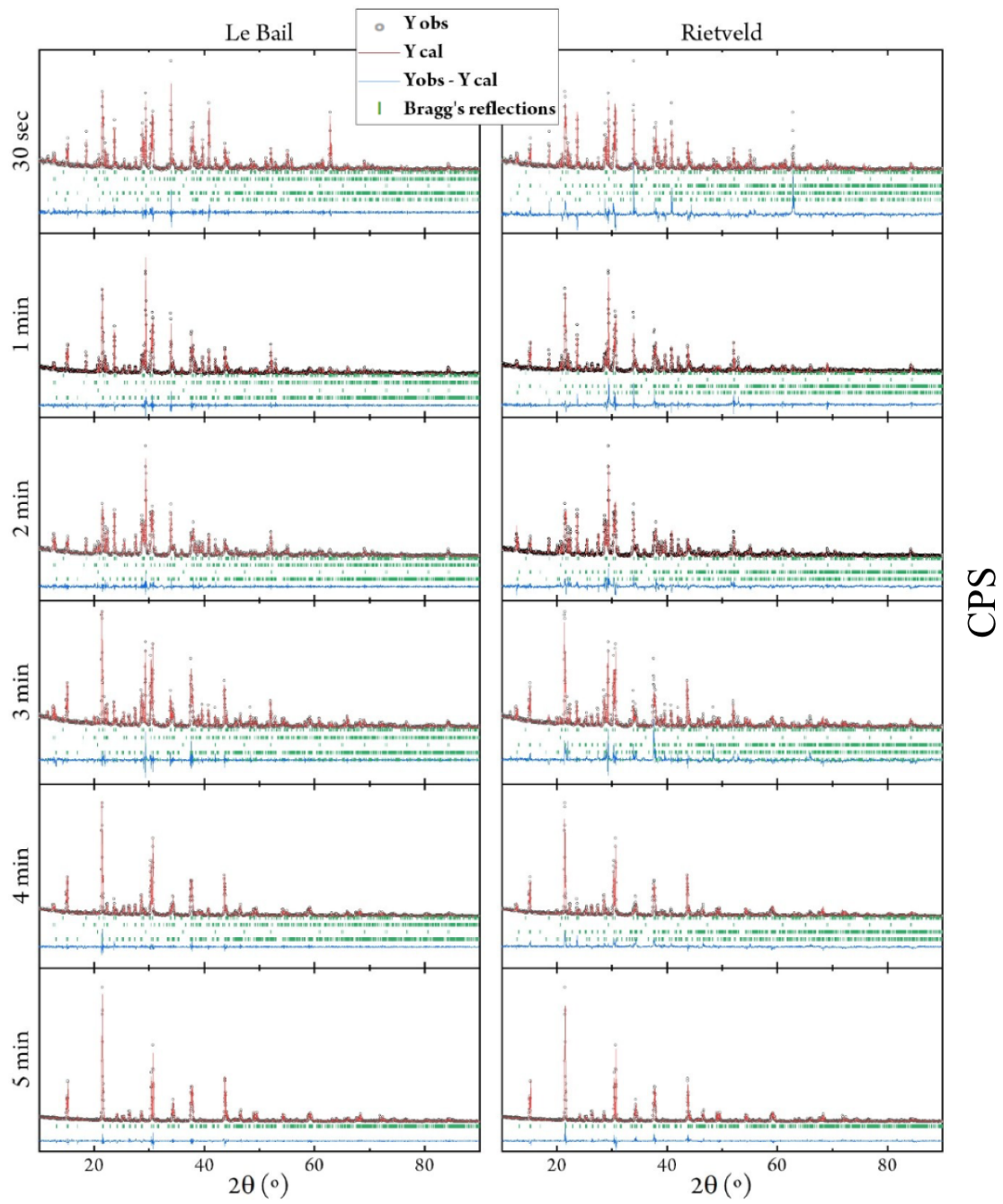


Figure A.1: Le Bail and Rietveld refinements of XRD data for stoichiometric  $\text{CsBr:PbBr}_2$  mixtures ball-milled for 30 seconds, 1 minute, 2 minutes, 3 minutes, 4 minutes and 5 minutes.

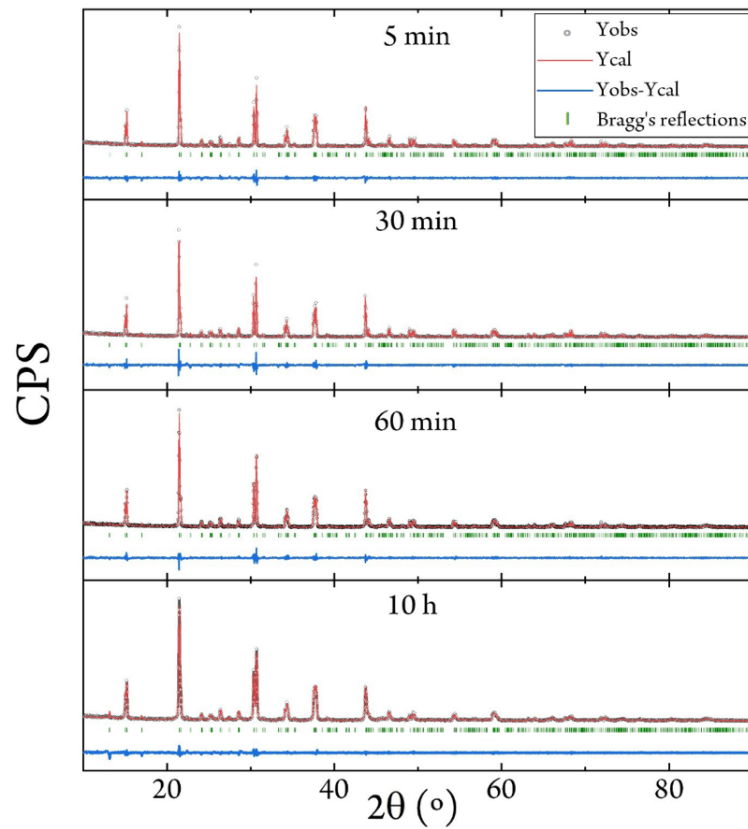


Figure A.2: X-ray diffractograms of stoichiometric  $\text{CsBr}:\text{PbBr}_2$  mixtures ball-milled for 5 minutes, 30 minutes, 1 hour and 10 hours, fitted with a single  $\text{CsPbBr}_3$  phase.

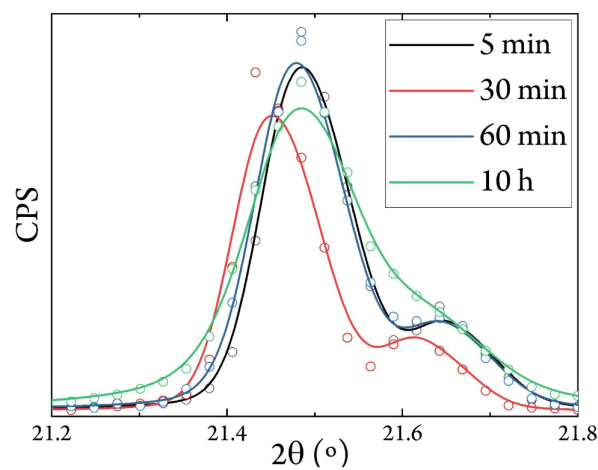


Figure A.3: X-ray diffractograms of the main  $\text{CsPbBr}_3$  diffraction peaks showing broadening at long milling times ( $t = 10$  h). A small shift of less than  $0.05^\circ$  is observed in one of the samples ( $t = 30$  min) for which the reason is unclear.

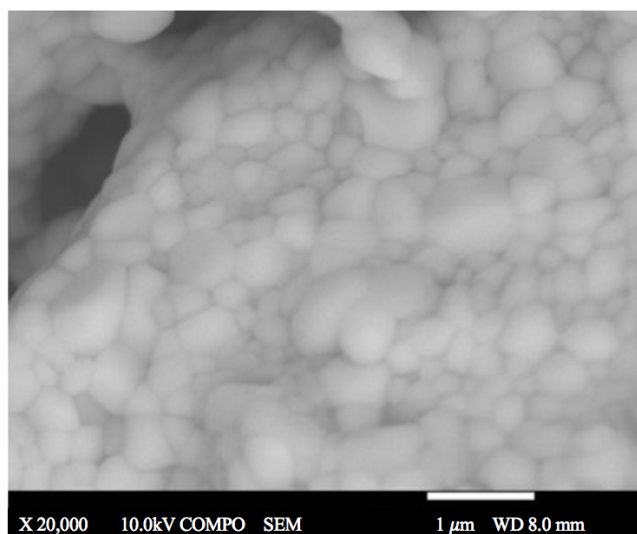


Figure A.4: SEM image of ball-milled  $\text{CsPbBr}_3$  for 10 hours.

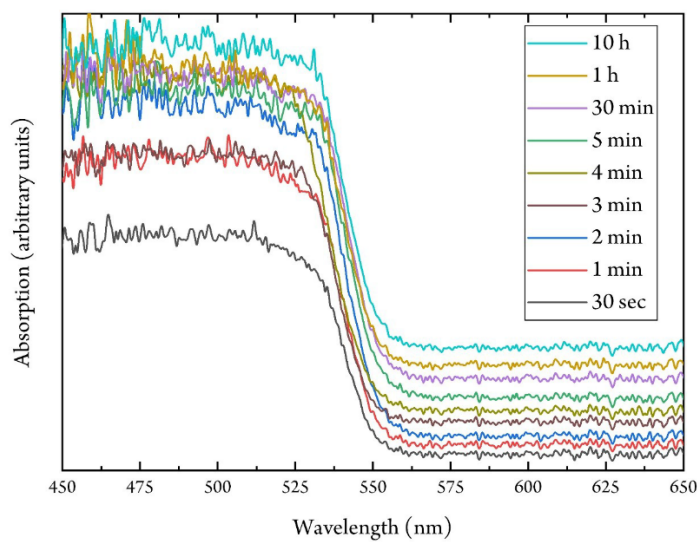


Figure A.5: Optical absorption spectra of all stoichiometric  $\text{CsBr}:\text{PbBr}_2$  mixtures ball-milled for different times showing similar onsets at approximately 540 nm, corresponding to “bulk”  $\text{CsPbBr}_3$ .

# Appendix B

Cite this: *RSC Adv.*, 2018, 8, 41548

## Incorporation of potassium halides in the mechanosynthesis of inorganic perovskites: feasibility and limitations of ion-replacement and trap passivation†

Yusra El Ajjouri,<sup>1a</sup> Vladimir S. Chirvony,<sup>1b</sup> Michele Sessolo,<sup>1a</sup> Francisco Palazon<sup>1c\*</sup> and Henk J. Bolink<sup>1a</sup>

Received 24th October 2018  
Accepted 3rd December 2018

DOI: 10.1039/c8ra08823c

rsc.li/rsc-advances

Potassium halides (KX; X = I, Br, or Cl) were incorporated as partial replacements of CsBr in the mechanosynthesis of CsPbBr<sub>3</sub>. This led to partial substitution of both monovalent ions forming mixed Cs<sub>1-x</sub>K<sub>x</sub>PbBr<sub>3-y</sub>X<sub>y</sub> perovskites. Longer photoluminescence lifetimes were also observed, possibly linked to the formation of a non-perovskite KPb<sub>2</sub>X<sub>5</sub> passivating layer.

In the past few years, organic metal halide perovskites (OHPs) have drawn considerable attention as promising materials for optoelectronic devices.<sup>1–5</sup> However, it is generally known that these materials make the development of stable solar cells and light emitting diodes rather difficult, due to their environmental instability related with the use of organic compounds.<sup>6–8</sup> Thus, fully inorganic halide perovskites, such as cesium-based perovskites are sought after for their increased stability.<sup>9–13</sup> The known poor solubility of cesium halides in common solvents may be bypassed by synthesizing inorganic perovskites in an all-dry manner such as by mechanosynthesis (*e.g.*, grinding or ball-milling)<sup>14–18</sup> and/or thermal vacuum deposition.<sup>19</sup> Recently, halide perovskites with an increasing complexity in formulation containing up to 6 or 7 different ions have proven to be beneficial for device performance.<sup>20–24</sup> In this context, mechanosynthesis by ball-milling represents an ideal platform to test different precursors or additives in a simple manner. Multi-cation perovskites enable tuning of the bandgap of the material<sup>23</sup> as well as its Goldschmidt tolerance factor (*t*),<sup>25,26</sup> which is calculated as follows:

$$t = (r_A + r_X) / [\sqrt{2}(r_B + r_X)]$$

where  $r_A$ ,  $r_B$  and  $r_X$  respectively stand for the ionic radiuses of the cation A, metal B and the anion X in the ABX<sub>3</sub> perovskite.

To obtain a stable cubic ABX<sub>3</sub> perovskite, it is generally accepted that the Goldschmidt tolerance factor should not be lower than 0.8 nor exceed a value of 1. A *t*-value outside of this

range usually results in non-perovskite structures. Examples of such crystalline structures are orthorhombic (so-called “yellow phase”) cesium lead iodide (CsPbI<sub>3</sub>) and formamidinium lead iodide (FAPbI<sub>3</sub>). In the case of CsPbI<sub>3</sub>, the tolerance factor is too small whereas in the case of FAPbI<sub>3</sub> the tolerance factor is too large to result in a stable cubic phase at room temperature. However, the multi-cation cesium formamidinium lead iodide perovskite ((Cs:FA)PbI<sub>3</sub>) was shown to be stable.<sup>23,27</sup> This is only an example of the interest of multi-cation perovskites. Among other cations, potassium has been recently used as an additive in perovskites, with different conclusions.<sup>22,28–33</sup> Some reports show a benefit from the presence of potassium in mixed (KCs) PbI<sub>3</sub>, where the guest cation is capable of stabilizing the perovskite structure.<sup>29</sup> Others, based on the small tolerance factor of such structure, have concluded that incorporating potassium halides in the synthesis does not lead to the effective incorporation of potassium as replacement of the “A” cation within the perovskite structure. As a result, potassium stays at the grain boundaries and indirectly contributes to surface passivation by providing additional halides (bound to K<sup>+</sup>), partially compensating the halide vacancies. The halide vacancies are believed to be one of the main quenching traps which need to be passivated to improve the optoelectronic properties of the perovskite.<sup>28,34</sup> On the contrary, other reports have concluded that addition of potassium halides leads to the formation of different separate phases.<sup>30,31</sup> These discrepancies might originate from the different perovskite crystallization processes used, which can result in different morphology, phase purity or stoichiometry of the final compound. Therefore, dry mechanosynthesis is an ideal preparation method, as it does not involve solvents, it avoids the formation of intermediate species, and eliminates the need of thermal treatments to foster the perovskite crystallization.

<sup>a</sup>Instituto de Ciencia Molecular, ICMol, Universidad de Valencia, C/ Catedrático J. Beltrán 2, 46980 Paterna, Spain. E-mail: Francisco.Palazon@uv.es

<sup>b</sup>UMDO (Unidad de Materiales y Dispositivos Optoelectrónicos), Instituto de Ciencia de los Materiales, Universidad de Valencia, Valencia 46071, Spain

† Electronic supplementary information (ESI) available. See DOI: 10.1039/c8ra08823c



In this work we synthesized halide perovskites by ball milling equimolar mixtures of  $\text{PbBr}_2$  and  $\text{ABr}$ , where  $\text{A} = \text{K}_{0.2}\text{Cs}_{0.8}$  and compared the resulting powders with the pure cesium reference ( $\text{A} = \text{Cs}$ ). High resolution X-ray diffraction (XRD) patterns as well as optical characterization are presented in Fig. 1. The main diffraction peaks from the resulting powder are presented in Fig. 1b, c and e. These peaks correspond to the orthorhombic  $\text{APbBr}_3$  perovskite (see Fig. S1† for the full diffractograms and reference pattern ICSD 97851). Hence, XRD confirms the formation of the perovskite phase from ball-milling of precursors. Furthermore, the high-resolution signals presented in Fig. 1b, c and e reveal a shift towards higher angles (smaller interatomic distances) when  $\text{CsBr}$  is partly replaced by  $\text{KBr}$ . This means that  $\text{K}^+$ , which has a smaller ionic radius than  $\text{Cs}^+$ , is effectively incorporated in the perovskite crystal structure, leading to mixed-cation ( $\text{KCs}$ ) $\text{PbBr}_3$ . Such

a cation-replacement is not trivial, as potassium is thought to be too small to occupy the “A” site in  $\text{APbBr}_3$ .<sup>28,30,31</sup> Indeed, concomitant to the shift of the main perovskite peaks, we also note that new peaks appear in the diffractogram (see Fig. S1† and 1a, d, f). These peaks are consistent with the non-perovskite  $\text{APb}_2\text{Br}_5$  phase. For potassium-based lead halide compounds, this phase is the most commonly reported.<sup>35,36</sup> We also ball-milled pure  $\text{KBr}$  and  $\text{PbBr}_2$  mixtures (without  $\text{CsBr}$ ) in different ratios and found that  $\text{KPb}_2\text{Br}_5$  was the dominant phase – along with unreacted  $\text{KBr}$  – even in  $\text{KBr}$ -rich conditions, see Fig. S2.† Therefore, we can conclude that the use of  $\text{KBr}$  as a source of  $\text{K}^+$  to replace  $\text{Cs}^+$  in inorganic perovskites is possible but limited by the higher stability of  $\text{KPb}_2\text{Br}_5$  as compared to  $\text{KPbBr}_3$ . When we reduced the amount of  $\text{KBr}$  to 5% ( $\text{A} = \text{K}_{0.05}\text{Cs}_{0.95}$ ) we also observed similar perovskite peak shifts and formation of  $\text{KPb}_2\text{Br}_5$ , although to a lesser extent (see Fig. S3†).

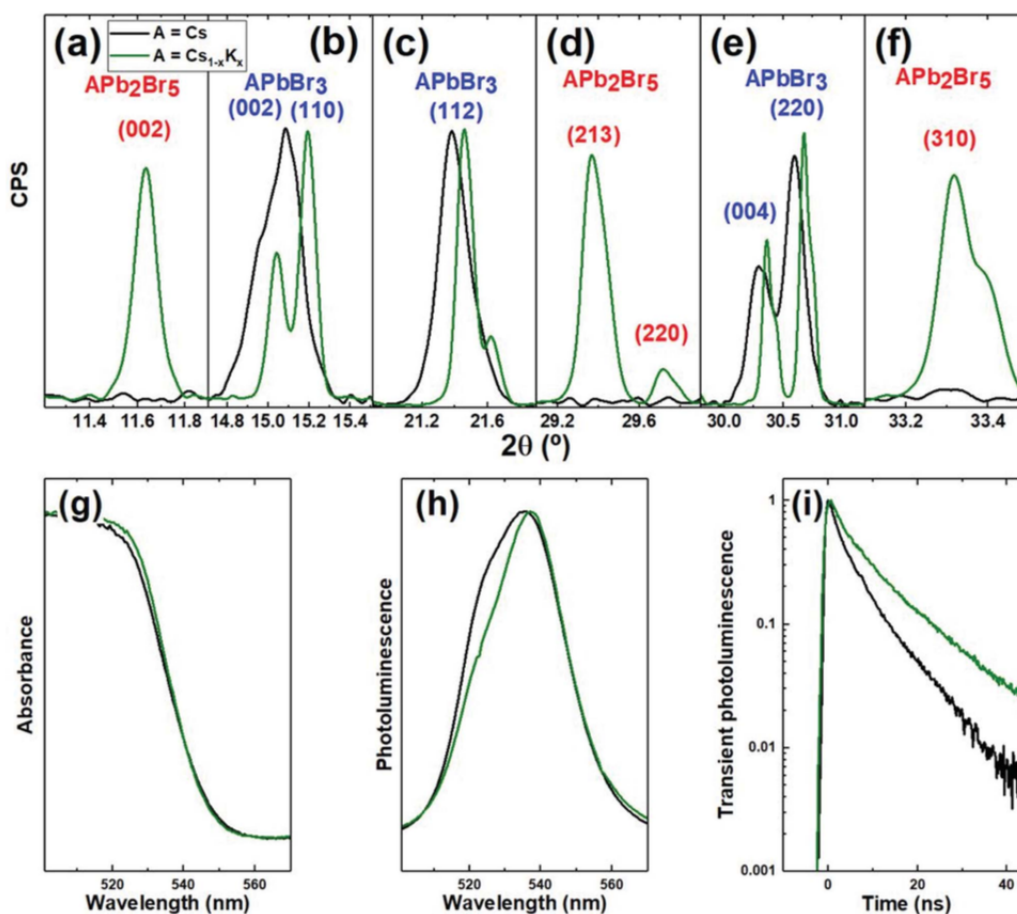


Fig. 1 XRD (a–f) and optical (g–i) characterization of powders prepared from addition of  $\text{PbBr}_2$  to  $\text{CsBr}$  (REF; black lines) or  $\text{Cs}_{0.8}\text{K}_{0.2}\text{Br}$  (green lines). XRD peaks corresponding to  $\text{APbBr}_3$  perovskite (b, c, and e) present a shift upon addition of  $\text{KBr}$ . Panels (a, d, and f) present a rise in intensity linked to the formation of non-perovskite  $\text{APb}_2\text{Br}_5$  phase. Full diffractograms are presented in Fig. S1.† Absorption (g) and photoluminescence (h) spectra remain mostly unchanged while photoluminescence lifetime (i) is increased.



This suggests that the amount of  $\text{Cs}^+$  that can be replaced by  $\text{K}^+$  in the perovskite structure (without leading to the formation of  $\text{KPb}_2\text{Br}_5$ ) is below 5%. This value is lower than previously reported by others.<sup>29</sup> Other characterization methods such as high-resolution transmission electron microscopy and energy dispersive X-ray spectroscopy could possibly further elucidate the amount of potassium that is present under each form (included in the perovskite lattice or as separated  $\text{KPb}_2\text{Br}_5$  compound). The optical characterization of the powders resulting from ball-milling equimolar  $\text{ABr:PbBr}_2$  mixtures with  $\text{A} = \text{K}_{0.2}\text{Cs}_{0.8}$  is presented in Fig. 1g–i. Absorption (g) and photoluminescence (h) spectra are mostly unchanged with respect to the reference sample ( $\text{A} = \text{Cs}$ ). Photoluminescence spectra (Fig. 1h) evidently consist of two sub-bands with maxima at about 522 and 540 nm (see deconvolution of the PL spectra as a sum of two Gaussian contours in ESI, Fig. S4†). Because of the broad and asymmetric nature of the PL spectra, it is not possible to unambiguously evaluate the impact of potassium incorporation on the optical bandgap. Indeed, it could be expected that the observed shrinkage of the lattice would affect the optical bandgap of the material and result in a shift of the PL peak. However, the origin of the two bands observed in both PL spectra might be due to different reasons. In a previous report on the mechano-synthesis of  $\text{CsPbBr}_3$  via ball-milling of  $\text{CsBr}$  and  $\text{PbBr}_2$  a similar asymmetric spectrum was obtained and attributed to the presence of bulk and nano-sized  $\text{CsPbBr}_3$ .<sup>16</sup> Another possible explanation is linked to the emission from free electrons in conducting band and trap-localized carriers.<sup>37</sup> In this second hypothesis, it is possible that an exchange of a part of  $\text{Cs}$  atoms by  $\text{K}$  decreases the relative contribution of the PL emission from free electrons at 522 nm and, respectively, increases contribution of the emission from trap states at 540 nm. Following the delayed luminescence model,<sup>38</sup> trap-assisted luminescence should be longer lived than the emission of free electrons from the conducting band, as is indeed observed in Fig. 1i. However, we cannot exclude other possible origins of this longer lifetime such as trap passivation by molecular  $\text{KBr}$  which fills halide vacancies at the surface<sup>28</sup> or by the other two mechanisms that our data prove to happen concomitantly: (i) replacement of  $\text{Cs}^+$  by  $\text{K}^+$  as monovalent cation in the perovskite structure, and (ii) formation of  $\text{KPb}_2\text{Br}_5$  which might act as passivating layer on top of  $\text{CsPbBr}_3$ . This passivation (independently on the exact mechanism from which it originates) should result in a higher photoluminescence quantum yield (PLQY). However, the absolute PLQY of these powder samples is too low for us to conduct reliable measurements.

We also replaced  $\text{KBr}$  by  $\text{KX}$  ( $\text{X} = \text{Cl}$  or  $\text{I}$ ) while keeping  $\text{CsBr}$  and  $\text{PbBr}_2$  as precursors in the mechano-synthesis. Fig. 2 shows XRD and optical characterization of the resulting powders. Fig. 2a–c demonstrate that the perovskite phase is formed in all cases and that the heteroanion ( $\text{Cl}$  or  $\text{I}$ ) introduced via the potassium salt is replacing  $\text{Br}$  in the  $\text{APbX}_3$  structure. Indeed, when  $\text{KI}$  is used the main perovskite peaks shift towards lower diffraction angles consistent with the introduction of the larger  $\Gamma^-$  anion compared to  $\text{Br}^-$ . The opposite applies when  $\text{KCl}$  is used. As a result, we observe significant shifts in the bandgap of

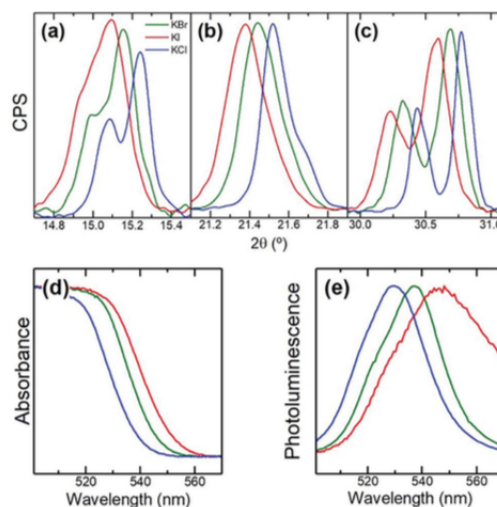


Fig. 2 XRD (a–c) and optical (d and e) characterization of powders prepared from  $\text{KI}$  (red),  $\text{KBr}$  (green), and  $\text{KCl}$  (blue). Shifts in diffractograms are consistent with the incorporation of the heteroanion ( $\text{I}$  or  $\text{Cl}$ ) in the perovskite structure. This translates into a smaller ( $\text{KI}$ ) or higher ( $\text{KCl}$ ) bandgap as observed in absorption (d) and photoluminescence (e).

the perovskite as shown by absorption and photoluminescence (Fig. 2d, e). Hence, our results show that  $\text{KX}$  can also be used as a source of anions to tune the optical properties of the resulting inorganic perovskite. This means that the  $\text{X}$  halide does not only remain tightly bound to  $\text{K}^+$  at the surface of the perovskite material affecting only surface-related effects (surface quenching traps) but also enters the structure and thus affects bulk-related properties (bandgap).

In conclusion, we have shown that incorporating potassium halides in the mechano-synthesis of inorganic cesium lead halide perovskites leads to several chemical, structural and optical effects. First of all, potassium partly replaces cesium in the  $\text{APbBr}_3$  perovskite structure. Second, the potassium salt can also act as a source of heteroanions to tune the bandgap of the resulting perovskite. Third,  $\text{KPb}_2\text{X}_5$  phase forms concomitantly with the perovskite phase. This phase may act as a surface passivation layer as longer lifetimes are observed on samples with added  $\text{KBr}$  with respect to pure  $\text{CsPbBr}_3$ . These findings will aid to further optimize thin film perovskite based devices such as LEDs and solar cells that recently have shown beneficial effects of incorporating potassium halides.

## Conflicts of interest

There are no conflicts to declare.

## Acknowledgements

The research leading to these results has received funding from the European Union Programme for Research and Innovation

Horizon 2020 (2014-2020) under the Marie Skłodowska-Curie Grant Agreement PerovSAMS No. 747599. We also acknowledge financial support from the Spanish Ministry of Economy and Competitiveness (MINECO) via the Unidad de Excelencia Maria de Maeztu MDM-2015-0538, MAT2017-88821-R, and the Generalitat Valenciana (Prometeo/2016/135 and GRISOLIAP/2017/089). M. S. thanks the MINECO for his RyC contract.

## Notes and references

- N. K. Noel, A. Abate, S. D. Stranks, E. S. Parrott, V. M. Burlakov, A. Goriely and H. J. Snaith, *ACS Nano*, 2014, **8**, 9815–9821.
- S. D. Stranks, G. E. Eperon, G. Grancini, C. Menelaou, M. J. P. Alcocer, T. Leijtens, L. M. Herz, A. Petrozza and H. J. Snaith, *Science*, 2013, **342**, 341–344.
- W. Li, Z. Wang, F. Deschler, S. Gao, R. H. Friend and A. K. Cheetham, *Nat. Rev. Mater.*, 2017, **2**(3), DOI: 10.1038/natrevmats.2016.99.
- T. M. Brenner, D. A. Egger, L. Kronik, G. Hodes and D. Cahen, *Nat. Rev. Mater.*, 2016, **1**(1), DOI: 10.1038/natrevmats.2015.7.
- S. D. Stranks and H. J. Snaith, *Nat. Nanotechnol.*, 2015, **10**, 391–402.
- J. S. Manser, M. I. Saidaminov, J. A. Christians, O. M. Bakr and P. V. Kamat, *Acc. Chem. Res.*, 2016, **49**, 330–338.
- S.-H. Turren-Cruz, A. Hagfeldt and M. Saliba, *Science*, 2018, **358**, 1–9.
- F. Palazon, D. Pérez-del-Rey, S. Marras, M. Prato, M. Sessolo, H. J. Bolink and L. Manna, *ACS Energy Lett.*, 2018, 835–839.
- F. Palazon, F. Chen, Q. A. Akkerman, M. Imran, R. Krahn and L. Manna, *ACS Appl. Nano Mater.*, 2018, **1**(10), 5396–5400.
- R. F. Service, *Science*, 2016, **351**, 113–114.
- M. Kulbak, S. Gupta, N. Kedem, I. Levine, T. Bendikov, G. Hodes and D. Cahen, *J. Phys. Chem. Lett.*, 2016, **7**, 167–172.
- L. Zhang, X. Yang, Q. Jiang, P. Wang, Z. Yin, X. Zhang, H. Tan, Y. M. Yang, M. Wei, B. R. Sutherland, E. H. Sargent and J. You, *Nat. Commun.*, 2017, **8**, 1–8.
- C. Y. Chen, H. Y. Lin, K. M. Chiang, W. L. Tsai, Y. C. Huang, C. S. Tsao and H. W. Lin, *Adv. Mater.*, 2017, **29**, 1–7.
- D. Prochowicz, M. Franckevičius, A. M. Cieślak, S. M. Zakeeruddin, M. Grätzel and J. Lewiński, *J. Mater. Chem. A*, 2015, **3**, 20772–20777.
- Z. Y. Zhu, Q. Q. Yang, L. F. Gao, L. Zhang, A. Y. Shi, C. L. Sun, Q. Wang and H. L. Zhang, *J. Phys. Chem. Lett.*, 2017, **8**, 1610–1614.
- L. Protesescu, S. Yakunin, O. Nazarenko, D. N. Dirin and M. V. Kovalenko, *ACS Appl. Nano Mater.*, 2018, **1**, 1300–1308.
- A. D. Jodlowski, A. Yépez, R. Luque, L. Camacho and G. de Miguel, *Angew. Chem., Int. Ed.*, 2016, **55**, 14972–14977.
- Y. El Ajjouri, F. Palazon, M. Sessolo and H. J. Bolink, *Chem. Mater.*, 2018, **30**, 7423–7427.
- J. Ávila, C. Momblona, P. P. Boix, M. Sessolo and H. J. Bolink, *Joule*, 2017, **1**, 431–442.
- L. Gil-Escrig, C. Momblona, M. G. La-Placa, P. P. Boix, M. Sessolo and H. J. Bolink, *Adv. Energy Mater.*, 2018, **8**, 1–6.
- D. Forgács, D. Pérez-del-Rey, J. Ávila, C. Momblona, L. Gil-Escrig, B. Dänekamp, M. Sessolo and H. J. Bolink, *J. Mater. Chem. A*, 2017, **5**, 3203–3207.
- T. Bu, X. Liu, Y. Zhou, J. Yi, X. Huang, L. Luo, J. Xiao, Z. Ku, Y. Peng, F. Huang, Y.-B. Cheng and J. Zhong, *Energy Environ. Sci.*, 2017, **10**(12), 2509–2515.
- M. Saliba, T. Matsui, K. Domanski, J. Seo, A. Ummadisingu, S. M. Zakeeruddin, J. P. Correa-Baena, W. R. Tress, A. Abate, A. Hagfeldt and M. Grätzel, *Science*, 2016, **355**, 1–8.
- B. Philippe, M. Saliba, J. P. Correa-Baena, U. B. Cappel, S. H. Turren-Cruz, M. Grätzel, A. Hagfeldt and H. Rensmo, *Chem. Mater.*, 2017, **29**, 3589–3596.
- Z. Li, M. Yang, J. S. Park, S. H. Wei, J. J. Berry and K. Zhu, *Chem. Mater.*, 2016, **28**, 284–292.
- C. J. Bartel, C. Sutton, B. R. Goldsmith, R. Ouyang, C. B. Musgrave, L. M. Ghiringhelli and M. Scheffler, arXiv Prepr. arXiv, 2018, **6**, 1–13.
- D. P. McMeekin, G. Sadoughi, W. Rehman, G. E. Eperon, M. Saliba, M. T. Hörantner, A. Haghighirad, N. Sakai, L. Korte, B. Rech, M. B. Johnston, L. M. Herz and H. J. Snaith, *Science*, 2016, **351**, 151–155.
- M. Abdi-Jalebi, Z. Andaji-Garmaroudi, S. Cacovich, C. Stavarakas, B. Philippe, J. M. Richter, M. Alsari, E. P. Booker, E. M. Hutter, A. J. Pearson, S. Lilliu, T. J. Savenije, H. Rensmo, G. Divitini, C. Ducati, R. H. Friend and S. D. Stranks, *Nature*, 2018, **555**, 497–501.
- J. K. Nam, S. U. Choi, W. Cha, Y. J. Choi, W. Kim, M. S. Jung, J. Kwon, D. Kim and J. H. Park, *Nano Lett.*, 2017, **17**, 2028–2033.
- D. J. Kubicki, D. Prochowicz, A. Hofstetter, S. M. Zakeeruddin, M. Grätzel and L. Emsley, *J. Am. Chem. Soc.*, 2018, **140**, 7232–7238.
- D. J. Kubicki, D. Prochowicz, A. Hofstetter, S. M. Zakeeruddin, M. Grätzel and L. Emsley, *J. Am. Chem. Soc.*, 2017, **139**, 14173–14180.
- Z. Tang, T. Bessho, F. Awai, T. Kinoshita, M. M. Maitani, R. Jono, T. N. Murakami, H. Wang, T. Kubo, S. Uchida and H. Segawa, *Sci. Rep.*, 2017, **7**, 1–7.
- S. Huang, B. Wang, Q. Zhang, Z. Li, A. Shan and L. Li, *Adv. Opt. Mater.*, 2018, **5**, 1701106.
- M. Abdi-Jalebi, Z. Andaji-Garmaroudi, A. J. Pearson, G. Divitini, S. Cacovich, B. Philippe, H. Rensmo, C. Ducati, R. H. Friend and S. D. Stranks, *ACS Energy Lett.*, 2018, **3**(11), 2671–2678.
- A. Y. Tarasova, L. I. Isaenko, V. G. Kesler, V. M. Pashkov, A. P. Yeliseyev, N. M. Denysyuk and O. Y. Khyzhun, *J. Phys. Chem. Solids*, 2012, **73**, 674–682.
- L. I. Isaenko, I. N. Ogorodnikov, V. A. Pustovarov, A. Y. Tarasova and V. M. Pashkov, *Opt. Mater.*, 2013, **35**, 620–625.
- P. Ščajev, C. Qin, R. Aleksiejūnas, P. Baronas, S. Miasojedovas, T. Fujihara, T. Matsushima, C. Adachi and S. Juršėnas, *J. Phys. Chem. Lett.*, 2018, **9**, 3167–3172.
- V. S. Chirvony, S. González-Carrero, I. Suárez, R. E. Galian, M. Sessolo, H. J. Bolink, J. P. Martínez-Pastor and J. Pérez-Prieto, *J. Phys. Chem. C*, 2017, **121**, 13381–13390.

## Supporting Information

### Incorporation of Potassium Halides in the Mechanochemical Synthesis of Inorganic Perovskites: Feasibility and Limitations of Ion-replacement and Trap Passivation

Yousra El Ajjouri,<sup>a</sup> Vladimir S. Chirvony,<sup>a,b</sup> Michele Sessolo,<sup>a</sup> Francisco Palazon<sup>a\*</sup> and Henk J. Bolink<sup>a</sup>

<sup>a</sup> Instituto de Ciencia Molecular, ICMol, Universidad de Valencia, C/ Catedrático J. Beltrán 2, 46980 Paterna, Spain

<sup>b</sup> UMDO (Unidad de Materiales y Dispositivos Optoelectrónicos), Instituto de Ciencia de los Materiales, Universidad de Valencia, Valencia 46071, Spain

#### Experimental details

##### Materials

Cesium bromide (CsBr, > 99 %), was purchased from TCI. Potassium bromide (KBr, > 99 %) and lead(II) bromide (PbBr<sub>2</sub>, ≥ 98 %) were purchased from Sigma-Aldrich. All chemicals were stored in a nitrogen-filled glovebox and used as received without further purification.

##### Mechanochemical synthesis

Equimolar AX:PbBr<sub>2</sub> powders (AX = CsBr or CsBr<sub>0.8</sub>KY<sub>0.2</sub>; where Y = I<sup>-</sup>, Br<sup>-</sup> or Cl<sup>-</sup>) were mixed inside a nitrogen-filled glovebox. Then, approximately 3 grams of the mixed precursors powders were introduced inside 10 mL zirconia ball-mill jars with 2 zirconia beads of 10 mm in diameter per jar. The jars were closed under nitrogen so that the powders were not exposed to air. Then ball-milling was performed with a MM-400 straight ball-mill from Retsch, at a frequency of 30 Hz for 5 hours.

##### XRD

X-ray diffraction was measured with a Panalytical Empyrean diffractometer equipped with a Cu-K $\alpha$  anode operated at 45 kV and 30 mA and a Pixel 1D detector in scanning line mode. Single scans were acquired in the  $2\theta = 10^\circ$  to  $50^\circ$  range in Bragg-Brentano geometry in air. Data analysis was performed with HighScore Plus software.

##### Absorbance and photoluminescence spectroscopy

Absorbance was measured with a High Power UV-Vis fiber light source, integrated sphere and Avantes Starline AVASpec-2048L spectrometer in reflection mode. Photoluminescence was measured with a continuous wave 375 nm diode laser with a 400nm filter and Hamamatsu PMA 11 spectrometer. For a typical spectrum 10 scans of 1 second were averaged.

##### Photoluminescence measurements

A third harmonic (355 nm) of a Nd:YAG pulsed laser with 1.1 ns pulse duration, 1 kHz pulse repetition frequency and 20  $\mu\text{J}/\text{cm}^2$  excitation density was used as an excitation source for the PL measurements. To detect the time-resolved PL kinetics an integrated PL signal was directed through a multimode optical fiber to a time correlated single photon counting electronic board. For the PL spectra measurements, the PL signal was directed through an optical fiber to an Ocean type spectrometer.

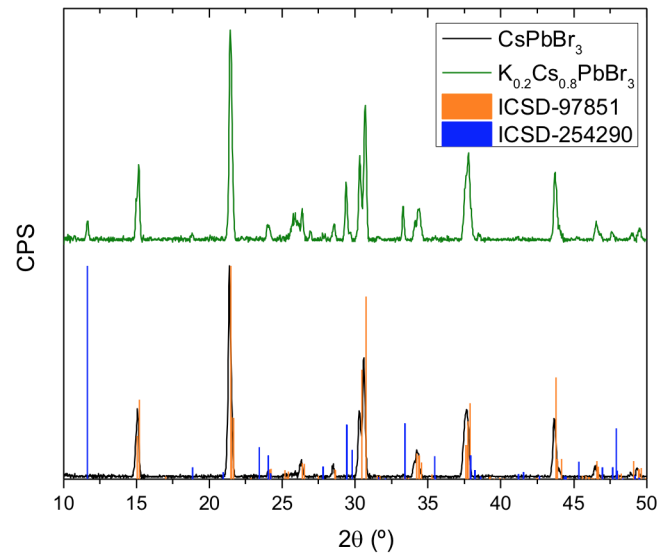


Figure B.1: XRD signals of samples prepared from pure CsBr (reference, black line) and partly (20 %) substituted by KBr ( $K_{0.2}Cs_{0.8}PbBr_3$ , green line) in the perovskite structure  $APbBr_3$ . Selected areas of the diffractograms are shown in Figure 4.1. The reference patterns for bulk orthorhombic  $CsPbBr_3$  (ICSD-97851) and  $CsPb_2Br_5$  (ICSD-254290) are shown as orange and blue columns, respectively.

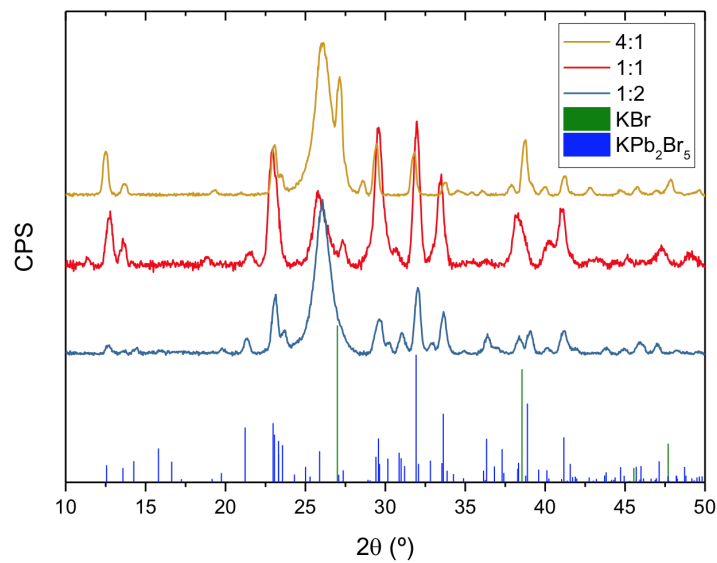


Figure B.2: X-ray diffractograms of powders prepared by dry ball-milling KBr and  $PbBr_2$  in different molar ratios (1:2, 1:1, and 4:1). The reference patterns for bulk KBr (ICSD-18015) and  $KPb_2Br_5$  (ICSD-250266) are presented as green and blue columns. The broad signal around  $2\theta = 26^\circ$  corresponds to the substrate on which the powders are deposited for XRD characterization (see Figure B.3).

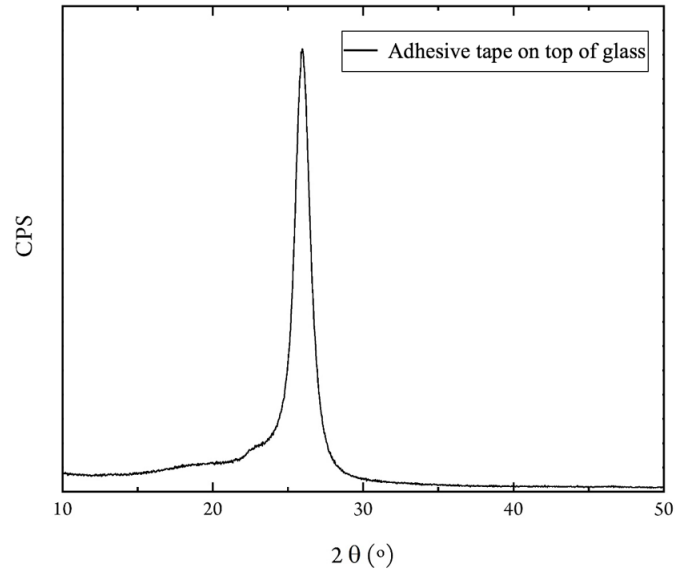


Figure B.3: X-ray diffractogram of adhesive tape used to fix powders on glass substrates. This signal, approximately  $2\theta = 26^\circ$ , appears sometimes as a parasitic diffraction peak in the samples' diffractograms.

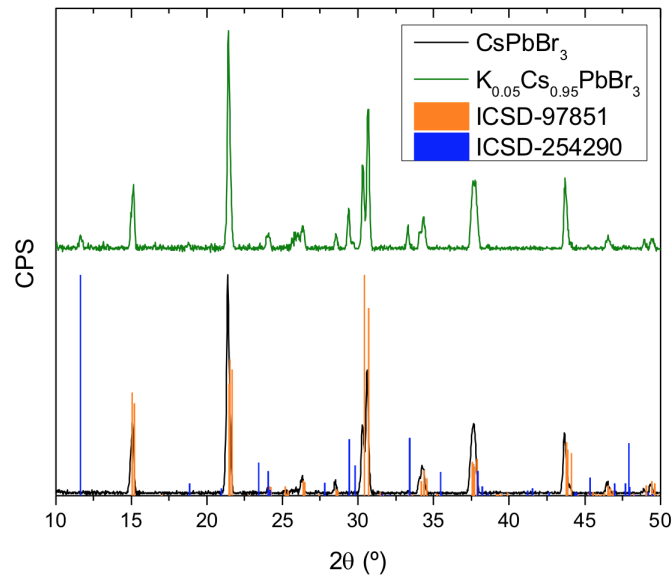


Figure B.4: XRD signals of samples prepared from pure  $\text{CsBr}$  (reference, black line) and partly (5 %) substituted by  $\text{KBr}$  (green line) in the perovskite structure  $\text{APbBr}_3$ . The effects of  $\text{KBr}$  are qualitatively similar than in the case of 20 % (Figure B.1 and Figure 4.1), although to a lesser extent, as may be expected by a lower percentage of  $\text{KBr}$ . The reference patterns for bulk orthorhombic  $\text{CsPbBr}_3$  (ICSD-97851) and  $\text{CsPb}_2\text{Br}_5$  (ICSD-254290) are shown as orange and blue columns, respectively.



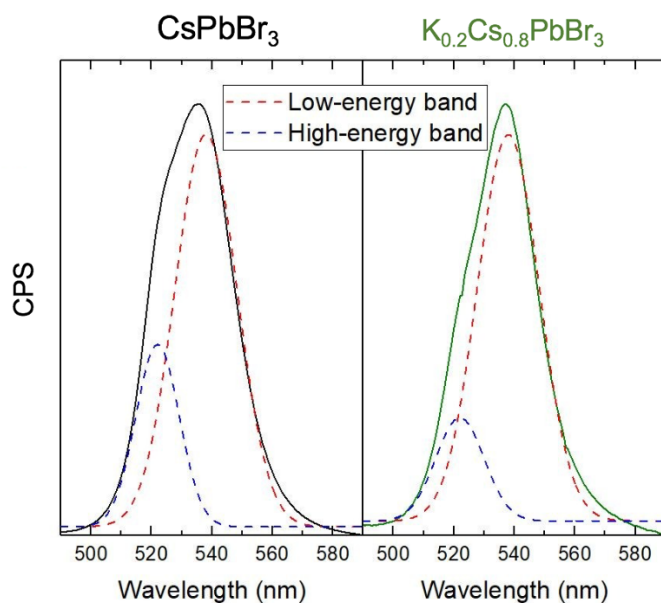


Figure B.5: Photoluminescence spectra of ball-milled  $A\text{Br}:\text{PbBr}_2$  mixtures (with  $A = \text{CsBr}$  (reference) or  $\text{K}_{0.2}\text{Cs}_{0.8}$ ) fitted with two Gaussian peaks (dashed red and blue curves). The potassium-containing sample ( $A = \text{K}_{0.2}\text{Cs}_{0.8}$ ) shows a reduction in the relative intensity of the high-energy component as explained in Section 4.3.

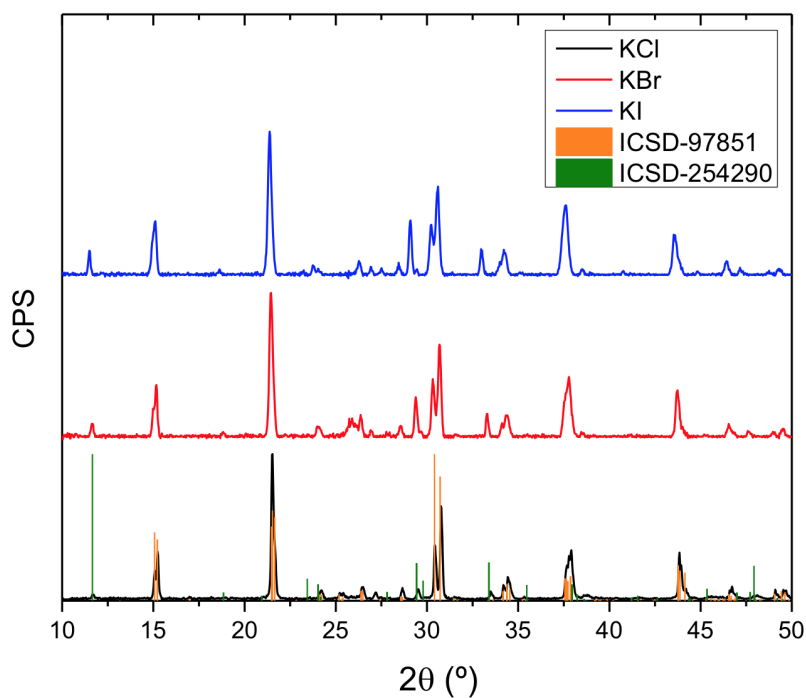


Figure B.6: XRD patterns of powders prepared by dry ball-milling of 20 % KI (blue), 20 % KBr (red) and 20 % KCl (black) with  $\text{CsBr}:\text{PbBr}_2$  (1:1) as the perovskite precursors. The reference patterns for bulk orthorhombic  $\text{CsPbBr}_3$  (ICSD-97851) and  $\text{CsPb}_2\text{Br}_5$  (ICSD-254290) are shown as orange and green columns, respectively.

# Appendix C



# Mechanochemical Synthesis of Sn(II) and Sn(IV) Iodide Perovskites and Study of Their Structural, Chemical, Thermal, Optical, and Electrical Properties

Yusra El Ajjouri, Federico Locardi, María C. Gélvez-Rueda, Mirko Prato, Michele Sessolo, Maurizio Ferretti, Ferdinand C. Grozema, Francisco Palazon,\* and Henk J. Bolink

Phase-pure  $\text{CsSnI}_3$ ,  $\text{FASnI}_3$ ,  $\text{Cs}(\text{PbSn})\text{I}_3$ ,  $\text{FA}(\text{PbSn})\text{I}_3$  perovskites (FA = formamidinium =  $\text{HC}(\text{NH}_2)_2^+$ ) as well as the analogous so-called vacancy-ordered double perovskites  $\text{Cs}_2\text{SnI}_6$  and  $\text{FA}_2\text{SnI}_6$  are mechanochemically synthesized. The addition of  $\text{SnF}_2$  is found to be crucial for the synthesis of Cs-containing perovskites but unnecessary for hybrid ones. All compounds show an absorption onset in the near-infrared (NIR) region, which makes them especially relevant for photovoltaic applications. The addition of Pb(II) and  $\text{SnF}_2$  is crucial to improve the electronic properties in 3D Sn(II)-based perovskites, in particular their charge carriers mobility ( $\approx 0.2 \text{ cm}^2 \text{ Vs}^{-1}$ ) which is enhanced upon reduction of the dark carrier conductivity. Stokes-shifted photoluminescence is observed on dry powders of Sn(II)-based perovskites, which makes these materials promising for light-emitting and sensing applications. Thermal stability of all compounds is examined, revealing no significant degradation up to at least  $200^\circ\text{C}$ . This meets the requirements for standard operation conditions of most optoelectronic devices and is potentially compatible with thermal vacuum deposition of polycrystalline thin films.

applications in both single junction and tandem solar cells.<sup>[35]</sup> One problem that arises with the use of Sn(II) is that it may be easily oxidized to Sn(IV). Two workarounds exist to this problem: 1) limiting the oxidation by using additives such as  $\text{SnF}_2$ <sup>[8,11,12,33,36]</sup> or 2) exploring the properties of Sn(IV)-based materials.<sup>[37–48]</sup>  $\text{A}_2\text{B}(\text{IV})\text{X}_6$  compounds can be seen as a similar structure to the  $\text{AB}(\text{II})\text{X}_3$  perovskite where every other  $\text{BX}_6$  octahedra is removed, and B is in +4 oxidation state to ensure charge neutrality (see Scheme 1).

These compounds are sometimes referred to as vacancy-ordered double perovskites, where the B-“vacancies” are described as virtual cations, also explaining why the stoichiometry of  $\text{A}_2\text{BX}_6$  is often written as  $2-\square-1-6$ .  $\text{Cs}_2\text{SnI}_6$  has been shown to be a degradation product of  $\text{CsSnI}_3$  upon air-exposure.<sup>[46]</sup> Although this compound can be seen as a 0D structure

due to the fact that adjacent  $\text{SnI}_6$  octahedra do not share any corners, their vicinity and consequent orbital overlap results in interesting optoelectronic properties for PV.<sup>[46]</sup> Mechanochemical synthesis via ball-milling or other techniques (e.g., hand grinding) provides an ideal platform to form a wide variety of perovskites in stoichiometric and solvent-free conditions.<sup>[49–70]</sup>

Additionally, these compounds may later be used for thin-film deposition by single-source thermal evaporation.<sup>[52]</sup> The high number of recent publications indicates that mechanochemical

## 1. Introduction

Lead iodide perovskites have shown excellent photovoltaic (PV) as well as electroluminescent properties.<sup>[1,2]</sup> In part due to the toxicity of  $\text{Pb}^{2+}$  ions, other metal halide perovskites are being investigated. Divalent tin is the most straightforward alternative to lead, considering their similar electronic configuration (group 14) and similar ionic radiuses.<sup>[3–34]</sup> Furthermore, mixed Sn-Pb iodide perovskites possess a lower bandgap than pure Pb and Sn ones, with

Y. El Ajjouri, Dr. M. Sessolo, Dr. F. Palazon, Prof. H. J. Bolink  
Instituto de Ciencia Molecular, ICMol  
Universidad de Valencia  
C/ Catedrático J. Beltrán 2, Paterna 46980, Spain  
E-mail: Francisco.palazon@uv.es

Dr. F. Locardi, Prof. M. Ferretti  
Dipartimento di Chimica e Chimica Industriale  
Università degli Studi di Genova  
Via Dodecaneso 31, Genova 16146, Italy

Dr. F. Locardi, Dr. F. Palazon  
Nanochemistry Department  
Istituto Italiano di Tecnologia  
Via Morego 30, Genova 16163, Italy

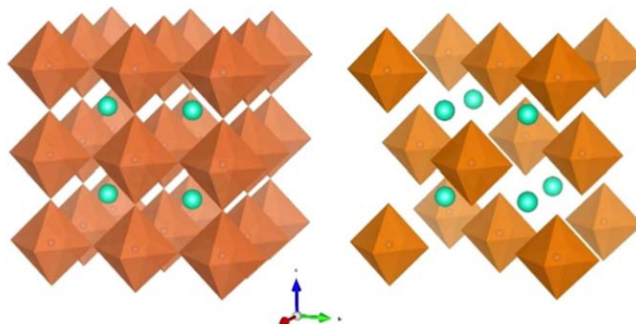
M. C. Gélvez-Rueda, Dr. F. C. Grozema  
Optoelectronic Materials Section  
Department of Chemical Engineering  
Delft University of Technology  
Van der Maasweg 9, Delft 2629 HZ, The Netherlands

The ORCID identification number(s) for the author(s) of this article can be found under <https://doi.org/10.1002/ente.201900788>.

DOI: 10.1002/ente.201900788

Dr. M. Prato  
Materials Characterization Facility  
Istituto Italiano di Tecnologia  
Via Morego 30, Genova 16163, Italy





**Scheme 1.** Crystal structures of  $\text{CsSnI}_3$  (left) and  $\text{Cs}_2\text{SnI}_6$  (right). Green balls represent  $\text{Cs}^+$  ions and orange octahedra represent  $\text{SnI}_6$  units.  $\text{Cs}_2\text{SnI}_6$  crystal structure can be viewed as a derivative from  $\text{CsSnI}_3$  where every other  $\text{SnI}_6$  octahedra is removed (the oxidation state of Sn is consequently +2 in  $\text{CsSnI}_3$  and +4 in  $\text{Cs}_2\text{SnI}_6$ ).

synthesis is starting to be a common practice in a few research groups focusing on halide perovskites and related compounds, and we foresee that it will be a widespread approach in the near future. Surprisingly, given the interest on tin perovskites, we could only find two publications focusing on mechanochemical synthesis of such compounds. The first one is the seminal work of Stoumpos et al.<sup>[71]</sup> where mechanochemical synthesis (grinding by hand with mortar and pestle) was found to yield non-pure perovskites with considerable amounts of unreacted precursors. The second reference is a recent work from Saski et al.<sup>[59]</sup> where several 3D pure-tin mixed iodide-bromide perovskites were synthesized. To the best of our knowledge, no reports either on mixed Sn-Pb (especially relevant for low bandgap applications as previously discussed) or on 0D iodide perovskites by mechanochemistry exist. Also, the only report of 3D iodide perovskites made by mechanochemical synthesis that we are aware of previous study<sup>[59]</sup> does not provide thermal stability or electrical conductivity characterization.

Hereafter, we have used ball-milling to synthesize the pure Sn and mixed Sn-Pb iodide perovskites  $\text{CsSnI}_3$ ,  $\text{FASnI}_3$ ,  $\text{Cs}(\text{PbSn})\text{I}_3$ , and  $\text{FA}(\text{PbSn})\text{I}_3$  as well as the Sn(IV)-based vacancy-ordered perovskites  $\text{Cs}_2\text{SnI}_6$  and  $\text{FA}_2\text{SnI}_6$  (FA = formamidinium =  $\text{HC}(\text{NH}_2)_2^+$ ). The influence of  $\text{SnF}_2$  as additive in the synthesis is also investigated. The elemental, chemical, and structural characteristics of the as-prepared compounds are investigated by X-ray diffraction (XRD) and X-ray photoelectron spectroscopy (XPS). Furthermore, the thermal stability is studied by means of differential thermal analysis and thermogravimetry (DTA/TG). The energy level diagram is estimated from optical characterization and ultraviolet photoelectron spectroscopy (UPS). In addition, the charge carrier mobility and lifetime of 3D Sn(II)-based perovskite and 0D Sn(IV)-based structure were investigated by time-resolved microwave conductivity (TRMC), revealing that the effective mobility is two orders of magnitude larger for 3D Sn(II)-based perovskites as compared with 0D Sn(IV)-based structures. These measurements show that the electronic properties of fully inorganic Sn(II)-based perovskites are improved during synthesis by Pb-mixing and addition of  $\text{SnF}_2$ , which decreases the charge carrier conductivity caused by oxidation to Sn(IV).

## 2. Results and Discussion

Sn(II)- and Sn(IV)-based compounds were synthesized by dry ball-milling of stoichiometric mixtures of the different precursors (see experimental section for details). **Figure 1** shows the XRD characterization of all metal iodide perovskites.

The X-ray diffractograms of  $\text{CsSnI}_3$ ,  $\text{FASnI}_3$ ,  $\text{Cs}_2\text{SnI}_6$ , and  $\text{FA}_2\text{SnI}_6$  match very well with the corresponding reference bulk patterns. The mixed tin-lead compounds  $\text{Cs}(\text{SnPb})\text{I}_3$  and  $\text{FA}(\text{SnPb})\text{I}_3$  have XRD signals comparable with the pure tin compounds albeit slightly shifted to lower angles, as expected from a partial replacement of tin with a bigger cation such as lead. Accordingly, we also observe a shift to lower diffraction angles in FA-based compounds compared with Cs-based ones. These differences are more clearly observed in Figure S2, Supporting Information, which shows the three more relevant regions of each diffractogram. The high phase purity and match with reference XRD patterns highlight the potential of mechanochemical synthesis to obtain high-quality materials. As noted in the legend of Figure 1,  $\text{CsSnI}_3$  and  $\text{Cs}(\text{PbSn})\text{I}_3$  were formed in the presence of  $\text{SnF}_2$ . This additive was found to be crucial in the synthesis of  $\text{CsSnI}_3$  (but not in the synthesis of  $\text{FASnI}_3$ ) to avoid the formation of  $\text{SnI}_4$ , as revealed by thermal analyses (**Figure 2**, and Figure S3–S5, Supporting Information). In particular, when comparing the DTA signal of  $\text{CsSnI}_3$  synthesized with and without  $\text{SnF}_2$  (Figure S3, Supporting Information), an endothermic peak around 160 °C, ascribed to the melting of  $\text{SnI}_4$ , is visible only in the case where no  $\text{SnF}_2$  is added. This peak is also absent in the case of  $\text{FASnI}_3$  even without additive (Figure 2).

In addition to the effect of  $\text{SnF}_2$ , all the samples were analyzed through DTA/TG to investigate their thermal stability (Figure 2).  $\text{CsSnI}_3$  is stable up to 450 °C, temperature at which it melts with the subsequent vaporization of  $\text{SnI}_2$  and  $\text{CsI}$ .<sup>[14]</sup> A very similar behavior was recorded for  $\text{Cs}(\text{SnPb})\text{I}_3$  (Figure S4, Supporting Information).  $\text{Cs}_2\text{SnI}_6$  seems less stable, decomposing at  $\approx 320$  °C due to  $\text{SnI}_4$  (b.p.  $\approx 350$  °C) which is more volatile than  $\text{SnI}_2$  (b.p.  $\approx 700$  °C). Indeed, the TG variations, equal to 53.6% and 47.0% in the first and second step, respectively, are

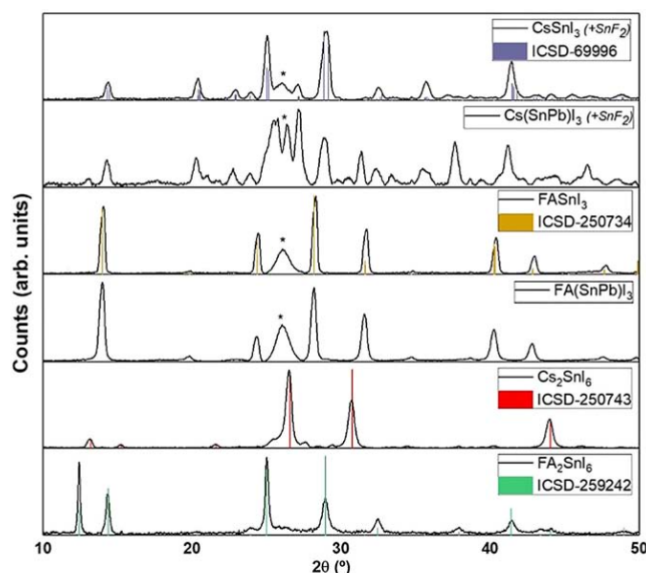


**Figure 1.** XRD diffractograms of mechanochemically synthesized tin perovskites (black lines) together with reference bulk patterns from Inorganic Crystal Structure Database (ICSD; color columns). A broad peak around  $2\theta = 26^\circ$  and marked with an asterisk is visible in most diffractograms due to parasitic diffraction from the adhesive tape used to fix the powder samples on the substrate (see Figure S1, Supporting Information). No reference pattern is available for mixed tin-lead perovskites. However, main peaks' positions match the reference pure-tin counterpart with a slight shift to lower angles due to the incorporation of the larger lead cation (see Figure S2, Supporting Information).

consistent with the loss of  $\text{SnI}_4$  and  $\text{CsI}$  (whose melting point is reported in the DTA curve at  $627^\circ\text{C}$ ).  $\text{FASnI}_3$  and  $\text{FA(SnPb)I}_3$  have considerable lower stability respect to the Cs-based counterparts because of the organic cation, which mainly drives the decomposition mechanism.<sup>[72]</sup> Interestingly,  $\text{FA}_2\text{SnI}_6$  is slightly more stable with respect to  $\text{FASnI}_3$  and  $\text{FA(SnPb)I}_3$ , with the initial weight loss starting around  $250^\circ\text{C}$  instead of  $200^\circ\text{C}$ . This might be due to a stronger interaction between FA molecules in  $\text{FA}_2\text{SnI}_6$ . However, the weight loss is much faster in this Sn(IV) compound, being completely vaporized at  $400^\circ\text{C}$ , consistent with the reaction:  $\text{FA}_2\text{SnI}_6 \rightarrow 2 \text{FAI} + \text{SnI}_4$ . Similarly, the decomposition mechanism for  $\text{FASnI}_3$  and  $\text{FA(SnPb)I}_3$  could be summarized, respectively, as  $\text{FASnI}_3 \rightarrow \text{FAI} + \text{SnI}_2$  and  $\text{FA(SnPb)I}_3 \rightarrow \text{FAI} + \frac{1}{2} \text{SnI}_2 + \frac{1}{2} \text{PbI}_2$ .<sup>[73]</sup> However, their TG and DTA curves evidence a more complex mechanism involving the formation of several intermediates. The last weight losses in TG curves of  $\text{FASnI}_3$  and  $\text{FA(SnPb)I}_3$  start at  $\approx 500^\circ\text{C}$ , temperature at which  $\text{SnI}_2$  is released, as also observed in the inorganic Cs-based counterparts (Figure S4, Supporting Information). This further confirms that Sn remains in +2 oxidation state in these hybrid perovskites without addition of  $\text{SnF}_2$ .

All Sn(II) and Sn(IV) perovskites were further analyzed by high-resolution XPS, to gather quantitative information on their chemical composition (XPS spectra of all compounds are shown in Figure 3 and atomic percentages of relevant elements are given in Table 1).

Carbon C 1s spectra of all samples show a peak at low binding energy (BE) which is ascribed to C—C bonds of adventitious carbon originating from exposure to organic volatile compounds in air. This peak is fixed to  $\text{BE} = 284.5 \text{ eV}$  for energy calibration, as standard practice. FA-based samples show a second peak at  $\text{BE} = 287.9 \pm 0.2 \text{ eV}$  assigned to the carbon atom in formamidinium cations. Although not shown in Figure 3,  $\text{CsSnI}_3$  and  $\text{Cs(SnPb)I}_3$  samples exhibit an additional peak at  $\text{BE} = 684.0 \text{ eV}$  corresponding to the F 1s orbital from  $\text{SnF}_2$  (see Figure S6, Supporting Information). Quantitative elemental analysis can be derived from these high-resolution spectra, after correcting for  $\text{SnF}_2$  contribution and considering only the highest energy component of C 1s. Atomic percentages of all relevant elements are given in Table 1.

Several observations can be made from Table 1. First of all,  $\text{FA}_2\text{SnI}_6$  seems highly degraded as only a very low amount of tin is detected. This suggests that this compound is severely affected by X-ray radiation and ultrahigh vacuum, leading most likely to the formation and subsequent loss of  $\text{SnI}_4$ . For all the other compounds, we note that the A:B ratios (where A is either Cs or FA and B is either Sn or SnPb) are very close to the expected 1:1 or 2:1 ratios, further confirming the material purity already observed by XRD. The same is true for the Sn:Pb ratios, which are close to 1:1 in both mixed tin-lead perovskites. The C:N ratios in FA-based samples are close to the expected 1:2 ratio for FA cations, confirming the assignment of the high-BE component

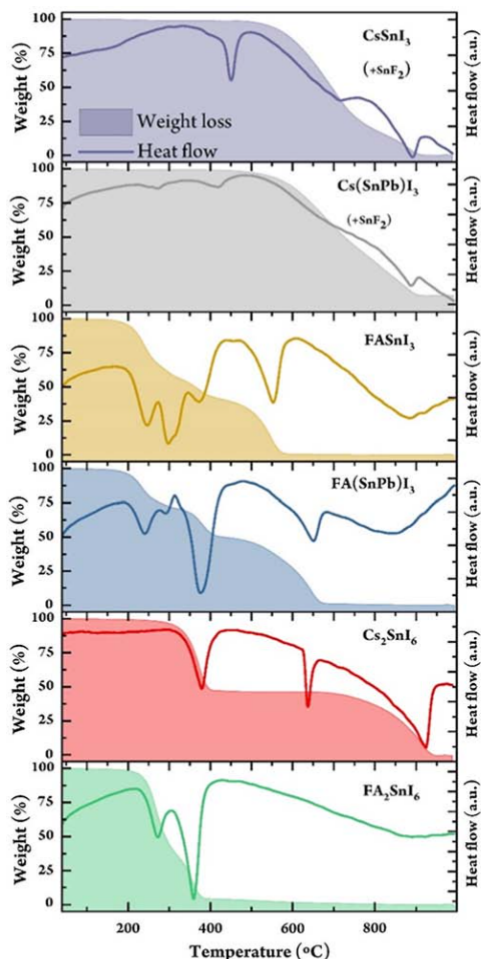


**Figure 2.** TG (filled area) and DTA (simple line) curves of all compounds in the 40–1000 °C range.

of C 1s spectra to FA and, importantly, suggesting that FA is not degraded during mechanochemical synthesis. This is not obvious a priori, as FAI is known to give different degradation byproducts, such as HCN or others, which could be volatile and hence alter the C:N ratio in the sample.<sup>[74]</sup> Nonetheless, we note that in all samples, the measured iodine concentration is lower than expected. In regards to this, it should be noted that we also observe oxygen (see Figure S7, Supporting Information), which is likely due to oxidation upon air exposure prior to analysis. Indeed, although the synthesis is carried out under nitrogen

(see experimental section for details), the samples are exposed to air for a short time before characterization. As photoelectron spectroscopies are surface-sensitive techniques (depth of analysis is typically few nanometers), even a small superficial oxidation will have a high impact on XPS results. In other words, it is unlikely that a significant formation of  $\text{SnO}_x$  affects the bulk of the perovskites here, as these species do not appear in the XRD signal (Figure 1). Furthermore, based on the literature, the formation of significant  $\text{SnO}_x$  in the bulk from air exposure is a process that typically takes several days or weeks.<sup>[46]</sup> A closer look at XPS spectra (Figure 3) allows to further discuss the oxidation states and chemical environments of the different elements in all samples. In the case of Cs-based samples, the Cs 3D spectra show a doublet with Cs  $3D_{5/2}$  peak located at  $\text{BE} = 724.0 \pm 0.3$  eV as well as I 3D spectra with I  $3D_{5/2}$  at  $\text{BE} = 618.7 \pm 0.2$  eV. These values are consistent with Cs(+1) and I(-1) oxidation states expected for inorganic iodide perovskites.<sup>[75]</sup> The Sn 3D spectra of  $\text{CsSnI}_3$  and  $\text{Cs}(\text{SnPb})\text{I}_3$  show two clear components (two doublets) ascribed to the addition of  $\text{SnF}_2$  in these samples, whereas  $\text{Cs}_2\text{SnI}_6$  shows only one component, as expected. Comparing the BE values of Sn(II) and Sn(IV) reported in the literature, it seems unlikely to easily distinguish them, as these values largely overlap.<sup>[76]</sup> In the case of  $\text{Cs}(\text{SnPb})\text{I}_3$ , we note that Pb 4f spectra are asymmetric with a low-BE component whose origin could not be clearly elucidated. Importantly, no metallic lead (or tin) was observed in any of the samples (the Sn 3D and Pb 4f peak positions for metallic tin and lead are indicated by dashed lines in Figure 2), which could otherwise have a detrimental effect on the perovskite optoelectronic properties.<sup>[77–79]</sup> In the case of FA-based samples, the peak at  $\text{BE} = 287.9 \pm 0.2$  eV is assigned to the carbon atom of FA cations. Accordingly, the N 1s peak is at  $\text{BE} = 400.2 \pm 0.1$  eV, corresponding to the N atoms of FA. Interestingly,  $\text{FASnI}_3$  sample shows a second peak at lower BE which may be ascribed to deprotonated amines in FA (noted in the graph as  $\text{C}-\text{NH}_2^0$ ).<sup>[80,81]</sup> Here, the deprotonation of FA is concomitant to the formation of different iodine species, as evidenced by the I 3D spectra, which only in the case of  $\text{FASnI}_3$  shows two different components. It is possible that a partial proton transfer from FA to  $\text{I}^-$  occurs. Nonetheless, the complexity of iodine chemistry in hybrid perovskites complicates the identification of the exact species formed here.<sup>[82]</sup> Sn 3D spectra of the three FA-based compounds show a main Sn  $3D_{5/2}$  peak centered at  $\text{BE} = 487.1 \pm 0.1$  eV, consistent both with Sn(II) and Sn(IV) iodide perovskites.<sup>[30]</sup> A small component at lower BE appears in the Sn 3D spectrum in the case of  $\text{FA}(\text{SnPb})\text{I}_3$  sample, somewhat similar to the lead signal in  $\text{Cs}(\text{SnPb})\text{I}_3$ . This low BE component might be due to oxidation as previously discussed. In summary, aside from  $\text{FA}_2\text{SnI}_6$  that is degraded under characterization, XPS spectra confirm overall the formation of the entire series of compounds, with signals that match with the expected spectra of the different perovskites (and the corresponding signal for  $\text{SnF}_2$  in the  $\text{CsSnI}_3$  and  $\text{Cs}(\text{SnPb})\text{I}_3$  samples).

Optical characterization (diffuse reflectance and photoluminescence) as well as UPS were performed to estimate the energetic positions of the valence band, Fermi level, and conduction band of these materials (Figure 4).

All compounds have an absorption onset in the near-infrared (NIR) region, suited for single-junction solar cells as well as rear



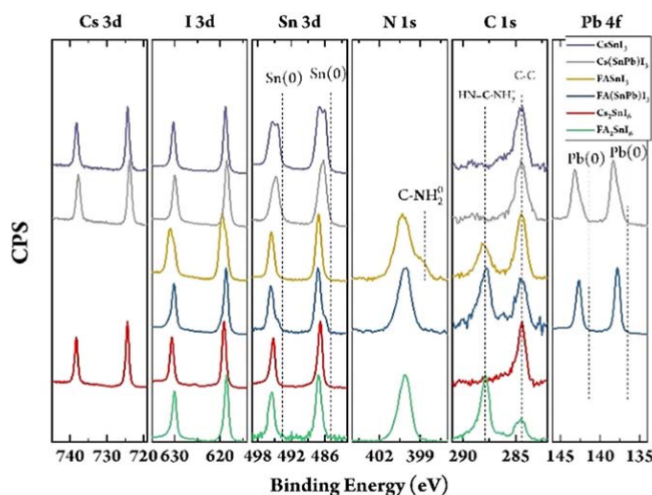


**Figure 3.** High-resolution XPS spectra of all main elements from the different compounds: Cs 3D, I 3D, Sn 3D, N 1s, C 1s, and Pb 4f regions. Additional O 1s and F 1s spectra are given as supporting information in Figure S6 and S7, Supporting Information.

**Table 1.** Atomic percentages of relevant elements based on high-resolution XPS spectra.

	Cs [at%]	I [at%]	Sn [at%]	N [at%]	C [at%]	Pb [at%]
CsSnI <sub>3</sub>	23.8	50.6	25.5	–	–	–
Cs(SnPb)I <sub>3</sub>	26.4	50.7	11.5	–	–	11.4
FASnI <sub>3</sub>	–	25.9	21.2	34.6	17.7	–
FA(SnPb)I <sub>3</sub>	–	34.5	9.3	31.0	17.0	8.2
Cs <sub>2</sub> SnI <sub>6</sub>	28.0	57.3	14.7	–	–	–
FA <sub>2</sub> SnI <sub>6</sub>	–	26.8	1.2	47.4	24.6	–

absorber in perovskite–perovskite tandem devices. All Sn(II)-based compounds have clear Stokes-shifted photoluminescence at room temperature (Figure 4), which make them potentially interesting also for NIR light-emitting diodes. The UPS secondary electron cutoff (Figure 4, middle column) and onset (right column) allow us to determine the work function and the energy difference between the Fermi level and the top of the valence band, respectively. Combining this information, we are able to estimate the characteristic energy levels as presented at the bottom of Figure 4. The addition of lead to Sn(II)-based perovskites results in deeper energy levels as compared with the pure-tin counterparts, which is consistent with the literature.<sup>[83]</sup> Furthermore, a red-shift in PL is clearly observed from pure-tin FASnI<sub>3</sub> to mixed tin-lead FA(SnPb)I<sub>3</sub>. Such behavior has also been noted by others, where mixed tin-lead perovskites were found to have a lower bandgap than both pure-tin and pure-lead compositions.<sup>[84]</sup> Interestingly, we do not observe this phenomenon in inorganic Cs-based perovskites. The apparent p-type

doping in FASnI<sub>3</sub> may be ascribed to a partial oxidation of Sn(II) to Sn(IV).<sup>[85]</sup> In contrast, mixed FA(SnPb)I<sub>3</sub> seems to be rather n-type. The origin of this effect is not fully elucidated. However, we already noted in the discussion of XPS data (Figure 3, blue spectra) that tin appeared to be slightly reduced, which might explain the n-type character observed here. Again, these effects do not seem to be significant for inorganic Cs-based compounds, as both appear rather intrinsic semiconductors. It must be noted though that these perovskites were formed with addition of SnF<sub>2</sub>. We therefore infer that SnF<sub>2</sub> helps maintaining the intrinsic nature of the semiconductor by preventing oxidation of tin. For Sn(IV) compounds, we clearly see a difference from the valence band maximum to the Fermi level (UPS onset, right column) of 1.5 eV, close to the reported bandgap for the same material.<sup>[86]</sup> Unfortunately, we cannot determine the optical bandgap, due to the smooth absorption onset and lack of photoluminescence. As it cannot be lower than 1.5 eV, we take this as the bandgap (it seems a reasonable assumption considering that the sample is clearly black; see Figure S8, Supporting Information). These observations mean that these materials are heavily n-doped. Again, this conclusion is in agreement with the literature, where Cs<sub>2</sub>SnI<sub>6</sub> has been reported by several groups to be intrinsically n-type.<sup>[45]</sup>

Eventually, we studied the mobility and lifetime of charge carriers by pulse-radiolysis TRMC (PR-TRMC). In this technique, materials are ionized with a high-energy electron pulse, and, subsequently, the change in conductivity is probed with GHz microwaves. If irradiation leads to mobile charge carriers, these will absorb part of the microwave power, decreasing the microwave power reflected by the cell. This decrease in microwave power is directly related to the change in conductivity and ultimately to the mobility of charge carriers.<sup>[87]</sup> We note that in

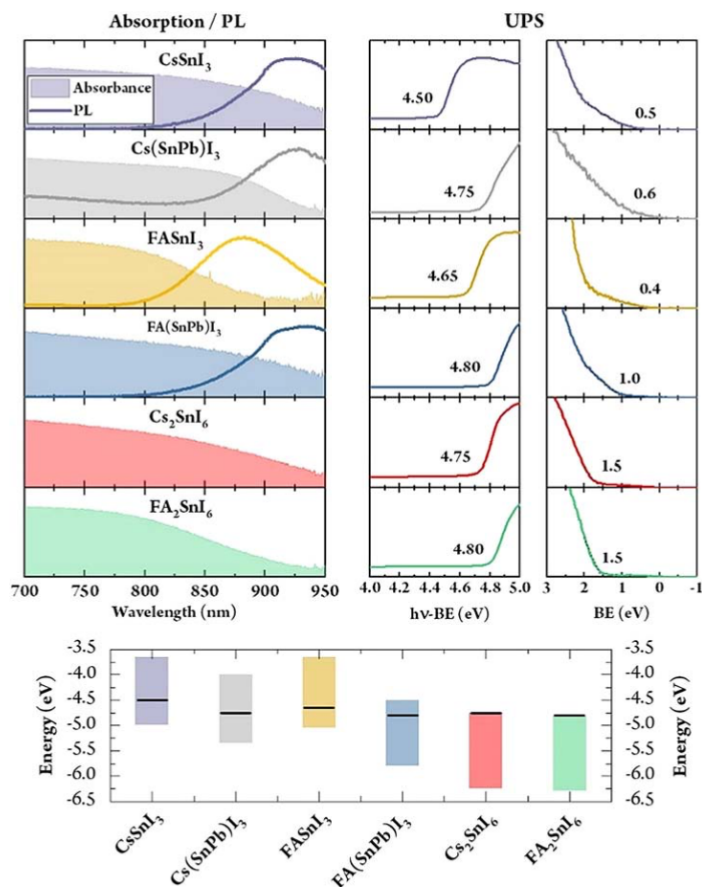
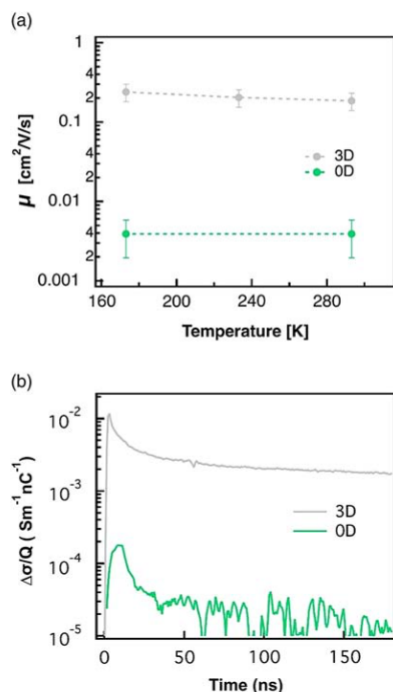


Figure 4. Optical characterization, UPS, and derived energy diagram.

most samples, measurements were not possible due to high or even complete absorption of the microwaves without irradiation. This is indicative of a considerable dark conductivity that hinders the detection of changes in conductivity upon irradiation. This behavior matches with the UPS measurements, where we observe that most samples are doped either with a p-type character, most likely caused by oxidation of Sn<sup>2+</sup> to Sn<sup>4+</sup>, or a n-type character. It has been shown in the literature that the presence of low concentrations of dark charge carriers has a strong detrimental effect on the electronic properties.<sup>[8,11,12,33,36]</sup> In fact, we are able to observe change of reflection (not quantifiable) that is very short-lived (<5 ns), which indicates that the generated charge carriers recombine or are trapped within the time resolution of the PR-TRMC experiment (see Figure S9, Supporting Information). Nevertheless, we were

able to obtain meaningful results on two compounds: a 3D Sn(II)-based compound (Cs(SnPb)I<sub>3</sub>) and a 0D Sn(IV)-based compound (FA<sub>2</sub>SnI<sub>6</sub>), which are hereafter simply referred to as 3D and 0D samples (Figure 5a). The fact that we can measure these samples matches with the UPS measurements, where Cs(SnPb)I<sub>3</sub> seems to be an intrinsic semiconductor. This intrinsic character is most likely achieved during synthesis. However, decreasing tin content with lead and adding SnF<sub>2</sub> suppresses Sn<sup>2+</sup> oxidation to Sn<sup>4+</sup> and as a result decreases the concentration of dark charge carriers. This is also in line with reported improved stabilities of tin-based perovskites when lead cations are present.<sup>[88]</sup>

As can be seen in Figure 5a, the 3D sample shows a charge carrier mobility is two orders of magnitude higher compared with the 0D sample (0.2 and 0.004 cm<sup>2</sup> Vs<sup>-1</sup>, respectively).



**Figure 5.** a) Mobility of charge carriers as a function of temperature and b) change of conductivity as a function of time of a Sn(II) 3D perovskite (grey) and a Sn(IV) 0D vacancy-ordered perovskite (green).

This is not surprising if we consider that the higher dimensionality of the 3D sample leads to a higher overlap of molecular orbitals. In both cases, the mobility was not found to significantly change when cooling from room temperature to 173 K. This indicates that the charge carrier mobility is not dominated by lattice scattering, but may be controlled by defects. The mobility of the 3D sample is of the same order of magnitude as for 3D lead-based perovskite samples prepared without the use of solvents,<sup>[89]</sup> whereas it is one to two orders of magnitude lower than 3D lead-based perovskites prepared by precipitation or single crystals, respectively.<sup>[89,90]</sup> This points out that dry mechanochemical synthesis as performed here might lead to a higher density of defects as opposed to solution-processing. Nonetheless, we believe that the synthesis may be optimized, for example by reducing the grinding time, which in this case was 5 h. Such a long time is probably unnecessary to yield phase-pure perovskites, and reducing it will likely limit detrimental effects of prolonged grinding (i.e., tin oxidation). The time-resolved conductivity (Figure 5b) of the 3D sample shows a fast-initial decay followed by a long-tail that does not decay to zero, even at very long times. Also, the maximum change in conductivity increases with the initial concentration of charge carriers (increase pulse

length; see Figure S10, Supporting Information). This behavior is similar to the observed for 3D  $\text{MAPbX}_3$  samples<sup>[89]</sup> and is attributed to second-order recombination with a limited concentration of trap states.<sup>[89]</sup> The fast-initial decay is caused by trapping of one of the charges, and the long tail signal comes from the remaining free charges.<sup>[89,90]</sup> As for the mobility, the carrier lifetime seems almost unaffected by temperature (see Figure S11, Supporting Information), indicating that the decay is still dominated by the recombination with a similar concentrations of the trap states as at room temperature. In the case of the 0D sample, the conductivity signal is very low and decays in less than 50 ns (Figure 5b). However, we observe a slight conductivity increase at low temperatures which may be related to less thermal vibration of the lattice (see Figure S12, Supporting Information).

### 3. Conclusion

In conclusion, we have been able to synthesize hybrid and inorganic pure-tin and mixed tin-lead iodide perovskites and vacancy-ordered perovskites with excellent phase purity as revealed by XRD. Detailed thermal stability studies were carried out revealing that all compounds are stable up to 200 °C, which is compatible with common operational conditions in optoelectronic devices. Inorganic perovskites based on Sn(II) were found to be stable beyond 400 °C, making them good candidates for single-source thermal deposition in thin films. Indeed, these compounds show a narrow bandgap suited for PVs and NIR light-emitting diodes. The charge carrier mobility was found to be rather low which could be due to oxidation during the long ball-milling mechanochemical synthesis. However, we demonstrated that the dark carrier conductivity in inorganic 3D Sn(II)-based compounds can be improved by the addition of Pb(II) and/or  $\text{SnF}_2$  during synthesis. Ongoing work is focused on optimizing the preparation conditions, especially reducing the grinding time to an ideal duration that will ensure a complete synthesis while avoiding possible detrimental effects.

### Supporting Information

Supporting Information is available from the Wiley Online Library or from the author.

### Acknowledgements

The research leading to these results has received funding from the European Union Programme for Research and Innovation Horizon 2020 (2014-2020) under the Marie Skłodowska-Curie Grant Agreement PerovSAMs No. 747599, and project INFORM (grant 675867), the Spanish Ministry of Economy and Competitiveness (MINECO) via the Unidad de Excelencia María de Maeztu MDM-2015-0538, MAT2017-88821-R and PCIN-2015-255, and the Generalitat Valenciana (Prometeo/2016/135 and GRISOLIAP/2017/089). H.J.B. acknowledges the support of ERA NET PCIN-2017-014. M.S. thanks the MINECO for his RyC contract. The research leading to these results in the Delft University of Technology has received funding from the European Research Council Horizon 2020 ERC Grant Agreement no. 648433.

### Conflict of Interest

The authors declare no conflict of interest.

### Keywords

low-bandgap, mechanochemistry, perovskites, solid-state, tin

Received: July 1, 2019

Published online:

- [1] B. Dänekamp, N. Droseros, F. Palazon, M. Sessolo, N. Banerji, H. J. Bolink, *ACS Appl. Mater. Interfaces* **2018**, *10*, 36193.
- [2] Q. A. Akkerman, L. Martínez-Sarti, L. Goldoni, M. Imran, D. Baranov, H. J. Bolink, F. Palazon, L. Manna, *Chem. Mater.* **2018**, *30*, 6915.
- [3] D. B. Mitzi, C. A. Feild, Z. Schlesinger, R. B. Laibowitz, *J. Solid State Chem.* **1995**, *114*, 159.
- [4] N. K. Noel, S. D. Stranks, A. Abate, C. Wehrenfennig, S. Guarnera, A. A. Haghighirad, A. Sadhanala, G. E. Eperon, S. K. Pathak, M. B. Johnston, A. Petrozza, L. M. Herz, H. J. Snaith, *Energy Environ. Sci.* **2014**, *7*, 3061.
- [5] Z. Zhao, F. Gu, Y. Li, W. Sun, S. Ye, H. Rao, Z. Liu, *Adv. Sci.* **2017**, *4*, 1700204.
- [6] J. Jiang, C. K. Onwudinanti, R. A. Hatton, P. A. Bobbert, S. Tao, *J. Phys. Chem. C* **2018**, *122*, 17660.
- [7] Z. Chen, J. J. Wang, Y. Ren, C. Yu, K. Shum, Z. Chen, J. J. Wang, Y. Ren, C. Yu, K. Shum, *Appl. Phys. Lett.* **2012**, *101*, 093901.
- [8] M. H. Kumar, S. Dharani, W. L. Leong, P. P. Boix, R. R. Prabhakar, T. Baikie, C. Shi, H. Ding, R. Ramesh, M. Asta, M. Graetzel, S. G. Mhaisalkar, N. Mathews, *Adv. Mater.* **2014**, *26*, 7122.
- [9] A. Wang, Y. Guo, F. Muhammad, Z. Deng, *Chem. Mater.* **2017**, *29*, 6493.
- [10] N. Wang, Y. Zhou, M. G. Ju, H. F. Garces, T. Ding, S. Pang, X. C. Zeng, N. P. Padture, X. W. Sun, *Adv. Energy Mater.* **2016**, *6*, 1.
- [11] S. Gupta, T. Bendikov, G. Hodes, D. Cahen, *ACS Energy Lett.* **2016**, *1*, 1028.
- [12] A. G. Kontos, A. Kaltzoglou, E. Siranidi, D. Palles, G. K. Angeli, M. K. Arfanis, V. Psycharis, Y. S. Raptis, E. I. Kamitsos, P. N. Trikalitis, C. C. Stoumpos, M. G. Kanatzidis, P. Falaras, *Inorg. Chem.* **2017**, *56*, 84.
- [13] P. Xu, S. Chen, H. J. Xiang, X. G. Gong, S. H. Wei, *Chem. Mater.* **2014**, *26*, 6068.
- [14] I. Chung, J. H. Song, J. Im, J. Androulakis, C. D. Malliakas, H. Li, A. J. Freeman, J. T. Kenney, M. G. Kanatzidis, *J. Am. Chem. Soc.* **2012**, *134*, 8579.
- [15] F. Hao, C. C. Stoumpos, D. H. Cao, R. P. H. Chang, M. G. Kanatzidis, *Nat. Photonics* **2014**, *8*, 489.
- [16] L. Y. Huang, W. R. L. Lambrecht, *Phys. Rev. B* **2013**, *88*, 1.
- [17] W. Li, J. Li, J. Li, J. Fan, Y. Mai, L. Wang, *J. Mater. Chem. A* **2016**, *4*, 17104.
- [18] D. Sabba, H. K. Mulmudi, R. R. Prabhakar, T. Krishnamoorthy, T. Baikie, P. P. Boix, S. Mhaisalkar, N. Mathews, *J. Phys. Chem. C* **2015**, *119*, 1763.
- [19] C. Grote, R. F. Berger, *J. Phys. Chem. C* **2015**, *119*, 22832.
- [20] D. E. Scaife, P. F. Weller, W. G. Fisher, *J. Solid State Chem.* **1974**, *9*, 308.
- [21] C. G. Ma, V. Krasnenko, M. G. Brik, *J. Phys. Chem. Solids* **2018**, *115*, 289.
- [22] E. L. Da Silva, J. M. Skelton, S. C. Parker, A. Walsh, *Phys. Rev. B* **2015**, *91*, 1.
- [23] K. P. Marshall, M. Walker, R. I. Walton, R. A. Hatton, *J. Mater. Chem. A* **2017**, *5*, 21836.
- [24] K. P. Marshall, M. Walker, R. I. Walton, R. A. Hatton, *Nat. Energy* **2016**, *1*, 1.
- [25] Y. K. Jung, J. H. Lee, A. Walsh, A. Soon, *Chem. Mater.* **2017**, *29*, 3181.
- [26] F. Hao, C. C. Stoumpos, R. P. H. Chang, M. G. Kanatzidis, *Nat. Photonics* **2014**, *8*, 489.
- [27] G. Thiele, B. R. Serr, *Zeitschrift für Krist. - New Cryst. Struct.* **1995**, *210*, 64.
- [28] K. P. Marshall, S. Tao, M. Walker, D. S. Cook, J. Lloyd-Hughes, S. Varagnolo, A. Wijesekara, D. Walker, R. I. Walton, R. A. Hatton, *Mater. Chem. Front.* **2018**, *2*, 1515.
- [29] F. Wang, J. Ma, F. Xie, L. Li, J. Chen, J. Fan, N. Zhao, *Adv. Funct. Mater.* **2016**, *26*, 3417.
- [30] T. Song, T. Yokoyama, C. C. Stoumpos, J. Logsdon, D. H. Cao, M. R. Wasielewski, S. Aramaki, M. G. Kanatzidis, *J. Am. Chem. Soc.* **2017**, *139*, 836.
- [31] F. Chiarella, A. Zappettini, F. Licci, I. Borriello, G. Cantele, D. Ninno, A. Cassinese, R. Vaglio, *Phys. Rev. B* **2008**, *77*, 1.
- [32] W. Liao, D. Zhao, Y. Yu, C. R. Grice, C. Wang, A. J. Cimaroli, P. Schulz, W. Meng, K. Zhu, R. Xiong, Y. Yan, *Adv. Mater.* **2016**, *28*, 9333.
- [33] S. J. Lee, S. S. Shin, Y. C. Kim, D. Kim, T. K. Ahn, J. H. Noh, J. Seo, S. I. Seok, *J. Am. Chem. Soc.* **2016**, *138*, 3974.
- [34] S. Shao, J. Liu, G. Portale, H. H. Fang, G. R. Blake, G. H. ten Brink, L. J. A. Koster, M. A. Loi, *Adv. Energy Mater.* **2018**, *8*, 1702019.
- [35] D. Zhao, C. Chen, C. Wang, M. M. Junda, Z. Song, C. R. Grice, Y. Yu, C. Li, B. Subedi, N. J. Podraza, X. Zhao, G. Fang, R. Xiong, K. Zhu, Y. Yan, *Nat. Energy* **2018**, *3*, 1093.
- [36] I. Chung, B. Lee, J. He, R. P. H. Chang, M. G. Kanatzidis, *Nature* **2012**, *485*, 486.
- [37] B. Lee, C. C. Stoumpos, N. Zhou, F. Hao, C. Malliakas, C. Y. Yeh, T. J. Marks, M. G. Kanatzidis, R. P. H. Chang, *J. Am. Chem. Soc.* **2014**, *136*, 15379.
- [38] Z. Xiao, H. Lei, X. Zhang, Y. Zhou, H. Hosono, T. Kamiya, *Bull. Chem. Soc. Jpn.* **2015**, *88*, 1250.
- [39] A. Kaltzoglou, M. Antoniadou, A. G. Kontos, C. C. Stoumpos, D. Perganti, E. Siranidi, V. Raptis, K. Trohidou, V. Psycharis, M. G. Kanatzidis, P. Falaras, *J. Phys. Chem. C* **2016**, *120*, 11777.
- [40] A. Kaltzoglou, M. Antoniadou, D. Perganti, E. Siranidi, V. Raptis, K. Trohidou, V. Psycharis, A. G. Kontos, P. Falaras, *Electrochim. Acta* **2015**, *184*, 466.
- [41] B. Saparov, J. P. Sun, W. Meng, Z. Xiao, H. S. Duan, O. Gunawan, D. Shin, I. G. Hill, Y. Yan, D. B. Mitzi, *Chem. Mater.* **2016**, *28*, 2315.
- [42] Z. Tan, J. Li, C. Zhang, Z. Li, Q. Hu, Z. Xiao, T. Kamiya, H. Hosono, G. Niu, E. Lifshitz, Y. Cheng, J. Tang, *Adv. Funct. Mater.* **2018**, *28*, 1801131.
- [43] A. E. Maughan, A. M. Ganose, A. M. Candia, J. T. Granger, D. O. Scanlon, J. R. Neilson, *Chem. Mater.* **2018**, *30*, 472.
- [44] A. E. Maughan, A. M. Ganose, M. A. Almaker, D. O. Scanlon, J. R. Neilson, *Chem. Mater.* **2018**, *30*, 3909.
- [45] Z. Xiao, Y. Zhou, H. Hosono, T. Kamiya, *Phys. Chem. Chem. Phys.* **2015**, *17*, 18900.
- [46] X. Qiu, B. Cao, S. Yuan, X. Chen, Z. Qiu, Y. Jiang, Q. Ye, H. Wang, H. Zeng, J. Liu, M. G. Kanatzidis, *Sol. Energy Mater. Sol. Cells* **2017**, *159*, 227.
- [47] J. C. R. Ke, D. J. Lewis, A. S. Walton, B. F. Spencer, P. O'Brien, A. G. Thomas, W. R. Flavell, *J. Mater. Chem. A* **2018**, *6*, 11205.
- [48] B. Lee, A. Krenselewski, S. Il Baik, D. N. Seidman, R. P. H. Chang, *Sustainable Energy Fuels* **2017**, *1*, 710.
- [49] O. Y. Posudievsky, N. V. Konoshchuk, V. L. Karbivskyy, O. P. Boiko, V. G. Koshechko, V. D. Pokhodenko, *Theor. Exp. Chem.* **2017**, *53*, 235.
- [50] D. Prochowicz, P. Yadav, M. Saliba, D. J. Kubicki, M. M. Tavakoli, S. M. Zakeeruddin, J. Lewiński, L. Emsley, M. Grätzel, *Nano Energy* **2018**, *49*, 523.



- [51] A. Karmakar, A. M. Askar, G. M. Bernard, V. V. Terskikh, M. Ha, S. Patel, K. Shankar, V. K. Michaelis, *Chem. Mater.* **2018**, *30*, 2309.
- [52] Y. El Ajjouri, F. Palazon, M. Sessolo, H. J. Bolink, *Chem. Mater.* **2018**, *30*, 7423.
- [53] D. J. Kubicki, D. Prochowicz, A. Hofstetter, S. M. Zakeeruddin, M. Grätzel, L. Emsley, *J. Am. Chem. Soc.* **2018**, *140*, 7232.
- [54] Z. Y. Zhu, Q. Q. Yang, L. F. Gao, L. Zhang, A. Y. Shi, C. L. Sun, Q. Wang, H. L. Zhang, *J. Phys. Chem. Lett.* **2017**, *8*, 1610.
- [55] D. Prochowicz, M. Franckevičius, A. M. Cie lak, S. M. Zakeeruddin, M. Grätzel, J. Lewiński, *J. Mater. Chem. A* **2015**, *3*, 20772.
- [56] A. D. Jodlowski, A. Yépez, R. Luque, L. Camacho, G. de Miguel, *Angew. Chem., - Int. Ed.* **2016**, *55*, 14972.
- [57] L. Protesescu, S. Yakunin, O. Nazarenko, D. N. Dirin, M. V. Kovalenko, *ACS Appl. Nano Mater.* **2018**, *1*, 1300.
- [58] D. J. Kubicki, D. Prochowicz, A. Hofstetter, S. M. Zakeeruddin, M. Grätzel, L. Emsley, *J. Am. Chem. Soc.* **2017**, *139*, 14173.
- [59] M. Sasaki, D. Prochowicz, W. Marynowski, J. Lewinski, *Eur. J. Inorg. Chem.* **2019**, *2019*, 2680.
- [60] Y. E. El Ajjouri, V. S. S. S. Chirvony, M. Sessolo, Y. El Ajjouri, V. S. Chirvony, M. Sessolo, F. Palazon, H. J. Bolink, *RSC Adv.* **2018**, *8*, 41548.
- [61] J. V. Milić, J. H. Im, D. J. Kubicki, A. Ummadisingsu, J. Y. Seo, Y. Li, M. A. Ruiz-Preciado, M. I. Dar, S. M. Zakeeruddin, L. Emsley, M. Grätzel, *Adv. Energy Mater.* **2019**, *1900284*, 1.
- [62] A. Karmakar, M. S. Dodd, X. Zhang, M. S. Oakley, M. Klobukowski, V. K. Michaelis, *Chem. Commun.* **2019**, *55*, 5079.
- [63] Y. El Ajjouri, V. S. Chirvony, N. Vassilyeva, M. Sessolo, F. Palazon, H. J. Bolink, *J. Mater. Chem. C* **2019**, *7*, 6240.
- [64] J. Breternitz, S. Levchenko, H. Hempel, G. Gurieva, A. Franz, A. Hoser, S. Schorr, *J. Phys. Energy* **2018**, *1*, 25003.
- [65] O. Y. Posudievsky, N. V. Konoshchuk, A. G. Shkavro, V. L. Karbivskiy, V. G. Koshechko, V. D. Pokhodenko, *ACS Appl. Nano Mater.* **2018**, *1*, 4145.
- [66] S. Yun, A. Kirakosyan, S. G. Yoon, J. Choi, *ACS Sustainable Chem. Eng.* **2018**, *6*, 3733.
- [67] M. Wilke, N. Casati, *Chem. - A: Eur. J.* **2018**, *24*, 17701.
- [68] D. Prochowicz, P. Yadav, M. Saliba, M. Sasaki, S. M. Zakeeruddin, J. Lewiński, M. Grätzel, *Sustainable Energy Fuels* **2017**, *1*, 689.
- [69] P. Pal, S. Saha, A. Banik, A. Sarkar, K. Biswas, *Chem. - A: Eur. J.* **2018**, *24*, 1811.
- [70] A. M. Askar, A. Karmakar, G. M. Bernard, M. Ha, V. V. Terskikh, B. D. Wiltshire, S. Patel, J. Fleet, K. Shankar, V. K. Michaelis, *J. Phys. Chem. Lett.* **2018**, *9*, 2671.
- [71] C. C. Stoumpos, C. D. Malliakas, M. G. Kanatzidis, *Inorg. Chem.* **2013**, *52*, 9019.
- [72] T. Leijtens, R. Prasanna, A. Gold-Parker, M. F. Toney, M. D. McGehee, *ACS Energy Lett.* **2017**, *2*, 2159.
- [73] Y. Dang, Y. Zhou, X. Liu, D. Ju, S. Xia, H. Xia, X. Tao, *Angew. Chem., - Int. Ed.* **2016**, *55*, 3447.
- [74] I. Lignos, L. Protesescu, D. B. Emiroglu, R. MacEiczky, S. Schneider, M. V. Kovalenko, A. J. DeMello, *Nano Lett.* **2018**, *18*, 1246.
- [75] K. Wang, Z. Jin, L. Liang, H. Bian, D. Bai, H. Wang, J. Zhang, Q. Wang, L. Shengzhong, *Nat. Commun.* **2018**, *9*, 1.
- [76] L. Jie, X. Chao, *J. Non-Cryst. Solids* **1990**, *119*, 37.
- [77] G. Sadoughi, D. E. Starr, E. Handick, S. D. Stranks, M. Gorgoi, R. G. Wilks, M. Bär, H. J. Snaith, *ACS Appl. Mater. Interfaces* **2015**, *7*, 13440.
- [78] H. Cho, S. H. Jeong, M. H. Park, Y. H. Kim, C. Wolf, C. L. Lee, J. H. Heo, A. Sadhanala, N. S. Myoung, S. Yoo, S. H. Im, R. H. Friend, T. W. Lee, *Science* **2015**, *350*, 1222.
- [79] W. Zhang, S. Pathak, N. Sakai, T. Stergiopoulos, P. K. Nayak, N. K. Noel, A. A. Haghighirad, V. M. Burlakov, D. W. Dequillettes, A. Sadhanala, W. Li, L. Wang, D. S. Ginger, R. H. Friend, H. J. Snaith, *Nat. Commun.* **2015**, *6*, 1.
- [80] A. Calloni, A. Abate, G. Bussetti, G. Berti, R. Yivlialin, F. Ciccacci, L. Duò, *J. Phys. Chem. C* **2015**, *119*, 21329.
- [81] G. Abdelmageed, L. Jewell, K. Hellier, L. Seymour, B. Luo, F. Bridges, J. Z. Zhang, S. Carter, *Appl. Phys. Lett.* **2016**, *109*, 233905.
- [82] D. Meggiolaro, S. G. Motti, E. Mosconi, A. J. Barker, J. Ball, C. A. Perini, F. Deschler, A. Petrozza, F. De Angelis, *Energy Environ. Sci.* **2018**, *11*, 702.
- [83] W. Ke, C. C. Stoumpos, M. G. Kanatzidis, *Adv. Mater.* **2018**, *182*, 1803230.
- [84] D. Zhao, Y. Yu, C. Wang, W. Liao, N. Shrestha, C. R. Grice, A. J. Cimaroli, L. Guan, R. J. Ellingson, K. Zhu, X. Zhao, R. G. Xiong, Y. Yan, *Nat. Energy* **2017**, *2*, 1.
- [85] S. J. Lee, S. S. Shin, J. Im, T. K. Ahn, J. H. Noh, N. J. Jeon, S. Il Seok, J. Seo, *ACS Energy Lett.* **2018**, *3*, 46.
- [86] H. O. Shin, B. M. Kim, T. Jang, K. M. Kim, D. H. Roh, J. S. Nam, J. S. Kim, U. Y. Kim, B. Lee, Y. Pang, T. H. Kwon, *Adv. Energy Mater.* **2019**, *9*, 1.
- [87] J. Warman, M. De Haas, G. Dicker, F. Grozema, *Chem. Mater.* **2004**, *16*, 4600.
- [88] T. Leijtens, R. Prasanna, K. A. Bush, G. E. Eperon, J. A. Raiford, A. Gold-Parker, E. J. Wolf, S. A. Swifter, C. C. Boyd, H. P. Wang, M. F. Toney, S. F. Bent, M. D. McGehee, *Sustainable Energy Fuels* **2018**, *2*, 2450.
- [89] M. C. Gélvez-Rueda, D. H. Cao, S. Patwardhan, N. Renaud, C. C. Stoumpos, G. C. Schatz, J. T. Hupp, O. K. Farha, T. J. Savenije, M. G. Kanatzidis, F. C. Grozema, *J. Phys. Chem. C* **2016**, *120*, 16577.
- [90] M. C. Gélvez-Rueda, N. Renaud, F. C. Grozema, *J. Phys. Chem. C* **2017**, *121*, 23392.



## Supporting Information

### Mechanochemical Synthesis of Sn(II) and Sn(IV) Iodide Perovskites and Study of Their Structural, Chemical, Thermal, Optical and Electrical Properties

Yousra El Ajjouri, Federico Locardi, María C. Gélvez-Rueda, Mirko Prato, Michele Sessolo, Maurizio Ferretti, Ferdinand C. Grozema, Francisco Palazon\* and Henk J. Bolink

#### Experimental details

##### Materials

Cesium iodide (CsI, > 99 %), tin(II) iodide (SnI<sub>2</sub>, > 97 %) and lead iodide (PbI<sub>2</sub>, 99.99 %) were purchased from TCI. Tin fluoride (SnF<sub>2</sub>, 99 %) and tin(IV) iodide (SnI<sub>4</sub>, 99.999 %) were purchased from Sigma-Aldrich. Formamidinium iodide (CH<sub>5</sub>N<sub>2</sub>I) was purchased from GreatCell Solar. All chemicals were stored in a nitrogen-filled glovebox and used as received without further purification.

##### Mechanochemical synthesis

AI:SnI<sub>2</sub> (1:1), AI:(Sn<sub>0.5</sub>Pb<sub>0.5</sub>)I<sub>2</sub> (1:1) and AI:SnI<sub>4</sub> (2:1) powders (A = Cs<sup>+</sup> or FA) were mixed inside a nitrogen-filled glovebox. Then, approximately 3 grams of the mixed precursors powder was introduced inside 10 mL zirconia ball-mill jars with 2 zirconia beads of 10 mm in diameter per jar. The jars were closed under nitrogen, preventing the powders to be exposed to air. Eventually, ball milling was performed with a MM-400 straight ball-mill from Retsch, at a frequency of 30 Hz for 5 hours.

##### XRD

X-ray diffraction was measured with a Panalytical Empyrean diffractometer equipped with a Cu-K $\alpha$  anode operated at 45 kV and 30 mA and a Pixel 1D detector in scanning line mode. Single scans were acquired in the  $2\theta = 10^\circ$  to  $50^\circ$  range in Bragg-Brentano geometry in air. Data analysis was performed with HighScore Plus software.

##### DTA/TGA

Differential thermal analysis (DTA) and thermogravimetric analysis (TGA) were performed using a LabsysEvo 1600 DTA/TGA (Setaram). The samples (approximately 15 mg) were put in an alumina crucible and heated from 30 to 1000 °C, at 45 °C min<sup>-1</sup> under an He atmosphere (30 mL min<sup>-1</sup>). The DTA and TGA curves were elaborated using the dedicated software Calisto (Setaram).

##### X-ray and ultraviolet photoelectron spectroscopy

X-ray and ultraviolet photoelectron spectroscopic (XPS) measurements were carried out with a Kratos Axis UltraDLD spectrometer. For this, high-resolution spectra were acquired at a pass energy of 10 eV using a monochromatic Al-K $\alpha$  source (15 kV, 20 mA). Ultraviolet photoelectron spectroscopic (UPS) measurements were performed using a He I (21.22 eV) discharge lamp, on an area of 55  $\mu\text{m}$  in diameter, at a pass energy of 5 eV and with a dwell time of 100 ms. The work function (the position of the Fermi level with respect to the vacuum level) was measured from the threshold energy for the emission of secondary electrons during He I excitation. A -9.0 V bias was applied to the sample to precisely determine the low-kinetic-energy cutoff. Then, the position of the valence band maximum (VBM) versus the vacuum level was estimated by measuring its distance from the Fermi level.

## Optical characterization

Absorbance was measured with a High Power UV-VIS fiber light source, integrated sphere and Avantes Starline AVASpec-2048L spectrometer in reflection mode. Photoluminescence was measured with a continuous wave 375 nm diode laser with a 400 nm filter and Hamamatsu PMA 11 spectrometer. For a typical spectrum 10 scans of 1 second were averaged.

## Pulse-radiolysis microwave conductivity measurements

Microwave conductivity measurements with irradiation by a high-energy electron pulse were made on micrometer crystals (approximately 45 mg) placed in a Polyether ether ketone (PEEK) holder. The PEEK holder is placed inside a rectangular waveguide cell (made of chemically inert gold-plated copper). The cell is contained in a cryostat in which the temperature can be varied between 123 K and 473 K. The irradiation intensity was varied between pulse lengths of 0.2 ns to 10 ns (charge carrier concentrations approx.  $1 \times 10^{15} \text{ cm}^{-3}$  to  $8 \times 10^{16} \text{ cm}^{-3}$ ). The frequency scan (28-38 GHz) fits were measured at a pulse length of 0.5 ns (approx.  $5.8 \times 10^{15} \text{ cm}^{-3}$ ).

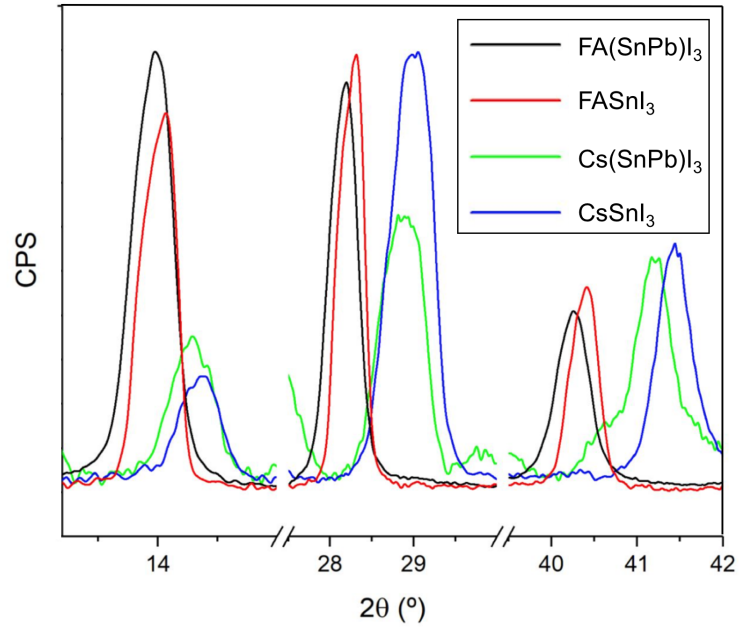


Figure C.1: Most representative parts of the X-ray diffractograms presented in Figure 5.2 for  $\text{CsSnI}_3$ ,  $\text{Cs}(\text{SnPb})\text{I}_3$ ,  $\text{FASnI}_3$  and  $\text{FA}(\text{SnPb})\text{I}_3$ . Larger ions (FA compared to  $\text{Cs}^+$  and  $\text{Pb}^{2+}$  compared to  $\text{Sn}^{2+}$ ) induce a shift towards lower diffraction angles.

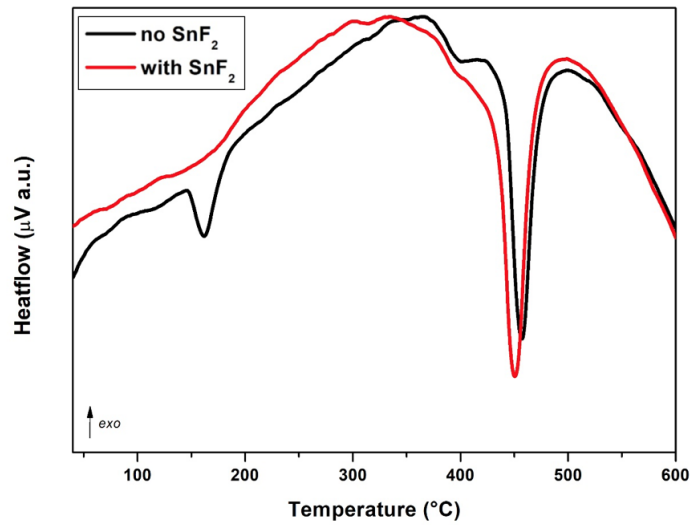


Figure C.2: Differential thermal analysis (DTA) of ball-milled  $\text{CsI} + \text{SnI}_2$  with (red curve) and without  $\text{SnF}_2$  (black curve).  $\text{SnI}_4$  is detected (identified by the peak at approximately  $160^{\circ}\text{C}$  in the black curve) only in the absence of  $\text{SnF}_2$ .

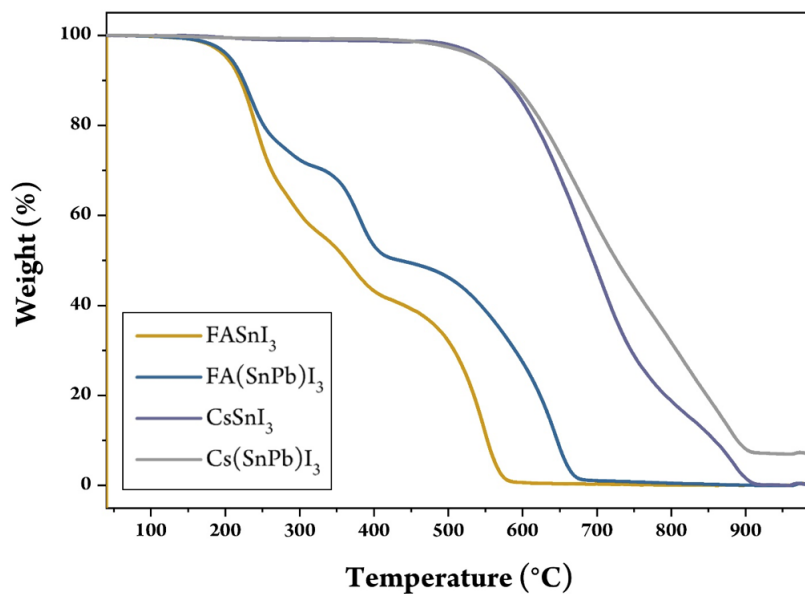


Figure C.3: Comparison between the thermogravimetric curves of  $\text{ASnI}_3$  and  $\text{A}(\text{SnPb})\text{I}_3$  ( $A = \text{Cs}^+$  or  $\text{FA}$ ).

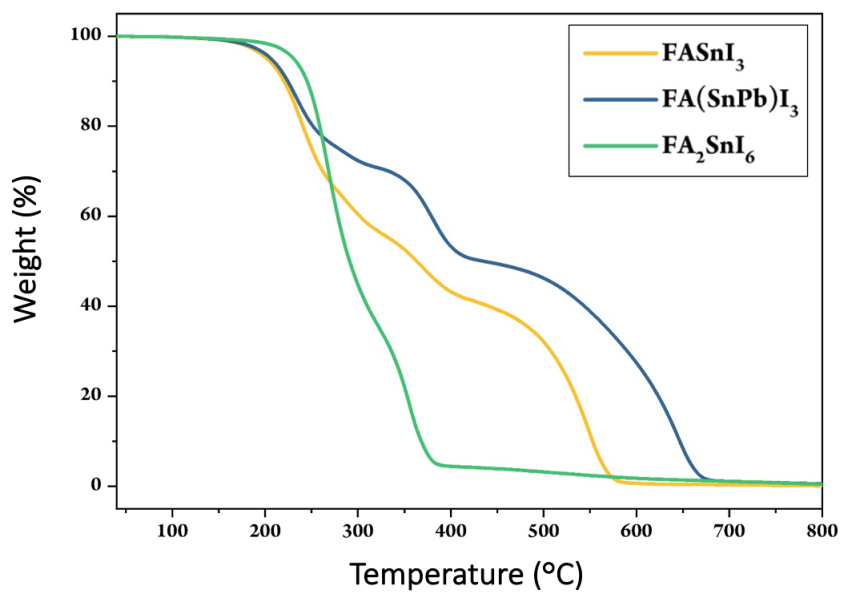


Figure C.4: Comparison between the thermogravimetric curves of  $\text{FASnI}_3$ ,  $\text{FA}(\text{SnPb})\text{I}_3$  and  $\text{FA}_2\text{SnPbI}_6$ .

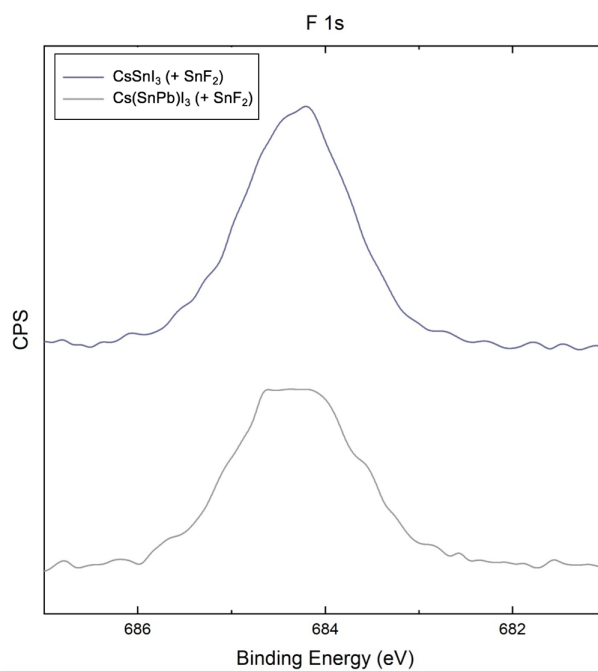


Figure C.5: *F 1s* XPS spectra of  $\text{CsSnI}_3$  and  $\text{Cs}(\text{SnPb})\text{I}_3$  prepared in the presence of  $\text{SnF}_2$ .

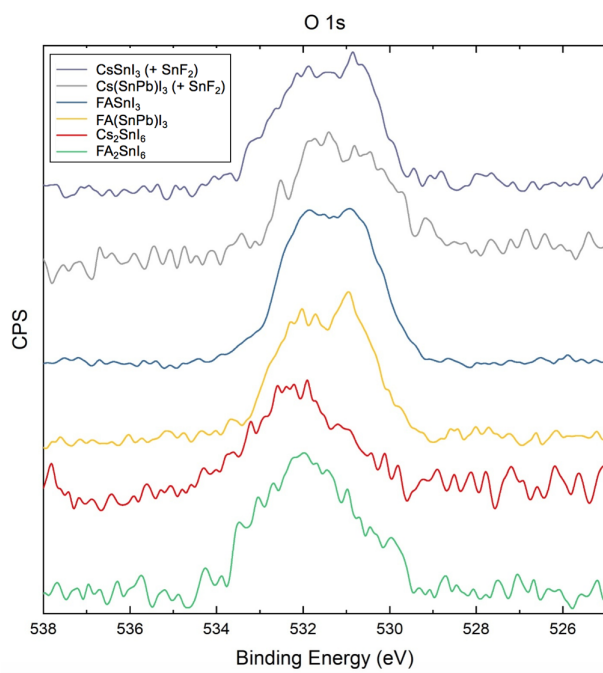


Figure C.6: *O 1s* XPS spectra of all *Sn(II)* and *Sn(IV)* compounds:  $\text{CsSnI}_3$  (+  $\text{SnF}_2$ ),  $\text{Cs}(\text{SnPb})\text{I}_3$  (+  $\text{SnF}_2$ ),  $\text{FASnI}_3$ ,  $\text{FA}(\text{SnPb})\text{I}_3$ ,  $\text{Cs}_2\text{SnI}_6$  and  $\text{FA}_2\text{SnI}_6$ .



Figure C.7: Photograph of  $\text{Cs}_2\text{SnI}_6$  powder – exposed to air – fixed on adhesive tape on a glass substrate.

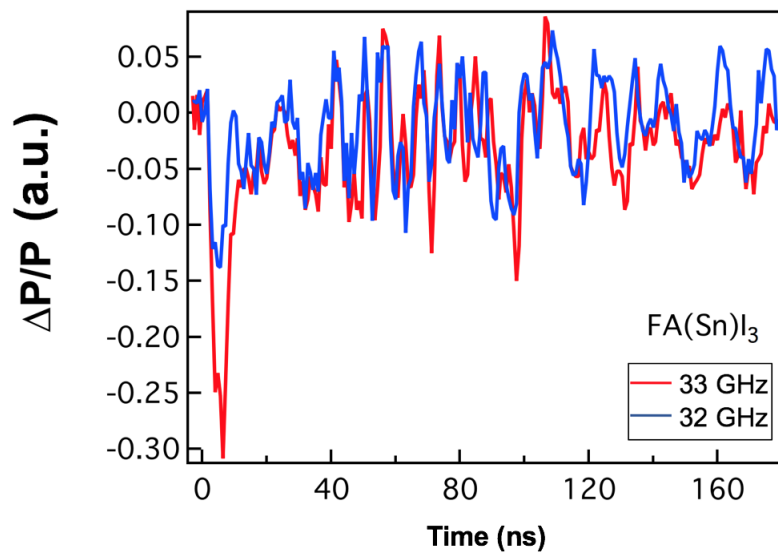


Figure C.8: Change of reflected microwave power ( $\Delta P/P$ ) as a function of time for  $\text{FASnI}_3$  presented at different microwave frequencies (32 to 33 GHz).

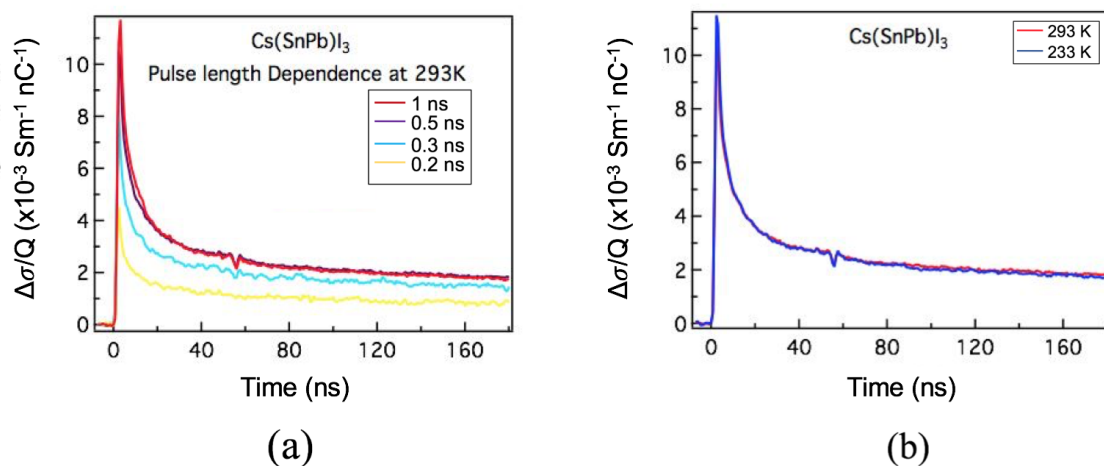


Figure C.9: Charge carrier lifetime ( $\Delta\sigma/Q$ ) of the 3D sample ( $\text{Cs}(\text{SnPb})\text{I}_3$ ) at (a) different pulse widths and (b) different temperatures.

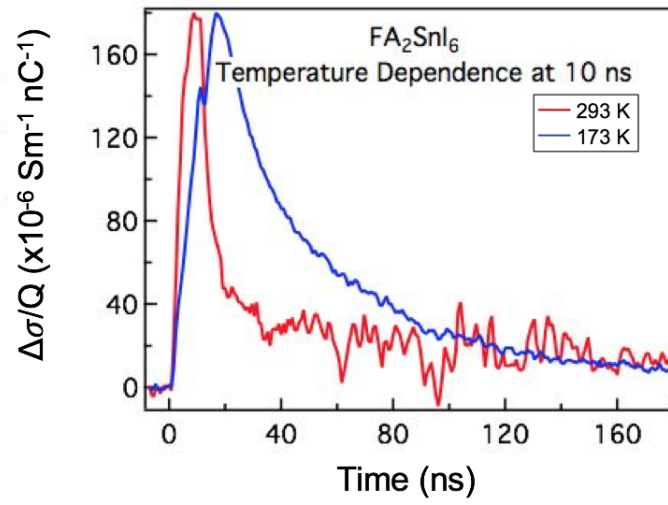


Figure C.10: Charge carrier lifetime ( $\Delta\sigma/Q$ ) of the 0D sample ( $FA_2SnI_6$ ) at different temperatures.

# Appendix D



Cite this: *J. Mater. Chem. C*, 2019, 7, 6236Received 2nd April 2019,  
Accepted 8th May 2019

DOI: 10.1039/c9tc01765h

rsc.li/materials-c

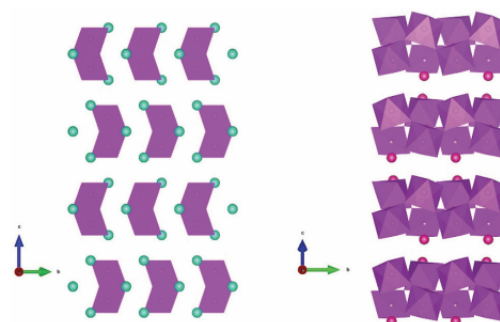
## Low-dimensional non-toxic $A_3Bi_2X_9$ compounds synthesized by a dry mechanochemical route with tunable visible photoluminescence at room temperature†

Yousra El Ajjouri,<sup>a</sup> Vladimir S. Chirvony,<sup>ab</sup> Natalia Vassilyeva,<sup>a</sup> Michele Sessolo,<sup>b</sup> Francisco Palazon<sup>✉\*</sup> and Henk J. Bolink<sup>✉</sup><sup>a</sup>

We have synthesized fifteen inorganic and hybrid organic–inorganic non-toxic  $A_3Bi_2X_9$  compounds ( $A = K^+, Rb^+, Cs^+, CH_3NH_3^+$  and  $HC(NH_2)_2^+$ ;  $X = I^-, Br^-, Cl^-$ ) through dry mechanochemistry. We demonstrate that this synthetic method is very well suited to prepare compounds from poorly soluble precursors, allowing thus the preparation of so far unreported compounds. X-ray diffraction analysis demonstrates the high crystallinity of the so-formed ternary bismuth halides. Furthermore, we show that, through substitution of the A-cation and X-anion, the bandgap of these compounds can be tuned to absorb throughout the whole visible spectrum. As-prepared powders of  $Cs_3Bi_2Br_9$  and  $Cs_3Bi_2I_9$ , without any passivating agents show room-temperature photoluminescence covering the visible spectrum from 450 nm to 800 nm, making them especially promising for white-light emission.

Over the past decade, lead-halide perovskites (LHPs) have been intensively investigated due to their excellent optoelectronic properties. These are the result, among other reasons, of the intrinsic point defect tolerance of LHPs, which has been suggested to be crucial in achieving long charge carrier diffusion lengths, enabling high efficiencies in perovskite devices.<sup>1</sup> However, the future commercialization of state-of-the-art perovskite optoelectronic devices is hampered by the use of toxic lead and the unclear environmental stability of LHPs. Therefore, lead-free perovskite alternatives are being sought. The defect-tolerant character of LHPs has been linked to the presence of the  $ns^2$  electron lone pair in  $Pb^{2+}$ , a characteristic that is shared with  $Bi^{3+}$  which has a  $6s^2$  electron configuration.<sup>2–7</sup> Hence,  $Bi(III)$ -halide compounds are envisioned as interesting alternatives, with potentially the same defect tolerance as LHPs. Moreover, bismuth is a very abundant element, as well as non-toxic and stable in

ambient conditions.<sup>3</sup> The replacement of  $Pb^{2+}$  with  $Bi^{3+}$  affects the stoichiometry of the ternary metal halides. The general formula for LHPs can be written as  $APbX_3$  where A is a monovalent cation and X a monovalent halide anion. The bismuth-counterparts, however, have a “3-2-9” stoichiometry corresponding to the general formula  $A_3Bi_2X_9$ . This is sometimes seen as a “defect” or “vacancy-ordered” perovskite. As explained by McCall *et al.* “defect perovskites are derivative structures that possess the same corner-sharing  $MX_6$  octahedra as the  $AMX_3$  aristotype but form different structures due to cation deficiencies in order to satisfy charge balance restrictions. . . trivalent cations form  $A_3M_2\Box X_9$  structures [ $\Box$  represents a vacancy] with 2/3 occupancy of the M sites of the  $A_3M_3X_9$  perovskite formula”.<sup>8</sup> In the case of  $A_3Bi_2X_9$  compounds, different crystal structures are obtained by varying the chemical composition. As an example, while  $Cs_3Bi_2I_9$  crystallizes in a zero-dimensional structure with fully decoupled dimers of  $BiI_6$  octahedra,  $Rb_3Bi_2I_9$  crystallizes in a 2D structure with layers of corner-sharing  $BiI_6$  octahedra (see Scheme 1).<sup>9</sup> This reduced dimensionality is the reason why these compounds



Scheme 1  $Cs_3Bi_2I_9$  (left) and  $Rb_3Bi_2I_9$  (right) crystal structures, viewed from the a-axis.  $Cs_3Bi_2I_9$  presents a zero-dimensional structure with dimers of  $BiI_6$  octahedra (pink) fully decoupled while  $Rb_3Bi_2I_9$  presents a 2D structure with layers of corner-sharing  $BiI_6$  octahedra. Green and red balls represent  $Cs^+$  and  $Rb^+$  cations.

<sup>a</sup> Instituto de Ciencia Molecular, Universidad de Valencia, C/ Catedrático J. Beltrán 2, 46100 Paterna, Spain. E-mail: francisco.palazon@uv.es

<sup>b</sup> UMDO (Unidad de Materiales y Dispositivos Optoelectrónicos), Instituto de Ciencia de los Materiales, Universidad de Valencia, Valencia 46071, Spain

† Electronic supplementary information (ESI) available: Experimental details and XRD. See DOI: 10.1039/c9tc01765h

are also referred to as low-dimensional perovskites, although the term perovskite is questionable here.

One of the main bottlenecks in developing bismuth-halide-based compounds resides in the poor solubility of bismuth salts in common solvents.<sup>10,11</sup> In this study, fifteen different  $A_3Bi_2X_9$  compounds ( $A = K^+, Rb^+, Cs^+, CH_3NH_3^+ -MA-$ , and  $HC(NH_2)_2^+ -FA-$ ;  $X = I^-, Br^-, Cl^-$ ) were synthesized by a dry mechanochemical approach *via* ball-milling of stoichiometric precursors. This technique allows the formation of multinary metal halide compounds in a simple and time-efficient manner.<sup>12–15</sup>

To the best of our knowledge, there is only one previous report on dry mechanochemical synthesis of ternary bismuth-iodide compounds.<sup>16</sup> We are unaware of reports about the synthesis (through any method) of several of the chloride and bromide analogues such as  $FA_3Bi_2Br_9$ ,  $FA_3Bi_2Cl_9$  or  $Rb_3Bi_2Cl_9$ . Hereby, we investigate the structural and optical characteristics of the fifteen compounds described above. X-ray diffraction (XRD) analyses show the excellent crystal quality of mechanochemically-synthesized powders. These have a tunable bandgap from the near-UV to the red part of the visible spectrum as shown by optical absorption. Furthermore, bulk  $Cs_3Bi_2I_9$  and  $Cs_3Bi_2Br_9$  show a broad visible

photoluminescence at room temperature, even without the addition of passivating agents. This paves the way to the use of these materials for lighting applications.

Powders obtained by ball-milling stoichiometric amounts of inorganic  $AX$  and  $BiX_3$  were analyzed by XRD (see Fig. 1). In the five cases ( $Cs_3Bi_2I_9$ ,  $Cs_3Bi_2Br_9$ ,  $Cs_3Bi_2Cl_9$ ,  $Rb_3Bi_2I_9$ , and  $Rb_3Bi_2Br_9$ ) where we could compare the diffractograms with bulk reference patterns published in the Inorganic Crystal Structure Database (ICSD), excellent matches are obtained. This points towards the high phase-purity obtained with this simple and dry method. No published reference pattern was found for  $Rb_3Bi_2Cl_9$ . However, when compared to  $Rb_3Bi_2I_9$  and  $Rb_3Bi_2Br_9$ , a clear gradual shift towards higher angles (smaller interatomic distances) is visible when the halide ionic radius is reduced from  $I^-$  to  $Cl^-$ . This suggests a shrinkage of the unit cell. In order to assess this more accurately, whole-pattern Le Bail fits were conducted on all three  $Rb_3Bi_2X_9$  compounds (see Fig. S2, ESI†). The refined cell parameters and unit cell volume are summarized in Table 1. This is strong evidence for the formation of  $Rb_3Bi_2Cl_9$ , which to the best of our knowledge has not been experimentally synthesized before. The potassium-based series

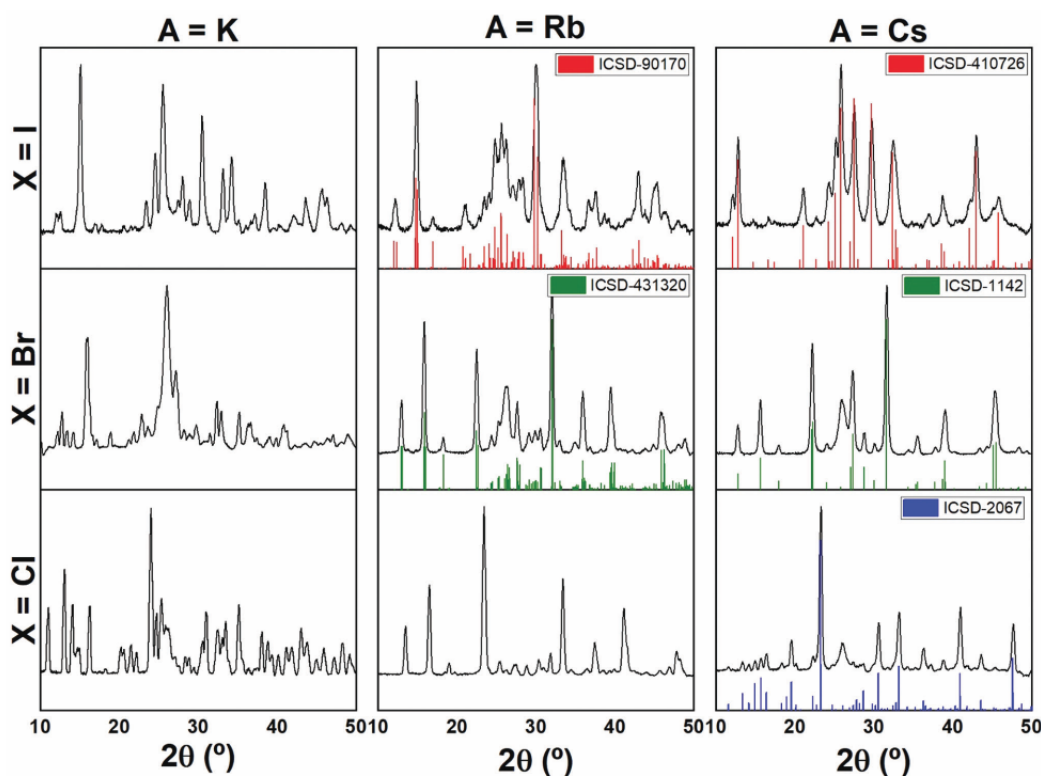


Fig. 1 XRD characterization of mechanochemically-synthesized inorganic  $A_3Bi_2X_9$  ( $A = K, Rb, Cs$ ;  $X = I, Br, Cl$ ; black lines) and reference bulk patterns when available from the Inorganic Crystal Structure Database (ICSD; color columns). A broad feature around  $2\theta = 26^\circ$  is sometimes visible, due to the parasitic diffraction of the underlying adhesive tape used to fix the powder samples on the holder (see Fig. S1, ESI†).

Table 1 Refined cell parameters for  $\text{Rb}_3\text{Bi}_2\text{X}_9$  compounds

	Reference	This work
$\text{Rb}_3\text{Bi}_2\text{I}_9$ ( $P1c1$ )	$a = 14.690 \text{ \AA}$ $b = 8.195 \text{ \AA}$ $c = 25.645 \text{ \AA}$ $V = 2516.82 \text{ \AA}^3$	$a = 14.6874(8) \text{ \AA}$ $b = 8.1982(6) \text{ \AA}$ $c = 25.646(1) \text{ \AA}$ $V = 2517.5(3) \text{ \AA}^3$
$\text{Rb}_3\text{Bi}_2\text{Br}_9$ ( $P12_1/a1$ )	$a = 13.5601(1) \text{ \AA}$ $b = 7.9124(5) \text{ \AA}$ $c = 19.3510(8) \text{ \AA}$ $V = 2076.13 \text{ \AA}^3$	$a = 13.570(1) \text{ \AA}$ $b = 7.913(5) \text{ \AA}$ $c = 19.351(1) \text{ \AA}$ $V = 2077.8(3) \text{ \AA}^3$
$\text{Rb}_3\text{Bi}_2\text{Cl}_9$ ( $P12_1/a1$ )	—	$a = 13.3655(9) \text{ \AA}$ $b = 7.9654(8) \text{ \AA}$ $c = 15.423(1) \text{ \AA}$ $V = 1641.8(2) \text{ \AA}^3$

are more difficult to analyze as no reference patterns could be found for any  $\text{K}_3\text{Bi}_2\text{X}_9$  compound. Nonetheless, when comparing the diffractograms after ball-milling with the reference patterns of the precursors (see Fig. S3, ESI†) it is clear that these have reacted to form a new phase, which it seems reasonable to attribute to  $\text{K}_3\text{Bi}_2\text{X}_9$ . This hypothesis is further supported by the optical absorption spectra (see Fig. 3).

Hybrid compounds with organic  $\text{MA}^+$  and  $\text{FA}^+$  cations were also formed by dry ball-milling of inorganic  $\text{BiX}_3$  salts and organic AX (A = MA or FA). Again, when comparing X-ray

Table 2 Refined cell parameters for hybrid organic–inorganic compounds

	Reference	This work
$\text{MA}_3\text{Bi}_2\text{I}_9$ ( $C12/c1$ )	$a = 8.4952(6) \text{ \AA}$ $b = 14.7126(10) \text{ \AA}$ $c = 21.6855(14) \text{ \AA}$ $V = 2710.39 \text{ \AA}^3$	$a = 8.5340(5) \text{ \AA}$ $b = 14.654(1) \text{ \AA}$ $c = 21.653(1) \text{ \AA}$ $V = 2707.9(3) \text{ \AA}^3$
$\text{FA}_3\text{Bi}_2\text{I}_9$ ( $C12/c1$ )	—	$a = 8.8389(8) \text{ \AA}$ $b = 14.909(2) \text{ \AA}$ $c = 21.851(3) \text{ \AA}$ $V = 2879.5(6) \text{ \AA}^3$
$\text{MA}_3\text{Bi}_2\text{Br}_9$ ( $P\bar{3}m1$ )	$a = 8.188(2) \text{ \AA}$ $b = 8.188(2) \text{ \AA}$ $c = 9.927(3) \text{ \AA}$ $V = 576.374 \text{ \AA}^3$	$a = 8.2086(2) \text{ \AA}$ $b = 8.2086(2) \text{ \AA}$ $c = 10.025(1) \text{ \AA}$ $V = 585.03(6) \text{ \AA}^3$
$\text{FA}_3\text{Bi}_2\text{Br}_9$ ( $P\bar{3}m1$ )	—	$a = 8.4071(8) \text{ \AA}$ $b = 8.4071(8) \text{ \AA}$ $c = 10.183(2) \text{ \AA}$ $V = 623.3(1) \text{ \AA}^3$
$\text{MA}_3\text{Bi}_2\text{Cl}_9$ ( $Pm\bar{c}n$ )	$a = 7.713(8) \text{ \AA}$ $b = 13.26(2) \text{ \AA}$ $c = 20.43(3) \text{ \AA}$ $V = 2089.47 \text{ \AA}^3$	$a = 7.7109(3) \text{ \AA}$ $b = 13.2628(6) \text{ \AA}$ $c = 20.4313(6) \text{ \AA}$ $V = 2089.5(1) \text{ \AA}^3$
$\text{FA}_3\text{Bi}_2\text{Cl}_9$ ( $Pm\bar{c}n$ )	—	$a = 8.045(1) \text{ \AA}$ $b = 13.387(2) \text{ \AA}$ $c = 21.062(3) \text{ \AA}$ $V = 2268.3(6) \text{ \AA}^3$

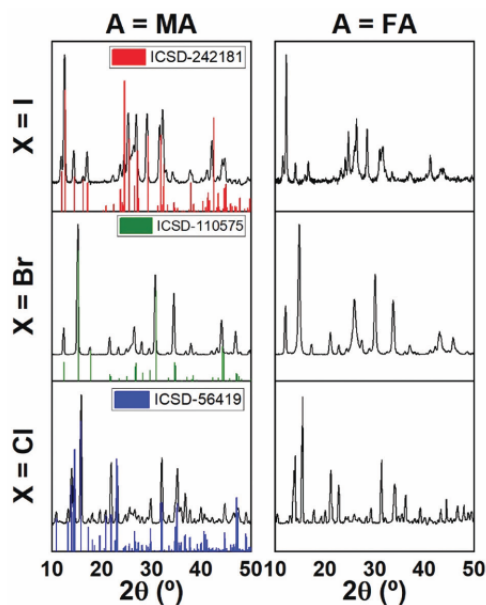


Fig. 2 XRD characterization of mechanochemically-synthesized hybrid  $\text{A}_3\text{Bi}_2\text{X}_9$  (A = MA, FA; X = I, Br, Cl; black lines) and reference bulk patterns from the Inorganic Crystal Structure Database (ICSD) for A = MA (color columns). A more detailed comparison on diffractograms of same halide composition but different A-cation is presented in Fig. S4–S6 (ESI†). A broad feature around  $2\theta = 26^\circ$  is sometimes visible, due to the parasitic diffraction of the underlying adhesive tape used to fix the powder samples on the holder (see Fig. S1, ESI†).

diffractograms of the resulting MA-powders with reference bulk patterns from ICSD (see Fig. 2) we observe a very good match, highlighting the high phase purity of the mechanochemically-synthesized hybrid  $\text{MA}_3\text{Bi}_2\text{X}_9$  compounds. To the best of our knowledge, only few reports on  $\text{FA}_3\text{Bi}_2\text{I}_9$  exist,<sup>10,17</sup> while we were unable to find any reports on  $\text{FA}_3\text{Bi}_2\text{Br}_9$  or  $\text{FA}_3\text{Bi}_2\text{Cl}_9$ . For the complete halide series, the diffractograms of the compounds obtained with FA closely match those of the corresponding MA analogues with a slight shift to lower angles, due to the higher ionic radius of FA compared to MA. Whole-pattern fits were conducted for all six hybrid compounds (see Fig. S4–S6, ESI†). Refined cell parameters confirm the cell expansion upon increase of the organic cation from MA to FA (see Table 2). Hence, again, we deduce the formation of highly phase-pure materials for all  $\text{FA}_3\text{Bi}_2\text{X}_9$  compounds.

The optical properties of the different inorganic and hybrid compounds (see Fig. 3) were analyzed by sandwiching the thin powders in between two quartz plates. The optical bandgaps of all materials, as derived from their absorption onsets (see Fig. 3) span from the near-UV (3.3 eV/380 nm for  $\text{K}_3\text{Bi}_2\text{Cl}_9$ ) to the red part of the visible spectrum (1.9 eV/650 nm for  $\text{Cs}_3\text{Bi}_2\text{I}_9$ ). Similar to what is observed in lead halide perovskites also for these “3-2-9” bismuth compounds the bandgap is strongly dependent on the X anion, with the smaller anion ( $\text{Cl}^-$ ) giving the larger bandgaps and *vice versa*.<sup>18</sup> To a lesser extent, the same trend is visible with varying the ionic radius of the A-cation with X =  $\text{Cl}^-$  and X =  $\text{Br}^-$ . Indeed, for these halides we observe that the bandgap is systematically wider for A =  $\text{K}^+$ , followed by A =  $\text{Rb}^+$  followed by the other cations. This trend, however, does not seem to apply for X =  $\text{I}^-$ . While the difference between the bandgaps of the iodide compounds is smaller (about 0.1 eV from 610 nm to 650 nm) as compared to the chloride series (about 0.3 eV difference corresponding to absorption onsets of



380 nm to 420 nm), it must be noted that, as opposed to 3D halide perovskites, these low-dimensional  $A_3Bi_2X_9$  compounds crystallize in very different structures depending on their composition, as explained in the introduction (see Scheme 1). Hence, it is not surprising that the variations of optical properties with composition do not follow a homogenous trend for all cases. Moreover, we note the presence of a secondary absorption peak blue-shifted by *ca.* 50 nm in almost all compounds. Though the origin of this feature is unclear, it is consistent with previous reports on the same and related materials.<sup>16,19</sup> Despite the not yet encouraging results in photovoltaics,<sup>3,20–22</sup> these materials are promising candidates in electroluminescence applications.<sup>8,23–28</sup> A few recent reports have demonstrated high photoluminescence (PL) quantum yields from ligand-passivated colloidal nanoparticles of  $Cs_3Bi_2Br_9$ ,  $MA_3Bi_2Br_9$ , and  $MA_3Bi_2Cl_9$  in solution.<sup>23,27–30</sup> Others in contrast have not detected visible PL in similar colloidal quantum dots,<sup>17</sup> or achieved photoluminescence quantum yields lower than 1%.<sup>31</sup> Here, we show that mechanochemically-synthesized dry powders of  $Cs_3Bi_2Br_9$  and  $Cs_3Bi_2I_9$  show clearly visible PL at room temperature (see Fig. 3). This photoluminescence is slightly Stokes-shifted from the absorption

edge, with maximums at 478 nm and 657 nm respectively for  $X = Br^-$  and  $X = I^-$ . In both cases the PL spectrum is broad and asymmetric, consistent with previous reports.<sup>23,27,28,31</sup> As a result, the visible spectrum is almost fully-covered from 450 nm to 800 nm with these two compounds, which is of interest for the generation of white light. In order to demonstrate this, as a proof of concept, we fabricated a pellet by pressing a finely ground mixture of both powders with transparent PMMA beads. The corresponding PL spectrum (Fig. S7, ESI†) presents a broad emission with CIE coordinates (0.42; 0.45) corresponding to a warm white light with correlated color temperature of 3615 K.

## Conclusions

In summary we have successfully synthesized fifteen different non-toxic bismuth halide ternary compounds by dry ball-milling of stoichiometric precursors. Structural characterization by X-ray diffraction revealed the excellent quality of the thus-formed materials, without noticeable unreacted precursors or byproducts. These materials have useful bandgaps for lighting applications as they cover most of the visible spectrum. Moreover, bulk dry  $Cs_3Bi_2Br_9$  and  $Cs_3Bi_2I_9$  exhibit photoluminescence at room temperature even without passivating agents. This holds promise to obtain high photoluminescence efficiency when passivating agents are added and paves the way to the widespread use of these non-toxic perovskite-related materials for lighting applications.

## Conflicts of interest

There are no conflicts to declare.

## Acknowledgements

The research leading to these results has received funding from the European Union Programme for Research and Innovation Horizon 2020 (2014–2020) under the Marie Skłodowska-Curie Grant Agreement PerovSAMS No. 747599, the Spanish Ministry of Economy and Competitiveness (MINECO) via the Unidad de Excelencia María de Maeztu MDM-2015-0538, MAT2017-88821-R and PCIN-2015-255, and the Generalitat Valenciana (Prometeo/2016/135 and GRISOLIAP/2017/089). H. J. B. acknowledges the support of ERA NET PCIN-2017-014. M. S. thanks the MINECO for his RyC contract.

## References

- J. L. Miller, *Phys. Today*, 2014, **67**, 13–15.
- N. Leblanc, N. Mercier, L. Zorina, S. Simonov, P. Auban-Senzier and C. Pasquier, *J. Am. Chem. Soc.*, 2011, **133**, 14924–14927.
- M. Lyu, J. H. Yun, M. Cai, Y. Jiao, P. V. Bernhardt, M. Zhang, Q. Wang, A. Du, H. Wang, G. Liu and L. Wang, *Nano Res.*, 2016, **9**, 692–702.
- D. B. Mitzi, P. Brock, I. B. M. T. J. Watson, P. O. Box, Y. Heights, N. York, I. B. M. Almaden, H. Road, S. Jose and R. V. June, *Inorg. Chem.*, 2001, **40**, 2096–2104.

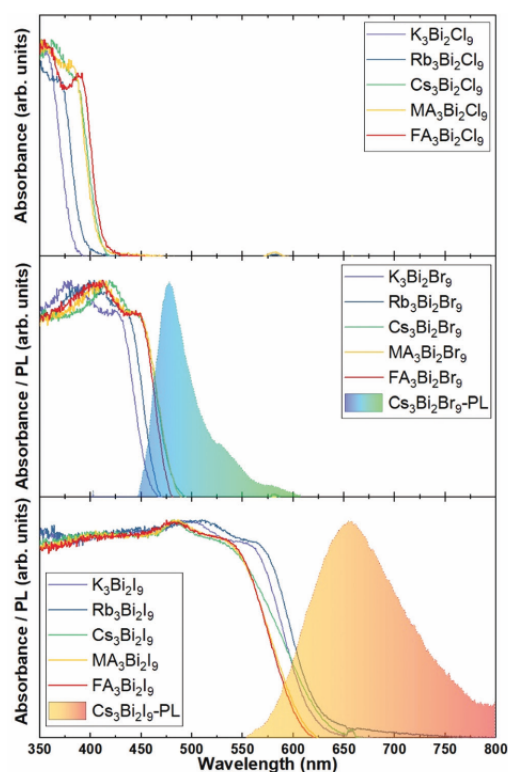


Fig. 3 Normalized absorbance spectra of all  $A_3Bi_2X_9$  compounds (solid lines) and photoluminescence spectra of  $Cs_3Bi_2Br_9$  and  $Cs_3Bi_2I_9$  (dashed lines with filled area under curve).

- 5 P. Szklarz, A. Pietraszko, R. Jakubas, G. Bator, P. Zieliński and M. Gałazka, *J. Phys.: Condens. Matter*, 2018, **20**, 255221.
- 6 N. C. Miller and M. Bernechea, *APL Mater.*, 2018, **6**, 084503.
- 7 T. Kawai, A. Ishii, T. Kitamura, S. Shimanuki, M. Iwata and Y. Ishibashi, *J. Phys. Soc. Jpn.*, 1996, **65**, 1464–1468.
- 8 K. M. McCall, C. C. Stoumpos, S. S. Kostina, M. G. Kanatzidis and B. W. Wessels, *Chem. Mater.*, 2017, **29**, 4129–4145.
- 9 M. Khazaee, K. Sardashti, J. P. Sun, H. Zhou, C. Clegg, I. G. Hill, J. L. Jones, D. C. Lupascu and D. B. Mitzi, *Chem. Mater.*, 2018, **30**, 3538–3544.
- 10 S. S. Shin, J. P. Correa Baena, R. C. Kurchin, A. Polizzotti, J. J. Yoo, S. Wiegold, M. G. Bawendi and T. Buonassisi, *Chem. Mater.*, 2018, **30**, 336–343.
- 11 T. Singh, A. Kulkarni, M. Ikegami and T. Miyasaka, *ACS Appl. Mater. Interfaces*, 2016, **8**, 14542–14547.
- 12 Y. El Ajjouri, F. Palazon, M. Sessolo and H. J. Bolink, *Chem. Mater.*, 2018, **30**, 7423–7427.
- 13 Y. El Ajjouri, V. S. Chirvony, M. Sessolo, F. Palazon and H. J. Bolink, *RSC Adv.*, 2018, **8**, 41548–41551.
- 14 A. D. Jodlowski, A. Yépez, R. Luque, L. Camacho and G. de Miguel, *Angew. Chem., Int. Ed.*, 2016, **55**, 14972–14977.
- 15 L. Protesescu, S. Yakunin, O. Nazarenko, D. N. Dirin and M. V. Kovalenko, *ACS Appl. Nano Mater.*, 2018, **1**, 1300–1308.
- 16 A. J. Lehner, D. H. Fabini, H. A. Evans, C. A. Hébert, S. R. Smock, J. Hu, H. Wang, J. W. Zwanziger, M. L. Chabinyk and R. Seshadri, *Chem. Mater.*, 2015, **27**, 7137–7148.
- 17 Q. A. Akkerman, L. Martínez-Sarti, L. Goldoni, M. Imran, D. Baranov, H. J. Bolink, F. Palazon and L. Manna, *Chem. Mater.*, 2018, **30**, 6915–6921.
- 18 Q. A. Akkerman, V. D'Innocenzo, S. Accornero, A. Scarpellini, A. Petrozza, M. Prato and L. Manna, *J. Am. Chem. Soc.*, 2015, **137**, 10276–10281.
- 19 S. Sun, S. Tominaka, J. H. Lee, F. Xie, P. D. Bristowe and A. K. Cheetham, *APL Mater.*, 2016, **4**, 031101.
- 20 B. W. Park, B. Philippe, X. Zhang, H. Rensmo, G. Boschloo and E. M. J. Johansson, *Adv. Mater.*, 2015, **27**, 6806–6813.
- 21 Z. Zhang, X. Li, X. Xia, Z. Wang, Z. Huang, B. Lei and Y. Gao, *J. Phys. Chem. Lett.*, 2017, **8**, 4300–4307.
- 22 H. Li, C. Wu, Y. Yan, B. Chi, J. Pu, J. Li and S. Priya, *ChemSusChem*, 2017, **10**, 3994–3998.
- 23 J. Pal, A. Bhunia, S. Chakraborty, S. Manna, S. Das, A. Dewan, S. Datta and A. Nag, *J. Phys. Chem. C*, 2018, **122**, 10643–10649.
- 24 K. K. Bass, L. Estergreen, C. N. Savory, J. Buckridge, D. O. Scanlon, P. I. Djurovich, S. E. Bradforth, M. E. Thompson and B. C. Melot, *Inorg. Chem.*, 2017, **56**, 42–45.
- 25 C. W. M. Timmermans and G. Blasse, *Phys. Status Solidi*, 1981, **647**, 647–655.
- 26 G. M. Paternò, N. Mishra, A. J. Barker, Z. Dang, G. Lanzani, L. Manna and A. Petrozza, *Adv. Funct. Mater.*, 2018, **1805299**, 1–6.
- 27 M. Leng, Z. Chen, Y. Yang, Z. Li, K. Zeng, K. Li, G. Niu, Y. He, Q. Zhou and J. Tang, *Angew. Chem., Int. Ed.*, 2016, **55**, 15012–15016.
- 28 M. Leng, Y. Yang, Z. Chen, W. Gao, J. Zhang, G. Niu, D. Li, H. Song, J. Zhang, S. Jin and J. Tang, *Nano Lett.*, 2018, **18**, 6076–6083.
- 29 A. Sarkar, P. Acharyya, R. Sasmal, P. Pal, S. S. Agasti and K. Biswas, *Inorg. Chem.*, 2018, **57**, 15558–15565.
- 30 L. Lian, G. Zhai, F. Cheng, Y. Xia, M. Zheng, J. Ke, M. Gao, H. Liu, D. Zhang, L. Li, J. Gao, J. Tang and J. Zhang, *CrystEngComm*, 2018, **20**, 7473–7478.
- 31 B. Yang, J. Chen, F. Hong, X. Mao, K. Zheng, S. Yang, Y. Li, T. Pullerits, W. Deng and K. Han, *Angew. Chem., Int. Ed.*, 2017, **56**, 12471–12475.

## Supporting Information

### Low-Dimensional Non-Toxic $A_3Bi_2X_9$ Compounds Synthesized by a Dry Mechanochemical Route with Tunable Visible Photoluminescence at Room Temperature

Yusra El Ajjouri,<sup>a</sup> Vladimir S. Chirvony,<sup>a,b</sup> Natalia Vassilyeva,<sup>a</sup> Michele Sessolo,<sup>a</sup> Francisco Palazon,<sup>a\*</sup> and Henk J. Bolink<sup>a</sup>

<sup>a</sup> Instituto de Ciencia Molecular, ICMol, Universidad de Valencia, C/ Catedrático J. Beltrán 2, 46980 Paterna, Spain <sup>b</sup> UMDO (Unidad de Materiales y Dispositivos Optoelectrónicos), Instituto de Ciencia de los Materiales, Universidad de Valencia, Valencia 46071, Spain

#### Experimental details

##### Materials

Cesium chloride (CsCl, > 99 %), cesium bromide (CsBr, > 99 %) and cesium iodide (CsI, > 99 %) were purchased from TCI. Potassium chloride (KCl,  $\geq$  99 %), potassium bromide (KBr, > 99 %) and potassium iodide (KI,  $\geq$  99.5 %) were purchased from Sigma-Aldrich. Rubidium chloride (RbCl, 99.975 %), rubidium bromide (RbBr, 99.8 %) and rubidium iodide (RbI, 99.8 %) were purchased from Alfa Aesar. Methylammonium bromide (CH<sub>3</sub>NH<sub>3</sub>Br), methylammonium iodide (CH<sub>3</sub>NH<sub>3</sub>I), formamidinium chloride (CH<sub>5</sub>N<sub>2</sub>Cl), formamidinium bromide (CH<sub>5</sub>N<sub>2</sub>Br) and formamidinium iodide (CH<sub>5</sub>N<sub>2</sub>I) were purchased from GreatCell Solar. Methylammonium chloride (CH<sub>3</sub>NH<sub>3</sub>Cl, > 99.5 %) was purchased from Lumtec. All chemicals were stored in a nitrogen-filled glovebox and used as received without further purification.

##### Mechanochemical synthesis

AX:BiX<sub>3</sub> (3:2) powders (A = Cs<sup>+</sup>, K<sup>+</sup>, Rb<sup>+</sup>, MA or FA and X = Cl<sup>-</sup>, Br<sup>-</sup> or I<sup>-</sup>) were mixed inside a nitrogen-filled glovebox. Then, approximately 3 grams of the mixed precursors powder was introduced inside 10 mL zirconia ball-mill jars with 2 zirconia beads of 10 mm in diameter per jar. The jars were closed under nitrogen, preventing the powders to be exposed to air. Eventually, ball milling was performed with a MM-400 straight ball-mill from Retsch, at a frequency of 30 Hz for 5 hours.

##### XRD characterization

X-ray diffraction was measured with a Panalytical Empyrean diffractometer equipped with a Cu-K $\alpha$  anode operated at 45 kV and 30 mA and a Pixel 1D detector in scanning line mode. Single scans were acquired in the  $2\theta = 10^\circ$  to  $50^\circ$  range in Bragg-Brentano geometry in air. Data analysis was performed with HighScore Plus and Fullprof software.

##### Optical characterization

Absorbance was measured with a High Power UV-Vis fiber light source, integrated sphere and Avantes Starline AVASpec2048L spectrometer in reflection mode. Photoluminescence was measured in back-scattering geometry with excitation by Nd<sup>3+</sup>YAG laser pulses at 355 nm (pulse duration 1 ns, repetition rate 1 kHz, average power 2.5 mW) and detection by USB 650 Ocean Optics spectrometer. All PL spectra were corrected for spectral sensitivity of the detection system.

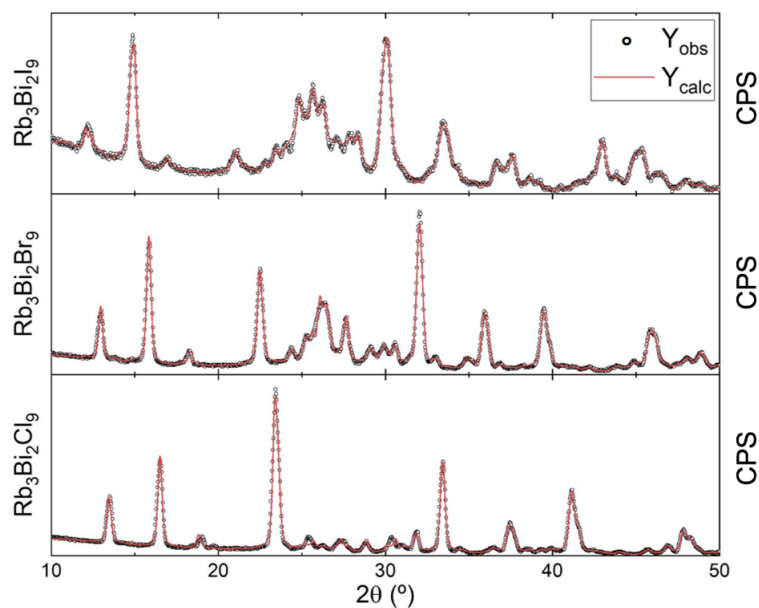


Figure D.1: Experimental ( $Y_{obs}$ ) and fitted ( $Y_{calc}$ ) XRD data for the dry mechanochemically-synthesized  $Rb_3Bi_2X_9$  compounds ( $X = Cl^-$ ,  $Br^-$  or  $I^-$ ). The refined lattice parameters derived from fitting are presented in Table 6.1.

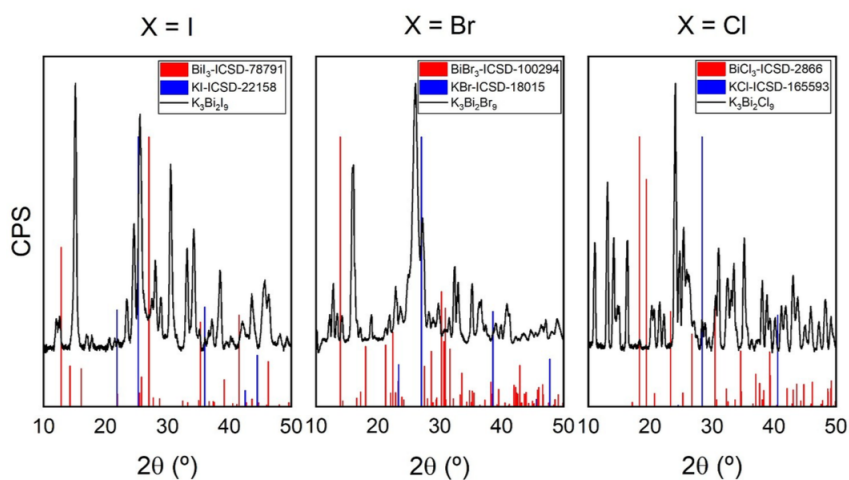


Figure D.2: Reference XRD patterns of  $KX$  (blue columns) and  $BiX_3$  (red columns) and diffractograms (black lines) of powders obtained by dry ball-milling thereof. The obtained crystals are clearly different than the precursors, suggesting the reaction of the latter to form  $K_3Bi_2X_9$ .

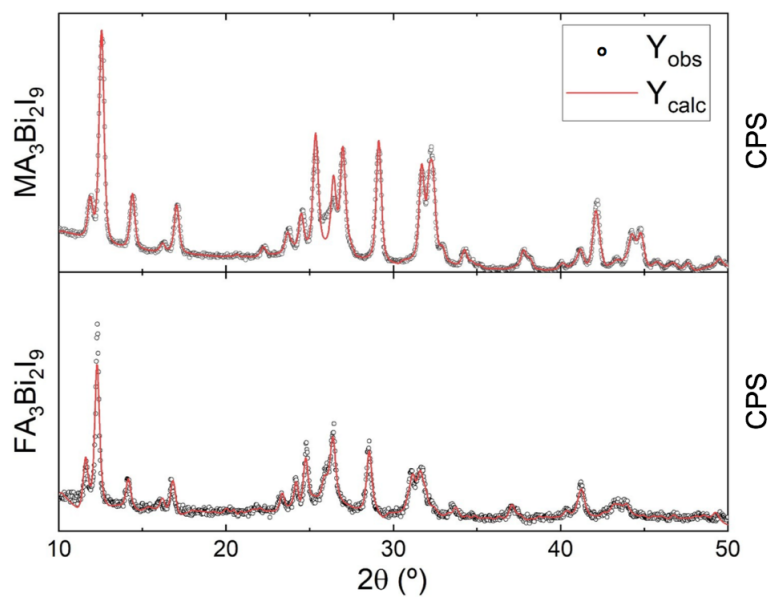


Figure D.3: Experimental ( $Y_{obs}$ ) and fitted ( $Y_{calc}$ ) data for  $MA_3Bi_2I_9$  and  $FA_3Bi_2I_9$ . The refined cell parameters are presented in Table 6.2.

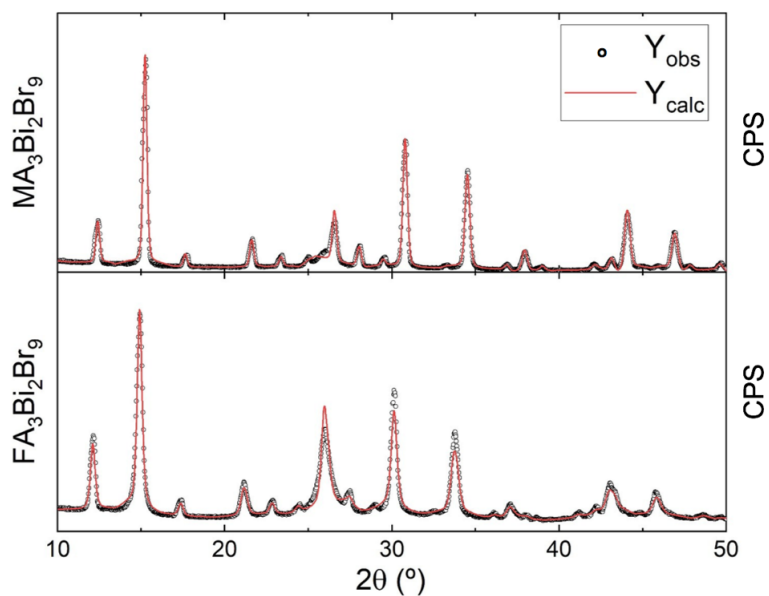


Figure D.4: Experimental ( $Y_{obs}$ ) and fitted ( $Y_{calc}$ ) data for  $MA_3Bi_2Br_9$  and  $FA_3Bi_2Br_9$ . The refined cell parameters are presented in Table 6.2.



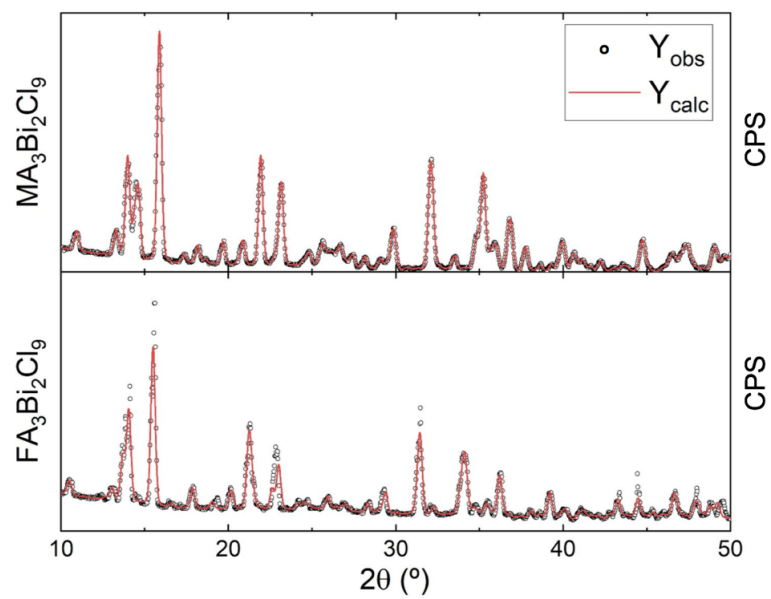


Figure D.5: Experimental ( $Y_{obs}$ ) and fitted ( $Y_{calc}$ ) data for  $MA_3Bi_2Cl_9$  and  $FA_3Bi_2Cl_9$ . The refined cell parameters are presented in Table 6.2.

# Appendix E

## Single-Source Vacuum Deposition of Mechanosynthesized Inorganic Halide Perovskites

Yousra El Ajjouri,<sup>†</sup> Francisco Palazon,<sup>†\*</sup> Michele Sessolo,<sup>†</sup> and Henk J. Bolink<sup>†</sup>

<sup>†</sup> Instituto de Ciencia Molecular, ICMol, Universidad de Valencia, C/ Catedrático J. Beltrán 2, 46980 Paterna, Spain

**Abstract:** Fully inorganic cesium lead halide perovskite thin films were prepared by an easy, fast and dry process based on single-source vacuum deposition. We investigated the structural and optical characteristics of the so-formed films as a function of chemical composition (chloride, bromide and iodide films were formed), post-deposition thermal annealing, as well as previous mechanosynthesis of perovskite powders. We found out that the CsPbX<sub>3</sub> perovskite was preferentially formed for the smaller halides and favored by previous ball-milling of CsX and PbX<sub>2</sub> precursors. When bigger halides were used and/or CsX and PbX<sub>2</sub> precursors were simply mixed without previous mechanosynthesis, PbX<sub>2</sub>-rich compounds such as CsPb<sub>2</sub>X<sub>5</sub> were preferentially formed in the thin films.

In the field of perovskite optoelectronics, organic-inorganic hybrid perovskites (OHPs) have been widely studied due to their attractive optical and electronic properties.<sup>1,2</sup> However, drawbacks such as their environmental instability due to the high volatility and moisture sensitivity of the organic compounds, might hinder the development of stable OHP optoelectronic devices.<sup>3,4</sup> For this reason, the more thermally stable cesium-based all-inorganic halide perovskites are being investigated.<sup>5-9</sup> However, conventional solution-processing for Cs-based perovskite synthesis is rather challenging due to the poor solubility of cesium halides in common solvents.<sup>10,11</sup> Vacuum deposition is an alternative method which allows the formation of high-quality perovskite thin films in dry process without the need of extra chemicals (*e.g.*, solvents) other than the salt precursors that form the perovskite compounds.<sup>12</sup> For standard dual-source thermal vacuum deposition of an ABX<sub>3</sub> perovskite (where A is a monovalent cation, B is a divalent metal and X the halide), AX and BX<sub>2</sub> precursors are simultaneously co-evaporated from two different sources.<sup>13,14</sup> In this case, the evaporation rates of both precursors need to be well adjusted in order to obtain the desired final composition in the film. Single-source vacuum deposition (SSVD) represents an interesting alternative to dual-source deposition due to its simplicity and speed.<sup>15,16</sup> Hereafter we have fabricated thin films of different cesium lead halide compounds by SSVD of CsX and PbX<sub>2</sub> (X = Cl, Br, and I) precursors simply mixed in a crucible. Furthermore, we have conducted dry mechanosynthesis of CsPbX<sub>3</sub> perovskites by ball-milling. This technique has recently been used for the synthesis of different hybrid and inorganic halide perovskites both in the form of colloidal nanocrystals and bulk powders.<sup>17-20</sup> Again, thin films were made by SSVD of these pre-synthesized perovskite powders. By performing a detailed and systematic structural and optical analysis we analyzed the different thin films that are formed through SSVD of pristine as well as ball-milled chloride, bromide, and iodide precursors at room temperature as well as upon thermal annealing.

First, thin films were prepared by SSVD of simply mixed CsX and PbX<sub>2</sub> precursors. Figures 1 and 2 show the structural

and optical characterization of the films as-prepared at room temperature as well as after thermal annealing at 225 °C for X = Cl and Br (for X = I see Figure S2).

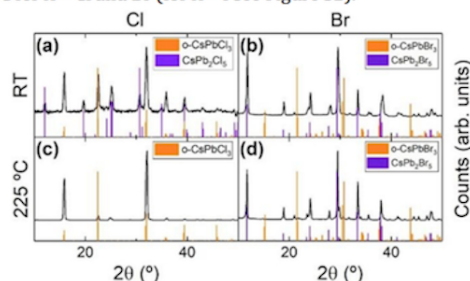


**Figure 1.** XRD characterization of films prepared by SSVD of CsCl+PbCl<sub>2</sub> (a, c) and CsBr+PbBr<sub>2</sub> (b, d) at room temperature (a, b) as well as after thermal annealing at 225 °C (c, d). Reference patterns for orthorhombic CsPbCl<sub>3</sub> (ICSD-243734), orthorhombic CsPbBr<sub>3</sub> (ICSD-97851), as well as CsPb<sub>2</sub>Cl<sub>5</sub> (ICSD-249888) and CsPb<sub>2</sub>Br<sub>5</sub> (PDF-25-0211) are shown along the experimental data.

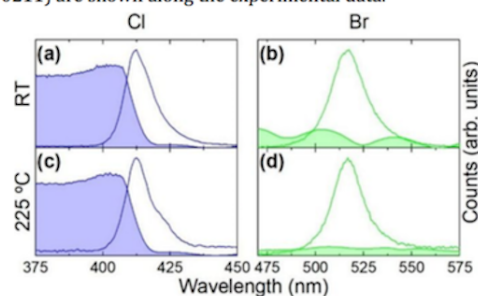


**Figure 2.** Normalized absorption and photoluminescence spectra of films prepared by SSVD of CsCl+PbCl<sub>2</sub> (a, c) and CsBr+PbBr<sub>2</sub> (b, d) at room temperature (a, b) as well as after thermal annealing at 225 °C (c, d). The absorption signal present in panel b is linked to optical interferences. Absorption

## Chemistry of Materials

spectra of this film throughout a broader wavelength range can be seen in Figure S1.

As can be seen by X-ray diffraction (XRD, Figure 1) the as-prepared films consist of a mixture of  $\text{CsPb}_2\text{X}_5$  and  $\text{CsPbX}_3$ .<sup>21</sup> However, the relative amounts of both compounds is different. In the case of the smaller anion ( $X = \text{Cl}$ ), the film is mostly consistent of  $\text{CsPbX}_3$  (Figure 1a) and exhibits the corresponding absorption onset around 400 nm and Stoke-shifted photoluminescence (PL) centered at 412 nm (Figure 2a).

For the larger anion ( $X = \text{Br}$ ) the  $\text{CsPb}_2\text{X}_5$  compound is dominant (Figure 1b). A close look reveals that reflections characteristics of  $\text{CsPbX}_3$  are also present although they are broad and not intense. This observation suggests that small domains of  $\text{CsPbBr}_3$  are embedded in a  $\text{CsPb}_2\text{Br}_5$  matrix. The optical characterization of these films (Figure 2b) shows no marked absorption onset in this range, but only a signal due to optical interferences (see Figure S1 for the full absorption spectrum). However, a rather intense photoluminescence peak centered at 517 nm is visible. This value is slightly blue-shifted from the bulk PL of  $\text{CsPbBr}_3$ .<sup>22</sup> This blue-shift is consistent with the hypothesis of small (tens of nanometers)  $\text{CsPbBr}_3$  domains in the weak quantum confinement regime,<sup>10</sup> possibly passivated by a  $\text{CsPb}_2\text{Br}_5$  matrix. When the chloride films are annealed at 225 °C, the fraction of  $\text{CsPb}_2\text{Cl}_5$  is substantially reduced so

that almost phase-pure  $\text{CsPbCl}_3$  is obtained (Figure 1c). This is not the case for the bromide films where  $\text{CsPb}_2\text{Br}_5$  remains the dominant crystalline compound (Figure 1d). The optical characteristics of both films remain similar after annealing (Figure 2 c-d). We conclude that SSVD of raw precursors can yield good-quality  $\text{CsPbX}_3$  perovskites only for the smaller halide ( $X = \text{Cl}$ ), while  $\text{PbX}_2$ -rich compounds are mainly formed for the larger halide ( $X = \text{Br}$ ). This trend is confirmed by looking at the results of iodide compounds (Figure S2) where no significant  $\text{CsPbI}_3$  could be formed with this method. In order to obtain higher purity perovskite films by SSVD, we performed dry ball-milling mechanosynthesis of  $\text{CsPbX}_3$  powders (see supporting information for experimental details). A few recent reports have demonstrated similar mechanosynthesis with highly energetic planetary ball-mills.<sup>17,19</sup> XRD and optical analyses (Figure 3a-c and Figure 4a-c) reveal that ball-milling  $\text{CsX}$  and  $\text{PbX}_2$  compounds at room temperature with a "straight" (non-planetary) setup (see experimental section for more details) results in the formation of high purity  $\text{CsPbX}_3$  perovskite powders for all halides.

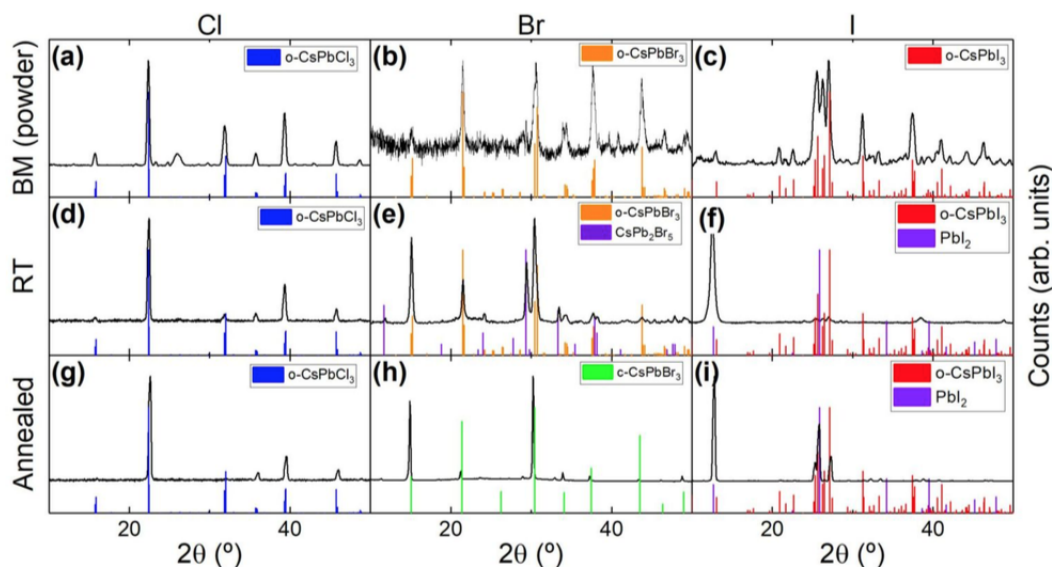


**Figure 3.** XRD characterization of ball-milled  $\text{CsX}+\text{PbX}_2$  powders (a-c) as well as films prepared by SSVD of the resulting powders at room temperature (d-f) and after thermal annealing (g-i). Note that the annealing temperature is 225 °C for  $X = \text{Cl}$  and  $\text{Br}$  (g, h) while it is 325 °C for  $X = \text{I}$  (i). Reference patterns for orthorhombic  $\text{CsPbCl}_3$  (ICSD-243734), orthorhombic  $\text{CsPbBr}_3$  (ICSD-97851), orthorhombic  $\text{CsPbI}_3$  (ICSD-161480), cubic  $\text{CsPbBr}_3$  (ICSD-29073),  $\text{CsPb}_2\text{Br}_5$  (PDF-25-0211) and  $\text{PbI}_2$  (ICSD-68819) are shown along the experimental data.



## Chemistry of Materials

When these powders are used for SSVD, the resulting films exhibit a higher purity (*i.e.*, higher relative concentration of  $\text{CsPbX}_3$ ) than when non-ball-milled powders are used. This suggests that the pre-formed perovskites sublime at least partially as a single compound ( $\text{CsPbX}_3$ ) instead of undergoing a transformation back into  $\text{CsX} + \text{PbX}_2$  followed by subsequent separate evaporation of both components. Indeed, in the case of the chloride-based compounds, the diffractogram of the film at room temperature (Figure 3d), which is essentially temperature-independent (Figure 3g), shows no signal for  $\text{CsPb}_2\text{Cl}_5$ . This means that the purity of the films deposited at room temperature is already higher than what can be achieved with non-ball-milled precursors even after they were annealed at 225 °C (Figure 1c). The difference is also evident for  $X = \text{Br}$ . Although  $\text{CsPb}_2\text{Br}_5$  is present in the as-deposited film (Figure 3e), its relative content is much reduced as compared to non-ball-milled samples (Figure 1b). Furthermore, this compound disappears after annealing at 225 °C (Figure 3h; see Figure S3 for XRD characterization at different temperatures) and  $\text{CsPbBr}_3$  remains the only crystalline compound detectable. This transformation suggests that the original film (before annealing) has an excess of CsBr that can lead to the formation of  $\text{CsPbBr}_3$  by reacting with  $\text{CsPb}_2\text{Br}_5$ . The other possible hypothesis would be the loss or amorphization of  $\text{PbBr}_2$ , which is unlikely due to its high melting point. The presence of CsBr together with  $\text{CsPb}_2\text{Br}_5$  is hard to detect since its main XRD peak located at  $2\theta = 29.38^\circ$  (ICSD: 98-005-3848) overlaps with the signal of  $\text{CsPb}_2\text{Br}_5$ , as already noted elsewhere.<sup>21</sup> It must also be noted that no residual powder is left in the crucible after SSVD, which again suggests the presence of excess CsBr in the film before annealing. Previous mechano-synthesis of  $\text{CsPbBr}_3$  also seems to result in better morphology of the final film (see Figure S4). Indeed, the film prepared from pristine  $\text{CsBr} + \text{PbBr}_2$  mixture presents a patchy morphology at high magnification and cracks are visible at lower magnification. In contrast to this, the film prepared from mechano-synthesized  $\text{CsPbBr}_3$  shows much higher homogeneity with typical grain sizes of several hundred nanometers. No obvious pinholes can be observed. Iodide perovskites remain the most difficult to form, as previously mentioned. Although mechano-synthesis of the  $\text{CsPbI}_3$  powder is achieved (see Figure 3c), the resulting films are mainly composed by  $\text{PbI}_2$  (Figure 3f). Only after thermal annealing at 325 °C (a higher temperature than used for the chloride and bromide based films), the fraction of  $\text{CsPbI}_3$  rises significantly, although  $\text{PbI}_2$  remains dominant. It must be noted that XRD characterization had to be carried out in air, due to restrictions in our experimental setup, where  $\text{CsPbI}_3$  is known to degrade.<sup>23,24</sup> This was also observed for the mechano-synthesized  $\text{CsPbI}_3$  powder. As prepared in nitrogen it is black indicating a cubic crystal structure and when this powder is kept under nitrogen, it remains black (cubic) for over one month (see Figure S5). However, it quickly turns to the “yellow” orthorhombic phase when it is exposed to air before XRD characterization can be completed (Figure 3c). A similar observation is made on the thin film after annealing: the partial conversion to the black phase is clearly visible by eye (Figure S6). It must be noted that the temperature of annealing (325 °C on a hot plate) is close to the phase transition.<sup>25</sup> Hence, it is possible that

annealing at higher temperature (which was impossible in our case for technical reasons) might result in a full conversion. When the samples are kept under inert atmosphere (Figure S6) this black phase remains stable for several days.

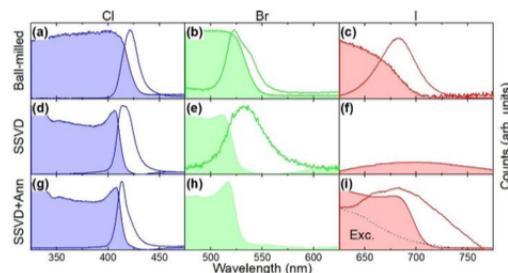


**Figure 4.** Normalized absorption and photoluminescence spectra of ball-milled  $\text{CsX} + \text{PbX}_2$  powders (a-c) as well as films prepared by SSVD of the resulting powders at room temperature (d-f) and after thermal annealing (g-i). Note that the annealing temperature is 225 °C for  $X = \text{Cl}$  and  $\text{Br}$  (g, h) while it is 325 °C for  $X = \text{I}$  (i). The absorption signal observed in panel f originates from optical interferences. The absorption spectrum of this film throughout a broader wavelength range can be seen in Figure S7.

The optical characterization of the ball-milled powders as well as the resulting films by SSVD is presented in Figure 4. All powders (Figure 4a-c) exhibit the expected absorbance and PL spectra for  $\text{CsPbX}_3$  compounds, confirming the high quality of mechano-synthesized inorganic halide perovskites. Thin films prepared thereof by SSVD present different characteristics as a function of the halide and temperature. For the smaller chloride anion, the expected absorbance and PL are present both at RT and after annealing at 225 °C, as in the case of non-ball-milled precursors (Figure 2 c,d). For  $X = \text{Br}$ , a strong absorption onset is visible already at RT (Figure 4e) and gets steeper after annealing (Figure 4h), indicating a higher degree of crystallinity and order in the material. This absorption was not seen in the case of non-ball-milled precursors (Figure 2b-d) and reinforces the conclusion that  $\text{CsPbBr}_3$  is favored when using previously mechano-synthesized powders while  $\text{CsPb}_2\text{Br}_5$  was mainly formed when using pristine precursors, as previously discussed. We note that the bromide sample shows a weak PL in the as-deposited film (Figure 4e), which is ultimately lost after annealing (Figure 4h). The PL quenching of  $\text{CsPbBr}_3$  upon thermal annealing is already reported and may be due to the creation of more trap states in the film.<sup>21,26-28</sup> Indeed XRD shows that peaks associated with  $\text{CsPbBr}_3$  get thinner upon annealing (Figure 3 e,h), which denotes a grain growth. Another possible explanation of the PL loss is linked to higher diffusivity of carriers. As grains become larger upon annealing, it may be expected that diffusion lengths increase and thus electrons and holes can reach surface trap states more easily. Eventually, for the iodide film, no significant absorption or PL is detected at room temperature at the wavelengths of interest (Figure 4f; see Figure S7 for full absorption spectrum). This is consistent with the almost inexistent XRD signal for  $\text{CsPbI}_3$  in the as-prepared film (Figure 3f).

## Chemistry of Materials

However, after annealing at 325 °C and rapid quenching, a clear absorption onset is visible around 680 nm. PL is also visible though not intense and broad. The broad PL signal is partly attributed to the overlap of the sample's PL with the excitation source which has a weak visible component in addition to the main UV peak at 375 nm, as represented as a reference in Figure 4i).

In summary, we fabricated fully inorganic cesium lead halide thin films by means of fast single-source vacuum deposition (SSVD). We note that in the case of SSVD of pristine mixed precursors, high-purity perovskite CsPbX<sub>3</sub> films could only be obtained for X = Cl after thermal annealing. However, when CsX and PbX<sub>2</sub> are previously ball-milled at room temperature, high purity CsPbX<sub>3</sub> powders are formed. SSVD of the so-formed perovskites results in much-improved films both as-prepared as well as after thermal annealing. Perovskite films with optical transitions throughout the visible spectrum from around 400 nm (X = Cl) to around 700 nm (X = I) could be obtained in this way. Thus, we have demonstrated that single-source vacuum deposition of ball-milled perovskites represents an easy, fast and dry process to form high-quality thin films of fully inorganic perovskites. Future work will focus on: (i) implementing these films into different optoelectronic devices such as light-emitting diodes or solar cells, where it will be crucial to avoid chemical impurities and to finely control the film morphology, and (ii) testing the effects of different additives that may work as dopants, passivating agents, or replacement of toxic elements such as lead by other metals such as tin or bismuth.

## ASSOCIATED CONTENT

## Supporting Information.

The Supporting Information is available free of charge on the ACS Publications website:

Experimental details, XRD and optical characterization of iodide films prepared from pristine precursors, XRD of bromide film under *in-situ* annealing, SEM of bromide films, absorption spectra and photographs of mechanosynthesized CsPbI<sub>3</sub> under inert atmosphere and thin films made thereof after annealing and ageing in nitrogen.

## AUTHOR INFORMATION

## Corresponding Author

\*E-mail: Francisco.Palazon@uv.es

## Notes

The authors declare no competing financial interest.

## ACKNOWLEDGMENT

The research leading to these results has received funding from the European Union Programme for Research and Innovation Horizon 2020 (2014-2020) under the Marie Skłodowska-Curie Grant Agreement PerovSAMS No. 747599, and project INFORM (grant 675867), the Spanish Ministry of Economy and Competitiveness (MINECO) via the Unidad de Excelencia María de Maeztu MDM-2015-0538, MAT2017-88821-R and PCIN-2015-255, and the Generalitat Valenciana (Prometeo/2016/135 and GRISOLIAP/2017/089). H. J. B.

acknowledges the support of ERA NET PCIN-2017-014. M. S. thanks the MINECO for his post-doctoral RyC contract.

## REFERENCES

- (1) Noel, N. K.; Abate, A.; Stranks, S. D.; Parrott, E. S.; Burlakov, V. M.; Goriely, A.; Snaith, H. J. Enhanced Photoluminescence and Solar Cell Performance via Lewis Base Passivation of Organic-Inorganic Lead Halide Perovskites. *ACS Nano* **2014**, *8* (10), 9815–9821.
- (2) Stranks, S. D.; Eperon, G. E.; Grancini, G.; Menelaou, C.; Alcocer, M. J. P.; Leijtens, T.; Herz, L. M.; Petrozza, A.; Snaith, H. J. Electron-Hole Diffusion Lengths Exceeding 1 Micrometer in an Organometal Trihalide Perovskite Absorber. *Science* (80-. J.) **2013**, *342* (6156), 341–344.
- (3) Palazon, F.; Pérez-del-Rey, D.; Marras, S.; Prato, M.; Sessolo, M.; Bolink, H. J.; Manna, L. Coating Evaporated MAPI Thin Films with Organic Molecules: Improved Stability at High Temperature and Implementation in High-Efficiency Solar Cells. *ACS Energy Lett.* **2018**, 835–839.
- (4) Manser, J. S.; Saidaminov, M. I.; Christians, J. A.; Bakr, O. M.; Kamat, P. V. Making and Breaking of Lead Halide Perovskites. *Acc. Chem. Res.* **2016**, *49* (2), 330–338.
- (5) Service, R. F. Cesium Fortifies Next-Generation Solar Cells. *Science* (80-. J.) **2016**, *351* (6269), 113–114.
- (6) Kulbak, M.; Gupta, S.; Kedem, N.; Levine, I.; Bendikov, T.; Hodes, G.; Cahen, D. Cesium Enhances Long-Term Stability of Lead Bromide Perovskite-Based Solar Cells. *J. Phys. Chem. Lett.* **2016**, *7* (1), 167–172.
- (7) Sutton, R. J.; Eperon, G. E.; Miranda, L.; Parrott, E. S.; Kamino, B. A.; Patel, J. B.; Hörantner, M. T.; Johnston, M. B.; Haghighirad, A. A.; Moore, D. T.; et al. Bandgap-Tunable Cesium Lead Halide Perovskites with High Thermal Stability for Efficient Solar Cells. *Adv. Energy Mater.* **2016**, *6* (8), 1–6.
- (8) Zhang, L.; Yang, X.; Jiang, Q.; Wang, P.; Yin, Z.; Zhang, X.; Tan, H.; Yang, Y. M.; Wei, M.; Sutherland, B. R.; et al. Ultra-Bright and Highly Efficient Inorganic Based Perovskite Light-Emitting Diodes. *Nat. Commun.* **2017**, *8*, 1–8.
- (9) Chen, C. Y.; Lin, H. Y.; Chiang, K. M.; Tsai, W. L.; Huang, Y. C.; Tsao, C. S.; Lin, H. W. All-Vacuum-Deposited Stoichiometrically Balanced Inorganic Cesium Lead Halide Perovskite Solar Cells with Stabilized Efficiency Exceeding 11%. *Adv. Mater.* **2017**, *29* (12), 1–7.
- (10) Protesescu, L.; Yakunin, S.; Bodnarchuk, M. I.; Krieg, F.; Caputo, R.; Hendon, C. H.; Yang, R. X.; Walsh, A.; Kovalenko, M. V. Nanocrystals of Cesium Lead Halide Perovskites (CsPbX<sub>3</sub>, X = Cl, Br, and I): Novel Optoelectronic Materials Showing Bright Emission with Wide Color Gamut. *Nano Lett.* **2015**, *15* (6), 3692–3696.
- (11) Dirin, D. N.; Cherniukh, I.; Yakunin, S.; Shynkarenko, Y.; Kovalenko, M. V. Solution-Grown CsPbBr<sub>3</sub> Perovskite Single Crystals for Photon Detection. *Chem. Mater.* **2016**, *28* (23), 8470–8474.
- (12) Ávila, J.; Momblona, C.; Boix, P. P.; Sessolo, M.; Bolink, H. J. Vapor-Deposited Perovskites: The Route to High-Performance Solar Cell Production? *Joule* **2017**, *1* (3), 431–442.
- (13) Liu, M.; Johnston, M. B.; Snaith, H. J. Efficient Planar Heterojunction Perovskite Solar Cells by Vapour Deposition. *Nature* **2013**, *501* (7467), 395–398.
- (14) Momblona, C.; Gil-Escrig, L.; Bandiello, E.; Hutter, E. M.; Sessolo, M.; Lederer, K.; Blochwitz-Nimoth, J.; Bolink, H. J. Efficient Vacuum Deposited P-i-n and n-i-p Perovskite Solar Cells Employing Doped Charge Transport Layers. *Energy Environ. Sci.* **2016**, *9* (11), 3456–3463.
- (15) Longo, G.; Gil-Escrig, L.; Degen, M. J.; Sessolo, M.; Bolink, H. J. Perovskite Solar Cells Prepared by Flash Evaporation. *Chem. Commun.* **2015**, *51* (34), 7376–7378.
- (16) Fan, P.; Gu, D.; Liang, G.-X.; Luo, J.-T.; Chen, J.-L.; Zheng, Z.-H.; Zhang, D.-P. High-Performance Perovskite CH<sub>3</sub>NH<sub>3</sub>PbI<sub>3</sub> Thin Films for Solar Cells Prepared by Single-Source Physical Vapour Deposition. *Sci. Rep.* **2016**, *6* (1), 29910.
- (17) Protesescu, L.; Yakunin, S.; Nazarenko, O.; Dirin, D. N.; Kovalenko, M. V. Low-Cost Synthesis of Highly Luminescent

## Chemistry of Materials

- Colloidal Lead Halide Perovskite Nanocrystals by Wet Ball Milling. *ACS Appl. Nano Mater.* **2018**, *1* (3), 1300–1308.
- (18) Jodlowski, A. D.; Yépez, A.; Luque, R.; Camacho, L.; de Miguel, G. Benign-by-Design Solventless Mechanochemical Synthesis of Three-, Two-, and One-Dimensional Hybrid Perovskites. *Angew. Chemie - Int. Ed.* **2016**, *55* (48), 14972–14977.
- (19) Zhu, Z. Y.; Yang, Q. Q.; Gao, L. F.; Zhang, L.; Shi, A. Y.; Sun, C. L.; Wang, Q.; Zhang, H. L. Solvent-Free Mechanochemical Synthesis of Composition-Tunable Cesium Lead Halide Perovskite Quantum Dots. *J. Phys. Chem. Lett.* **2017**, *8* (7), 1610–1614.
- (20) Prochowicz, D.; Franckevičius, M.; Cieślak, A. M.; Zakeeruddin, S. M.; Grätzel, M.; Lewiński, J. Mechanochemical Synthesis of the Hybrid Perovskite CH<sub>3</sub>NH<sub>3</sub>PbI<sub>3</sub>: Characterization and the Corresponding Solar Cell Efficiency. *J. Mater. Chem. A* **2015**, *3* (41), 20772–20777.
- (21) Palazon, F.; Dogan, S.; Marras, S.; Locardi, F.; Nelli, I.; Rastogi, P.; Ferretti, M.; Prato, M.; Krahne, R.; Manna, L. From CsPbBr<sub>3</sub> Nano-Inks to Sintered CsPbBr<sub>3</sub>-CsPb<sub>2</sub>Br<sub>5</sub> Films via Thermal Annealing: Implications on Optoelectronic Properties. *J. Phys. Chem. C* **2017**, *121* (21), 11956–11961.
- (22) Akkerman, Q. A.; Motti, S. G.; Srimath Kandada, A. R.; Mosconi, E.; D'Innocenzo, V.; Bertoni, G.; Marras, S.; Kamino, B. A.; Miranda, L.; De Angelis, F.; et al. Solution Synthesis Approach to Colloidal Cesium Lead Halide Perovskite Nanoplatelets with Monolayer-Level Thickness Control. *J. Am. Chem. Soc.* **2016**, *138* (3), 1010–1016.
- (23) Swarnkar, A.; Marshall, A. R.; Sanehira, E. M.; Chernomordik, B. D.; Moore, D. T.; Christians, J. A.; Chakrabarti, T.; Luther, J. M. Quantum Dot-induced Phase Stabilization of A-CsPbI<sub>3</sub> Perovskite for High-Efficiency Photovoltaics. *Science (80-. )* **2016**, *354* (6308), 92–95.
- (24) Liu, F.; Zhang, Y.; Ding, C.; Kobayashi, S.; Izuishi, T.; Nakazawa, N.; Toyoda, T.; Ohta, T.; Hayase, S.; Minemoto, T.; et al. Highly Luminescent Phase-Stable CsPbI<sub>3</sub> Perovskite Quantum Dots Achieving Near 100% Absolute Photoluminescence Quantum Yield. *ACS Nano* **2017**, *11* (10), 10373–10383.
- (25) Moller, C. K. Crystal Structure and Photoconductivity of Caesium Plumbahalides. *Nature* **1958**, *182*, 1436.
- (26) Diroll, B. T.; Nedelcu, G.; Kovalenko, M. V.; Schaller, R. D. High-Temperature Photoluminescence of CsPbX<sub>3</sub> (X = Cl, Br, I) Nanocrystals. *Adv. Funct. Mater.* **2017**, *27* (21), 1606750.
- (27) Palazon, F.; Di Stasio, F.; Lauciello, S.; Krahne, R.; Prato, M.; Manna, L. Evolution of CsPbBr<sub>3</sub> Nanocrystals upon Post-Synthesis Annealing under an Inert Atmosphere. *J. Mater. Chem. C* **2016**, *4* (39), 9179–9182.
- (28) Yuan, X.; Jing, P.; Li, J.; Wei, M.; Hua, J.; Zhao, J.; Tian, L.; Li, J. Temperature-Dependent Photoluminescence of Inorganic Perovskite Nanocrystal Films. *RSC Adv.* **2016**, *6* (82), 78311–78316.



## Supporting Information

### Single-Source Vacuum Deposition of Mechanochemically-Synthesized Inorganic Halide Perovskites

Yusra El Ajjouri,<sup>a</sup> Francisco Palazon,<sup>a\*</sup> Michele Sessolo<sup>a</sup> and Henk J. Bolink<sup>a</sup>

<sup>a</sup> Instituto de Ciencia Molecular, ICMol, Universidad de Valencia, C/ Catedrático J. Beltrán 2, 46980 Paterna, Spain

#### Experimental details

##### Materials

Cesium chloride (CsCl, > 99 %), cesium bromide (CsBr, > 99 %), cesium iodide (CsI, > 99 %) and lead(II) iodide (PbI<sub>2</sub>, ≥ 98 %) were purchased from TCI. Lead(II) bromide (PbBr<sub>2</sub>, ≥ 98 %) and lead(II) chloride (PbCl<sub>2</sub>, 98 %) were purchased from Sigma-Aldrich. All chemicals were stored in a nitrogen-filled glovebox and used as received without further purification.

##### Mechanochemical synthesis

Equimolar CsX:PbX<sub>2</sub> powders (X = Cl<sup>-</sup>, Br<sup>-</sup> or I<sup>-</sup>) were mixed inside a nitrogen-filled glovebox. Then, approximately 3 grams of the mixed precursors powders was introduced inside 10 mL zirconia ball-mill jars with 2 zirconia beads of 10 mm in diameter per jar. The jars were closed under nitrogen so that the powders were not exposed to air. Then ball-milling was performed with a MM-400 straight ball-mill from Retsch, at a frequency of 30 Hz for 5 hours.

##### Single-source vacuum deposition

Pristine as well as ball-milled perovskite precursors were deposited by means of a single-source vacuum deposition technique. Perovskite thin films were deposited in a high vacuum chamber (Vaksis R&D and Engineering) equipped with temperature controlled alumina thermal sources (Creaphys GmbH) and quartz crystal microbalance thickness sensors. Mechanical shutters both at the thermal source and at the substrate holder were used to control the deposition process. The obtained thin films were kept in a nitrogen-filled glovebox.

##### XRD characterization

X-ray diffraction was measured with a Panalytical Empyrean diffractometer equipped with a Cu-K $\alpha$  anode operated at 45 kV and 30 mA and a Pixel 1D detector in scanning line mode. Single scans were acquired in the  $2\theta = 10^\circ$  to  $50^\circ$  range in Bragg-Brentano geometry in air. Data analysis was performed with HighScore Plus software.

##### Optical characterization

Absorbance was measured with a High Power UV-Vis fiber light source, integrated sphere and Avantes Starline AVASpec-2048L spectrometer in reflection mode. Photoluminescence was measured with a continuous wave 375 nm diode laser with a 400 nm filter, and Hamamatsu PMA 11 spectrometer. For a typical spectrum 10 scans of 1 second were averaged.



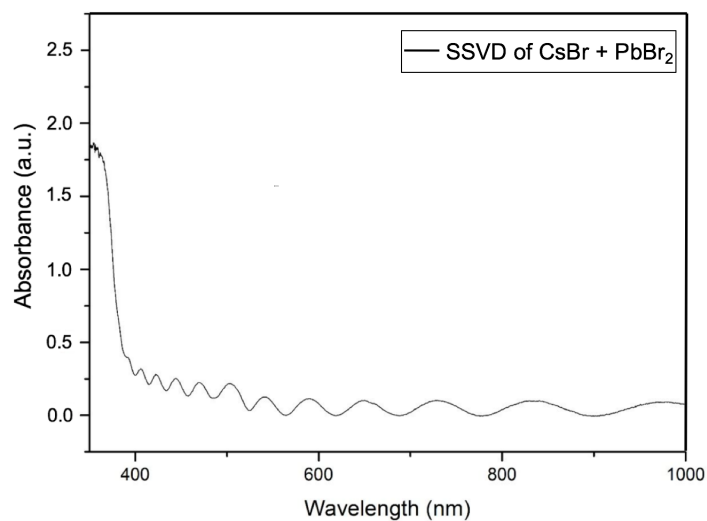


Figure E.1: Absorption spectrum of a thin film formed by SSVD of simply mixed CsBr + PbBr<sub>2</sub>, showing optical interferences. Figure 7.2b presents a "zoom" of this spectrum showing no marked absorption onset around 520 nm.

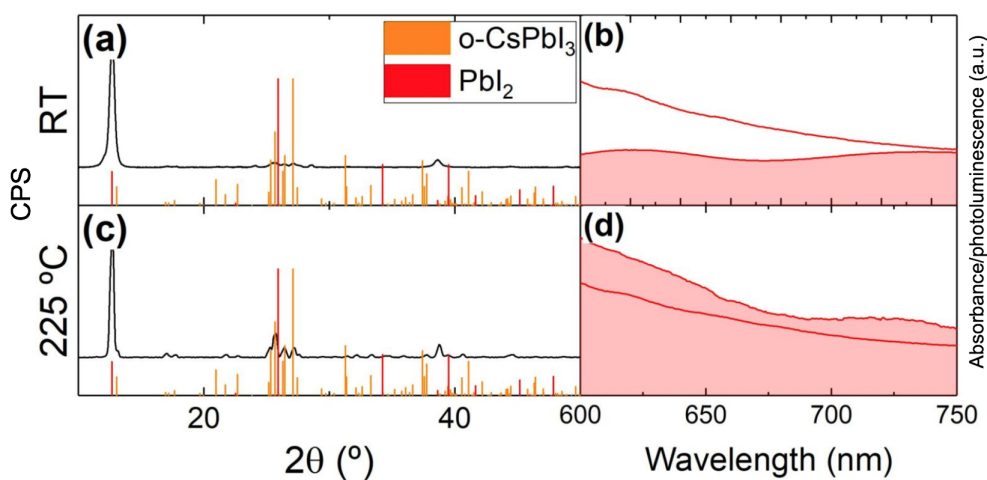


Figure E.2: XRD (a,c) and optical (b,d) characterization of thin films made by SSVD of simply mixed CsI and PbI<sub>2</sub> at room temperature (RT) and after annealing at 225 °C for 15 minutes on a hotplate in a nitrogen-filled glovebox.

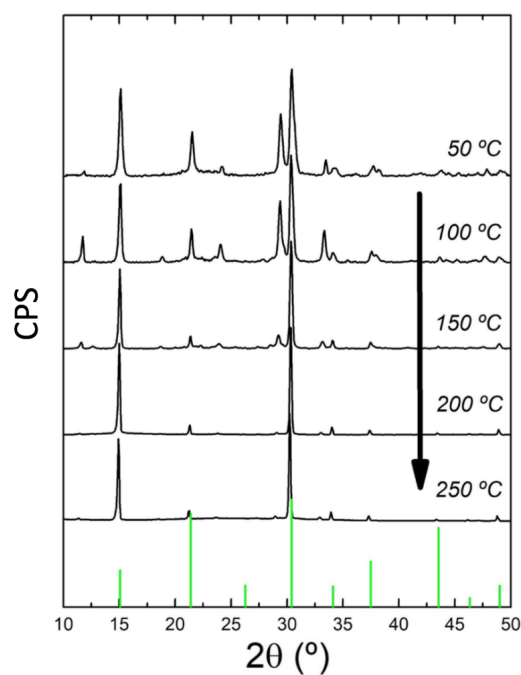


Figure E.3: XRD characterization of a thin film formed by SSVD of ball-milled CsBr + PbBr<sub>2</sub> at different annealing temperatures. The green columns represent the reference pattern (ICSD-97851) for cubic CsPbBr<sub>3</sub>.

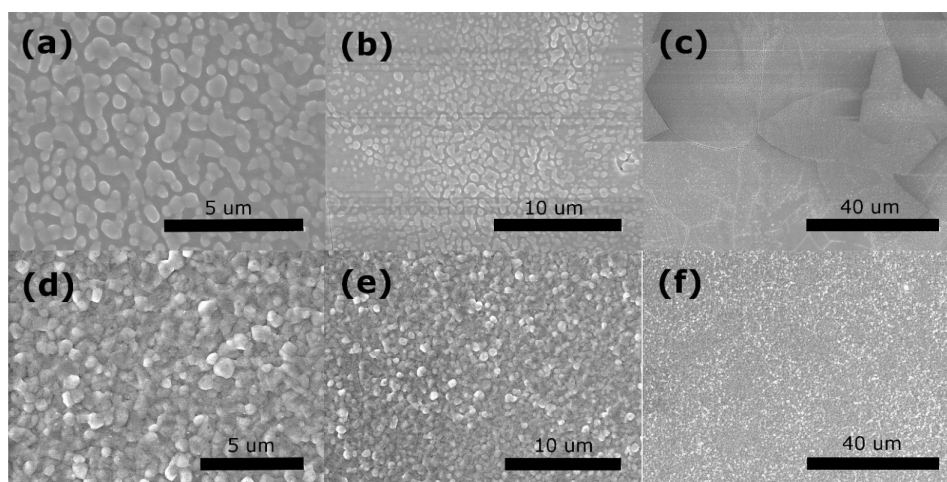


Figure E.4: Scanning electron microscopic images of films prepared by SSVD of pristine CsBr + PbBr<sub>2</sub> powders (a-c) and mechanochemically-synthesized CsPbBr<sub>3</sub> (d-f) after thermal annealing. In the case of the films composed of ball-milled powders, small grains with an average size of < 10 nm are observed at room temperature, whereas after annealing of the ball-milled film, on average much larger grains (> 100 nm) are observed.

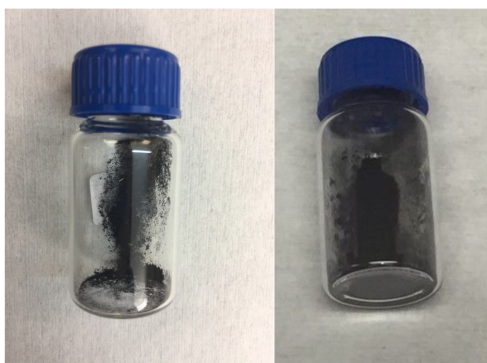


Figure E.5: Photographs of a ball-milled sample of  $\text{CsI} + \text{PbI}_2$  in inert atmosphere (nitrogen). The black powder is characteristic of cubic  $\text{CsPbI}_3$ . The picture on the left was taken just after mechanochemical synthesis, while the picture on the right was taken one month later. As can be seen, the cubic perovskite powder is not degraded when stored under nitrogen, since otherwise a yellow discoloration would be observed, indicating the conversion into the “yellow” orthorhombic phase.

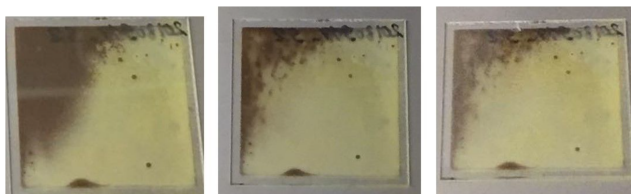


Figure E.6: Photographs of a mixed cubic/orthorhombic (black/yellow)  $\text{CsPbI}_3$  film upon aging at room temperature in nitrogen. The photograph on the left is taken just after annealing, the middle one is taken after 3 days in air and the right one is taken after 5 days.

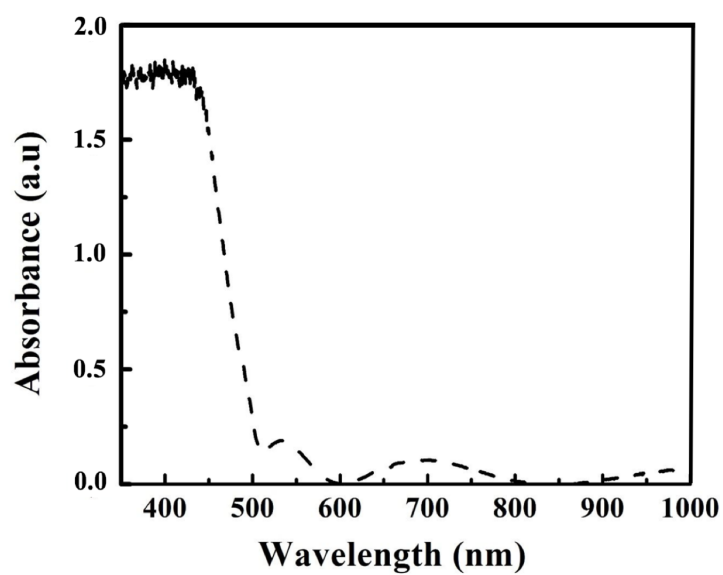


Figure E.7: Absorption spectrum of a thin film prepared by SSVD of ball-milled  $\text{CsPbI}_3$ . The absorption onset corresponds to  $\text{PbI}_2$ , whereas no marked onset is visible around 700 nm, as would be expected from  $\text{CsPbI}_3$ .

# List of Publications

## Prior to Ph.D.

S. Hollevoet, K. B. Gandrud, M. Y. Timmermans, B. Put, Y. El Ajjouri, K. Van de Kerckhove, C. Detavernier, M. Mees, P. M. Vereecken, Novel Thin-Film Solid Nanocomposite Electrolyte for Lithium-Ion Batteries by Combined MLD and ALD. *Adv. Mater. Interfaces*, **2019**, 1901407. [IF: 4.370 (2019), Q1]

## Included in the doctoral thesis

F. Palazón, Y. El Ajjouri, P. Sebastia-Luna, S. Lauciello, L. Manna and H. J. Bolink, Mechanochemical Synthesis of Inorganic Halide Perovskites: Evolution of Phase-purity, Morphology and Photoluminescence. *J. Mater. Chem. C*, **2019**, 7, 11406-11410. [IF: 6.641 (2019), Q1]

Y. El Ajjouri, V. S. Chirvony, M. Sessolo, F. Palazón and H. J. Bolink, Incorporation of potassium halides in the mechanochemical synthesis of inorganic perovskites: feasibility and limitations of ion-replacement and trap passivation. *RSC Adv.*, **2018**, 8, 41548-41551. [IF: 3.049 (2018), Q1]

Y. El Ajjouri, F. Locardi, M. C. Gélvez-Rueda, M. Prato, M. Sessolo, M. Ferretti, F. C. Grozema, F. Palazón and H. J. Bolink, Mechanochemical Synthesis of Sn(II) and Sn(IV) Iodide Perovskites and Study of Their Structural, Chemical, Thermal, Optical and Electrical Properties. *Energy Technol.*, **2019**, 1900788. [IF: 3.020 (2019), Q1]

Y. El Ajjouri, V. S. Chirvony, N. Vassilyeva, M. Sessolo, F. Palazón and H. J. Bolink, Low-Dimensional Non-Toxic  $A_3Bi_2X_9$  Compounds Synthesized by a Dry Mechanochemical Route with Tunable Visible Photoluminescence at Room Temperature. *J. Mater. Chem. C*, **2019**, 7, 6236-6240. [IF: 6.641 (2019), Q1]

Y. El Ajjouri, F. Palazón, M. Sessolo and H. J. Bolink, Single-Source Vacuum Deposition of Mechanochemical Synthesized Inorganic Halide Perovskites. *Chem. Mater.*, **2018**, 30 (21), 7423-7427. [IF: 10.159 (2018), Q1]

## Other publications

Y. El Ajjouri, A. M. Igual-Muñoz, M. Sessolo, F. Palazón and H. J. Bolink, Tunable Wide-Bandgap Monohalide Perovskites. *Adv. Opt. Mater.*, **2020**, 2000423, 1-5. [IF: 7.020 (2020), Q1]

F. Palazón, Y. El Ajjouri and H. J. Bolink, Making by grinding: mechanochemistry boosts the development of halide perovskites and other multinary metal halides. *Adv. Energy Mater.*, **2019**, 1902499. [IF: 24.884 (2019), Q1]

# List of Figures

1.1	Illustration of (a) a unit cell composed of eight corner-sharing octahedra intercalated with an A-cation and (b) a repetition of the unit cell in three dimensions. . . . .	2
1.2	Goldschmidt tolerance factor of lead halide perovskites as a function of the A-cation ionic radius. . . . .	2
1.3	(a) Anion-exchange allowing tuning of the bandgap of halide perovskites and (b) orbital diagrams of CsPbI <sub>3</sub> (green), CsPbBr <sub>3</sub> (blue) and CsPbCl <sub>3</sub> (orange). . . . .	3
1.4	Unit cell illustrations of (a) Cs <sub>2</sub> SnI <sub>6</sub> , (b) Rb <sub>3</sub> Bi <sub>2</sub> I <sub>9</sub> , (c) Cs <sub>3</sub> Bi <sub>2</sub> I <sub>9</sub> , (d) RbPbBr <sub>3</sub> , (e) Cs <sub>4</sub> PbBr <sub>6</sub> and (f) CsPb <sub>2</sub> Br <sub>5</sub> . . . . .	4
1.5	Illustration of (a) a unit cell of (BA) <sub>2</sub> (MA)Pb <sub>2</sub> I <sub>7</sub> and (b) a repetition of the unit cell in two dimensions. . . . .	5
1.6	Photograph of a ball-mill jar and two zirconia beads used for the mechanochemical synthesis of multinary metal halide semiconductors. The left vial contains the pristine stoichiometric perovskite precursors (CsBr and PbBr <sub>2</sub> ). The right vial contains the CsPbBr <sub>3</sub> perovskite that has been formed by solvent-free ball-milling of the stoichiometric perovskite precursors. . . . .	6
1.7	Solution-based deposition techniques for the formation of perovskite thin films. . . . .	11
1.8	Vapor deposition techniques for the formation of perovskite thin films. . . . .	13
1.9	Illustration of the single-source vacuum deposition (SSVD) of solvent-free mechanochemically-synthesized perovskite powders. . . . .	16
2.1	Illustration of the methodological approach of the mechanochemical synthesis of multinary metal halide semiconductors and the subsequent conversion of the synthesized powders into thin films via single-source vacuum deposition (SSVD). . . . .	19
2.2	X-ray tube as the source of X-rays in an X-ray diffraction tool. . . . .	21
2.3	Bragg-Brentano setup where both the X-ray source and the detector can rotate relative to a fixed sample holder in order to encounter the lattice spacing using Bragg's law. . . . .	22
2.4	Incident X-ray beam interacting with periodically-arranged atoms (green dots) in a crystalline material. . . . .	22
2.5	(a) Illustration of (1) electron emission, (2) relaxation and (3) recombination. HOMO and LUMO stand for the highest occupied molecular orbital and lowest unoccupied molecular orbital, respectively. Different energy levels are represented by $H_0$ , $H_1$ , $H_2$ , $L_0$ , $L_1$ and $L_2$ in order of increasing energy. (b) Illustration of energy loss due to electron relaxation. . . . .	24
2.6	Illustration of typical DTA plots of a hypothetical material, where (a) the difference of sample temperature is plotted as a function of the temperature of the reference material and (b) the difference in temperature is plotted as a function of the applied temperature. . . . .	26
3.1	X-ray diffraction analysis of stoichiometric CsBr:PbBr <sub>2</sub> mixtures ball-milled for different times up to 5 minutes, with a close view of the $2\theta = 10^\circ - 20^\circ$ range (see full patterns in Figure A.1 in Appendix A) of the diffractograms where characteristic peaks of different phases are highlighted in different colors. . . . .	29
3.2	(a) Weight fraction and (b) molar fraction of different species as derived from the RIR method and Rietveld refinement. . . . .	30

3.3	Scanning electron microscopic images of the different phases found in the samples and identified by EDX analysis. . . . .	31
3.4	SEM images and corresponding EDX maps for Cs (green), Br (red) and Pb (blue). . . . .	31
3.5	Microstructural XRD analysis. (a) Williamson-Hall (WH) plots obtained from Le Bail fits of XRD data acquired on stoichiometric CsBr:PbBr <sub>2</sub> mixtures ball-milled for 5 minutes up to 10 hours (see Figure A.3 in Appendix A). (b) Apparent isotropic average crystal size deduced from extrapolated value at origin from the WH plots as a function of the ball-milling time. . . . .	32
3.6	(a) Absolute and (b) normalized photoluminescence intensities of samples ball-milled for different times under identical measurement conditions. . . . .	33
4.1	XRD (a–f) and optical (g–i) characterization of powders prepared from an equimolar CsBr:PbBr <sub>2</sub> mixture (Reference; black lines) or K <sub>0.2</sub> Cs <sub>0.8</sub> Br:PbBr <sub>2</sub> (green lines). . . . .	38
4.2	XRD (a–c) and optical (d and e) characterization of powders prepared by dry ball-milling of 20 % KI (red), 20 % KBr (green) and 20 % KCl (blue) with CsBr:PbBr <sub>2</sub> (1:1) as the perovskite precursors. . . . .	39
5.1	Crystal structures of CsSnI <sub>3</sub> (left) and Cs <sub>2</sub> SnI <sub>6</sub> (right). . . . .	42
5.2	X-ray diffractograms of mechanochemically-synthesized tin perovskites (black lines), along with the reference bulk patterns retrieved from the Inorganic Crystal Structure Database (ICSD; colored columns). . . . .	45
5.3	Thermogravimetric (TGA, filled area) and differential thermal (DTA, simple line) analysis curves of all compounds in the 40–1000 °C range. . . . .	46
5.4	High-resolution XPS spectra of all main elements from the different compounds: Cs 3d, I 3d, Sn 3d, N 1s, C 1s and Pb 4f regions. . . . .	47
5.5	Optical characterization (absorbance – presented by the filled areas – and photoluminescence – presented by the simple lines – in the left column), UPS and derived energy diagrams of all Sn(II) and Sn(IV) compounds: CsSnI <sub>3</sub> (+ SnF <sub>2</sub> ), Cs(SnPb)I <sub>3</sub> (+ SnF <sub>2</sub> ), FASnI <sub>3</sub> , FA(SnPb)I <sub>3</sub> , Cs <sub>2</sub> SnI <sub>6</sub> and FA <sub>2</sub> SnI <sub>6</sub> . . . . .	49
5.6	(a) Mobility of charge carriers ( $\mu$ ) as a function of temperature and (b) change of conductivity ( $\Delta\sigma/Q$ ) as a function of time of a Sn(II) 3D perovskite (grey) and a Sn(IV) 0D vacancy-ordered perovskite (green). . . . .	51
6.1	Crystal structures of (a) Cs <sub>3</sub> Bi <sub>2</sub> I <sub>9</sub> and (b) Rb <sub>3</sub> Bi <sub>2</sub> I <sub>9</sub> viewed from the a-axis. . . . .	54
6.2	XRD characterization of mechanochemically-synthesized inorganic A <sub>3</sub> Bi <sub>2</sub> X <sub>9</sub> (A = K <sup>+</sup> , Rb <sup>+</sup> , Cs <sup>+</sup> ; X = I <sup>-</sup> , Br <sup>-</sup> , Cl <sup>-</sup> ; black lines) and reference bulk patterns when available from the Inorganic Crystal Structure Database (ICSD; colored columns). . . . .	56
6.3	XRD characterization of mechanochemically-synthesized hybrid A <sub>3</sub> Bi <sub>2</sub> X <sub>9</sub> (A = MA or FA; X = I <sup>-</sup> , Br <sup>-</sup> or Cl <sup>-</sup> ; black lines) and reference bulk patterns from the Inorganic Crystal Structure Database (ICSD) for the MA-based compounds (colored columns). . . . .	58
6.4	Normalized absorbance spectra of all A <sub>3</sub> Bi <sub>2</sub> X <sub>9</sub> compounds (solid lines) and photoluminescence spectra of Cs <sub>3</sub> Bi <sub>2</sub> Br <sub>9</sub> and Cs <sub>3</sub> Bi <sub>2</sub> I <sub>9</sub> (dashed lines with filled area under curve). . . . .	60
6.5	Photoluminescence spectrum of a solid pellet made from a finely ground mixture of mechanochemically-synthesized Cs <sub>3</sub> Bi <sub>2</sub> Br <sub>9</sub> and Cs <sub>3</sub> Bi <sub>2</sub> I <sub>9</sub> together with transparent PMMA beads. . . . .	61
7.1	XRD characterization of thin films prepared by SSVD of simply mixed CsCl + PbCl <sub>2</sub> (a, c) and CsBr + PbBr <sub>2</sub> (b, d) at room temperature (a, b), as well as after thermal annealing at 225 °C (c, d). . . . .	64
7.2	Normalized absorption and photoluminescence spectra of thin films prepared by SSVD of simply mixed CsCl + PbCl <sub>2</sub> (a, c) and CsBr + PbBr <sub>2</sub> (b, d) at room temperature (a, b), as well as after thermal annealing at 225 °C (c, d) for 15 minutes. . . . .	65

7.3	XRD characterization of ball-milled (BM) CsX + PbX <sub>2</sub> powders (a-c), as well as thin films prepared by SSVD of the resulting powders at room temperature (d-f) and after thermal annealing (g-i). . . . .	66
7.4	Normalized absorption and photoluminescence spectra of ball-milled CsX + PbX <sub>2</sub> powders (a-c), as well as thin films prepared by SSVD of the resulting powders at room temperature (d-f) and after thermal annealing (g-i). . . . .	67
A.1	Le Bail and Rietveld refinements of XRD data for stoichiometric CsBr:PbBr <sub>2</sub> mixtures ball-milled for 30 seconds, 1 minute, 2 minutes, 3 minutes, 4 minutes and 5 minutes.	90
A.2	X-ray diffractograms of stoichiometric CsBr:PbBr <sub>2</sub> mixtures ball-milled for 5 minutes, 30 minutes, 1 hour and 10 hours, fitted with a single CsPbBr <sub>3</sub> phase. . . . .	91
A.3	X-ray diffractograms of the main CsPbBr <sub>3</sub> diffraction peaks showing broadening at long milling times (t = 10 h). . . . .	91
A.4	SEM image of ball-milled CsPbBr <sub>3</sub> for 10 hours. . . . .	92
A.5	Optical absorption spectra of all stoichiometric CsBr:PbBr <sub>2</sub> mixtures ball-milled for different times showing similar onsets at approximately 540 nm, corresponding to "bulk" CsPbBr <sub>3</sub> . . . . .	92
B.1	XRD signals of samples prepared from pure CsBr (reference, black line) and partly (20 %) substituted by KBr (K <sub>0.2</sub> Cs <sub>0.8</sub> PbBr <sub>3</sub> , green line) in the perovskite structure APbBr <sub>3</sub> . . . . .	99
B.2	X-ray diffractograms of powders prepared by dry ball-milling of KBr and PbBr <sub>2</sub> in different molar ratios (1:2, 1:1, and 4:1). The reference patterns for bulk KBr (ICSD-18015) and KPb <sub>2</sub> Br <sub>5</sub> (ICSD-250266) are presented as green and blue columns.	99
B.3	X-ray diffractogram of adhesive tape used to fix powders on glass substrates. This signal, approximately 2θ = 26°, appears sometimes as a parasitic diffraction peak in the samples' diffractograms. . . . .	100
B.4	XRD signals of samples prepared from pure CsBr (reference, black line) and partly (5 %) substituted by KBr (green line) in the perovskite structure APbBr <sub>3</sub> . . . . .	100
B.5	Photoluminescence spectra of ball-milled ABr:PbBr <sub>2</sub> mixtures (with A = CsBr (reference) or K <sub>0.2</sub> Cs <sub>0.8</sub> ) fitted with two Gaussian peaks (dashed red and blue curves).	101
B.6	XRD patterns of powders prepared by dry ball-milling of 20 % KI (blue), 20 % KBr (red) and 20 % KCl (black) with CsBr:PbBr <sub>2</sub> (1:1) as the perovskite precursors. . . . .	101
C.1	Most representative parts of the X-ray diffractograms presented in Figure 5.2 for CsSnI <sub>3</sub> , Cs(SnPb)I <sub>3</sub> , FASnI <sub>3</sub> and FA(SnPb)I <sub>3</sub> . . . . .	114
C.2	Differential thermal analysis (DTA) of ball-milled CsI:SnI <sub>2</sub> (1:1) with (red curve) and without SnF <sub>2</sub> (black curve). . . . .	114
C.3	Comparison between the thermogravimetric curves of ASnI <sub>3</sub> and A(SnPb)I <sub>3</sub> (A = Cs <sup>+</sup> or FA). . . . .	115
C.4	Comparison between the thermogravimetric curves of FASnI <sub>3</sub> , FA(SnPb)I <sub>3</sub> and FA <sub>2</sub> SnPbI <sub>6</sub> . . . . .	115
C.5	F 1s XPS spectra of CsSnI <sub>3</sub> and Cs(SnPb)I <sub>3</sub> prepared in the presence of SnF <sub>2</sub> . . . . .	116
C.6	O 1s XPS spectra of all Sn(II) and Sn(IV) compounds: CsSnI <sub>3</sub> (+ SnF <sub>2</sub> ), Cs(SnPb)I <sub>3</sub> (+ SnF <sub>2</sub> ), FASnI <sub>3</sub> , FA(SnPb)I <sub>3</sub> , Cs <sub>2</sub> SnI <sub>6</sub> and FA <sub>2</sub> SnI <sub>6</sub> . . . . .	116
C.7	Photograph of Cs <sub>2</sub> SnI <sub>6</sub> powder – exposed to air – fixed on adhesive tape on a glass substrate. . . . .	117
C.8	Change of reflected microwave power (ΔP/P) as a function of time for FASnI <sub>3</sub> presented at different microwave frequencies (32 to 33 GHz). . . . .	117
C.9	Charge carrier lifetime (Δσ/Q) of the 3D sample (Cs(SnPb)I <sub>3</sub> ) at (a) different pulse widths and (b) different temperatures. . . . .	117
C.10	Charge carrier lifetime (Δσ/Q) of the 0D sample (FA <sub>2</sub> SnI <sub>6</sub> ) at different temperatures.	118
D.1	Experimental (Y <sub>obs</sub> ) and fitted (Y <sub>calc</sub> ) XRD data for the dry mechanochemically-synthesized Rb <sub>3</sub> Bi <sub>2</sub> X <sub>9</sub> compounds (X = Cl <sup>-</sup> , Br <sup>-</sup> or I <sup>-</sup> ). . . . .	126



D.2	Reference XRD patterns of KX (blue columns) and BiX <sub>3</sub> (red columns) and diffractograms (black lines) of powders obtained by dry ball-milling thereof. . . . .	126
D.3	Experimental ( $Y_{obs}$ ) and fitted ( $Y_{calc}$ ) data for MA <sub>3</sub> Bi <sub>2</sub> I <sub>9</sub> and FA <sub>3</sub> Bi <sub>2</sub> I <sub>9</sub> . . . . .	127
D.4	Experimental ( $Y_{obs}$ ) and fitted ( $Y_{calc}$ ) data for MA <sub>3</sub> Bi <sub>2</sub> Br <sub>9</sub> and FA <sub>3</sub> Bi <sub>2</sub> Br <sub>9</sub> . . . . .	127
D.5	Experimental ( $Y_{obs}$ ) and fitted ( $Y_{calc}$ ) data for MA <sub>3</sub> Bi <sub>2</sub> Cl <sub>9</sub> and FA <sub>3</sub> Bi <sub>2</sub> Cl <sub>9</sub> . . . . .	128
E.1	Absorption spectrum of a thin film formed by SSVD of simply mixed CsBr + PbBr <sub>2</sub> , showing optical interferences. . . . .	136
E.2	XRD (a,c) and optical (b,d) characterization of thin films made by SSVD of simply mixed CsI and PbI <sub>2</sub> at room temperature (RT) and after annealing at 225 °C for 15 minutes on a hotplate in a nitrogen-filled glovebox. . . . .	136
E.3	XRD characterization of a thin film formed by SSVD of ball-milled CsBr + PbBr <sub>2</sub> at different annealing temperatures. . . . .	137
E.4	Scanning electron microscopic images of films prepared by SSVD of pristine CsBr + PbBr <sub>2</sub> powders (a-c) and mechanochemically-synthesized CsPbBr <sub>3</sub> (d-f) after thermal annealing. In the case of the films composed of ball-milled powders, small grains with an average size of < 10 nm are observed at room temperature, whereas after annealing of the ball-milled film, on average much larger grains (> 100 nm) are observed. . . . .	137
E.5	Photographs of a ball-milled sample of CsI + PbI <sub>2</sub> in inert atmosphere (nitrogen). The black powder is characteristic of cubic CsPbI <sub>3</sub> . . . . .	138
E.6	Photographs of a mixed cubic/orthorhombic (black/yellow) CsPbI <sub>3</sub> film upon aging at room temperature in nitrogen. . . . .	138
E.7	Absorption spectrum of a thin film prepared by SSVD of ball-milled CsPbI <sub>3</sub> . . . . .	139

# List of Tables

5.1	Atomic percentages of relevant elements based on high-resolution XPS spectra. CsSnI <sub>3</sub> and Cs(SnPb)I <sub>3</sub> were synthesized in the presence of SnF <sub>2</sub> . . . . .	47
6.1	Refined cell parameters for Rb <sub>3</sub> Bi <sub>2</sub> X <sub>9</sub> compounds (X = I <sup>-</sup> , Br <sup>-</sup> or Cl <sup>-</sup> ). . . . .	57
6.2	Refined cell parameters for the hybrid organic-inorganic compounds MA <sub>3</sub> Bi <sub>2</sub> X <sub>9</sub> and FA <sub>3</sub> Bi <sub>2</sub> X <sub>9</sub> (X = I <sup>-</sup> , Br <sup>-</sup> or Cl <sup>-</sup> ). . . . .	59

# List of Abbreviations and Symbols

## Abbreviations

Abs	Absorption
Ann.	Annealed
a.u.	Arbitrary unit
BA	Butylammonium
BE	Binding energy
BM	Ball-milled
b.p.	Boiling point
BRR	Bead-to-reactant weight ratio
CBM	Conduction band maximum
CIE	<i>Commission Internationale de l'Éclairage</i>
CPS	Counts per second
Cs <sub>x</sub> FA <sub>1-x</sub> PbI <sub>3</sub>	x-Cesium (1-x)-formamidinium lead tri-iodide
CVD	Chemical vapor deposition
DEE	Diethyl ether
DFT	Density functional theory
DMF	Dimethylformamide
DMSO	Dimethyl sulfoxide
DTA	Differential thermal analysis
EA	Ethylammonium
EDX	Energy-dispersive X-ray spectroscopy
FA	Formamidinium
FAPbI <sub>3</sub>	Formamidinium lead tri-iodide
FA(SnPb)I <sub>3</sub>	Formamidinium (tin-lead) tri-iodide
FASnI <sub>3</sub>	Formamidinium tin tri-iodide
FEG	Field-emission gun
FWHM	Full width at half maximum
GBL	γ-butyro-lactone
GUA	Guanidinium
HCN	Hydrogen cyanide
HOMO	Highest occupied molecular orbital
ICSD	Inorganic crystal structure database
IF	Impact factor
IPA	Isopropanol
KX	Potassium halide
LA	Long-chain ammonium cation
LAG	Liquid-assisted grinding
LED	Light-emitting diode
LHP	Lead halide perovskite
LUMO	Lowest unoccupied molecular orbital
MA	Methylammonium
MAI	Methylammonium iodide

---

MAPbBr <sub>3</sub>	Methylammonium lead tribromide
MAPbCl <sub>3</sub>	Methylammonium lead trichloride
MAPbI <sub>3</sub>	Methylammonium lead tri-iodide
MCS	Mechanochemical synthesis
MINECO	Ministry of economy and competitiveness
MOF	Metal organic framework
NC	Nanocrystal
NIR	Near-infrared
NMR	Nuclear magnetic resonance
Norm.	Normalized
OHP	Organic-inorganic hybrid perovskite
PCE	Power conversion efficiency
PEEK	Polyether ether ketone
PL	Photoluminescence
PLQY	Photoluminescence quantum yield
PMMA	Poly(methyl methacrylate)
PR-TRMC	Pulse-radiolysis time-resolved microwave conductivity
PTFE	Polytetrafluoroethylene
PV	Photovoltaic
PXRD	Powder X-ray diffraction
Q	Quartile
QCM	Quartz crystal micro-balance
rad	Radians
RIR	Relative intensity ratio
rpm	Revolutions per minute
RT	Room temperature
SA	Short-chain ammonium cation
SEM	Scanning electron microscopy
SSVD	Single-source vacuum deposition
TCH	Thompson-Cox-Hastings
TGA	Thermogravimetric analysis
TRMC	Time-resolved microwave conductivity
UPS	Ultraviolet photoelectron spectroscopy
UV	Ultra-violet
UV-Vis	Ultra-violet visible
VBM	Valence band maximum
WH	Williamson-Hall
XPS	X-ray photoelectron spectroscopy
XRD	X-ray diffraction
ZnX <sub>2</sub>	Zinc halide
0D	Zero-dimensional
1D	One-dimensional
2D	Two-dimensional
3D	Three-dimensional
δ-FAPbI <sub>3</sub>	Orthorhombic non-perovskite phase of formamidinium lead tri-iodide

## Symbols

$A$	Absorbance
$c$	(1) Speed of light (2) Concentration of the absorbing species in Lambert Beer's law
$d$	Inter-planar spacing of a crystal in Bragg's law
$E$	Photon energy
$E_{binding}$	Binding energy
$E_{kinetic}$	Kinetic energy
$h$	Planck's constant
$I$	Intensity of an excited light source
$I_0$	Intensity of the emitted light
$k$	Shape factor
$l$	Thickness of a sample in Lambert Beer's law
$L$	Wavelength of incident radiation
$n$	(1) Thickness of the inorganic framework in $(LA)_2(SA)_{n-1}Pb_nX_{3n+1}$ and thus the amount of $[BX_6]^{4-}$ octahedra that are separated by the long-chain ammonium cations (LA) and where the short-chain ammonium cations (SA) intercalate with (2) Integer representing the order of diffraction peak in Bragg's law
$r_A$	Ionic radius of cation $A$ in the $ABX_3$ crystal structure
$r_B$	Ionic radius of metal $B$ in the $ABX_3$ crystal structure
$r_X$	Ionic radius of anion $X$ in the $ABX_3$ crystal structure
$s$	Inverse of the inter-planar spacing ( $d$ ) of a crystal in Bragg's law
$t$	Goldschmidt tolerance factor
$t_0$	Set-point identifying that no ball-milling has taken place
$T$	Transmittance
$\beta_\epsilon$	Strain broadening
$\beta_{hkl}$	Total broadening due to strain and size in a particular peak having the (hkl) value
$\beta_L$	Size broadening
$\epsilon$	(1) Molar absorptivity of the molar extinction coefficient in Lambert Beer's law (2) Intrinsic strain in the WH-equation
$\Delta\sigma/Q$	Change in electrical conductivity
$\Delta P/P$	Change in reflected microwave power
$\theta$	Angle of incidence in Bragg's law
$\lambda$	Wavelength
$\mu$	Mobility of charge carriers
$\phi$	Work function
$\omega$	Angle between the X-ray source and the sample holder in an XRD setup

# Bibliography

- [1] Hans-rudolf Wenk and Andrei Bulakh. Minerals: their constitution and origin. *Choice Reviews Online*, 42(04):42–2243–42–2243, 2004.
- [2] Zhen Li, Mengjin Yang, Ji Sang Park, Su Huai Wei, Joseph J. Berry, and Kai Zhu. Stabilizing Perovskite Structures by Tuning Tolerance Factor: Formation of Formamidineum and Cesium Lead Iodide Solid-State Alloys. *Chemistry of Materials*, 28(1):284–292, 2016.
- [3] Christopher J. Bartel, Christopher Sutton, Bryan R. Goldsmith, Runhai Ouyang, Charles B. Musgrave, Luca M. Ghiringhelli, and Matthias Scheffler. New tolerance factor to predict the stability of perovskite oxides and halides. *Science Advances*, 5(2):1–19, 2019.
- [4] Piet Hartman and Hak Kim Chan. Application of the Periodic Bond Chain (PBC) Theory and Attachment Energy Consideration to Derive the Crystal Morphology of Hexamethylmelamine. *Pharmaceutical Research: An Official Journal of the American Association of Pharmaceutical Scientists*, 10(7):1052–1058, 1993.
- [5] Gregor Kieslich, Shijing Sun, and Anthony K. Cheetham. An extended Tolerance Factor approach for organic-inorganic perovskites. *Chemical Science*, 6(6):3430–3433, 2015.
- [6] Samuel D. Stranks, Giles E. Eperon, Giulia Grancini, Christopher Menelaou, Marcelo J P Alcocer, Tomas Leijtens, Laura M. Herz, Annamaria Petrozza, and Henry J. Snaith. Electron-hole diffusion lengths exceeding 1 micrometer in an organometal trihalide perovskite absorber. *Science*, 342(6156):341–344, 2013.
- [7] Stefaan De Wolf, Jakub Holovsky, Soo Jin Moon, Philipp Löper, Bjoern Niesen, Martin Ledinsky, Franz Josef Haug, Jun Ho Yum, and Christophe Ballif. Organometallic halide perovskites: Sharp optical absorption edge and its relation to photovoltaic performance. *Journal of Physical Chemistry Letters*, 5(6):1035–1039, 2014.
- [8] Nam Gyu Park. Perovskite solar cells: An emerging photovoltaic technology. *Materials Today*, 18(2):65–72, 2015.
- [9] Himchan Cho, Young Hoon Kim, Christoph Wolf, Hyeon Dong Lee, and Tae Woo Lee. Improving the Stability of Metal Halide Perovskite Materials and Light-Emitting Diodes. *Advanced Materials*, 30(42):1–24, 2018.
- [10] Loredana Protesescu, Sergii Yakunin, Maryna I. Bodnarchuk, Franziska Krieg, Riccarda Caputo, Christopher H. Hendon, Ruo Xi Yang, Aron Walsh, and Maksym V. Kovalenko. Nanocrystals of Cesium Lead Halide Perovskites (CsPbX<sub>3</sub>, X = Cl, Br, and I): Novel Optoelectronic Materials Showing Bright Emission with Wide Color Gamut. *Nano Letters*, 15(6):3692–3696, 2015.
- [11] Nakita K. Noel, Antonio Abate, Samuel D. Stranks, Elizabeth S. Parrott, Victor M. Burlakov, Alain Goriely, and Henry J. Snaith. Enhanced photoluminescence and solar cell performance via Lewis base passivation of organic-inorganic lead halide perovskites. *ACS Nano*, 8(10):9815–9821, 2014.

- [12] Rebecca J. Sutton, Giles E. Eperon, Laura Miranda, Elizabeth S. Parrott, Brett A. Kamino, Jay B. Patel, Maximilian T. Hörantner, Michael B. Johnston, Amir Abbas Haghighirad, David T. Moore, and Henry J. Snaith. Bandgap-Tunable Cesium Lead Halide Perovskites with High Thermal Stability for Efficient Solar Cells. *Advanced Energy Materials*, 6(8):1502458, 2016.
- [13] Giles E. Eperon, Samuel D. Stranks, Christopher Menelaou, Michael B. Johnston, Laura M. Herz, and Henry J. Snaith. Formamidinium lead trihalide: A broadly tunable perovskite for efficient planar heterojunction solar cells. *Energy and Environmental Science*, 7(3):982–988, 2014.
- [14] Yousra El Ajjouri, Ana M Igual-muñoz, Michele Sessolo, Francisco Palazon, and Henk J Bolink. Tunable Wide-Bandgap Monohalide Perovskites. 2000423:1–5, 2020.
- [15] Abdelrahman M. Askar, Abhoy Karmakar, Guy M. Bernard, Michelle Ha, Victor V. Terskikh, Benjamin D. Wiltshire, Sahil Patel, Jonathan Fleet, Karthik Shankar, and Vladimir K. Michaelis. Composition-Tunable Formamidinium Lead Mixed Halide Perovskites via Solvent-Free Mechanochemical Synthesis: Decoding the Pb Environments Using Solid-State NMR Spectroscopy. *Journal of Physical Chemistry Letters*, 9(10):2671–2677, may 2018.
- [16] Yousra El Ajjouri, Vladimir S. Chirvony, Natalia Vassilyeva, Michele Sessolo, Francisco Palazon, and Henk J. Bolink. Low-dimensional non-toxic A<sub>3</sub>Bi<sub>2</sub>X<sub>9</sub> compounds synthesized by a dry mechanochemical route with tunable visible photoluminescence at room temperature. *Journal of Materials Chemistry C*, 2019.
- [17] Abhoy Karmakar, Abdelrahman M. Askar, Guy M. Bernard, Victor V. Terskikh, Michelle Ha, Sahil Patel, Karthik Shankar, and Vladimir K. Michaelis. Mechanochemical Synthesis of Methylammonium Lead Mixed-Halide Perovskites: Unraveling the Solid-Solution Behavior Using Solid-State NMR. *Chemistry of Materials*, 30(7):2309–2321, apr 2018.
- [18] Mojtaba Abdi-Jalebi, Zahra Andaji-Garmaroudi, Stefania Cacovich, Camille Stavarakas, Bertrand Philippe, Johannes M. Richter, Mejd Alsari, Edward P. Booker, Eline M. Hutter, Andrew J. Pearson, Samuele Lilliu, Tom J. Savenije, Håkan Rensmo, Giorgio Divitini, Caterina Ducati, Richard H. Friend, and Samuel D. Stranks. Maximizing and stabilizing luminescence from halide perovskites with potassium passivation. *Nature*, 555(7697):497–501, 2018.
- [19] Aurélien M.A. Leguy, Pooya Azarhoosh, M. Isabel Alonso, Mariano Campoy-Quiles, Oliver J. Weber, Jizhong Yao, Daniel Bryant, Mark T. Weller, Jenny Nelson, Aron Walsh, Mark Van Schilfgaarde, and Piers R.F. Barnes. Experimental and theoretical optical properties of methylammonium lead halide perovskites. *Nanoscale*, 8(12):6317–6327, 2016.
- [20] Yousra El Ajjouri, Vladimir S. S. S. Chirvony, Michele Sessolo, Francisco Palazon, Henk J. Bolink, Yousra El El Ajjouri, Vladimir S. S. S. Chirvony, Michele Sessolo, Yousra El Ajjouri, Vladimir S. S. S. Chirvony, Michele Sessolo, Francisco Palazon, Henk J. Bolink, Yousra El El Ajjouri, Vladimir S. S. S. Chirvony, Michele Sessolo, Yousra El Ajjouri, Vladimir S. S. S. Chirvony, Michele Sessolo, Francisco Palazon, and Henk J. Bolink. Incorporation of potassium halides in the mechanochemical synthesis of inorganic perovskites: feasibility and limitations of ion-replacement and trap passivation. *RSC Advances*, 8(72):41548–41551, 2018.
- [21] Marcin Saski, Daniel Prochowicz, Wojciech Marynowski, and Janusz Lewiński. Mechanochemical Synthesis, Optical, and Morphological Properties of MA, FA, Cs-SnX<sub>3</sub> (X = I, Br) and Phase-Pure Mixed-Halide MASnI<sub>x</sub>Br<sub>3-x</sub> Perovskites. *European Journal of Inorganic Chemistry*, 2019(22):2680–2684, 2019.
- [22] Zonghan Hong, Davin Tan, Rohit Abraham John, Yong Kang Eugene Tay, Yan King Terence Ho, Xin Zhao, Tze Chien Sum, Nripan Mathews, Felipe García, and Han Sen Soo. Completely Solvent-free Protocols to Access Phase-Pure, Metastable Metal Halide Perovskites and Functional Photodetectors from the Precursor Salts. *iScience*, 16:312–325, 2019.

- [23] Yousra El Ajjouri, Federico Locardi, María C. Gélvez-Rueda, Mirko Prato, Michele Sessolo, Maurizio Ferretti, Ferdinand C. Grozema, Francisco Palazon, and Henk J. Bolink. Mechanochemical Synthesis of Sn(II) and Sn(IV) Iodide Perovskites and Study of Their Structural, Chemical, Thermal, Optical, and Electrical Properties. *Energy Technology*, 1900788(Ii):1900788, 2019.
- [24] A. M. Elseman, A. E. Shalan, M. M. Rashad, and A. M. Hassan. Experimental and simulation study for impact of different halides on the performance of planar perovskite solar cells. *Materials Science in Semiconductor Processing*, 66(April 2018):176–185, 2017.
- [25] Tomas Leijtens, Beat Lauber, Giles E. Eperon, Samuel D. Stranks, and Henry J. Snaith. The importance of perovskite pore filling in organometal mixed halide sensitized TiO<sub>2</sub>-based solar cells. *Journal of Physical Chemistry Letters*, 5(7):1096–1102, 2014.
- [26] Prasenjit Maji, Apurba Ray, Priyabrata Sadhukhan, Souvik Chatterjee, and Sachindranath Das. Study on charge transfer mechanism and dielectric relaxation of cesium lead bromide (CsPbBr<sub>3</sub>). *Journal of Applied Physics*, 124(12), 2018.
- [27] Abhoy Karmakar, Mya S. Dodd, Xiaoyue Zhang, Meagan S. Oakley, Mariusz Klobukowski, and Vladimir K. Michaelis. Mechanochemical synthesis of 0D and 3D cesium lead mixed halide perovskites. *Chemical Communications*, 55(35):5079–5082, 2019.
- [28] Jiajun Lu, Shan Ci Chen, and Qingdong Zheng. Defect passivation of CsPbI<sub>2</sub>Br perovskites through Zn(II) doping: toward efficient and stable solar cells. *Science China Chemistry*, 62(8):1044–1050, 2019.
- [29] Kenichiro Tanaka and Takashi Kondo. Bandgap and exciton binding energies in lead-iodide-based natural quantum-well crystals. *Science and Technology of Advanced Materials*, 4(6):599–604, 2003.
- [30] Giles E. Eperon, Samuel D. Stranks, Christopher Menelaou, Michael B. Johnston, Laura M. Herz, and Henry J. Snaith. Formamidinium lead trihalide: A broadly tunable perovskite for efficient planar heterojunction solar cells. *Energy and Environmental Science*, 7(3):982–988, 2014.
- [31] Shuxia Tao, Ines Schmidt, Geert Brocks, Junke Jiang, Ionut Tranca, Klaus Meerholz, and Selina Olthof. Absolute energy level positions in tin- and lead-based halide perovskites. *Nature Communications*, 10(1):1–10, 2019.
- [32] T. Umebayashi, K. Asai, T. Umebayashi, K. Asai, T. Kondo, T. Kondo, and A. Nakao. Electronic structures of lead iodide based low-dimensional crystals. *Physical Review B - Condensed Matter and Materials Physics*, 67(15):2–7, 2003.
- [33] Rashid Ahmed, Fazal e Aleem, S. Javad Hashemifar, and Hadi Akbarzadeh. First-principles study of the structural and electronic properties of III-phosphides. *Physica B: Condensed Matter*, 403(10-11):1876–1881, 2008.
- [34] Federico Brivio, Alison B. Walker, and Aron Walsh. Structural and electronic properties of hybrid perovskites for high-efficiency thin-film photovoltaics from first-principles. *APL Materials*, 1(4), 2013.
- [35] Georgian Nedelcu, Loredana Protesescu, Sergii Yakunin, Maryna I. Bodnarchuk, Matthias J. Grotevent, and Maksym V. Kovalenko. Fast Anion-Exchange in Highly Luminescent Nanocrystals of Cesium Lead Halide Perovskites (CsPbX<sub>3</sub>, X = Cl, Br, I). *Nano Letters*, 15(8):5635–5640, 2015.
- [36] Quinten A. Akkerman and Liberato Manna. What Defines a Halide Perovskite? *ACS Energy Letters*, pages 604–610, 2020.
- [37] Chonghea Li, Xionggang Lu, Weizhong Ding, Liming Feng, Yonghui Gao, and Ziming Guo. Formability of ABX<sub>3</sub> (X = F, Cl, Br, I) halide perovskites. *Acta Crystallographica Section B: Structural Science*, 64(6):702–707, 2008.



- [38] Christopher J. Bartel, Christopher Sutton, Bryan R. Goldsmith, Runhai Ouyang, Charles B. Musgrave, Luca M. Ghiringhelli, and Matthias Scheffler. New tolerance factor to predict the stability of perovskite oxides and halides. *Science Advances*, 5(2):1–10, 2019.
- [39] Quinten A. Akkerman, Ahmed L. Abdelhady, and Liberato Manna. Zero-Dimensional Cesium Lead Halides: History, Properties, and Challenges. *Journal of Physical Chemistry Letters*, 9(9):2326–2337, 2018.
- [40] Constantinos C. Stoumpos and Mercuri G. Kanatzidis. The Renaissance of Halide Perovskites and Their Evolution as Emerging Semiconductors. *Accounts of Chemical Research*, 48(10):2791–2802, 2015.
- [41] Quinten A. Akkerman, Laura Martínez-Sarti, Luca Goldoni, Muhammad Imran, Dmitry Baranov, Henk J. Bolink, Francisco Palazon, and Liberato Manna. Molecular Iodine for a General Synthesis of Binary and Ternary Inorganic and Hybrid Organic-Inorganic Iodide Nanocrystals. *Chemistry of Materials*, 30(19):6915–6921, 2018.
- [42] Sidney E. Creutz, Hongbin Liu, Mitchell E. Kaiser, Xiaosong Li, and Daniel R. Gamelin. Structural Diversity in Cesium Bismuth Halide Nanocrystals. *Chemistry of Materials*, 31(13):4685–4697, 2019.
- [43] Jawaher Almutlaq, Jun Yin, Omar F. Mohammed, and Osman M. Bakr. The Benefit and Challenges of Zero-Dimensional Perovskites. *Journal of Physical Chemistry Letters*, 9(14):4131–4138, 2018.
- [44] Mingyu Hu, Chunyu Ge, Jie Yu, and Jing Feng. Mechanical and Optical Properties of Cs<sub>4</sub>BX<sub>6</sub> (B = Pb, Sn; X = Cl, Br, I) Zero-Dimension Perovskites. *Journal of Physical Chemistry C*, 121(48):27053–27058, 2017.
- [45] Ibrahim Dursun, Michele De Bastiani, Bekir Turedi, Badriah Alamer, Aleksander Shkurenko, Jun Yin, Ahmed M. El-Zohry, Issam Gereige, Ahmed AlSaggaf, Omar F. Mohammed, Mohamed Eddaoudi, and Osman M. Bakr. CsPb<sub>2</sub>Br<sub>5</sub> Single Crystals: Synthesis and Characterization. *ChemSusChem*, 10(19):3746–3749, 2017.
- [46] Manuel Wilke and Nicola Casati. Frontispiece: Insight into the Mechanochemical Synthesis and Structural Evolution of Hybrid Organic-Inorganic Guanidinium Lead(II) Iodides. *Chemistry - A European Journal*, 24(67):17711, 2018.
- [47] Alexander D. Jodlowski, Alfonso Yépez, Rafael Luque, Luis Camacho, and Gustavo de Miguel. Benign-by-Design Solventless Mechanochemical Synthesis of Three-, Two-, and One-Dimensional Hybrid Perovskites. *Angewandte Chemie - International Edition*, 55(48):14972–14977, 2016.
- [48] Enrico Greul, Michiel L. Petrus, Andreas Binek, Pablo Docampo, and Thomas Bein. Highly stable, phase pure Cs<sub>2</sub>AgBiBr<sub>6</sub> double perovskite thin films for optoelectronic applications. *Journal of Materials Chemistry A*, 5(37):19972–19981, 2017.
- [49] Jieli Yan, Weiming Qiu, Gang Wu, Paul Heremans, and Hongzheng Chen. Recent progress in 2D/quasi-2D layered metal halide perovskites for solar cells. *Journal of Materials Chemistry A*, 6(24):11063–11077, 2018.
- [50] Ian C. Smith, Eric T. Hoke, Diego Solis-Ibarra, Michael D. McGehee, and Hemamala I. Karunadasa. A Layered Hybrid Perovskite Solar-Cell Absorber with Enhanced Moisture Stability. *Angewandte Chemie - International Edition*, 53(42):11232–11235, 2014.
- [51] Duyen H. Cao, Constantinos C. Stoumpos, Omar K. Farha, Joseph T. Hupp, and Mercuri G. Kanatzidis. 2D Homologous Perovskites as Light-Absorbing Materials for Solar Cell Applications. *Journal of the American Chemical Society*, 137(24):7843–7850, 2015.
- [52] Zhiping Wang, Qianqian Lin, Francis P. Chmiel, Nobuya Sakai, Laura M. Herz, and Henry J. Snaith. Efficient ambient-air-stable solar cells with 2D-3D heterostructured butylammonium-caesium-formamidinium lead halide perovskites. *Nature Energy*, 2(9):1–10, 2017.

- [53] Constantinos C. Stoumpos, Duyen H. Cao, Daniel J. Clark, Joshua Young, James M. Rondinelli, Joon I. Jang, Joseph T. Hupp, and Mercouri G. Kanatzidis. Ruddlesden-Popper Hybrid Lead Iodide Perovskite 2D Homologous Semiconductors. *Chemistry of Materials*, 28(8):2852–2867, 2016.
- [54] Davin Tan and Felipe García. Main group mechanochemistry: from curiosity to established protocols. *Chemical Society Reviews*, 48(8):2274–2292, 2019.
- [55] R. P. Rastogi and N. B. Singh. Solid-state reactivity of picric acid and substituted hydrocarbons. *Journal of Physical Chemistry*, 72(13):4446–4449, 1968.
- [56] G. Rothenberg, A. P. Downie, C. L. Raston, and J. L. Scott. Understanding solid/solid organic reactions. *Journal of the American Chemical Society*, 123(36):8701–8708, 2001.
- [57] Tomislav Friscic and William Jones. Recent advances in understanding the mechanism of cocrystal formation via grinding. *Crystal Growth and Design*, 9(3):1621–1637, 2009.
- [58] Gerd Kaupp. Solid-state molecular syntheses: Complete reactions without auxiliaries based on the new solid-state mechanism. *CrystEngComm*, 5(23):117–133, 2003.
- [59] Zhi-Yuan Yuan Zhu, Qi-Qi Qi Yang, Lin-Feng Feng Gao, Lei Zhang, An-Ye Ye Shi, Chun-Lin Lin Sun, Qiang Wang, and Hao-Li Li Zhang. Solvent-Free Mechanochemical Synthesis of Composition-Tunable Cesium Lead Halide Perovskite Quantum Dots. *Journal of Physical Chemistry Letters*, 8(7):1610–1614, 2017.
- [60] Tomislav Friščić, Ivan Halasz, Patrick J. Beldon, Ana M. Belenguer, Frank Adams, Simon A.J. Kimber, Veijo Honkimäki, and Robert E. Dinnebier. Real-time and in situ monitoring of mechanochemical milling reactions. *Nature Chemistry*, 5(1):66–73, 2013.
- [61] Jean Louis Do and Tomislav Friščić. Mechanochemistry: A Force of Synthesis. *ACS Central Science*, 3(1):13–19, 2017.
- [62] Martin K. Beyer and Hauke Clausen-Schaumann. Mechanochemistry: The mechanical activation of covalent bonds. *Chemical Reviews*, 105(8):2921–2948, 2005.
- [63] Joseph L. Howard, Qun Cao, and Duncan L. Browne. Mechanochemistry as an emerging tool for molecular synthesis: What can it offer? *Chemical Science*, 9(12):3080–3094, 2018.
- [64] Marco Leonardi, Mercedes Villacampa, and J. Carlos Menéndez. Multicomponent mechanochemical synthesis. *Chemical Science*, 9(8):2042–2064, 2018.
- [65] Maria Klimakow, Peter Klobes, Andreas F. Thünemann, Klaus Rademann, and Franziska Emmerling. Mechanochemical synthesis of metal-organic frameworks: A fast and facile approach toward quantitative yields and high specific surface areas. *Chemistry of Materials*, 22(18):5216–5221, 2010.
- [66] Min Zhou, Jiahua Zhao, Pengfei Zhang, Nanqing Chen, and Shize Yang. Solvent-free and rapid synthesis of mesoporous Pt-iron oxide catalysts: Via mechanochemical assembly. *Catalysis Science and Technology*, 9(15):3907–3913, 2019.
- [67] Peter Baláž, Marcela Achimovicová, Matej Baláž, Peter Billik, Cherkezova Zheleva Zara, José Manuel Criado, Francesco Delogu, Erika Dutková, Eric Gaffet, Francisco José Gotor, Rakesh Kumar, Ivan Mitov, Tadej Rojac, Mamoru Senna, Andrey Streletskii, and Wieszorek Ciurawa Krystyna. Hallmarks of mechanochemistry: From nanoparticles to technology. *Chemical Society Reviews*, 42(18):7571–7637, 2013.
- [68] A. Urbieto, P. Fernández, and J. Piqueras. Growth and luminescence properties of micro- and nanoneedles in sintered CdSe. *Applied Physics Letters*, 85(24):5968–5970, 2004.
- [69] S. Patra and S. K. Pradhan. Microstructure and optical characterization of CdTe quantum dots synthesized in a record minimum time. *Journal of Applied Physics*, 108(8), 2010.

- [70] Loredana Protesescu, Sergii Yakunin, Olga Nazarenko, Dmitry N. Dirin, and Maksym V. Kovalenko. Low-Cost Synthesis of Highly Luminescent Colloidal Lead Halide Perovskite Nanocrystals by Wet Ball Milling. *ACS Applied Nano Materials*, 1(3):1300–1308, mar 2018.
- [71] Jun Xing, Yongbiao Zhao, Mikhail Askerka, Li Na Quan, Xiwen Gong, Weijie Zhao, Jiixin Zhao, Hairen Tan, Guankui Long, Liang Gao, Zhenyu Yang, Oleksandr Voznyy, Jiang Tang, Zheng Hong Lu, Qihua Xiong, and Edward H. Sargent. Color-stable highly luminescent sky-blue perovskite light-emitting diodes. *Nature Communications*, 9(1):1–8, 2018.
- [72] Tomas Leijtens, Kevin A. Bush, Rohit Prasanna, and Michael D. McGehee. Opportunities and challenges for tandem solar cells using metal halide perovskite semiconductors. *Nature Energy*, 3(10):828–838, 2018.
- [73] Benedikt Dänekamp, Nikolaos Droseros, Francisco Palazon, Michele Sessolo, Natalie Banerji, and Henk J. Bolink. Efficient Photo- and Electroluminescence by Trap States Passivation in Vacuum-Deposited Hybrid Perovskite Thin Films. *ACS Applied Materials and Interfaces*, 10(42):36187–36193, 2018.
- [74] Quinten A. Akkerman, Laura Martínez-Sarti, Luca Goldoni, Muhammad Imran, Dmitry Baranov, Henk J. Bolink, Francisco Palazon, and Liberato Manna. Molecular Iodine for a General Synthesis of Binary and Ternary Inorganic and Hybrid Organic-Inorganic Iodide Nanocrystals. *Chemistry of Materials*, 30(19):6915–6921, 2018.
- [75] Lingling Zheng, Danfei Zhang, Yingzhuang Ma, Zelin Lu, Zhijian Chen, Shufeng Wang, Lixin Xiao, and Qihuang Gong. Morphology control of the perovskite films for efficient solar cells. *Dalton Transactions*, 44(23):10582–10593, 2015.
- [76] Giles E. Eperon, Victor M. Burlakov, Pablo Docampo, Alain Goriely, and Henry J. Snaith. Morphological control for high performance, solution-processed planar heterojunction perovskite solar cells. *Advanced Functional Materials*, 24(1):151–157, 2014.
- [77] James M. Ball, Michael M. Lee, Andrew Hey, and Henry J. Snaith. Low-temperature processed meso-superstructured to thin-film perovskite solar cells. *Energy and Environmental Science*, 6(6):1739–1743, 2013.
- [78] Zhengguo Xiao, Cheng Bi, Yuchuan Shao, Qingfeng Dong, Qi Wang, Yongbo Yuan, Cheng-gong Wang, Yongli Gao, and Jinsong Huang. Efficient, high yield perovskite photovoltaic devices grown by interdiffusion of solution-processed precursor stacking layers. *Energy and Environmental Science*, 7(8):2619–2623, 2014.
- [79] Matthew R. Leyden, Luis K. Ono, Sonia R. Raga, Yuichi Kato, Shenghao Wang, and Yabing Qi. High performance perovskite solar cells by hybrid chemical vapor deposition. *Journal of Materials Chemistry A*, 2(44):18742–18745, 2014.
- [80] Chang-Wen Chen, Hao-Wei Kang, Sheng-Yi Hsiao, Po-Fan Yang, Kai-Ming Chiang, and Hao-Wu Lin. Efficient and Uniform Planar-Type Perovskite Solar Cells by Simple Sequential Vacuum Deposition. *Advanced Materials*, 26(38):6647–6652, 2014.
- [81] Richard Swartwout, Maximilian T. Hoerantner, and Vladimir Bulović. Scalable Deposition Methods for Large-Area Production of Perovskite Thin Films. *Energy & Environmental Materials*, 2(2):119–143, 2019.
- [82] Jorge Ávila, Cristina Momblona, Pablo P. Boix, Michele Sessolo, and Henk J. Bolink. Vapor-Deposited Perovskites: The Route to High-Performance Solar Cell Production? *Joule*, 1(3):431–442, 2017.
- [83] Francisco Palazon, Daniel Pérez-del-Rey, Benedikt Dänekamp, Chris Dreesen, Michele Sessolo, Pablo P. Boix, and Henk J. Bolink. Room-Temperature Cubic Phase Crystallization and High Stability of Vacuum-Deposited Methylammonium Lead Triiodide Thin Films for High-Efficiency Solar Cells. *Advanced Materials*, 1902692:1–6, 2019.

- [84] Constantinos C. Stoumpos, Christos D. Malliakas, and Mercouri G. Kanatzidis. Semiconducting tin and lead iodide perovskites with organic cations: Phase transitions, high mobilities, and near-infrared photoluminescent properties. *Inorganic Chemistry*, 52(15):9019–9038, 2013.
- [85] D. Prochowicz, M. Franckevis, S. M. Zakeeruddin, M. Gratzel, and J. Lewinski. Mechano-synthesis of the hybrid perovskite CH<sub>3</sub>NH<sub>3</sub>PbI<sub>3</sub>: Characterization and the corresponding solar cell efficiency. *Journal of Materials Chemistry A*, 3(41):20772–20777, 2015.
- [86] Francisco Palazon, Yousra El Ajjouri, and Henk J. Bolink. Making by Grinding: Mechanochemistry Boosts the Development of Halide Perovskites and Other Multinary Metal Halides. *Advanced Energy Materials*, 1902499:1902499, 2019.
- [87] Nico Leupold, Konstantin Schötz, Stefania Cacovich, Irene Bauer, Maximilian Schultz, Monika Daubinger, Leah Kaiser, Amelle Rebai, Jean Rousset, Anna Köhler, Philip Schulz, Ralf Moos, and Fabian Panzer. High Versatility and Stability of Mechanochemically Synthesized Halide Perovskite Powders for Optoelectronic Devices. *ACS Applied Materials & Interfaces*, 11:30259–30268, 2019.
- [88] Benjia Dou, Lance M. Wheeler, Jeffrey A. Christians, David T. Moore, Steven P. Harvey, Joseph J. Berry, Frank S. Barnes, Sean E. Shaheen, and Maikel F.A.M. Van Hest. Degradation of Highly Alloyed Metal Halide Perovskite Precursor Inks: Mechanism and Storage Solutions. *ACS Energy Letters*, 3(4):979–985, 2018.
- [89] Roberto Grisorio, Luisa De Marco, Carlo Baldisserri, Francesca Martina, Marina Serantoni, Giuseppe Gigli, and Gian Paolo Suranna. Sustainability of organic dye-sensitized solar cells: The role of chemical synthesis. *ACS Sustainable Chemistry and Engineering*, 3(4):770–777, 2015.
- [90] Atanu Jana, Mona Mittal, Aayushi Singla, and Sameer Sapra. Solvent-free, mechanochemical syntheses of bulk trihalide perovskites and their nanoparticles. *Chemical Communications*, 53(21):3046–3049, 2017.
- [91] A. M. Elseman, A. E. Shalan, M. M. Rashad, and A. M. Hassan. Experimental and simulation study for impact of different halides on the performance of planar perovskite solar cells. *Materials Science in Semiconductor Processing*, 66(April 2018):176–185, 2017.
- [92] Benjia Dou, Lance M. Wheeler, Jeffrey A. Christians, David T. Moore, Steven P. Harvey, Joseph J. Berry, Frank S. Barnes, Sean E. Shaheen, and Maikel F.A.M. Van Hest. Degradation of Highly Alloyed Metal Halide Perovskite Precursor Inks: Mechanism and Storage Solutions. *ACS Energy Letters*, 3(4):979–985, 2018.
- [93] Dominik J. Kubicki, Daniel Prochowicz, Albert Hofstetter, Marcin Sasaki, Pankaj Yadav, Dongqin Bi, Norman Pellet, Janusz Lewiński, Shaik M. Zakeeruddin, Michael Grätzel, and Lyndon Emsley. Formation of Stable Mixed Guanidinium-Methylammonium Phases with Exceptionally Long Carrier Lifetimes for High-Efficiency Lead Iodide-Based Perovskite Photovoltaics. *Journal of the American Chemical Society*, 140(9):3345–3351, 2018.
- [94] Provas Pal, Sujoy Saha, Ananya Banik, Arka Sarkar, and Kanishka Biswas. All-Solid-State Mechanochemical Synthesis and Post-Synthetic Transformation of Inorganic Perovskite-type Halides. *Chemistry - A European Journal*, 24(8):1811–1815, 2018.
- [95] Yousra El Ajjouri, Vladimir S. Chirvony, Michele Sessolo, Francisco Palazon, and Henk J. Bolink. Incorporation of potassium halides in the mechano-synthesis of inorganic perovskites: feasibility and limitations of ion-replacement and trap passivation. *RSC Advances*, 8(72):41548–41551, 2018.
- [96] Oleg Yu. Posudievsky, Natalia V. Konoshchuk, Anatoliy G. Shkavro, Volodymyr L. Karbivskiy, Vyacheslav G. Koshechko, and Vitaly D. Pokhodenko. Nanostructured Mechanochemically Prepared Hybrid Perovskites Based on PbI<sub>2</sub> and Alkylammonium Halides for Optoelectronic Applications. *ACS Applied Nano Materials*, 1(8):4145–4155, 2018.

- [97] Joachim Breternitz, Sergiu Levcenko, Hannes Hempel, Galina Gurieva, Alexandra Franz, Andreas Hoser, and Susan Schorr. Mechanochemical synthesis of the lead-free double perovskite Cs<sub>2</sub>[AgIn]Br<sub>6</sub> and its optical properties. *Journal of Physics: Energy*, 1(2):025003, 2019.
- [98] Dominik J. Kubicki, Daniel Prochowicz, Albert Hofstetter, Shaik M. Zakeeruddin, Michael Grätzel, and Lyndon Emsley. Phase Segregation in Potassium-Doped Lead Halide Perovskites from <sup>39</sup>K Solid-State NMR at 21.1 T. *Journal of the American Chemical Society*, 140(23):7232–7238, 2018.
- [99] Mohammad Mahdi Tavakoli, Wolfgang Tress, Jovana V. Milić, Dominik Kubicki, Lyndon Emsley, and Michael Grätzel. Addition of adamantylammonium iodide to hole transport layers enables highly efficient and electroluminescent perovskite solar cells. *Energy and Environmental Science*, 11(11):3310–3320, 2018.
- [100] Jovana V. Milić, Jeong Hyeok Im, Dominik J. Kubicki, Amita Ummadisingu, Ji Youn Seo, Yang Li, Marco A. Ruiz-Preciado, M. Ibrahim Dar, Shaik M. Zakeeruddin, Lyndon Emsley, and Michael Grätzel. Supramolecular Engineering for Formamidinium-Based Layered 2D Perovskite Solar Cells: Structural Complexity and Dynamics Revealed by Solid-State NMR Spectroscopy. *Advanced Energy Materials*, 9(20):1–12, apr 2019.
- [101] Nicolas Riesen, Mark Lockrey, Kate Badek, and Hans Riesen. On the origins of the green luminescence in the "zero-dimensional perovskite" Cs<sub>4</sub>PbBr<sub>6</sub>: Conclusive results from cathodoluminescence imaging. *Nanoscale*, 11(9):4001–4007, 2019.
- [102] Dominik J. Kubicki, Daniel Prochowicz, Arthur Pinon, Gabriele Stevanato, Albert Hofstetter, Shaik M. Zakeeruddin, Michael Grätzel, and Lyndon Emsley. Doping and phase segregation in Mn<sup>2+</sup>- and Co<sup>2+</sup>-doped lead halide perovskites from <sup>133</sup>Cs and <sup>1</sup>H NMR relaxation enhancement. *Journal of Materials Chemistry A*, 7(5):2326–2333, 2019.
- [103] Mohammad Mahdi Tavakoli, Hadi Tavakoli Dastjerdi, Daniel Prochowicz, Pankaj Yadav, Rouhollah Tavakoli, Michael Saliba, and Zhiyong Fan. Highly efficient and stable inverted perovskite solar cells using down-shifting quantum dots as a light management layer and moisture-assisted film growth. *Journal of Materials Chemistry A*, 7(24):14753–14760, 2019.
- [104] D. Prochowicz, P. Yadav, M. Saliba, M. Sasaki, S. M. Zakeeruddin, J. Lewiński, and M. Grätzel. Mechanochemical synthesis of pure phase mixed-cation MA<sub>x</sub>FA<sub>1-x</sub>PbI<sub>3</sub> hybrid perovskites: Photovoltaic performance and electrochemical properties. *Sustainable Energy and Fuels*, 1(4):689–693, 2017.
- [105] K. V. Manukyan, A. V. Yeghishyan, D. O. Moskovskikh, J. Kapaldo, A. Mintairov, and A. S. Mukasyan. Mechanochemical synthesis of methylammonium lead iodide perovskite. *Journal of Materials Science*, 51(19):9123–9130, oct 2016.
- [106] Dominik J. Kubicki, Daniel Prochowicz, Albert Hofstetter, Péter Péchy, Shaik M. Zakeeruddin, Michael Grätzel, and Lyndon Emsley. Cation Dynamics in Mixed-Cation (MA)<sub>x</sub>(FA)<sub>1-x</sub>PbI<sub>3</sub> Hybrid Perovskites from Solid-State NMR. *Journal of the American Chemical Society*, 139(29):10055–10061, 2017.
- [107] Yousra El Ajjouri, Francisco Palazon, Michele Sessolo, and Henk J. Bolink. Single-Source Vacuum Deposition of Mechanochemical Synthesized Inorganic Halide Perovskites. *Chemistry of Materials*, 30(21):7423–7427, 2018.
- [108] Manuel Wilke and Nicola Casati. Insight into the Mechanochemical Synthesis and Structural Evolution of Hybrid Organic–Inorganic Guanidinium Lead(II) Iodides. *Chemistry - A European Journal*, 24(67):17701–17711, 2018.
- [109] Stuart L. James, Christopher J. Adams, Carsten Bolm, Dario Braga, Paul Collier, Tomislav Friščić, Fabrizia Grepioni, Kenneth D.M. Harris, Geoff Hyett, William Jones, Anke Krebs, James Mack, Lucia Maini, A. Guy Orpen, Ivan P. Parkin, William C. Shearouse, Jonathan W.

- Steed, and Daniel C. Waddell. Playing with organic radicals as building blocks for functional molecular materials. *Chemical Society Reviews*, 41(1):413–447, 2012.
- [110] Adam A.L. Michalchuk, Ivan A. Tumanov, Sumit Konar, Simon A.J. Kimber, Colin R. Pulham, and Elena V. Boldyreva. Challenges of Mechanochemistry: Is In Situ Real-Time Quantitative Phase Analysis Always Reliable? A Case Study of Organic Salt Formation. *Advanced Science*, 4(9), 2017.
- [111] Adam A.L. Michalchuk, Karl S. Hope, Stuart R. Kennedy, Maria V. Blanco, Elena V. Boldyreva, and Colin R. Pulham. Ball-free mechanochemistry:: In situ real-time monitoring of pharmaceutical co-crystal formation by resonant acoustic mixing. *Chemical Communications*, 54(32):4033–4036, 2018.
- [112] Adam A.L. Michalchuk, Ivan A. Tumanov, Valeri A. Drebuschak, and Elena V. Boldyreva. Advances in elucidating mechanochemical complexities via implementation of a simple organic system. *Faraday Discussions*, 170:311–335, 2014.
- [113] Verena A. Hintermayr, Alexander F. Richter, Florian Ehrat, Markus Döblinger, Willem Vanderlinden, Jasmina A. Sichert, Yu Tong, Lakshminarayana Polavarapu, Jochen Feldmann, and Alexander S. Urban. Perovskite Nanoplatelets: Tuning the Optical Properties of Perovskite Nanoplatelets through Composition and Thickness by Ligand-Assisted Exfoliation. *Advanced Materials*, 28(43):9441–9441, nov 2016.
- [114] Yi Chen, Maurizio Mazzocco, and Béla Személy. Explaining the Decline of the U.S. Saving Rate: the Role of Health Expenditure. *International Economic Review*, 60(4):1–37, 2019.
- [115] Daniel Prochowicz, Pankaj Yadav, Michael Saliba, Dominik J. Kubicki, Mohammad Mahdi Tavakoli, Shaik M. Zakeeruddin, Janusz Lewiński, Lyndon Emsley, and Michael Grätzel. One-step mechanochemical incorporation of an insoluble cesium additive for high performance planar heterojunction solar cells. *Nano Energy*, 49(May):523–528, 2018.
- [116] Dominik J. Kubicki, Daniel Prochowicz, Albert Hofstetter, Péter Péchy, Shaik M. Zakeeruddin, Michael Grätzel, and Lyndon Emsley. Cation Dynamics in Mixed-Cation (MA)<sub>x</sub>(FA)<sub>1-x</sub>PbI<sub>3</sub> Hybrid Perovskites from Solid-State NMR. *Journal of the American Chemical Society*, 139(29):10055–10061, jul 2017.
- [117] Dominik J. Kubicki, Daniel Prochowicz, Albert Hofstetter, Shaik M. Zakeeruddin, Michael Grätzel, and Lyndon Emsley. Phase Segregation in Cs-, Rb- and K-Doped Mixed-Cation (MA)<sub>x</sub>(FA)<sub>1-x</sub>PbI<sub>3</sub> Hybrid Perovskites from Solid-State NMR. *Journal of the American Chemical Society*, 139(40):14173–14180, oct 2017.
- [118] Xiaozhi Lim. Grinding Chemicals Together in an Effort to be Greener. *The New York Times*, 2016.
- [119] Bianca Foggiatto. Modelling and Simulation Approaches for Exploiting Multi-Component Characteristics of Ores in Mineral Processing Circuits. 2017.
- [120] A. Shrivastava, S. Sakthivel, B. Pitchumani, and A. S. Rathore. A statistical approach for estimation of significant variables in wet attrition milling. *Powder Technology*, 211(1):46–53, 2011.
- [121] Satoshi Ohara, Akira Kondo, Hirofumi Shimoda, Kazuyoshi Sato, Hiroya Abe, and Makio Naito. Rapid mechanochemical synthesis of fine barium titanate nanoparticles. *Materials Letters*, 62(17-18):2957–2959, 2008.
- [122] Gyoung Ja Lee, Eun Kwang Park, Sun A. Yang, Jin Ju Park, Sang Don Bu, and Min Ku Lee. Rapid and direct synthesis of complex perovskite oxides through a highly energetic planetary milling. *Scientific Reports*, 7(April):1–11, 2017.
- [123] C. Frances, C. Laguérie, B. Mazzarotta, and T. Veccia. On the analysis of fine wet grinding in a batch ball mill. *Chemical Engineering Journal and the Biochemical Engineering Journal*, 63(3):141–147, 1996.

- [124] Chetan M. Patel, Z. V.P. Murthy, and Mousumi Chakraborty. Effects of operating parameters on the production of barium sulfate nanoparticles in stirred media mill. *Journal of Industrial and Engineering Chemistry*, 18(4):1450–1457, 2012.
- [125] Adam A.L. Michalchuk, Ivan A. Tumanov, and Elena V. Boldyreva. Ball size or ball mass-what matters in organic mechanochemical synthesis? *CrystEngComm*, 21(13):2174–2179, 2019.
- [126] Hannes Kulla, Franziska Fischer, Sigrid Benemann, Klaus Rademann, and Franziska Emmerling. The effect of the ball to reactant ratio on mechanochemical reaction times studied by: In situ PXRD. *CrystEngComm*, 19(28):3902–3907, 2017.
- [127] Patrick A. Julien, Ivani Malvestiti, and Tomislav Friščić. The effect of milling frequency on a mechanochemical organic reaction monitored by in situ Raman spectroscopy. *Beilstein Journal of Organic Chemistry*, 13:2160–2168, 2017.
- [128] G. B. Schaffer and J. S. Forrester. The influence of collision energy and strain accumulation on the kinetics of mechanical alloying. *Journal of Materials Science*, 32(12):3157–3162, 1997.
- [129] Francisco Palazon, Daniel Pérez-del-Rey, Benedikt Dänekamp, Chris Dreesen, Michele Sessolo, Pablo P. Boix, and Henk J. Bolink. Room-Temperature Cubic Phase Crystallization and High Stability of Vacuum-Deposited Methylammonium Lead Triiodide Thin Films for High-Efficiency Solar Cells. *Advanced Materials*, 1902692:1–6, 2019.
- [130] L Liu, A Mei, X Li, H Han, Y Dkhissi, A D Scully, R A Caruso, Y B Cheng, I Jeong, J Lee, M J Ko, K Yong, B S Richards, T L Kelly, N Pellet, M Levi, S Turri, M Levi, and S Turri. Incorporation of rubidium cations into perovskite solar cells improves photovoltaic performance. *Science*, 354(6309):206–209, 2016.
- [131] Nadja Giesbrecht, Johannes Schlipf, Irene Grill, Philipp Rieder, Vladimir Dyakonov, Thomas Bein, Achim Hartschuh, Peter Müller-Buschbaum, and Pablo Docampo. Single-crystal-like optoelectronic-properties of MAPbI<sub>3</sub> perovskite polycrystalline thin films. *Journal of Materials Chemistry A*, 6(11):4822–4828, 2018.
- [132] Francis Paquin, Jonathan Rivnay, Alberto Salleo, Natalie Stingelin, and Carlos Silva. Multi-phase semicrystalline microstructures drive exciton dissociation in neat plastic semiconductors. *J. Mater. Chem. C*, 3:10715 – 10722, 2015.
- [133] Claudio Quarti, Edoardo Mosconi, James M. Ball, Valerio D’Innocenzo, Chen Tao, Sandeep Pathak, Henry J. Snaith, Annamaria Petrozza, and Filippo De Angelis. Structural and optical properties of methylammonium lead iodide across the tetragonal to cubic phase transition: Implications for perovskite solar cells. *Energy and Environmental Science*, 9(1):155–163, 2016.
- [134] Dominik J. Kubicki, Daniel Prochowicz, Albert Hofstetter, Shaik M. Zakeeruddin, Michael Grätzel, and Lyndon Emsley. Phase Segregation in Cs-, Rb- and K-Doped Mixed-Cation (MA)<sub>x</sub>(FA)<sub>1-x</sub>PbI<sub>3</sub> Hybrid Perovskites from Solid-State NMR. *Journal of the American Chemical Society*, 139(40):14173–14180, 2017.
- [135] Amalie Dualeh, Nicolas Tétreault, Thomas Moehl, Peng Gao, Mohammad Khaja Nazeeruddin, and Michael Grätzel. Effect of annealing temperature on film morphology of organic-inorganic hybrid perovskite solid-state solar cells. *Advanced Functional Materials*, 24(21):3250–3258, 2014.
- [136] Yixin Zhao and Kai Zhu. Solution chemistry engineering toward high-efficiency perovskite solar cells. *Journal of Physical Chemistry Letters*, 5(23):4175–4186, 2014.
- [137] Zhengguo Xiao, Qingfeng Dong, Cheng Bi, Yuchuan Shao, Yongbo Yuan, and Jinsong Huang. Solvent Annealing of Perovskite-Induced Crystal Growth for Photovoltaic-Device Efficiency Enhancement. *Advanced Materials*, 26(37):6503–6509, 2014.
- [138] Julian Burschka, Norman Pellet, Soo Jin Moon, Robin Humphry-Baker, Peng Gao, Mohammad K. Nazeeruddin, and Michael Grätzel. Sequential deposition as a route to high-performance perovskite-sensitized solar cells. *Nature*, 499(7458):316–319, 2013.

- [139] Mingzhen Liu, Michael B. Johnston, and Henry J. Snaith. Efficient planar heterojunction perovskite solar cells by vapour deposition. *Nature*, 501(7467):395–398, 2013.
- [140] Qi Chen, Huanping Zhou, Ziruo Hong, Song Luo, Hsin Sheng Duan, Hsin Hua Wang, Yongsheng Liu, Gang Li, and Yang Yang. Planar heterojunction perovskite solar cells via vapor-assisted solution process. *Journal of the American Chemical Society*, 136(2):622–625, 2014.
- [141] Michele Sessolo, Cristina Momblona, Lidón Gil-Escrig, and Henk J. Bolink. Photovoltaic devices employing vacuum-deposited perovskite layers. *MRS Bulletin*, 40(8):660–666, 2015.
- [142] Olga Malinkiewicz, Aswani Yella, Yong Hui Lee, Guillermo Mínguez Espallargas, Michael Graetzel, Mohammad K. Nazeeruddin, and Henk J. Bolink. Perovskite solar cells employing organic charge-transport layers. *Nature Photonics*, 8(2):128–132, 2014.
- [143] Luis K. Ono, Shenghao Wang, Yuichi Kato, Sonia R. Raga, and Yabing Qi. Fabrication of semi-transparent perovskite films with centimeter-scale superior uniformity by the hybrid deposition method. *Energy and Environmental Science*, 7(12):3989–3993, 2014.
- [144] Dianyi Liu, Mahesh K. Gangishetty, and Timothy L. Kelly. Effect of CH<sub>3</sub>NH<sub>3</sub>PbI<sub>3</sub> thickness on device efficiency in planar heterojunction perovskite solar cells. *Journal of Materials Chemistry A*, 2(46):19873–19881, 2014.
- [145] Po Wei Liang, Chien Yi Liao, Chu Chen Chueh, Fan Zuo, Spencer T. Williams, Xu Kai Xin, Jiangjen Lin, and Alex K.Y. Jen. Additive enhanced crystallization of solution-processed perovskite for highly efficient planar-heterojunction solar cells. *Advanced Materials*, 26(22):3748–3754, 2014.
- [146] Yixin Zhao and Kai Zhu. CH<sub>3</sub>NH<sub>3</sub>Cl-assisted one-step solution growth of CH<sub>3</sub>NH<sub>3</sub>PbI<sub>3</sub>: Structure, charge-carrier dynamics, and photovoltaic properties of perovskite solar cells. *Journal of Physical Chemistry C*, 118(18):9412–9418, 2014.
- [147] Dinghan Shen, Xiao Yu, Xin Cai, Ming Peng, Yingzhuang Ma, Xin Su, Lixin Xiao, and Dechun Zou. Understanding the solvent-assisted crystallization mechanism inherent in efficient organic-inorganic halide perovskite solar cells. *Journal of Materials Chemistry A*, 2(48):20454–20461, 2014.
- [148] Francis Paquin, Jonathan Rivnay, Alberto Salleo, Natalie Stingelin, and Carlos Silva. Multi-phase semicrystalline microstructures drive exciton dissociation in neat plastic semiconductors. *J. Mater. Chem. C*, 3:10715 – 10722, 2015.
- [149] Yuhei Ogomi, Atsushi Morita, Syota Tsukamoto, Takahiro Saitho, Naotaka Fujikawa, Qing Shen, Taro Toyoda, Kenji Yoshino, Shyam S. Pandey, Tingli Ma, and Shuzi Hayase. CH<sub>3</sub>NH<sub>3</sub>S<sub>n</sub>xPb(1-x)I<sub>3</sub> perovskite solar cells covering up to 1060 nm. *Journal of Physical Chemistry Letters*, 5(6):1004–1011, 2014.
- [150] Nam Joong Jeon, Jun Hong Noh, Young Chan Kim, Woon Seok Yang, Seungchan Ryu, and Sang Il Seok. Solvent engineering for high-performance inorganic-organic hybrid perovskite solar cells. *Nature Materials*, 13(9):897–903, 2014.
- [151] Sanghyun Paek, Nara Cho, Hyeju Choi, Hanbin Jeong, Jin Sung Lim, Jun Yeon Hwang, Jae Kwan Lee, and Jaejung Ko. Improved External Quantum Efficiency from Solution-Processed (CH<sub>3</sub>NH<sub>3</sub>)PbI<sub>3</sub> Perovskite/PC71BM Planar Heterojunction for High Efficiency Hybrid Solar Cells. *Journal of Physical Chemistry C*, 118(45):25899–25905, 2014.
- [152] Jun Yuan Jeng, Yi Fang Chiang, Mu Huan Lee, Shin Rung Peng, Tzung Fang Guo, Peter Chen, and Ten Chin Wen. CH<sub>3</sub>NH<sub>3</sub>PbI<sub>3</sub> perovskite/fullerene planar-heterojunction hybrid solar cells. *Advanced Materials*, 25(27):3727–3732, 2013.
- [153] Rira Kang, Jeung Eun Kim, Jun Seok Yeo, Sehyun Lee, Ye Jin Jeon, and Dong Yu Kim. Optimized organometal halide perovskite planar hybrid solar cells via control of solvent evaporation rate. *Journal of Physical Chemistry C*, 118(46):26513–26520, 2014.



- [154] Amalie Dualeh, Thomas Moehl, Nicolas T etreault, Jo el Teuscher, Peng Gao, Mohammad Khaja Nazeeruddin, and Michael Gr atzel. Impedance spectroscopic analysis of lead iodide perovskite-sensitized solid-state solar cells. *ACS Nano*, 8(1):362–373, 2014.
- [155] Jingbi You, Ziruo Hong, Tze Bin Song, Lei Meng, Yongsheng Liu, Chengyang Jiang, Huanping Zhou, Wei Hsuan Chang, Gang Li, and Yang Yang. Moisture assisted perovskite film growth for high performance solar cells. *Applied Physics Letters*, 105(18), 2014.
- [156] Stefano Razza, Francesco Di Giacomo, Fabio Matteocci, Lucio Cin a, Alessandro Lorenzo Palma, Simone Casaluci, Petra Cameron, Alessandra D’Epifanio, Silvia Licoccia, Andrea Reale, Thomas M. Brown, and Aldo Di Carlo. Perovskite solar cells and large area modules (100 cm<sup>2</sup>) based on an air flow-assisted PbI<sub>2</sub> blade coating deposition process. *Journal of Power Sources*, 277(2015):286–291, 2015.
- [157] Li Li Gao, Cheng Xin Li, Chang Jiu Li, and Guan Jun Yang. Large-area high-efficiency perovskite solar cells based on perovskite films dried by the multi-flow air knife method in air. *Journal of Materials Chemistry A*, 5(4):1548–1557, 2017.
- [158] Xiong Li, Dongqin Bi, Chenyi Yi, Jean David D ecoppet, Jingshan Luo, Shaik Mohammed Zakeeruddin, Anders Hagfeldt, and Michael Gr atzel. A vacuum flash-assisted solution process for high-efficiency large-area perovskite solar cells. *Science*, 353(6294):58–62, 2016.
- [159] James E. Bishop, Joel A. Smith, Claire Greenland, Vikas Kumar, Naoum Vaenas, Onkar S. Game, Thomas J. Routledge, Michael Wong-Stringer, Cornelia Rodenburg, and David G. Lidzey. High-Efficiency Spray-Coated Perovskite Solar Cells Utilizing Vacuum-Assisted Solution Processing. *ACS Applied Materials and Interfaces*, 10(46):39428–39434, 2018.
- [160] Li Chen, Hui Cao, Shurong Wang, Yuxing Luo, Tao Tao, Jinwei Sun, and Mingdao Zhang. Efficient air-stable perovskite solar cells with a (FAI)<sub>0.46</sub>(MAI)<sub>0.40</sub>(MABr)<sub>0.14</sub>(PbI<sub>2</sub>)<sub>0.86</sub>(PbBr<sub>2</sub>)<sub>0.14</sub> active layer fabricated: Via a vacuum flash-assisted method under RH > 50%. *RSC Advances*, 9(18):10148–10154, 2019.
- [161] Yafei Wang, Jiang Wu, Peng Zhang, Detao Liu, Ting Zhang, Long Ji, Xiangling Gu, Zhi David Chen, and Shibin Li. Stitching triple cation perovskite by a mixed anti-solvent process for high performance perovskite solar cells. *Nano Energy*, 39:616–625, 2017.
- [162] Xiaojia Zheng, Bo Chen, Congcong Wu, and Shashank Priya. Room temperature fabrication of CH<sub>3</sub>NH<sub>3</sub>PbBr<sub>3</sub> by anti-solvent assisted crystallization approach for perovskite solar cells with fast response and small J-V hysteresis. *Nano Energy*, 17:269–278, 2015.
- [163] Min Zhang, Zenghua Wang, Bin Zhou, Xuguang Jia, Qingshan Ma, Ningyi Yuan, Xiaojia Zheng, Jianing Ding, and Wen Hua Zhang. Green Anti-Solvent Processed Planar Perovskite Solar Cells with Efficiency Beyond 19%. *Solar RRL*, 2(2):1–6, 2018.
- [164] Zhihui Liu, Miaomiao Chen, Li Wan, Yue Liu, Yulong Wang, Yisheng Gan, Zhiguang Guo, Dominik Eder, and Shimin Wang. Anti-solvent spin-coating for improving morphology of lead-free (CH<sub>3</sub>NH<sub>3</sub>)<sub>3</sub>Bi<sub>2</sub>I<sub>9</sub> perovskite films. *SN Applied Sciences*, 1(7), 2019.
- [165] Mahdi Malekshahi Byranvand, Seulki Song, Limok Pyeon, Gyeongho Kang, Gang Young Lee, and Taiho Park. Simple post annealing-free method for fabricating uniform, large grain-sized, and highly crystalline perovskite films. *Nano Energy*, 34:181–187, 2017.
- [166] Sawanta S. Mali, Hyungjin Kim, Do Heyoung Kim, and Chang Kook Hong. Anti-Solvent Assisted Crystallization Processed Methylammonium Bismuth Iodide Cuboids towards Highly Stable Lead-Free Perovskite Solar Cells. *ChemistrySelect*, 2(4):1578–1585, 2017.
- [167] Maoshu Yin, Fengxian Xie, Han Chen, Xudong Yang, Fei Ye, Enbing Bi, Yongzhen Wu, Molang Cai, and Liyuan Han. Annealing-free perovskite films by instant crystallization for efficient solar cells. *Journal of Materials Chemistry A*, 4(22):8548–8553, 2016.

- [168] Na Lin, Juan Qiao, Haopeng Dong, Fusheng Ma, and Liduo Wang. Morphology-controlled CH<sub>3</sub>NH<sub>3</sub>PbI<sub>3</sub> films by hexane-assisted one-step solution deposition for hybrid perovskite mesoscopic solar cells with high reproductivity. *Journal of Materials Chemistry A*, 3(45):22839–22845, 2015.
- [169] Koray Kara, Duygu Akin Kara, Cisem Kirbiyik, Mustafa Ersoz, Ozlem Usluer, Alejandro L. Briseno, and Mahmut Kus. Solvent washing with toluene enhances efficiency and increases reproducibility in perovskite solar cells. *RSC Advances*, 6(32):26606–26611, 2016.
- [170] NREL. Best Research-Cell Efficiencies: Rev. 04-06-2020, 2020.
- [171] Lingling Zheng, Yingzhuang Ma, Saisai Chu, Shufeng Wang, Bo Qu, Lixin Xiao, Zhijian Chen, Qihuang Gong, Zhaoxin Wu, and Xun Hou. Improved light absorption and charge transport for perovskite solar cells with rough interfaces by sequential deposition. *Nanoscale*, 6(14):8171–8176, 2014.
- [172] Jin Wook Lee, Dong Jin Seol, An Na Cho, and Nam Gyu Park. High-efficiency perovskite solar cells based on the black polymorph of HC(NH<sub>2</sub>)<sub>2</sub>PbI<sub>3</sub>. *Advanced Materials*, 26(29):4991–4998, 2014.
- [173] Pablo Docampo, Fabian C. Hanusch, Samuel D. Stranks, Markus Döblinger, Johann M. Feckl, Martin Ehrensperger, Norma K. Minar, Michael B. Johnston, Henry J. Snaith, and Thomas Bein. Solution deposition-conversion for planar heterojunction mixed halide perovskite solar cells. *Advanced Energy Materials*, 4(14):1–6, 2014.
- [174] Loredana Protesescu, Sergii Yakunin, Maryna I. Bodnarchuk, Franziska Krieg, Riccarda Caputo, Christopher H. Hendon, Ruo Xi Yang, Aron Walsh, and Maksym V. Kovalenko. Nanocrystals of Cesium Lead Halide Perovskites (CsPbX<sub>3</sub>, X = Cl, Br, and I): Novel Optoelectronic Materials Showing Bright Emission with Wide Color Gamut. *Nano Letters*, 15(6):3692–3696, 2015.
- [175] Dmitry N. Dirin, Ihor Cherniukh, Sergii Yakunin, Yevhen Shynkarenko, and Maksym V. Kovalenko. Solution-Grown CsPbBr<sub>3</sub>Perovskite Single Crystals for Photon Detection. *Chemistry of Materials*, 28(23):8470–8474, 2016.
- [176] Jorge Ávila, Cristina Momblona, Pablo Boix, Michele Sessolo, Miguel Anaya, Gabriel Lozano, Koen Vandewal, Hernán Míguez, and Henk J. Bolink. High voltage vacuum-deposited CH<sub>3</sub>NH<sub>3</sub>PbI<sub>3</sub>-CH<sub>3</sub>NH<sub>3</sub>PbI<sub>3</sub> tandem solar cells. *Energy and Environmental Science*, 11(11):3292–3297, 2018.
- [177] Vittal Prakasam, Francesco Di Giacomo, Robert Abbel, Daniel Tordera, Michele Sessolo, Gerwin Gelinck, and Henk J. Bolink. Efficient Perovskite Light-Emitting Diodes: Effect of Composition, Morphology, and Transport Layers. *ACS Applied Materials and Interfaces*, 10(48):41586–41591, 2018.
- [178] Hong Duc Pham, Lidón Gil-Escrig, Krishna Feron, Sergei Manzhos, Steve Albrecht, Henk J. Bolink, and Prashant Sonar. Boosting inverted perovskite solar cell performance by using 9,9-bis(4-diphenylaminophenyl)fluorene functionalized with triphenylamine as a dopant-free hole transporting material. *Journal of Materials Chemistry A*, 7(20):12507–12517, 2019.
- [179] Daniel Pérez-del Rey, Dávid Forgács, Eline M. Hutter, Tom J. Savenije, Dennis Nordlund, Philip Schulz, Joseph J. Berry, Michele Sessolo, and Henk J. Bolink. Strontium Insertion in Methylammonium Lead Iodide: Long Charge Carrier Lifetime and High Fill-Factor Solar Cells. *Advanced Materials*, 28(44):9839–9845, 2016.
- [180] Maria Grazia La-Placa, Dengyang Guo, Lidón Gil-Escrig, Francisco Palazon, Michele Sessolo, and Henk J. Bolink. Dual-source vacuum deposition of pure and mixed halide 2D perovskites: Thin film characterization and processing guidelines. *Journal of Materials Chemistry C*, 8(6):1902–1908, 2020.

- [181] Dávid Forgács, Daniel Pérez-Del-Rey, Jorge Ávila, Cristina Momblona, Lidón Gil-Escrig, Benedikt Dänekamp, Michele Sessolo, and Henk J. Bolink. Efficient wide band gap double cation-double halide perovskite solar cells. *Journal of Materials Chemistry A*, 5(7):3203–3207, 2017.
- [182] Tongle Bu, Xueping Liu, Yuan Zhou, Jianpeng Yi, Xin Huang, Long Luo, Junyan Xiao, Zhiliang Ku, Yong Peng, Fuzhi Huang, Yi Bing Cheng, and Jie Zhong. A novel quadruple-cation absorber for universal hysteresis elimination for high efficiency and stable perovskite solar cells. *Energy and Environmental Science*, 10(12):2509–2515, 2017.
- [183] Juan Pablo Correa-Baena, Antonio Abate, Michael Saliba, Wolfgang Tress, T. Jesper Jacobsen, Michael Grätzel, and Anders Hagfeldt. The rapid evolution of highly efficient perovskite solar cells. *Energy and Environmental Science*, 10(3):710–727, 2017.
- [184] Yang Zhou, Jie Chen, Osman M. Bakr, and Hong Tao Sun. Metal-Doped Lead Halide Perovskites: Synthesis, Properties, and Optoelectronic Applications. *Chemistry of Materials*, 30(19):6589–6613, 2018.
- [185] Christopher J. Bartel, Christopher Sutton, Bryan R. Goldsmith, Runhai Ouyang, Charles B. Musgrave, Luca M. Ghiringhelli, and Matthias Scheffler. New tolerance factor to predict the stability of perovskite oxides and halides. *Science Advances*, 5(2):1–13, 2019.
- [186] Michael Saliba, Laura M. Herz, Golnaz Sadoughi, Bernd Rech, Michael B. Johnston, Henry J. Snaith, M. T. Horantner, Lars Korte, David P. McMeekin, Nobuya Sakai, Amir Haghighirad, Waqaas Rehman, and Giles E. Eperon. A mixed-cation lead mixed-halide perovskite absorber for tandem solar cells. *Science*, 351(6269):151–155, 2016.
- [187] Giulia Longo, Lidón Gil-Escrig, Maarten J. Degen, Michele Sessolo, and Henk J. Bolink. Perovskite solar cells prepared by flash evaporation. *Chemical Communications*, 51(34):7376–7378, 2015.
- [188] Ping Fan, Di Gu, Guang Xing Liang, Jing Ting Luo, Ju Long Chen, Zhuang Hao Zheng, and Dong Ping Zhang. High-performance perovskite CH<sub>3</sub>NH<sub>3</sub>PbI<sub>3</sub> thin films for solar cells prepared by single-source physical vapour deposition. *Scientific Reports*, 6(July):1–9, 2016.
- [189] Oleg Yu Posudievsky, Natalia V. Konoshchuk, Anatoliy G. Shkavro, Volodymyr L. Karbivskiy, Vyacheslav G. Koshechko, and Vitaly D. Pokhodenko. Nanostructured Mechanochemically Prepared Hybrid Perovskites Based on PbI<sub>2</sub> and Alkylammonium Halides for Optoelectronic Applications. *ACS Applied Nano Materials*, 1(8):4145–4155, 2018.
- [190] Daniel Prochowicz, Pankaj Yadav, Michael Saliba, Marcin Sasaki, Shaik M. Zakeeruddin, Janusz Lewiński, and Michael Grätzel. Reduction in the Interfacial Trap Density of Mechanochemically Synthesized MAPbI<sub>3</sub>. *ACS Applied Materials and Interfaces*, 9(34):28418–28425, 2017.
- [191] Daniel Prochowicz, Mohammad Mahdi Tavakoli, Silver Hamill Turren-Cruz, Kavita Pandey, Michael Saliba, and Pankaj Yadav. Blue and red wavelength resolved impedance response of efficient perovskite solar cells. *Sustainable Energy and Fuels*, 2(11):2407–2411, 2018.
- [192] Francisco Palazon, Yousra El Ajjouri, Paz Sebastia-Luna, Simone Lauciello, Liberato Manna, and Henk J. Bolink. Mechanochemical synthesis of inorganic halide perovskites: Evolution of phase-purity, morphology, and photoluminescence. *Journal of Materials Chemistry C*, 7(37):11406–11410, 2019.
- [193] J. G. Brown and J. G. Brown. Diffraction of X-Rays. *X-Rays and Their Applications*, pages 95–121, 1966.
- [194] Andrei A. Bunaciu, Elena gabriela Udriștioiu, and Hassan Y. Aboul-Enein. X-Ray Diffraction: Instrumentation and Applications. *Critical Reviews in Analytical Chemistry*, 45(4):289–299, 2015.

- [195] Katherine Cantwell Cantwell. Stanford synchrotron radiation laboratory. *Synchrotron Radiation News*, 1(6):14–20, 1988.
- [196] Douglas L. Dorset and Douglas L. Dorset. Crystal Structure Analysis. *Structural Electron Crystallography*, pages 95–133, 1995.
- [197] Yves Fleming and Jérôme Bour. Xrd : Structural Analysis At List. pages 1–22.
- [198] Thomas G. Mayerhöfer and Jürgen Popp. Beer’s law derived from electromagnetic theory. *Spectrochimica Acta - Part A: Molecular and Biomolecular Spectroscopy*, 215(February):345–347, 2019.
- [199] Vidya Kothekar. Basic UV-Vis Theory, Concepts and Applications Basic UV-Vis Theory, Concepts and Applications. *Protocol*, pages 1–28, 2012.
- [200] Sally Eaton-Magaña and Christopher M. Breeding. An introduction to photoluminescence spectroscopy for diamond and its applications in gemology. *Gems and Gemology*, 52(1):2–17, 2016.
- [201] H. Barry Bebb and E. W. Williams. Photoluminescence I: Theory. *Semiconductors and Semimetals*, 8(C):181–320, 1972.
- [202] M. Aziz and A. F. Ismail. X-Ray Photoelectron Spectroscopy (XPS). *Membrane Characterization*, pages 81–93, 2017.
- [203] John L. Bahr. Photoelectron spectroscopy. *Contemporary Physics*, 14(4):329–355, 1973.
- [204] Justin Iveland, James S. Speck, Lucio Martinelli, Jacques Peretti, and Claude Weisbuch. Auger effect identified as main cause of efficiency droop in LEDs. *SPIE Newsroom*, (September 2016):2–6, 2014.
- [205] Raymond A. Serway and John W. Jewett. *Physics 6th*. 2004.
- [206] Aaron D. Weiss. Scanning Electron Microscopes. *Semiconductor International*, 6(10):90–94, 1983.
- [207] Manuel Scimeca, Simone Bischetti, Harpreet Kaur Lamsira, Rita Bonfiglio, and Elena Bonanno. Energy dispersive X-ray (EDX) microanalysis: A powerful tool in biomedical research and diagnosis. *European Journal of Histochemistry*, 62(1):89–99, 2018.
- [208] Don A Samuelson. X-Ray Microanalysis. 108.
- [209] Dianne M Finkelstein, Randall E. Schumacker, and Richard G. Lomax. A Beginner’s Guide to Thermogravimetric Analysis. *Technometrics*, 47(4):522–522, 2005.
- [210] C. H. LLOYD. A differential thermal analysis (DTA) for the heats of reaction and temperature rises produced during the setting of tooth coloured restorative materials. *Journal of Oral Rehabilitation*, 11(2):111–121, 1984.
- [211] Majed Jaradeh and Torbjörn Carlberg. Differential thermal analysis and differential scanning calorimetry studies of aluminum 3003 alloys with Zn and Cu additions. *Metallurgical and Materials Transactions A: Physical Metallurgy and Materials Science*, 38 A(9):2138–2147, 2007.
- [212] Shaoqiang Dong, Hongkun Tian, De Song, Zhenhua Yang, Donghang Yan, Yanhou Geng, and Fosong Wang. The first liquid crystalline phthalocyanine derivative capable of edge-on alignment for solution processed organic thin-film transistors. *Chemical Communications*, (21):3086–3088, 2009.
- [213] Francisco Palazon, Daniel Pérez-Del-Rey, Sergio Marras, Mirko Prato, Michele Sessolo, Henk J. Bolink, and Liberato Manna. Coating Evaporated MAPI Thin Films with Organic Molecules: Improved Stability at High Temperature and Implementation in High-Efficiency Solar Cells. *ACS Energy Letters*, 3(4):835–839, 2018.

- [214] Joseph S. Manser, Makhsud I. Saidaminov, Jeffrey A. Christians, Osman M. Bakr, and Prashant V. Kamat. Making and Breaking of Lead Halide Perovskites. *Accounts of Chemical Research*, 49(2):330–338, 2016.
- [215] Francisco Palazon, Sedat Dogan, Sergio Marras, Federico Locardi, Ilaria Nelli, Prachi Rastogi, Maurizio Ferretti, Mirko Prato, Roman Krahne, and Liberato Manna. From CsPbBr<sub>3</sub> Nano-Inks to Sintered CsPbBr<sub>3</sub>-CsPb<sub>2</sub>Br<sub>5</sub> Films via Thermal Annealing: Implications on Optoelectronic Properties. *Journal of Physical Chemistry C*, 121(21):11956–11961, 2017.
- [216] Michael Kulbak, Satyajit Gupta, Nir Kedem, Igal Levine, Tatyana Bendikov, Gary Hodes, and David Cahen. Cesium Enhances Long-Term Stability of Lead Bromide Perovskite-Based Solar Cells. *Journal of Physical Chemistry Letters*, 7(1):167–172, 2016.
- [217] Liuqi Zhang, Xiaolei Yang, Qi Jiang, Pengyang Wang, Zhigang Yin, Xingwang Zhang, Hairen Tan, Yang Michael Yang, Mingyang Wei, Brandon R. Sutherland, Edward H. Sargent, and Jingbi You. Ultra-bright and highly efficient inorganic based perovskite light-emitting diodes. *Nature Communications*, 8:1–8, 2017.
- [218] Chien-Yu Chen, Hung-Yu Lin, Kai-Ming Chiang, Wei-Lun Tsai, Yu-Ching Huang, Cheng-Si Tsao, and Hao-Wu Lin. All-Vacuum-Deposited Stoichiometrically Balanced Inorganic Cesium Lead Halide Perovskite Solar Cells with Stabilized Efficiency Exceeding 11%. *Advanced Materials*, 29(12):1605290, 2017.
- [219] Seokjin Yun, Artavazd Kirakosyan, Soon Gil Yoon, and Jihoon Choi. Scalable Synthesis of Exfoliated Organometal Halide Perovskite Nanocrystals by Ligand-Assisted Ball Milling. *ACS Sustainable Chemistry and Engineering*, 6(3):3733–3738, 2018.
- [220] Persson Kristin. Materials Data on CsPbBr<sub>3</sub> (SG:62) by Materials Project. *Materials Project*, 7, 2014.
- [221] Persson Kristin. Materials Data on Cs<sub>4</sub>PbBr<sub>6</sub> (SG:167) by Materials Project. *Materials Project*, 11, 2014.
- [222] Francisco Palazon, Guilherme Almeida, Quinten A. Akkerman, Luca De Trizio, Zhiya Dang, Mirko Prato, and Liberato Manna. Changing the Dimensionality of Cesium Lead Bromide Nanocrystals by Reversible Postsynthesis Transformations with Amines. *Chemistry of Materials*, 29(10):4167–4171, 2017.
- [223] Francisco Palazon, Carmine Urso, Luca De Trizio, Quinten Akkerman, Sergio Marras, Federico Locardi, Ilaria Nelli, Maurizio Ferretti, Mirko Prato, and Liberato Manna. Postsynthesis Transformation of Insulating Cs<sub>4</sub>PbBr<sub>6</sub> Nanocrystals into Bright Perovskite CsPbBr<sub>3</sub> through Physical and Chemical Extraction of CsBr. *ACS Energy Letters*, 2(10):2445–2448, 2017.
- [224] Xiaoya Yu, Linzhong Wu, Huicheng Hu, Min Chen, Yeshu Tan, Di Yang, Qi Pan, Qixuan Zhong, Thidarat Supasai, and Qiao Zhang. Cs<sub>4</sub>PbX<sub>6</sub> (X = Cl, Br, I) Nanocrystals: Preparation, Water-Triggered Transformation Behavior, and Anti-Counterfeiting Application. *Langmuir*, 34(35):10363–10370, 2018.
- [225] Linzhong Wu, Huicheng Hu, Yong Xu, Shu Jiang, Min Chen, Qixuan Zhong, Di Yang, Qipeng Liu, Yun Zhao, Baoquan Sun, Qiao Zhang, and Yadong Yin. From Nonluminescent Cs<sub>4</sub>PbX<sub>6</sub> (X = Cl, Br, I) Nanocrystals to Highly Luminescent CsPbX<sub>3</sub> Nanocrystals: Water-Triggered Transformation through a CsX-Stripping Mechanism. *Nano Letters*, 17(9):5799–5804, 2017.
- [226] Armel Le Bail. Whole powder pattern decomposition methods and applications: A retrospective. *Powder Diffraction*, 20(4):316–326, 2005.
- [227] Debojyoti Nath, Fouran Singh, and Ratan Das. X-ray diffraction analysis by Williamson-Hall, Halder-Wagner and size-strain plot methods of CdSe nanoparticles- a comparative study. *Materials Chemistry and Physics*, 239(July 2019):122021, 2020.

- [228] M. Nikl, K. Nitsch, E. Mihokova, K. Polak, P. Fabeni, G. P. Pazzi, M. Gurioli, R. Phani, S. Santucci, A. Scacco, and F. Somma. Optical properties of Pb<sup>2+</sup>-based aggregated phases in CsBr thin film and single crystal matrices. *Radiation Effects and Defects in Solids*, 150(1-4):341–345, 1999.
- [229] Sneha A. Kulkarni, Subodh G. Mhaisalkar, Nripan Mathews, and Pablo P. Boix. Perovskite Nanoparticles: Synthesis, Properties, and Novel Applications in Photovoltaics and LEDs. *Small Methods*, 3(1):1–16, 2019.
- [230] Roberto Grisorio, Milvia Elena Di Clemente, Elisabetta Fanizza, Ignazio Allegretta, Davide Altamura, Marinella Striccoli, Roberto Terzano, Cinzia Giannini, Mihai Irimia-Vladu, and Gian Paolo Suranna. Exploring the surface chemistry of cesium lead halide perovskite nanocrystals. *Nanoscale*, 11(3):986–999, 2019.
- [231] Dávid Forgács, Daniel Pérez-Del-Rey, Jorge Ávila, Cristina Momblona, Lidón Gil-Escrig, Benedikt Dänekamp, Michele Sessolo, and Henk J. Bolink. Efficient wide band gap double cation-double halide perovskite solar cells. *Journal of Materials Chemistry A*, 5(7):3203–3207, 2017.
- [232] Mojtaba Abdi-Jalebi, Zahra Andaji-Garmaroudi, Stefania Cacovich, Camille Stavarakas, Bertrand Philippe, Johannes M. Richter, Mejd Alsari, Edward P. Booker, Eline M. Hutter, Andrew J. Pearson, Samuele Lilliu, Tom J. Savenije, Håkan Rensmo, Giorgio Divitini, Caterina Ducati, Richard H. Friend, and Samuel D. Stranks. Maximizing and stabilizing luminescence from halide perovskites with potassium passivation. *Nature*, 555(7697):497–501, 2018.
- [233] Jae Keun Nam, Sung Uk Chai, Wonhee Cha, Yung Ji Choi, Wanjung Kim, Myung Sun Jung, Jeong Kwon, Dongho Kim, and Jong Hyeok Park. Potassium Incorporation for Enhanced Performance and Stability of Fully Inorganic Cesium Lead Halide Perovskite Solar Cells. *Nano Letters*, 17(3):2028–2033, 2017.
- [234] Zeguo Tang, Takeru Bessho, Fumiyasu Awai, Takumi Kinoshita, Masato M. Maitani, Ryota Jono, Takuro N. Murakami, Haibin Wang, Takaya Kubo, Satoshi Uchida, and Hiroshi Segawa. Hysteresis-free perovskite solar cells made of potassium-doped organometal halide perovskite. *Scientific Reports*, 7(1):1–7, 2017.
- [235] Shouqiang Huang, Bo Wang, Qi Zhang, Zhichun Li, Aidang Shan, and Liang Li. Postsynthesis Potassium-Modification Method to Improve Stability of CsPbBr<sub>3</sub> Perovskite Nanocrystals. *Advanced Optical Materials*, 6(6):1–7, 2018.
- [236] Mojtaba Abdi-Jalebi, Zahra Andaji-Garmaroudi, Andrew J. Pearson, Giorgio Divitini, Stefania Cacovich, Bertrand Philippe, Håkan Rensmo, Caterina Ducati, Richard H. Friend, and Samuel D. Stranks. Potassium-and rubidium-passivated alloyed perovskite films: Optoelectronic properties and moisture stability. *ACS Energy Letters*, 3(11):2671–2678, 2018.
- [237] A. Yu Tarasova, L. I. Isaenko, V. G. Kesler, V. M. Pashkov, A. P. Yelisseyev, N. M. Denysyuk, and O. Yu Khyzhun. Electronic structure and fundamental absorption edges of KPb<sub>2</sub>Br<sub>5</sub>, K<sub>0.5</sub>Rb<sub>0.5</sub>Pb<sub>2</sub>Br<sub>5</sub>, and RbPb<sub>2</sub>Br<sub>5</sub> single crystals. *Journal of Physics and Chemistry of Solids*, 73(5):674–682, 2012.
- [238] L. I. Isaenko, I. N. Ogorodnikov, V. A. Pustovarov, A. Yu Tarasova, and V. M. Pashkov. Optical and photoelectron spectroscopy studies of KPb<sub>2</sub>Cl<sub>5</sub> and RbPb<sub>2</sub>Cl<sub>5</sub> laser crystals. *Optical Materials*, 35(3):620–625, 2013.
- [239] Patrik Ščajev, Chuanjiang Qin, Ramunas Aleksiejunas, Paulius Baronas, Saulius Miasojedovas, Takashi Fujihara, Toshinori Matsushima, Chihaya Adachi, and Saulius Juršėnas. Diffusion Enhancement in Highly Excited MAPbI<sub>3</sub> Perovskite Layers with Additives. *Journal of Physical Chemistry Letters*, 9(12):3167–3172, 2018.

- [240] Vladimir S. Chirvony, Soranyel González-Carrero, Isaac Suárez, Raquel E. Galian, Michele Sessolo, Henk J. Bolink, Juan P. Martínez-Pastor, and Julia Pérez-Prieto. Delayed Luminescence in Lead Halide Perovskite Nanocrystals. *Journal of Physical Chemistry C*, 121(24):13381–13390, 2017.
- [241] Liang Kuai, Yusheng Wang, Zixiang Zhang, Yingguo Yang, Yuanshuai Qin, Tian Wu, Yajuan Li, Youyong Li, Tao Song, Xingyu Gao, Lu Wang, and Baoquan Sun. Passivating Crystal Boundaries with Potassium-Rich Phase in Organic Halide Perovskite. *Solar RRL*, 3(5):1–9, 2019.
- [242] Yin Yang, Lili Wu, Xia Hao, Zeguo Tang, Huagui Lai, Jingquan Zhang, Wenwu Wang, and Lianghuan Feng. Beneficial effects of potassium iodide incorporation on grain boundaries and interfaces of perovskite solar cells. *RSC Advances*, 9(49):28561–28568, 2019.
- [243] Fei Yang, Hongting Chen, Rui Zhang, Xiaoke Liu, Weizhuo Zhang, Ji Bin Zhang, Feng Gao, and Lei Wang. Efficient and Spectrally Stable Blue Perovskite Light-Emitting Diodes Based on Potassium Passivated Nanocrystals. *Advanced Functional Materials*, 30(10):1–7, 2020.
- [244] Jun Nan Yang, Yang Song, Ji Song Yao, Kun Hua Wang, Jing Jing Wang, Bai Sheng Zhu, Ming Ming Yao, Sami Ur Rahman, Yi Feng Lan, Feng Jia Fan, and Hong Bin Yao. Potassium Bromide Surface Passivation on CsPbI<sub>3</sub>-xBr<sub>x</sub> Nanocrystals for Efficient and Stable Pure Red Perovskite Light-Emitting Diodes. *Journal of the American Chemical Society*, 142(6):2956–2967, 2020.
- [245] D. B. Mitzi, C. A. Feild, Z. Schlesinger, and R. B. Laibowitz. Transport, optical, and magnetic properties of the conducting halide perovskite ch<sub>3</sub>nh<sub>3</sub>sn<sub>3</sub>, 1995.
- [246] Nakita K. Noel, Samuel D. Stranks, Antonio Abate, Christian Wehrenfennig, Simone Guarnera, Amir Abbas Haghighirad, Aditya Sadhanala, Giles E. Eperon, Sandeep K. Pathak, Michael B. Johnston, Annamaria Petrozza, Laura M. Herz, and Henry J. Snaith. Lead-free organic-inorganic tin halide perovskites for photovoltaic applications. *Energy and Environmental Science*, 7(9):3061–3068, 2014.
- [247] Ziran Zhao, Feidan Gu, Yunlong Li, Weihai Sun, Senyun Ye, Haixia Rao, Zhiwei Liu, Zuqiang Bian, and Chunhui Huang. Mixed-Organic-Cation Tin Iodide for Lead-Free Perovskite Solar Cells with an Efficiency of 8.12%. *Advanced Science*, 4(11), 2017.
- [248] Junke Jiang, Chidozie K. Onwudinanti, Ross A. Hatton, Peter A. Bobbert, and Shuxia Tao. Stabilizing Lead-Free All-Inorganic Tin Halide Perovskites by Ion Exchange. *Journal of Physical Chemistry C*, 122(31):17660–17667, 2018.
- [249] Zhuo Chen, Jian J. Wang, Yuhang Ren, Chonglong Yu, and Kai Shum. Schottky solar cells based on CsSnI<sub>3</sub> thin-films. *Applied Physics Letters*, 101(9), 2012.
- [250] Mulmudi Hemant Kumar, Sabba Dharani, Wei Lin Leong, Pablo P. Boix, Rajiv Ramanujam Prabhakar, Tom Baikie, Chen Shi, Hong Ding, Ramamoorthy Ramesh, Mark Asta, Michael Graetzel, Subodh G. Mhaisalkar, and Nripan Mathews. Lead-Free Halide Perovskite Solar Cells with High Photocurrents Realized Through Vacancy Modulation. *Advanced Materials*, 26(41):7122–7127, 2014.
- [251] Aifei Wang, Yanyan Guo, Faheem Muhammad, and Zhengtao Deng. Controlled Synthesis of Lead-Free Cesium Tin Halide Perovskite Cubic Nanocages with High Stability. *Chemistry of Materials*, 29(15):6493–6501, 2017.
- [252] Ning Wang, Yuanyuan Zhou, Ming Gang Ju, Hector F. Garces, Tao Ding, Shuping Pang, Xiao Cheng Zeng, Nitin P. Padture, and Xiao Wei Sun. Heterojunction-Depleted Lead-Free Perovskite Solar Cells with Coarse-Grained B- $\gamma$ -CsSnI<sub>3</sub> Thin Films. *Advanced Energy Materials*, 6(24):1–10, 2016.

- [253] Satyajit Gupta, Tatyana Bendikov, Gary Hodes, and David Cahen. CsSnBr<sub>3</sub>, A Lead-Free Halide Perovskite for Long-Term Solar Cell Application: Insights on SnF<sub>2</sub> Addition. *ACS Energy Letters*, 1(5):1028–1033, 2016.
- [254] Athanassios G. Kontos, Andreas Kaltzoglou, Eirini Siranidi, Dimitrios Palles, Giasemi K. Angeli, Michalis K. Arfanis, Vassilis Psycharis, Yannis S. Raptis, Efstratios I. Kamitsos, Pantelis N. Trikalitis, Constantinos C. Stoumpos, Mercouri G. Kanatzidis, and Polycarpus Falaras. Structural Stability, Vibrational Properties, and Photoluminescence in CsSnI<sub>3</sub> Perovskite upon the Addition of SnF<sub>2</sub>. *Inorganic Chemistry*, 56(1):84–91, 2017.
- [255] Peng Xu, Shiyu Chen, Hong Jun Xiang, Xin Gao Gong, and Su Huai Wei. Influence of defects and synthesis conditions on the photovoltaic performance of perovskite semiconductor CsSnI<sub>3</sub>. *Chemistry of Materials*, 26(20):6068–6072, 2014.
- [256] In Chung, Jung Hwan Song, Jino Im, John Androulakis, Christos D. Malliakas, Hao Li, Arthur J. Freeman, John T. Kenney, and Mercouri G. Kanatzidis. CsSnI<sub>3</sub>: Semiconductor or metal? High electrical conductivity and strong near-infrared photoluminescence from a single material. High hole mobility and phase-transitions. *Journal of the American Chemical Society*, 134(20):8579–8587, 2012.
- [257] Feng Hao, Constantinos C. Stoumpos, Duyen Hanh Cao, Robert P.H. Chang, and Mercouri G. Kanatzidis. Lead-free solid-state organic-inorganic halide perovskite solar cells. *Nature Photonics*, 8(6):489–494, 2014.
- [258] Ling Yi Huang and Walter R.L. Lambrecht. Electronic band structure, phonons, and exciton binding energies of halide perovskites CsSnCl<sub>3</sub>, CsSnBr<sub>3</sub>, and CsSnI<sub>3</sub>. *Physical Review B - Condensed Matter and Materials Physics*, 88(16):1–12, 2013.
- [259] Wenzhe Li, Jiangwei Li, Jiaoli Li, Jiandong Fan, Yaohua Mai, and Liduo Wang. Additive-assisted construction of all-inorganic CsSnI<sub>3</sub> mesoscopic perovskite solar cells with superior thermal stability up to 473 K. *Journal of Materials Chemistry A*, 4(43):17104–17110, 2016.
- [260] Satyajit Gupta, Tatyana Bendikov, Gary Hodes, and David Cahen. CsSnBr<sub>3</sub>, A Lead-Free Halide Perovskite for Long-Term Solar Cell Application: Insights on SnF<sub>2</sub> Addition. *ACS Energy Letters*, 1(5):1028–1033, 2016.
- [261] Christopher Grote and Robert F. Berger. Strain Tuning of Tin-Halide and Lead-Halide Perovskites: A First-Principles Atomic and Electronic Structure Study. *Journal of Physical Chemistry C*, 119(40):22832–22837, 2015.
- [262] David E. Scaife, Paul F. Weller, and Wayne G. Fisher. Crystal preparation and properties of cesium tin(II) trihalides. *Journal of Solid State Chemistry*, 9(3):308–314, 1974.
- [263] C. G. Ma, V. Krasnenko, and M. G. Brik. First-principles calculations of different (001) surface terminations of three cubic perovskites CsCaBr<sub>3</sub>, CsGeBr<sub>3</sub> and CsSnBr<sub>3</sub>. *Journal of Physics and Chemistry of Solids*, 115(001):289–299, 2018.
- [264] E. Lora Da Silva, Jonathan M. Skelton, Stephen C. Parker, and Aron Walsh. Phase stability and transformations in the halide perovskite CsSnI<sub>3</sub>. *Physical Review B - Condensed Matter and Materials Physics*, 91(14):1–12, 2015.
- [265] K. P. Marshall, M. Walker, R. I. Walton, and R. A. Hatton. Elucidating the role of the hole-extracting electrode on the stability and efficiency of inverted CsSnI<sub>3</sub>/C60 perovskite photovoltaics. *Journal of Materials Chemistry A*, 5(41):21836–21845, 2017.
- [266] K. P. Marshall, M. Walker, R. I. Walton, and R. A. Hatton. Enhanced stability and efficiency in hole-transport-layer-free CsSnI<sub>3</sub> perovskite photovoltaics. *Nature Energy*, 1(12):1–9, 2016.
- [267] Young Kwang Jung, Ji Hwan Lee, Aron Walsh, and Aloysius Soon. Influence of Rb/Cs Cation-Exchange on Inorganic Sn Halide Perovskites: From Chemical Structure to Physical Properties. *Chemistry of Materials*, 29(7):3181–3188, 2017.



- [268] Kenneth P. Marshall, Shuxia Tao, Marc Walker, Daniel S. Cook, James Lloyd-Hughes, Silvia Varagnolo, Anjana Wijesekara, David Walker, Richard I. Walton, and Ross A. Hatton. Cs 1-: X Rb x SnI 3 light harvesting semiconductors for perovskite photovoltaics. *Materials Chemistry Frontiers*, 2(8):1515–1522, 2018.
- [269] Tze Bin Song, Takamichi Yokoyama, Constantinos C. Stoumpos, Jenna Logsdon, Duyen H. Cao, Michael R. Wasielewski, Shinji Aramaki, and Mercouri G. Kanatzidis. Importance of reducing vapor atmosphere in the fabrication of Tin-based perovskite solar cells. *Journal of the American Chemical Society*, 139(2):836–842, 2017.
- [270] Fabio Chiarella, Andrea Zappettini, Francesca Licci, Ivo Borriello, Giovanni Cantele, Domenico Ninno, Antonio Cassinese, and Ruggero Vaglio. Combined experimental and theoretical investigation of optical, structural, and electronic properties of C H3 N H3 Sn X3 thin films (X=Cl,Br). *Physical Review B - Condensed Matter and Materials Physics*, 77(4):1–6, 2008.
- [271] Weiqiang Liao, Dewei Zhao, Yue Yu, Corey R. Grice, Changlei Wang, Alexander J. Cimaroli, Philip Schulz, Weiwei Meng, Kai Zhu, Ren Gen Xiong, and Yanfa Yan. Lead-Free Inverted Planar Formamidinium Tin Triiodide Perovskite Solar Cells Achieving Power Conversion Efficiencies up to 6.22%. *Advanced Materials*, 28(42):9333–9340, 2016.
- [272] Seon Joo Lee, Seong Sik Shin, Young Chan Kim, Dasom Kim, Tae Kyu Ahn, Jun Hong Noh, Jangwon Seo, and Sang Il Seok. Fabrication of Efficient Formamidinium Tin Iodide Perovskite Solar Cells through SnF2-Pyrazine Complex. *Journal of the American Chemical Society*, 138(12):3974–3977, 2016.
- [273] Shuyan Shao, Jian Liu, Giuseppe Portale, Hong Hua Fang, Graeme R. Blake, Gert H. ten Brink, L. Jan Anton Koster, and Maria Antonietta Loi. Highly Reproducible Sn-Based Hybrid Perovskite Solar Cells with 9% Efficiency. *Advanced Energy Materials*, 8(4), 2018.
- [274] Dewei Zhao, Cong Chen, Changlei Wang, Maxwell M. Junda, Zhaoning Song, Corey R. Grice, Yue Yu, Chongwen Li, Biwas Subedi, Nikolas J. Podraza, Xingzhong Zhao, Guojia Fang, Ren Gen Xiong, Kai Zhu, and Yanfa Yan. Efficient two-terminal all-perovskite tandem solar cells enabled by high-quality low-bandgap absorber layers. *Nature Energy*, 3(12):1093–1100, 2018.
- [275] In Chung, Byunghong Lee, Jiaqing He, Robert P.H. Chang, and Mercouri G. Kanatzidis. All-solid-state dye-sensitized solar cells with high efficiency. *Nature*, 485(7399):486–489, 2012.
- [276] Byunghong Lee, Constantinos C. Stoumpos, Nanjia Zhou, Feng Hao, Christos Malliakas, Chen Yu Yeh, Tobin J. Marks, Mercouri G. Kanatzidis, and Robert P.H. Chang. Air-stable molecular semiconducting iodosalts for solar cell applications: Cs<sub>2</sub>SnI<sub>6</sub> as a hole conductor. *Journal of the American Chemical Society*, 136(43):15379–15385, 2014.
- [277] Zewen Xiao, Hechang Lei, Xiao Zhang, Yuanyuan Zhou, Hideo Hosono, Toshio Kamiya, and United States. \*,1,2 1. pages 1–20, 2015.
- [278] Andreas Kaltzoglou, Maria Antoniadou, Athanassios G. Kontos, Constantinos C. Stoumpos, Dorothea Perganti, Eirini Siranidi, Vasilios Raptis, Kalliopi Trohidou, Vassilis Psycharis, Mercouri G. Kanatzidis, and Polycarpos Falaras. Optical-Vibrational Properties of the Cs<sub>2</sub>SnX<sub>6</sub> (X = Cl, Br, I) Defect Perovskites and Hole-Transport Efficiency in Dye-Sensitized Solar Cells. *Journal of Physical Chemistry C*, 120(22):11777–11785, 2016.
- [279] Sebastian F. Hoeffler, Gregor Trimmel, and Thomas Rath. Progress on lead-free metal halide perovskites for photovoltaic applications: a review. *Monatshefte fur Chemie*, 148(5):795–826, 2017.
- [280] Bayrammurad Saporov, Jon Paul Sun, Weiwei Meng, Zewen Xiao, Hsin Sheng Duan, Oki Gunawan, Donghyeop Shin, Ian G. Hill, Yanfa Yan, and David B. Mitzi. Thin-Film Deposition and Characterization of a Sn-Deficient Perovskite Derivative Cs<sub>2</sub>SnI<sub>6</sub>. *Chemistry of Materials*, 28(7):2315–2322, 2016.

- [281] Zhifang Tan, Jinghui Li, Cheng Zhang, Zha Li, Qingsong Hu, Zewen Xiao, Toshio Kamiya, Hideo Hosono, Guangda Niu, Efrat Lifshitz, Yibing Cheng, and Jiang Tang. Highly Efficient Blue-Emitting Bi-Doped Cs<sub>2</sub>SnCl<sub>6</sub> Perovskite Variant: Photoluminescence Induced by Impurity Doping. *Advanced Functional Materials*, 28(29):1–10, 2018.
- [282] Annalise E. Maughan, Alex M. Ganose, Andrew M. Candia, Juliette T. Granger, David O. Scanlon, and James R. Neilson. Anharmonicity and Octahedral Tilting in Hybrid Vacancy-Ordered Double Perovskites. *Chemistry of Materials*, 30(2):472–483, 2018.
- [283] Annalise E. Maughan, Alex M. Ganose, Mohammed A. Almaker, David O. Scanlon, and James R. Neilson. Tolerance Factor and Cooperative Tilting Effects in Vacancy-Ordered Double Perovskite Halides. *Chemistry of Materials*, 30(11):3909–3919, 2018.
- [284] Zewen Xiao, Yuanyuan Zhou, Hideo Hosono, and Toshio Kamiya. Intrinsic defects in a photovoltaic perovskite variant Cs<sub>2</sub>SnI<sub>6</sub>. *Physical Chemistry Chemical Physics*, 17(29):18900–18903, 2015.
- [285] Xiaofeng Qiu, Bingqiang Cao, Shuai Yuan, Xiangfeng Chen, Zhiwen Qiu, Yanan Jiang, Qian Ye, Hongqiang Wang, Haibo Zeng, Jian Liu, and Mercuri G. Kanatzidis. From unstable CsSnI<sub>3</sub> to air-stable Cs<sub>2</sub>SnI<sub>6</sub>: A lead-free perovskite solar cell light absorber with bandgap of 1.48 eV and high absorption coefficient. *Solar Energy Materials and Solar Cells*, 159:227–234, 2017.
- [286] Jack Chun Ren Ke, David J. Lewis, Alex S. Walton, Ben F. Spencer, Paul O’Brien, Andrew G. Thomas, and Wendy R. Flavell. Ambient-air-stable inorganic Cs<sub>2</sub>SnI<sub>6</sub> double perovskite thin films: Via aerosol-assisted chemical vapour deposition. *Journal of Materials Chemistry A*, 6(24):11205–11214, 2018.
- [287] Byunghong Lee, Anthony Krenselewski, Sung Il Baik, David N. Seidman, and Robert P.H. Chang. Solution processing of air-stable molecular semiconducting iodosalts, Cs<sub>2</sub>SnI<sub>6</sub>-: XBr<sub>x</sub>, for potential solar cell applications. *Sustainable Energy and Fuels*, 1(4):710–724, 2017.
- [288] Joachim Breternitz, Sergiu Levcenko, Hannes Hempel, Galina Gurieva, Alexandra Franz, Andreas Hoser, and Susan Schorr. Mechanochemical synthesis of the lead-free double perovskite Cs<sub>2</sub>[AgIn]Br<sub>6</sub> and its optical properties. *Journal of Physics: Energy*, 1(2):025003, 2019.
- [289] Tomas Leijtens, Rohit Prasanna, Aryeh Gold-Parker, Michael F. Toney, and Michael D. McGehee. Mechanism of Tin Oxidation and Stabilization by Lead Substitution in Tin Halide Perovskites. *ACS Energy Letters*, 2(9):2159–2165, 2017.
- [290] Yangyang Dang, Yian Zhou, Xiaolong Liu, Dianxing Ju, Shengqing Xia, Haibing Xia, and Xutang Tao. Formation of Hybrid Perovskite Tin Iodide Single Crystals by Top-Seeded Solution Growth. *Angewandte Chemie - International Edition*, 55(10):3447–3450, 2016.
- [291] Ioannis Lignos, Loredana Protesescu, Dilara Börte Emiroglu, Richard MacEiczyk, Simon Schneider, Maksym V. Kovalenko, and Andrew J. DeMello. Unveiling the Shape Evolution and Halide-Ion-Segregation in Blue-Emitting Formamidinium Lead Halide Perovskite Nanocrystals Using an Automated Microfluidic Platform. *Nano Letters*, 18(2):1246–1252, 2018.
- [292] Kang Wang, Zhiwen Jin, Lei Liang, Hui Bian, Dongliang Bai, Haoran Wang, Jingru Zhang, Qian Wang, and Liu Shengzhong. All-inorganic cesium lead iodide perovskite solar cells with stabilized efficiency beyond 15%. *Nature Communications*, 9(1):1–8, 2018.
- [293] Peak Decreases. 119:37–40, 1990.
- [294] Golnaz Sadoughi, David E. Starr, Evelyn Handick, Samuel D. Stranks, Mihaela Gorgoi, Regan G. Wilks, Marcus Bär, and Henry J. Snaith. Observation and Mediation of the Presence of Metallic Lead in Organic-Inorganic Perovskite Films. *ACS Applied Materials and Interfaces*, 7(24):13440–13444, 2015.

- [295] Himchan Cho, Su Hun Jeong, Min Ho Park, Young Hoon Kim, Christoph Wolf, Chang Lyoul Lee, Jin Hyuck Heo, Aditya Sadhanala, No Soung Myoung, Seunghyup Yoo, Sang Hyuk Im, Richard H. Friend, and Tae Woo Lee. Overcoming the electroluminescence efficiency limitations of perovskite light-emitting diodes. *Science*, 350(6265):1222–1225, 2015.
- [296] Wei Zhang, Sandeep Pathak, Nobuya Sakai, Thomas Stergiopoulos, Pabitra K. Nayak, Nakita K. Noel, Amir A. Haghighirad, Victor M. Burlakov, Dane W. Dequilettes, Aditya Sadhanala, Wenzhe Li, Liduo Wang, David S. Ginger, Richard H. Friend, and Henry J. Snaith. Enhanced optoelectronic quality of perovskite thin films with hypophosphorous acid for planar heterojunction solar cells. *Nature Communications*, 6(May):1–9, 2015.
- [297] A. Calloni, A. Abate, G. Bussetti, G. Berti, R. Yivlialin, F. Ciccacci, and L. Duò. Stability of Organic Cations in Solution-Processed CH<sub>3</sub>NH<sub>3</sub>PbI<sub>3</sub> Perovskites: Formation of Modified Surface Layers. *Journal of Physical Chemistry C*, 119(37):21329–21335, 2015.
- [298] Ghada Abdelmageed, Leila Jewell, Kaitlin Hellier, Lydia Seymour, Binbin Luo, Frank Bridges, Jin Z. Zhang, and Sue Carter. Mechanisms for light induced degradation in MAPbI<sub>3</sub> perovskite thin films and solar cells. *Applied Physics Letters*, 109(23):0–5, 2016.
- [299] Daniele Meggiolaro, Silvia G. Motti, Edoardo Mosconi, Alex J. Barker, James Ball, Carlo Andrea Riccardo Perini, Felix Deschler, Annamaria Petrozza, and Filippo De Angelis. Iodine chemistry determines the defect tolerance of lead-halide perovskites. *Energy and Environmental Science*, 11(3):702–713, 2018.
- [300] Weijun Ke, Constantinos C. Stoumpos, and Mercouri G. Kanatzidis. “Unleaded” Perovskites: Status Quo and Future Prospects of Tin-Based Perovskite Solar Cells. *Advanced Materials*, 31(47), 2019.
- [301] Dewei Zhao, Yue Yu, Changlei Wang, Weiqiang Liao, Niraj Shrestha, Corey R. Grice, Alexander J. Cimaroli, Lei Guan, Randy J. Ellingson, Kai Zhu, Xingzhong Zhao, Ren Gen Xiong, and Yanfa Yan. Low-bandgap mixed tin-lead iodide perovskite absorbers with long carrier lifetimes for all-perovskite tandem solar cells. *Nature Energy*, 2(4):1–7, 2017.
- [302] Seon Joo Lee, Seong Sik Shin, Jino Im, Tae Kyu Ahn, Jun Hong Noh, Nam Joong Jeon, Sang Il Seok, and Jangwon Seo. Reducing Carrier Density in Formamidinium Tin Perovskites and Its Beneficial Effects on Stability and Efficiency of Perovskite Solar Cells. *ACS Energy Letters*, 3(1):46–53, 2018.
- [303] Jeongjoo Lee, You-Hyun Seo, Sung-Nam Kwon, Do-Hyung Kim, Seokhoon Jang, Hyeonwoo Jung, Youngu Lee, Hasitha Weerasinghe, Taehyo Kim, Jin Young Kim, Doojin Vak, and Seok-In Na. Photovoltaic Devices: Slot-Die and Roll-to-Roll Processed Single Junction Organic Photovoltaic Cells with the Highest Efficiency (Adv. Energy Mater. 36/2019). *Advanced Energy Materials*, 9(36):1970138, 2019.
- [304] John M. Warman, Matthijs P. De Haas, Gerald Dicker, Ferdinand C. Grozema, Jorge Piris, and Michael G. Debije. Charge mobilities in organic semiconducting materials determined by pulse-radiolysis time-resolved microwave conductivity:  $\pi$ -Bond-conjugated polymers versus  $\pi$ - $\pi$ -stacked discotics. *Chemistry of Materials*, 16(23):4600–4609, 2004.
- [305] Tomas Leijtens, Rohit Prasanna, Kevin A. Bush, Giles E. Eperon, James A. Raiford, Aryeh Gold-Parker, Eli J. Wolf, Simon A. Swifter, Caleb C. Boyd, Hsin Ping Wang, Michael F. Toney, Stacey F. Bent, and Michael D. McGehee. Tin-lead halide perovskites with improved thermal and air stability for efficient all-perovskite tandem solar cells. *Sustainable Energy and Fuels*, 2(11):2450–2459, 2018.
- [306] María C. Gélvez-Rueda, Eline M. Hutter, Duyen H. Cao, Nicolas Renaud, Constantinos C. Stoumpos, Joseph T. Hupp, Tom J. Savenije, Mercouri G. Kanatzidis, and Ferdinand C. Grozema. Interconversion between Free Charges and Bound Excitons in 2D Hybrid Lead Halide Perovskites. *Journal of Physical Chemistry C*, 121(47):26566–26574, 2017.

- [307] María C. Gélvez-Rueda, Nicolas Renaud, and Ferdinand C. Grozema. Temperature Dependent Charge Carrier Dynamics in Formamidinium Lead Iodide Perovskite. *Journal of Physical Chemistry C*, 121(42):23392–23397, 2017.
- [308] María C. Gélvez-Rueda, Duyen H. Cao, Sameer Patwardhan, Nicolas Renaud, Constantinos C. Stoumpos, George C. Schatz, Joseph T. Hupp, Omar K. Farha, Tom J. Savenije, Mercouri G. Kanatzidis, and Ferdinand C. Grozema. Effect of cation rotation on charge dynamics in hybrid lead halide perovskites. *Journal of Physical Chemistry C*, 120(30):16577–16585, 2016.
- [309] Johanna L. Miller. Unusual defect physics underlies perovskite solar cells’ exceptional performance. *Physics Today*, 67(5):13–15, 2014.
- [310] Nicolas Leblanc, Nicolas Mercier, Leokadiya Zorina, Sergey Simonov, Pascale Auban-Senzier, and Claude Pasquier. Large spontaneous polarization and clear hysteresis loop of a room-temperature hybrid ferroelectric based on mixed-halide [Bi 3 Cl 2 ] polar chains and methylviologen dication. *Journal of the American Chemical Society*, 133(38):14924–14927, 2011.
- [311] Miaoqiang Lyu, Jung Ho Yun, Molang Cai, Yalong Jiao, Paul V. Bernhardt, Meng Zhang, Qiong Wang, Aijun Du, Hongxia Wang, Gang Liu, and Lianzhou Wang. Organic–inorganic bismuth (III)-based material: A lead-free, air-stable and solution-processable light-absorber beyond organolead perovskites. *Nano Research*, 9(3):692–702, 2016.
- [312] D. B. Mitzi and P. Brock. Structure and optical properties of several organic-inorganic hybrids containing corner-sharing chains of bismuth iodide octahedra. *Inorganic Chemistry*, 40(9):2096–2104, 2001.
- [313] P. Szklarz, A. Pietraszko, R. Jakubas, G. Bator, P. Zieliński, and M. Gałazka. Structure, phase transitions and molecular dynamics of [C(NH 2)3]3[M2I9], M = Sb, Bi. *Journal of Physics Condensed Matter*, 20(25), 2008.
- [314] Nichole Cates Miller and María Bernechea. Research Update: Bismuth based materials for photovoltaics. *APL Materials*, 6(8), 2018.
- [315] T Kawai, A Ishii, and T Kitamura. Optical Absorption in Band-Edge Region of ( C H 3 N H 3 ) 3 B i 2 I 9 Single Crystals, 1996.
- [316] Kyle M. McCall, Constantinos C. Stoumpos, Svetlana S. Kostina, Mercouri G. Kanatzidis, and Bruce W. Wessels. Strong Electron-Phonon Coupling and Self-Trapped Excitons in the Defect Halide Perovskites A3M2I9 (A = Cs, Rb; M = Bi, Sb). *Chemistry of Materials*, 29(9):4129–4145, 2017.
- [317] Zhaoyang Qi, Xianwei Fu, Tiefeng Yang, Dong Li, Peng Fan, Honglai Li, Feng Jiang, Lihui Li, Ziyu Luo, Xiujuan Zhuang, and Anlian Pan. Highly stable lead-free Cs3Bi2I9 perovskite nanoplates for photodetection applications. *Nano Research*, 12(8):1894–1899, 2019.
- [318] Seong Sik Shin, Juan Pablo Correa Baena, Rachel C. Kurchin, Alex Polizzotti, Jason Jungwan Yoo, Sarah Wieghold, Mouni G. Bawendi, and Tonio Buonassisi. Solvent-Engineering Method to Deposit Compact Bismuth-Based Thin Films: Mechanism and Application to Photovoltaics. *Chemistry of Materials*, 30(2):336–343, 2018.
- [319] Trilok Singh, Ashish Kulkarni, Masashi Ikegami, and Tsutomu Miyasaka. Effect of Electron Transporting Layer on Bismuth-Based Lead-Free Perovskite (CH3NH3)3 Bi2I9 for Photovoltaic Applications. *ACS Applied Materials and Interfaces*, 8(23):14542–14547, 2016.
- [320] Anna J. Lehner, Douglas H. Fabini, Hayden A. Evans, Claire Alice Hébert, Sara R. Smock, Jerry Hu, Hengbin Wang, Josef W. Zwanziger, Michael L. Chabinyc, and Ram Seshadri. Crystal and Electronic Structures of Complex Bismuth Iodides A3Bi2I9 (A = K, Rb, Cs) Related to Perovskite: Aiding the Rational Design of Photovoltaics. *Chemistry of Materials*, 27(20):7137–7148, 2015.

- [321] Quinten A. Akkerman, Valerio D’Innocenzo, Sara Accornero, Alice Scarpellini, Annamaria Petrozza, Mirko Prato, and Liberato Manna. Tuning the optical properties of cesium lead halide perovskite nanocrystals by anion exchange reactions. *Journal of the American Chemical Society*, 137(32):10276–10281, 2015.
- [322] Shijing Sun, Satoshi Tominaka, Jung Hoon Lee, Fei Xie, Paul D. Bristowe, and Anthony K. Cheetham. Synthesis, crystal structure, and properties of a perovskite-related bismuth phase,  $(\text{NH}_4)_3\text{Bi}_2\text{I}_9$ . *APL Materials*, 4(3), 2016.
- [323] Byung Wook Park, Bertrand Philippe, Xiaoliang Zhang, Håkan Rensmo, Gerrit Boschloo, and Erik M.J. Johansson. Bismuth Based Hybrid Perovskites  $\text{A}_3\text{Bi}_2\text{I}_9$  (A: Methylammonium or Cesium) for Solar Cell Application. *Advanced Materials*, 27(43):6806–6813, 2015.
- [324] Zheng Zhang, Xiaowei Li, Xiaohong Xia, Zhuo Wang, Zhongbing Huang, Binglong Lei, and Yun Gao. High-Quality  $(\text{CH}_3\text{NH}_3)_3\text{Bi}_2\text{I}_9$  Film-Based Solar Cells: Pushing Efficiency up to 1.64%. *Journal of Physical Chemistry Letters*, 8(17):4300–4307, 2017.
- [325] Haijin Li, Congcong Wu, Yongke Yan, Bo Chi, Jian Pu, Jian Li, and Shashank Priya. Fabrication of Lead-Free  $(\text{CH}_3\text{NH}_3)_3\text{Bi}_2\text{I}_9$  Perovskite Photovoltaics in Ethanol Solvent. *ChemSusChem*, 10(20):3994–3998, 2017.
- [326] Jaya Pal, Amit Bhunia, Sudip Chakraborty, Suman Manna, Shyamashis Das, Anweshi Dewan, Shouvik Datta, and Angshuman Nag. Synthesis and Optical Properties of Colloidal  $\text{M}_3\text{Bi}_2\text{I}_9$  ( $\text{M} = \text{Cs}, \text{Rb}$ ) Perovskite Nanocrystals. *Journal of Physical Chemistry C*, 122(19):10643–10649, 2018.
- [327] Kelsey K. Bass, Laura Estergreen, Christopher N. Savory, John Buckeridge, David O. Scanlon, Peter I. Djurovich, Stephen E. Bradforth, Mark E. Thompson, and Brent C. Melot. Vibronic Structure in Room Temperature Photoluminescence of the Halide Perovskite  $\text{Cs}_3\text{Bi}_2\text{Br}_9$ . *Inorganic Chemistry*, 56(1):42–45, 2017.
- [328] Valentina Chiricenco, M. Caraman, I. I. Rusu, and L. Leontie. On the luminescence of  $\text{GaS}(\text{Cu})$  single crystals. *Journal of Luminescence*, 101(1-2):71–77, 2003.
- [329] Giuseppe M. Paternò, Nimai Mishra, Alex J. Barker, Zhiya Dang, Guglielmo Lanzani, Liberato Manna, and Annamaria Petrozza. Broadband Defects Emission and Enhanced Ligand Raman Scattering in 0D  $\text{Cs}_3\text{Bi}_2\text{I}_9$  Colloidal Nanocrystals. *Advanced Functional Materials*, 29(21):1–6, 2019.
- [330] Meiyong Leng, Zhengwu Chen, Ying Yang, Zha Li, Kai Zeng, Kanghua Li, Guangda Niu, Yisu He, Qingchao Zhou, and Jiang Tang. Lead-Free, Blue Emitting Bismuth Halide Perovskite Quantum Dots. *Angewandte Chemie - International Edition*, 55(48):15012–15016, 2016.
- [331] Meiyong Leng, Ying Yang, Zhengwu Chen, Wanru Gao, Jian Zhang, Guangda Niu, Dengbing Li, Haisheng Song, Jianbing Zhang, Song Jin, and Jiang Tang. Surface Passivation of Bismuth-Based Perovskite Variant Quantum Dots to Achieve Efficient Blue Emission. *Nano Letters*, 18(9):6076–6083, 2018.
- [332] Arka Sarkar, Paribesh Acharyya, Ranjan Sasmal, Provas Pal, Sarit S. Agasti, and Kanishka Biswas. Synthesis of Ultrathin Few-Layer 2D Nanoplates of Halide Perovskite  $\text{Cs}_3\text{Bi}_2\text{I}_9$  and Single-Nanoplate Super-Resolved Fluorescence Microscopy. *Inorganic Chemistry*, 57(24):15558–15565, 2018.
- [333] Linyuan Lian, Guangmei Zhai, Feng Cheng, Yong Xia, Moyan Zheng, Jiangping Ke, Mingyang Gao, Huan Liu, Daoli Zhang, Luying Li, Jianbo Gao, Jiang Tang, and Jianbing Zhang. Colloidal synthesis of lead-free all-inorganic cesium bismuth bromide perovskite nanoplatelets. *CrystEngComm*, 20(46):7473–7478, 2018.
- [334] Bin Yang, Junsheng Chen, Feng Hong, Xin Mao, Kaibo Zheng, Songqiu Yang, Yajuan Li, Tōnu Pullerits, Weiqiao Deng, and Keli Han. Lead-Free, Air-Stable All-Inorganic Cesium Bismuth Halide Perovskite Nanocrystals. *Angewandte Chemie - International Edition*, 56(41):12471–12475, 2017.

- [335] Quinten A. Akkerman, Silvia Genaro Motti, Ajay Ram Srimath Kandada, Edoardo Mosconi, Valerio D’Innocenzo, Giovanni Bertoni, Sergio Marras, Brett A. Kamino, Laura Miranda, Filippo De Angelis, Annamaria Petrozza, Mirko Prato, and Liberato Manna. Solution Synthesis Approach to Colloidal Cesium Lead Halide Perovskite Nanoplatelets with Monolayer-Level Thickness Control. *Journal of the American Chemical Society*, 138(3):1010–1016, 2016.
- [336] Francisco Palazon, Sedat Dogan, Sergio Marras, Federico Locardi, Ilaria Nelli, Prachi Rastogi, Maurizio Ferretti, Mirko Prato, Roman Krahne, and Liberato Manna. From CsPbBr<sub>3</sub> Nano-Inks to Sintered CsPbBr<sub>3</sub>-CsPb<sub>2</sub>Br<sub>5</sub> Films via Thermal Annealing: Implications on Optoelectronic Properties. *Journal of Physical Chemistry C*, 121(21):11956–11961, 2017.
- [337] QuanxinZhang. that generally depends on the asperity size and stress drop and on the resistance of the matrix. This effective radius R. *Electrochemistry Communications*, 12(6308):92–96, 2010.
- [338] Feng Liu, Yaohong Zhang, Chao Ding, Syuusuke Kobayashi, Takuya Izuishi, Naoki Nakazawa, Taro Toyoda, Tsuyoshi Ohta, Shuzi Hayase, Takashi Minemoto, Kenji Yoshino, Songyuan Dai, and Qing Shen. Highly Luminescent Phase-Stable CsPbI<sub>3</sub> Perovskite Quantum Dots Achieving Near 100% Absolute Photoluminescence Quantum Yield. *ACS Nano*, 11(10):10373–10383, 2017.
- [339] Chr Kn Møller. Crystal structure and photoconductivity of caesium plumbohalides, 1958.
- [340] Benjamin T. Diroll, Georgian Nedelcu, Maksym V. Kovalenko, and Richard D. Schaller. High-Temperature Photoluminescence of CsPbX<sub>3</sub> (X = Cl, Br, I) Nanocrystals. *Advanced Functional Materials*, 27(21):1–7, 2017.
- [341] F. Palazon, F. Di Stasio, S. Lauciello, R. Krahne, M. Prato, and L. Manna. Evolution of CsPbBr<sub>3</sub> nanocrystals upon post-synthesis annealing under an inert atmosphere. *Journal of Materials Chemistry C*, 4(39):9179–9182, 2016.
- [342] Xi Yuan, Pengtao Jing, Ji Li, Maobin Wei, Jie Hua, Jialong Zhao, Lianhua Tian, and Jiaming Li. Temperature-dependent photoluminescence of inorganic perovskite nanocrystal films. *RSC Advances*, 6(82):78311–78316, 2016.
- [343] Constantinos C Stoumpos, Christos D Malliakas, and Mercouri G Kanatzidis. <Ic401215X\_Si\_001.Pdf>.









